UNIVERSITY OF SOUTHAMPTON

Numerical study of high speed separated flows

Kangping Zhang

A thesis submitted for the degree of Doctor of Philosophy

Aerodynamics and Flight Mechanics Research Group
FACULTY OF ENGINEERING AND THE ENVIRONMENT

March 2014

UNIVERSITY OF SOUTHAMPTON

ABSTRACT

FACULTY OF ENGINEERING AND THE ENVIRONMENT

Numerical study of high speed separated flows

by Kangping Zhang

Instability, flow separation and transition are essential aspects of high speed flows with shock-wave/boundary-layer interaction. Supersonic flows with jet injection, compression ramp and cavity, either individually or in combination, are numerically studied by solving directly the compressible Navier-Stokes equations to better understand the transition of high speed laminar boundary layer to turbulence and the influence of flow separation. A sonic jet injected into a Mach 6.69 crossflow is studied through both two-dimensional (2D) and three-dimensional (3D) simulations. Effects of the momentum flux ratio (J_p) are evaluated. A 3D global instability is observed with a critical value of J_p below but close to 0.1. The most unstable mode is found to have a spanwise wavelength of 8 times the incoming boundary layer displacement thickness. Streamwise vortices are observed at the saturated stage. Ramp flow is studied at Mach number 4.8 and Reynolds numbers of 6,843 and 3,422. The flow is stable in two dimensions. Simulations in 3D show that the flow is globally unstable at higher Reynolds number, while being stable at the lower Reynolds number, suggesting that a critical Reynolds number for instability exists between these two Reynolds numbers. The most unstable mode for the ramp flow has a spanwise wavelength of 12 times the incoming boundary layer displacement thickness. For the ramp flow with higher Reynolds number, breakdown to turbulence is observed, however this occurs downstream of the region where the global mode is active, suggesting that the global mode does not lead to transition directly but provides a disturbance seed which gives rise to transient growth, leading to streaks which subsequently breakdown to turbulence. Effects of an upstream cavity and a downstream sonic jet injection on the Mach 4.8 ramp flow are studied. It is found that the jet could greatly increase flow separation while the cavity has little effect. Similar configuration is studied for a supersonic ramp flow at Mach 5.3 with a Mach 3.6 jet injection for a practical application to rocket stage separation. Effects of cavity and jet on laminar boundary layer separation are firstly evaluated through a 2D parametric study. Ramp flow with turbulent boundary layer is simulated at greater detail in 3D. Then a slot jet is switched on to evaluate the laminar and turbulent inflow effect on the flow separation. A shorter separation bubble is observed, though the rates at which the separation point moves upstream are comparable for laminar and turbulent inflow.

Contents

List of Figures

List of Tables

Nomenclature

Roman Symbols

a	Speed of sound
a_{l1}, a_{l2}	Runge-Kutta constants
a, b	Stretching coefficients for mesh generation
B	Eigenvector of the flux Jacobian
C	A coefficient used in turbulence generator
c_p	Specific heat capacity at constant pressure
C_f	Skin friction coefficient
d	Distance to the closest wall, or a coefficient used in turbulence generator
e	Internal energy
E	Total energy
$\tilde{F}$	Modified form of the numerical flux term
$G(x,t)$	Green's function
J_p	Momentum flux ratio of jet injection
k^*	Thermal conductivity
L^*	Characteristic length
L_s	Distance from the slot centre to the plate leading edge
L_y	Height of the computational domain
L_z	Spanwise length
N_x, N_y, N_z	Number of the streamweise, wall-normal and spanwise grid points
N	A coefficient used in turbulence generator
p_{0_j}	Stagnation pressure of the jet
p_j	Pressure across jet
$\bar{p}$	Mean pressure
p_∞	Free stream pressure
q_i	Heat flux vector
Q	The second invariant
M	Mach number
M_j	Mach number at jet exit
N_z^*	Half of the total stretched spanwise grid number used in Chapter 6

Pr	Prandtl number
Re	Reynolds number used in the calculation
Re_{x^*}	Local Reynolds number based on the dimensional x coordinate
R_x	$\sqrt{Re_{x^*}}$
r	Recovery factor
St	Stanton number
t	Time
T	Temperature
u, v, w	Non-dimensional streamwise, wall-normal and spanwise velocities
$U(y; Re)$	Parallel basic flow for stability analysis
u_*	The friction velocity
ν	The local kinematic viscosity of the fluid
τ_w	The wall shear stress
$\dot{U}_i,\ \ddot{U}_i$	First and second derivative of U_i
v_g	Group velocity
w	Slot width for the jet
w'	Spanwise perturbation
$x,\ y,\ z$	Non-dimensional streamwise, wall-normal and spanwise coordinates
x_0^* and x_0	Dimensioinal (unit: mm) and nondimensional distance from the plate leading edge to the computational domain inlet
$x_c,\ y_c$	Centre of the Gaussian profile
$< . >$	Span-averaged quantity

Greek Symbols

α_0	Angle of jet injection to upstream wall
α	Wavenumber
γ	Ratio of specific heats
δ_{ij}	Kronecker delta function used in Chapter 1 and Chapter 2
δ	Jet profile control parameter
δ_0^*	Dimensional boundary layer displacement thickness at inlet (unit: mm)
δ_{in}	Inflow boundary layer thickness at 99% of the free stream velocity
Δ	A scale factor
Δh	Grid spacing
Δt	Time step
ξ^*	Rescaled dimensional value used in similarity solution
η	Rescaled non-dimensional value used in similarity solution
$\varepsilon(x,\ y)$	Parameter measuring the mean square fluctuation of the spanwise velocity

$\xi,\ \eta$	Uniform streamwise and wall-normal coordinates in the computational domain
ϑ^l	A sensor separating highly vortical region from high shear region
κ	A constant in TVD with a standard range from 0.0 to 0.7
λ	Spanwise wavelength of the added perturbation for stability study
μ	Dynamic viscosity
ρ	Density
σ	Maximum attainable temporal growth rate
τ	Shear stress tensor
$\Phi(y)$	Eigenfunction used in instability analysis
$\tilde{\Phi}$	Term used in TVD/ACM procedure
$\tilde{\phi}^l$	Components of $\tilde{\Phi}$
ϕ^l	Standard TVD 'limiter'
ω	Complex frequency in Chapter 1, or angular frequency in turbulence generator
ω_x	Streamwise vorticity quantity

Abbreviation

2D, 3D	Two-dimensional, three-dimensional
ACM	Artificial compression method
BL	Boundary layer
CFD	Computational fluid dynamics
CRVP	Counter-rotating vortex pair
CPU	Central processing unit
DES	Detached eddy simulation
DNS	Direct numerical simulation
DLR	German Aerospace Center
GPU	Graphics processing unit
LES	Large eddy simulation
LST	Linear stability theory
NS	Navier-Stokes
RANS	Reynolds-averaged Navier-Stokes
RMS	Root-mean-square
SL	Shear layer
SGS	Sub-grid scale
SW	Shock-wave
SWBLI	Shock-wave/boundary-layer interaction
TKE	Turbulence kinetic energy

TVD	Total variation diminishing
URANS	Unsteady Reynolds-averaged Navier-Stokes

Subscripts

∞	Free stream quantities
0	Stagnation values unless otherwise specified
i, j, k	The streamwise, wall-normal and spanwise direction
$inflow$	Value at inflow boundary on the wall
j	Injected jet
$normal$	normal to the wall
sep	Value at the upstream separation point
w	Wall quantity

Superscripts

$*$	Dimensional quantities
$'$	Fluctuating values

Acknowledgements

Four years have passed when I piled up all the chapters and saw this thesis being printed out page by page, I realized that my PhD study is finishing and I need to say goodbye to my supervisors, colleagues and all the friends I met in Southampton.

I must say thank you to my honoured supervisors, Prof. Neil Sandham and Dr. Zhiwei Hu. Without their help, it is impossible for me to study in Southampton and finish my PhD in time. Neil is a well-read professor with a strategic vision. He is honest and selfishless. He always guides me out of the mist to the correct way. Zhiwei is a very nice and kind supervisor. He is warm-hearted and friendly. He always supervise and help me in details. He cares for all my progress. Our meeting scenario will always be in my mind. I will always be moved when I think of your help correcting my paper time after time. I appreciate all of your help. Computational time on Hector was provided by UK Turbulence Consortium under EPSRC grant EP/G069581/1 and EPSRC Project 'Thermal and Reactive Flow Simulation on High-End Computers' under Grand EP/J016381/2.

I would say thank you to my internal examiner Dr. Graham Roberts, who was my transfer examiner and always gives me beneficial advices. I also want to say thank you for the supports from my external examiner Prof. Qin Ning who is a kind person and travelled long distance for my viva. Thanks for the support from Prof. Philippa Reed and Prof. Gary Coleman. I would also like to thank Prof. Xin Zhang for his support at the initial stage of my PhD studying in Southampton.

I want to take this opportunity to say thank you to my home supervisor Prof. Hua Li in NUDT, China. I obtained my Master degree from Prof. Hua Li and get his generosity and selfless support on studying abroad to realize my dream of childhood. I also obtained great help on studying and life from him. Thank you for Chinese Scholarship Council who supported my living costs here. I hope I can do my best to reward my motherland.

Thanks for Dr. Wen Liu, Dr. Roderick Johnstone and Dr. Nico De Tulio from whom I obtained much help on programming and debugging. Thanks to my nice colleagues in Room 2071, Tizard building including Dr. R.J. Koopmans, Dr. Matthew Palmer, Dr. Agissilaos Kourmatzis, Dr. Andy Ju, Dr. Sina Haeri, Dr. Jianyue Zhu, Patrick Bechlars, Jacques Vdk, Javier Otero, Angeliki Laskari. I also benefit much to discuss with Jeroen and Andrea. With them I spent my happy and substantial UK days.

(to be continued)

It is my pleasure to know so many good friends like Prof. Jing Lei, Prof. Ping Zhang, Prof. Qunzheng Zhang, Prof. Guanhong Li, Prof. Chunhua Zhang, Dr. Qifeng Chen, Dr. Ping Wang, Dr. Yongchun Liang, Dr. Prateek Mustafi, Junling Bie, Ruofan Zhang, Jingjing Wang, Amy, Jianfa Zhang, Shufeng Zhang, Susan, Bo Wang, Berber Zhang, Anna Guo and Joyce Fu. They helped a lot in daily life. Thanks for the Skydive club, which help me realize my first static Line jump, Jubilee sport centre, the Eagles Badminton Club and Recreational Badminton Club which made my spare time fulfilled and offer chance to know good friends like Gayan, Aingaran, Rebecca James, Chris Merrifield, Jenny Whiffin, Chris Hugs and Louise Palmour.

Finally, I want to say thank you to my family. Because of some historic reason, my parents did not study at university and lived in a county. But both of them knew the importance of knowledge and wisdom. They afforded too much for my elder sister and I. They are also taking care of my little daughter, heart and soul. They should have a healthy and happy old age. My dear elder sister is talented and hard working as well. I always learnt a lot from her even from childhood when I was a mischievous boy. In the past 10 years whenever I was studying in Changsha 1,000 km away from home or Southampton more than 8,000 km away, my sister has been working in the Kangjie Middle School in Yuncheng and taking more responsibility to care my parents which makes it possible for me to set my mind on study. I also need to say thank you to my dear daughter. Each time after our video meeting and heard your child's tone, I feel happiness and have endless power to make our future life better.

Looking forward, China is waiting for me. No matter where I am, I will always remember the attitude to research learnt from my supervisors and try my best to devote all I could in all my endeavours.

Kangping Zhang
Southampton, U.K.

To my beloved parents, Baozhi Zhang and Ailian Lou, and my dear elder sister, Leping Zhang, your suport is my endless power. To my beloved 5-years old daughter Zexin Zhang. I am so sorry that I cannot accompany with you in the early days of your life. . . .

Chapter 1

Introduction

1.1 Background and motivation

With the development of materials and propulsion systems, high speed commercial aircraft have become more cost effective. Despite the tragedy of the Concorde accident on 25 July 2000 (Orlebar, 2004), many next generation high speed commercial aircraft have been designed and studied, such as HISAC (Grewe et al., 2010), LAPCAT (Serre and Defoort, 2009) and ZEHST (Defoort et al., 2012). On the other hand, issues on supersonic flow are also confronted in rocket applications. In high speed flows, the adverse pressure gradient caused by shock-wave/boundary-layer interaction (SWBLI) can lead to flow separation, which significantly affects the aerothermodynamic loads such as wall pressure, skin friction and heat transfer. The separated flow induced by SWBLI can also cause flow instability. Investigations on SWBLI started in the 1940s by Ferri (1940) and the phenomenon has been studied extensively since Dolling (2001). However, some important aspects of flow with SWBLI are still lack of clear explanation and accurate prediction by either numerical simulations or laboratory experiments. These include the unsteady pressure loading caused by flow unsteadiness, as stated by Adams (2000), Dolling (2001), Touber (2010) and Touber and Sandham (2009a,b, 2011), and flow transition from laminar to turbulent especially at high Mach numbers, which is closely related with flow instability (Robinet, 2007).

For practical applications to supersonic intakes and rockets, simplified configurations of ramp, jet, cavity and shock-wave impingement onto a solid wall are the main components, which involve complex flowfields due to SWBLI and flow separation. High speed flow over a ramp, with jet injection and shock-wave impingement also has been used to study the instability of high speed SWBLI. Predicting these flows accurately is of both practical importance on the design and evaluation of aerospace vehicles and academic value in developing theories of flow stability and transition. Further study with experiments for more detailed description of various phenomena related to SWBLI relies

on new measurement techniques and material improvements, such as the liquid crystal technique for heat-flux measurement with higher spatial resolution used by Roberts and East (1996) and Roberts et al. (1998) who successfully observed enhanced heat transfer upstream and to the side of the jet which is injected into high speed crossflow. For numerical predictions, the use of more accurate methods is constrained by the capability of computer hardware. As stated by Hadjadj and Dussauge (2009), numerical methods based on the Reynolds-averaged Navier-Stokes (RANS) and the unsteady Reynolds-averaged Navier-Stokes (URANS) approaches fail to capture the unsteadiness in the shock-wave system observed in experiments and cannot predict fluctuating surface pressure and heat transfer accurately. Recently, more powerful simulation tools, such as the large eddy simulation (LES) approach used by Larchevêque et al. (2004), Loginov et al. (2006), Grilli et al. (2012) and the direct numerical simulations (DNS) approach used by Adams (1998, 2000), Marini (2001), Pagella et al. (2002, 2004), Yao et al. (2006), Brès and Colonius (2008) and Lüdeke and Sandham (2010), have been applied for more substantive understanding on SWBLI based on configurations of jet-in-crossflow, ramp flow, supersonic flow with cavity, and shock-wave impingement flow.

For a flow with shock-wave impingement, Pagella et al. (2002, 2004) performed 2D investigations of small-amplitude disturbances in boundary layers with an impinging shock and for a compression ramp, using linear stability theory and DNS at a freestream Mach number of 4.8. The same flow conditions were applied to a ramp and a flat plate with an impinging shock. The wall-pressure distribution, streamwise velocity components and skin friction coefficient distribution between ramp flow and impinging shock flow agreed well when the impinging shock angle was set two times the ramp angle, illustrating the free interaction theory concept (Chapman et al., 1957) that boundary layer is independent of the kind of SWBLI when Reynolds number is small (Arnal and Délery, 2001b). However, differences near the corner and the impinging shock were also observed by both linear stability theory and DNS of small-amplitude disturbances. The reason was that the amplification rate for the flow with an impinging shock was slightly damped near the shock impingement point. Robinet (2007) showed that flow with shock-wave impingement became 3D and unsteady with certain spanwise wavelengths as the incident shock angle increased. After a critical shock angle, flow became unstable at a wider range of spanwise wavelengths. He suggested that the physical origin for the 3D behaviour was a 3D stationary global instability. However, his work focused on flow with shock impingement only. Stability studies on other flow configurations such as ramp flow and jet in crossflow could enrich the understanding of SWBLI with flow transition. In view of progress made in the past in these areas, part of the present contribution extends this approach for ramp and jet flows, aiming at proving the existence of the same instability phenomena. The present work will also investigate a practical problem of a model rocket separation, which includes both 2D and 3D cavity, ramp and jet injection studies.

A detailed introduction to the relevant studies and theory are provided in the following

sections. Studies on a jet in high speed crossflow, supersonic ramp flow, supersonic flow with cavity and the flows with multiple elements are introduced firstly, then the instability theory and the introduction of DNS are briefly presented, followed by the objectives of the present study.

1.2 Separated flows with SWBLI

1.2.1 Jet in high speed crossflow

The review of a jet in crossflow here concentrates on a sonic or supersonic transverse jet injected into a supersonic crossflow. Such jets can be used for vehicle control both in high altitude rarefied flow and in lower altitude continuum flow. At high altitude where aerodynamic forces are insufficient, a lateral jet is mainly used to steer rockets or re-entry vehicles to improve their manoeuvrability. Lower in the atmosphere, lateral jets may be used for force enhancement, fuel injection and mixing. They may also be used in an intake to promote transition to turbulence.

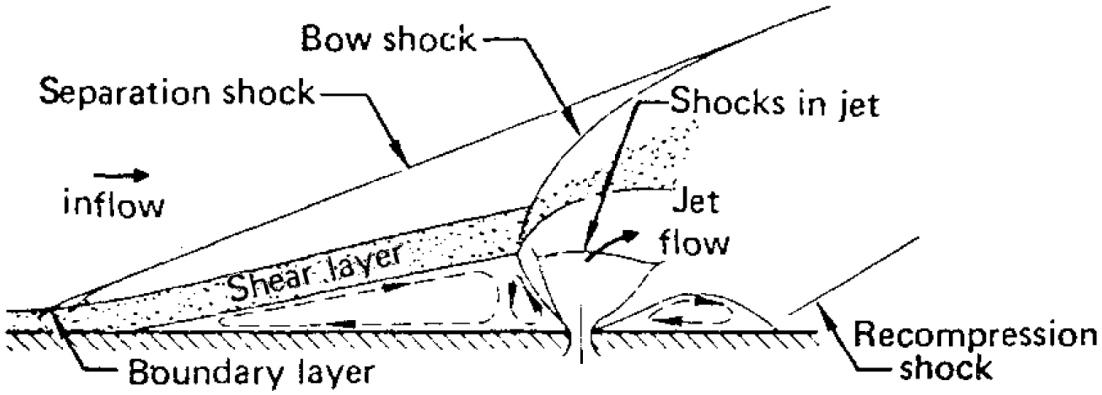

FIGURE 1.1: Sketch of main flow features for jet in crossflow (Spaid, 1975).

Taking a 2D supersonic flow over flat plate with a sonic jet injection as an example, flow mechanisms and main structures are summarized in figure 1.1 as sketched by Spaid (1975). The jet is injected through the bottom wall slot perpendicular to the supersonic crossflow and obstructs the freestream flow, inducing a bow shock in the flow before turning downstream. Two recirculation regions are formed upstream and downstream of the jet injection slot near the wall where the flow is deflected. Because of the upstream flow separation, a detached shear layer and separation shock are formed which interact with the bow shock and shocks around the jet. Downstream of the jet, flow reattachment causes recompression shocks.

Early research on jets in supersonic crossflow was mainly experimental and focused on the flowfield around the injection port. Based on the laminar incoming flow, Cubbison

et al. (1961) and Kaufman (1967) noticed an increase in both upstream and downstream surface pressure caused by the interaction between the jet and the laminar incoming flow. Cubbison et al. (1961) studied a sonic jet injected into supersonic laminar flow and found that the Mach number and jet pressure ratio, rather than the Reynolds number, were the two main factors affecting the pressure distribution. Based on turbulent boundary layer on a flat plate, Spaid (1975) found that variations in external Mach number, Reynolds number and jet-to-main-stream pressure ratio in his 2D experiment had little influence on the upstream surface pressure amplification. Theoretical analysis (Lee and Barfield, 1971) determined the 2D flowfield near the injection port based on coupling the jet flowfield with the external flowfield. They showed that the upstream high-pressure region extended when the jet total pressure increased.

To provide experimental data for numerical analysis, Powrie (1996) did extensive experiments on 2D slot and 3D sonic/supersonic round jet injection into a Mach 6.69 flat plate flow and obtained data on surface pressure, separation length, as well as flow visualisations. For a 2D slot jet, Powrie found that the separation length is determined by the momentum flux ratio (J_p) which is defined as

$$J_p = \frac{p_{0_j} w}{p_\infty L_s}, \tag{1.1}$$

where p_{0_j} is the stagnation pressure of the jet, w is the jet slot width, p_∞ is the freestream pressure and L_s is the distance from the slot centre to the leading edge of the flat plate. For a 3D round jet, a counter-rotating vortex pair (CRVP) was observed ahead of the jet, while longitudinal streamwise Görtler vortices were observed downstream of jet exit. Roberts et al. (1998) used the same facility as Powrie to quantify the heat transfer using thermochromic liquid crystals. The boundary layer developing on the plate ahead of the jet was also laminar. It was found that the heat fluxes along flow reattachment lines were up to several times those of the undisturbed laminar flow. Warburton (1999) carried out experiments for Mach number 9.84 in low density flow for cones and flat plates. The mean free path was estimated at 0.118 mm and Knudsen numbers of around 0.03, which corresponded to the continuum end of the transition to rarefied flow. Several techniques were used for the surface flow measurement and flow visualisation for axisymmetric slot injection and for 3D sonic orifice injection into a 3D flat plate. Numerical simulations were also carried out and compared with the experimental results, showing that improved result could be obtained by using a finer mesh.

Further developments of computing techniques and numerical methods at the end of 20^{th} century make numerical simulation more significant in the research of jet in crossflow. LES by Jones and Wille (1996), Bonelli et al. (2013) and Watanabe et al. (2012), DES by Peterson et al. (2006) and DNS by Yao et al. (2006), Qin and Redlich (1999), Gajbhiye (2010) and Ilak et al. (2012) were all applied in crossflow jet calculation. RANS is considered not accurate enough for jet in crossflow. It is unable to capture the large

scale flow structures due to the closure models for turbulence, as stated by Kim and Benson (1992), Fric and Roshiko (1994), You et al. (2013) and Yao et al. (2006).

Jones and Wille (1996) performed imcompressible flow simulations of air jet injected perpendicularly into a duct with cross-flowing air, the velocity ratio of jet to the freestream was 7.34. They compared results from the standard Smagorinsky-Lilly model, a one-equation model and a dynamic model, and found small differences between different subgrid-scale (SGS) models, but the LES results compared reasonable well with experimental data. Bonelli et al. (2013) used LES on a Mach 0.8 high-density ratio hydrogen jet into still air to study turbulent mixing of compressible jets. They admitted that it was challenging to study compressible jets with the presence of high density gradients. Result agreed with theoretical findings by comparing the decay rate of normalized centreline velocity. Watanabe et al. (2012) studied effect of injectant species from a circular hole on jet injection in Mach 1.9 crossflow based on the same jet-to-crossflow momentum flux ratio ($\gamma_j p_j M_j^2 / \gamma_\infty p_\infty M_\infty^2$) (Papamoschou and Hubbard, 1993). Result showed that different species affected the velocity field, turbulence kinetic energy (TKE) and the mixing efficiency. Peterson et al. (2006) showed the ability of detached eddy simulations (DES) for a complex flowfield around jet injection in supersonic crossflow. Although DES sometimes predicted the mean and fluctuating quantities better than RANS, there was still an over-prediction of the jet plume height and width compared with experiments done by Hollo et al. (1994).

Kawai and Lele (2007, 2009) carried out simulations on an under-expanded sonic jet injected into a supersonic turbulent crossflow with LES to study the physics of jet mixing underlying the unsteady phenomena observed. They demonstrated the importance of eddy structures on the behaviour of jet stirring and mixing. However, Yao et al. (2006) concluded that there was inevitable uncertainty in LES brought in by the SGS model, which was key to the prediction of small scale fluctuations. They considered that LES couldn't provide knowledge at a fundamental level. With DNS performed for square jet injection, Yao et al. (2006) also observed the CRVP as was reported in experiments by Andreopoulos and Rod (1984), Kelsot et al. (1996) and Powrie (1996).

Numerical work based on Powrie's 2D slot case was first done by Qin and Redlich (1999) using 2D DNS with the assumption that flow is laminar in the computational domain and SWBLI would not trigger transition. They successfully predicted the massively separated upstream interaction region, agreeing well with experimental observations. Therefore laminar flows was proved to dominate the upstream interaction, although the simulation was limited to 2D steady flow. Gajbhiye (2010) simulated a sonic jet in supersonic crossflow and also compared with Powrie's experiments. It was found that the flow became unsteady when the momentum flux ratio (J_p) increased to 0.4 and widening the slot jet pushed the separation point move further upstream.

Schlatter et al. (2011) found two foundamental frequencies for the self-sustained oscillations of a round jet in crossflow. Both frequencies were related to a separated region downstream of the jet. Ilak et al. (2012) studied instability of a round jet in crossflow at low values of the velocity inflow ratio by DNS. Results showed how a self-sustained oscillation developed in the shear layer downstream of the jet which was also the source of instability.

1.2.2 Supersonic ramp flow

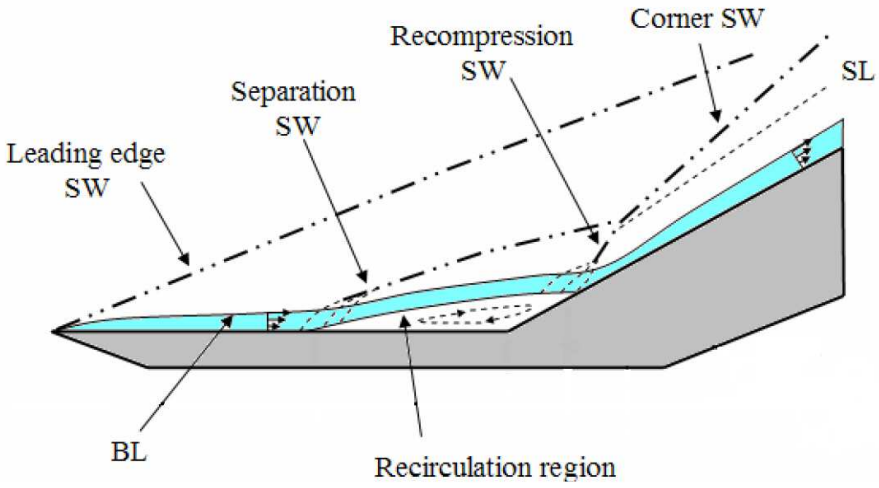

FIGURE 1.2: Schematic representation of 2D ramp flow (BL = Boundary Layer, SW = Shock-Wave, SL = Shear Layer) from Bono et al. (2008).

Ramp flow has been frequently used to study the flowfield with shock-wave interaction, owing to its relatively simple configuration while still including all the main flow characteristics for SWBLI. Taking the flowfield over a ramp with a laminar boundary layer as an example, as shown in figure 1.2, a weak shock is formed when the supersonic flow passes the leading edge. Further downstream, a corner shock is induced by the compression ramp. Formation of the adverse pressure gradient by the corner shock causes flow separation. The separation bubble then induces a separation shock which merges with a reattachment shock. Flow features under turbulent conditions remain similar, except in two aspects. One aspect is that a very thin subsonic layer is caused by the fuller velocity profile of the turbulent boundary layer (Arnal and Délery, 2001a). The other is that the separation region becomes much smaller (Yu et al., 2013) as the turbulent boundary layer is more energetic and can better resist the adverse pressure gradient.

1.2.2.1 Laminar ramp flow

Both experimental and numerical studies have been carried out for hypersonic laminar ramp flow. Chanetz et al. (1998) performed an experimental study for flow over a 2D ramp at Mach 10 and compared the performance of Navier-Stokes (NS) solvers and Direct Simulation Monte Carlo (DSMC) solver by simulating the experimental configuration. The conclusion was that DSMC solvers performed less well than solvers based on the NS equations. Based on Chanetz's work, Marini (2001) studied the effect of different parameters on ramp flow with the NS solver and showed that ramp angle, wall temperature assumption and geometric configuration were the main factors for mechanical and thermal loads, as well as the separation characteristics over the ramp. Navarro-Martinez and Tutty (2005) studied the formation and evolution of Görtler type vortices with a 15 degree compression ramp in a hypersonic laminar flow with Mach number of 6.85. They found that a 1% velocity fluctuation at the surface could lead to a 20% variation of heat transfer when forcing was added, and that the heat transfer values increased if the forcing was moved upstream or the spatial wavenumber was reduced. Görtler vortices could be observed even if no forcing was added when higher spanwise resolution was applied.

1.2.2.2 Transitional ramp flow

For pipe flows and other internal flows with disturbances present, laminar flow will generally become turbulent when the Reynolds number exceeds a certain value. This transition Reynolds number value depends on the inlet geometry and often on other environment conditions, like sound, vibration and freestream turbulence. Turbulent flow is hard to realize when the corresponding Reynolds number is small, whereas in controlled conditions, laminar flow can be maintained at higher Reynolds numbers. The phenomenon of flow instability has a close relationship with flow transition. Fundamental mechanisms relating to flow transition can be divided into receptivity, linear stability, and nonlinear processes (Reshotko, 1976).The first step is receptivity where disturbances such as freestream noise, freestream turbulence and others enter the laminar boundary layer and excite the eigenmodes. In the next phase, periodic waves are formed based on the eigenmodes of the disturbances, with disturbance energy convected by the mean flow. Some of the periodic waves are amplified. Linear stability theory describes their evolution fairly well during this stage. However, nonlinear interactions can then occur and lead rapidly to turbulence when the wave amplitude becomes finite, which is the third phase. The linear phase is quite well understood, but the nonlinear phase and the receptivity still require further study (Arnal and Délery, 2001a). In fact, flow transition is hard to predict, but it is worth studying as important aerodynamic quantities such as drag and heat transfer are all closely related to transition. Taking heat transfer as an example, the heat conduction rate on the wall under a turbulent boundary layer may

be many times higher than that of a laminar boundary layer as mentioned by Hombsch and Olivier (2013) and Franko and Lele (2013). In that case, the correct prediction of the transition location is of great importance for design including the distribution of the thermal protection system for spacecraft undergoing re-entry to the atmosphere.

Recently, transitional ramp flow has been studied both numerically and experimentally. Bedarev et al. (2002) performed both experimental and 2D axisymmetric numerical study based on a Mach 6 cone-flare model. They found the computed result could accord with experimental result well only when including the transition process rather than with a laminar assumption in the simulation. Benay et al. (2006) were able to obtain a non-turbulent SWBLI at Mach number 5 for Reynolds numbers up to 0.83×10^6 in experiment based on a hollow cylinderflare model. However, 2D axisymmetric numerical simulations of the cylinder-flare configuration only compare well with their experimental result at low Reynolds numbers up to 0.68×10^6. Benay et al. showed that the heat flux peak found in natural transition, when Görtler vortices appeared, was higher than that observed when transition was forced in the upstream boundary layer. With a Mach 7.5 double compression ramp, Schrijer (2010) observed a transitional interaction, laminar at separation and turbulent at reattachment, with highly 3D flow inside the separated region. With the help of infrared thermography, he measured the amplification of the Görtler vortices with varying spanwise wavelengths generated by the centrifugal instability and found that the highest growth rate of vortex appeared for the case with the largest second ramp angle. Lüdeke and Sandham (2010) studied ramp flow with Mach number 4.8 for different Reynolds numbers. Small secondary recirculation zone was found at a Reynolds number of 3,422. It was clearly demonstrated that the length of the separation zone increased with ramp angle and Reynolds number. They observed a convective transition process in a 3D ramp flow, starting from a laminar 2D flow.

Instability studies can be carried out within the context of flow transition (Robinet, 2007). Balakumar et al. (2005) studied the stability of high speed compression corners by both DNS and LST and showed that the disturbance added grew exponentially both upstream and downstream of the separation region but remained neutral across the separation area. The transition to turbulence could only occur downstream rather than in the separation region. In fact, what Balakumar et al. (2005) found was based on second-mode (now called Mack mode) of instability (details will be introduced in later section). Yao et al. (2007) believed that oblique first modes determined the transition within the separation bubble. Theofilis and Colonius (2011) proposed that the primary goal of current stability study was to find the key factors of global instability, such as critical Reynolds numbers, and the frequency of different modes. With the help of these, it might be possible to find the key point or area in the flowfield to determine the global instability of the entire flowfield.

1.2.3 Supersonic flow with cavity

Supersonic cavity flow is a fundamental problem and can be found in many practical applications, such as supersonic flow passing a gap on a flat plate, flow in combustion chambers (Yu and Schadow, 1994). As introduced by Kim et al. (2004), Zhuang (2007) and Wang et al. (2013), cavity flows can be categorised in different ways. They can be described as supersonic or subsonic according to the inflow Mach number, which affects the flow mode to be discussed later. According to the length-to-depth ratio (L/D), a cavity can be classified as either open or closed. For open cavity flow, the mixing layer from the leading edge, reattaches to the trailing edge of the cavity, while for closed cavity flow the mixing layer impinges on the floor of the cavity before hitting the trailing edge, inducing higher drag coefficients and heat transfer. In consideration of this, open cavity flow is more preferred in aerodynamics application and is studied here. General speaking, the ratio L/D for an open cavity flow is less than 10, while it is larger than 13 for closed cavity flow. It is transitional in between.

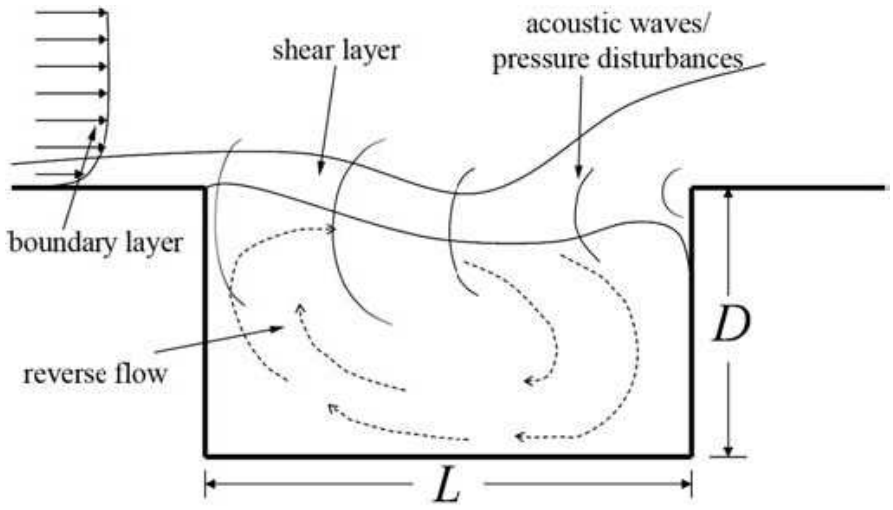

FIGURE 1.3: Schematic representation of 2D cavity flow, from Zhuang (2007).

As stated by Li et al. (2013), one important phenomenon of open cavity flow is the feedback mechanism which makes the flowfield complex and unstable. Taking a cavity on flat plate as an example, figure 1.3 shows the flowfield around and within the cavity. The feedback mechanism includes the following processes. Firstly, an unstable mixing layer is excited by acoustic disturbances and consequently vortices are formed in the separated shear layer. Secondly, the shed vortices are convected downstream and hit the trailing edge of the cavity, forming 2D spanwise vortices in and below the mixing layer. Finally, the pressure perturbation and acoustic waves generated by the impingement of vortices propagate upstream to the leading edge of the cavity and force the shear layer.

The feedback mechanism is particularly important in the study of aeroacoustics and combustion.

However, not all cavity flows are unstable. Krishnamurty (1956) proposed a minimal cavity length for the flow to oscillate. It is a parameter depending on the inflow Mach number and whether the approaching boundary layer is turbulent. When the cavity length is shorter than the minimal length, the cavity flow does not oscillate. In a further investigation, Sarohia (1977) extended the minimal length to take into account cavity depth and boundary layer momentum thickness at the leading edge. Rowley et al. (2002) proposed that stability of a cavity is dependent on the cavity length, freestream Mach number and Reynolds number.

According to the inflow Mach number and cavity configuration (e.g. L/D), the mechanism of unsteady cavity flow can be classified as an acoustic mode, Helmholtz mode, Rossiter mode or wake mode (Rockwell and Naudascher, 1978). The acoustic mode always appears in low speed cavity flow with either shallow or deep cavity, otherwise a Helmholtz mode would apply. The Rossiter mode and wake mode are dominant in high speed flow. The Rossiter mode corresponds to an oscillating mixing layer while the wake mode exists in the flow whose oscillating flow above the cavity resembles the wake behind a bluff body. Different interpretations on the mode mechanisms can be found in Wang et al. (2013).

The cavity flows to be studied in this thesis belongs to the class of supersonic open cavity flows. More specifically, ramp flow with rectangular cavity as shown in figure 1.4 is to be studied. Interactions among cavity, ramp flow separation and separation shock are included in the flowfield. Further description of the flowfield will be given in later chapters.

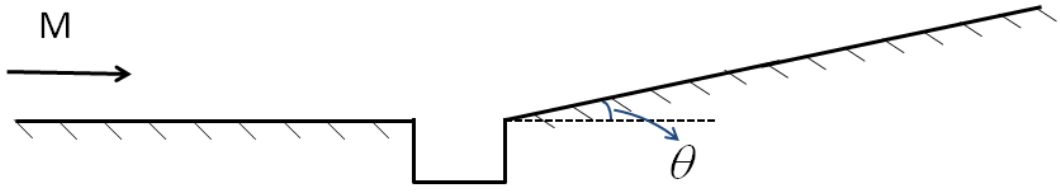

FIGURE 1.4: Geometry of 2D ramp flow with cavity studied in the thesis.

Intensive work was done to study supersonic cavity flows by Rizzetta and Visbal (2003), Bower et al. (2004), Rowley et al. (2002), Yu and Schadow (1994), Yilmaz et al. (2013), Das and Kurian (2013) and Yokoi et al. (2012). Rizzetta and Visbal (2003) proved the capability of LES on predicting cavity resonance of supersonic flow by comparing with experimental data. Rowley et al. (2002) used DNS to study laminar compressible open

cavity flow and proved its capability by comparing results with schlieren photographs from experiments. Yu and Schadow (1994) used cavity flow for mixing enhancement of supersonic combustion and reduced the afterburning flame length of 20% - 30% with the help of cavity-actuated forcing.

Yilmaz et al. (2013) investigated the effect of L/D on a Mach 1.5 supersonic cavity. With the measured sound pressure levels, they found a low level of flow structure interaction and almost no pressure oscillation were observed when L/D used equal to 1. Li et al. (2013) identified the feedback mechanics as the dominant mechanics of the self-sustained oscillation in supersonic cavity flow in spite of the upstream boundary layer thickness and flow status (laminar or turbulent). They also proposed that thickening the upstream boundary layer suppressed the cavity oscillations. Das and Kurian (2013) studied the 3D supersonic cavity flow with different widths. The dominant frequency for pressure oscillation increased rapidly as the cavity narrowed down from width/length ratio (W/L) of 3∼4. In current work, 3D aspects (W/D or W/L) will not be considered.

1.2.4 Flows with multiple elements

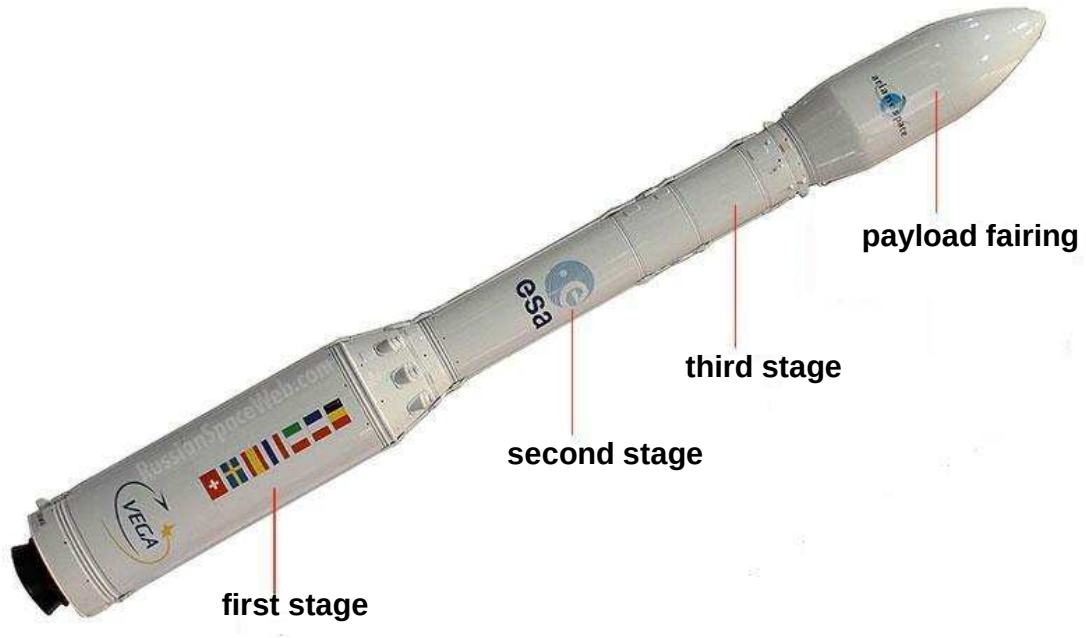

FIGURE 1.5: Basic rocket components for a three-stage rocket (image by Zak (2012)).

Practical supersonic flows usually appear with combination of the basic flows mentioned above. Taking the VEGA multi-stage rocket (Gallucci et al., 2012; Bianchi, 2008; Camussi et al., 2007) as an example, figure 1.5 shows components of a three-stage rocket configuration. A small gap would be left between the stages when assembled for wind

tunnel measurement of the forces on the different stages. This gap can initially be considered as a deep cavity flow with the cavity length increasing during the stage separation process. As a consequence, flow over second and first stages can be considered as a ramp flow with cavity. For some rockets like VEGA, jets are installed to help stage separation (Genito et al., 2011).

Some of the relevant latest works carried out for combination flows are introduced here. Yokoi et al. (2012) studied interaction between Mach 8.1 hypersonic laminar ramp flow and an open cavity both numerically and experimentally. A base flow without a cavity was simulated, then a cavity centred at or 10 mm downstream of the reattachment point was added. Results showed that the heat flux was 10 times larger at the trailing edge of the cavity than that for the flow without a cavity. However, when the cavity was moved downstream for 10 mm, the heat flux at the trailing edge was 2.4 times lower.

Wang et al. (2014) used LES to study supersonic jet-cavity interaction based on Mach 2.52 combustion chamber with sonic fuel injection. The jet was located upstream of the cavity. Results showed that the interaction could promote mass exchange inside the cavity, while this exchange was weakened when the distance between the jet and cavity was increased.

Sonic circular jet interaction with a Mach 4 laminar ramp flow with a ramp angle of 10° was studied by Zhen et al. (2013). Higher pressure levels before the jet and a shorter low-pressure area were observed, compared with a jet injected normal to a flat plate. Jet temperature was shown to have less effect on the pressure distribution. The separation length and the pressure peak in the vicinity of the jet varied with the injection angle. An angle of 120° was shown to accomplish the most effective jet/ramp interactions. They proposed that the location of separation for the ramp flow was the same no matter whether the jet was before or on the ramp. However, this conclusion was based on the fact that the largest distance between the jet and ramp was 10 times the jet diameter.

1.3 Instability analysis

Linear stability theory (LST) has been proven to be a valuable tool to study laminar-turbulent transition. Lees and Lin (1946) proposed a 2D asymptotic theory and discovered the important role of the generalized inflection point on making a compressible flat-plate boundary layer unstable due to inviscid disturbances. This generalized inflection point moved away from the wall when the inflow Mach number increased and promoted an inviscid instability. Mack (1984) discovered higher acoustics mode in transition at high Mach number. According to his theory, the property of the stability equation would be changed if a wave is locally supersonic, and an infinite sequence of neutral solutions would appear for the eigenvalue problem. When the incoming freestream Mach number is higher than 4, Mack (1984) found that a 2D wave, known as the second mode (also

known as a Mack mode), is the most unstable wave for supersonic boundary layers. At lower Mach number, the oblique first-mode waves were more unstable than the 2D waves predicted by LST. In the following paragraph, a brief introduction of the stability theory is provided following Huerre and Monkewitz (1990) and Drazin (2002).

Linear stability analysis can predict the flow behaviour very well during its linear growth stage (Coenen, 2010). The classical LST studies the development of small perturbations in space and time (t) around a parallel base flow $U(y; Re)$ with only one velocity component in the streamwise direction (x-direction). The parallel base flow is assumed to be independent of the streamwise location x but is dependent on control parameters such as Reynolds number, Re. The fluctuations can be expressed in the form of elementary instability waves $\phi(y)e^{i(\alpha x-\omega t)}$, where α is a complex wave number and ω is a complex frequency. α and ω could be real depends on which approach (temporal or spatial) is used. $\phi(y)$ is the eigenfunction and describes the wall-normal variation of the perturbation. An ordinary differential equation (the Orr-Sommerfeld equation) can be derived from the governing equation for the eigenfunction, which can be solved together with proper boundary conditions, while a dispersion relation should be satisfied by α and ω in the form of

$$D[\alpha, \omega; Re] = 0. \tag{1.2}$$

According to the development of infinitesimal perturbations, the parallel base flow could be divided into three different categories based on the impulse responses as shown in figure 1.6. It is called to be linearly stable as shown in figure 1.6(a) if the impulse decay to zero. For the linearly unstable case, the flow is linearly convectively unstable if the impulse response advects away from the source ultimately as shown in figure 1.6(b). In the other case, it is linearly absolutely unstable if the impulse response develops at the source and gradually contaminates the whole flow as shown in figure 1.6(c).

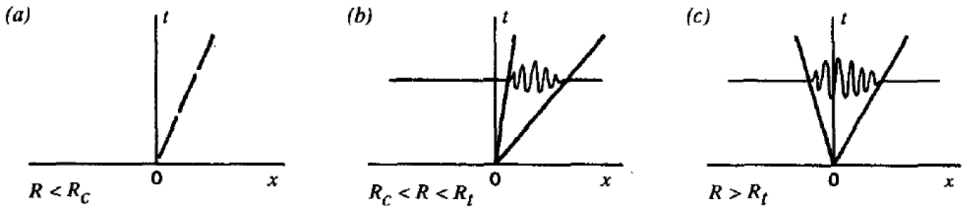

FIGURE 1.6: Sketches of typical impulse responses: (a) stable, (b) convectively unstable, (c) absolutely unstable from Huerre and Monkewitz (1990).

To perform instability analysis, either the spatial or the temporal approach could be used. For a spatial approach, the complex wavenumber α is determined as a function of the real frequency ω.

For the temporal approach, disturbances with certain real wavenumber are allowed to develop in time. Their frequencies are calculated from LST, which yields a complex number for the frequency. Its real part corresponds to the phase of disturbances, and

the imaginary part is relevant to the magnitude of disturbances. According to the expression of perturbations in elementary instability waves, we could get the following criterion for temporal linear stability,

$$\begin{aligned} &\mathrm{Im}(\omega)_{\max} < 0 \quad \text{linearly stable flow,} \\ &\mathrm{Im}(\omega)_{\max} > 0 \quad \text{linearly unstable flow,} \end{aligned} \tag{1.3}$$

where Im represents the imaginary part. To distinguish between convective and absolute instabilities, we take a specified location in the flow with wavenumber α_0 where the group velocity is zero ($v_g = \partial\omega/\partial\alpha$). The difference of convective and absolute instabilities can be expressed as

$$\begin{aligned} &\mathrm{Im}(\omega)_0 < 0 \quad \text{convectively unstable flow,} \\ &\mathrm{Im}(\omega)_0 > 0 \quad \text{absolutely unstable flow,} \end{aligned} \tag{1.4}$$

where subscript 0 means at the specified location. For a general base flows $U(x, y, Re)$, the fluctuations can be expressed in the form of $\phi(x, y; \alpha)e^{-i\omega t}$. The global instability of flow depends on the imaginary part of the complex frequency ω.

$$\begin{aligned} &\sigma = \mathrm{Im}(\omega) < 0 \quad \text{globally stable flow,} \\ &\sigma = \mathrm{Im}(\omega) > 0 \quad \text{globally unstable flow.} \end{aligned} \tag{1.5}$$

1.4 Direction Numerical Simulation

In the past few decades, with the improvements in computer hardware and algorithms, DNS has been increasingly used for simulating flowfields with shock-waves. It solves the time dependent NS equations without any modelling, so the solution includes eddies of all scales if the grids are fine enough to capture the motions down to the smallest dissipative Kolmogorov scales. However, in that case the simulation will be so computationally costly for high Reynolds number flow that it is unfeasible to run on current computers. For example, the 3D mesh required is proportional to $Re^{9/4}$ (Rogallo and Moin, 1984; Huang, 2006) and the time steps needed is $Re^{3/4}$ (Huang, 2006) to resolve different time scales. Moin and Mahesh (1998) proposed that the smallest resolved length scales did not have to equal to Kolmogorov length scale, but in the order of the Kolmogorov length scales (Araya and Castillo, 2013). At present, DNS is limited to solve flows with moderate Reynolds numbers in simple geometry. An important scale for DNS is the y^+ value defined as

$$y^+ = \frac{u_* y}{\nu}, \tag{1.6}$$

where u_* ($u_* = \sqrt{\tau_w/\rho_w}$, $\tau_w = \mu(\partial u/\partial y)_{y=0}$ is the wall shear stress, μ is the dynamic viscosity) is the friction velocity, y is the distance to the nearest wall and ν is the

local kinematic viscosity of the fluid. Approximately 10 point should be in the sublayer $y^+ <10$. For attached turbulent boundary layer flows, the y^+ should be less than 1 for the first layer of mesh with corresponding x^+ and z^+ less than 15 and 7.5, respectively (Sandham et al., 2002).

DNS has been extensively used as numerical tool for flows with SWBLI. Adams (1998, 2000) and Marini (2001) used DNS to study turbulent and laminar compression ramp flow, respectively. Pagella et al. (2002, 2004) applied it on both 2D shock impingement flow and 2D ramp flow. Yao et al. (2006) used it to study supersonic jet in crossflow, while Brès and Colonius (2008) used it in supersonic flow with cavity. Khoury et al. (2013) applied it to turbulent pipe flow.

The current work aims to investigate SWBLI of simple configurations, i.e. supersonic ramp flow, jet in high speed crossflow and cavity flow with moderate Reynolds number. Therefore, we choose DNS as the numerical tool. Detailed information is introduced in Chapter 2.

1.5 Objectives

The current work focuses on the flow mechanisms of high speed laminar boundary layer stability and transition, considering jets in supersonic crossflow and supersonic compression ramp flow, as well as interaction cases with different combinations of jet, ramp and cavity to simulate a problem relevant to rocket stage separation (both laminar and turbulent). DNS is used to solve the compressible NS equations for the investigation. Both 2D and 3D simulations of ramp flow, jet in crossflow and combined flows are carried out. Two-dimensional cases are used to capture the main flow structures of the 2D laminar flow and to find the flowfield variation with different flow parameters. Mesh dependency studied is also carried out mainly based on 2D simulations. Three-dimensional simulations aim to investigate the flow mechanisms in more detail, including the instability characteristics and the likelihood of transition. Turbulence effect on flow separation is also evaluated.

The objectives for the current investigation are as follows:

• To study the 3D instability characteristics of a jet in hypersonic crossflow and supersonic ramp flow, based on 2D grid-independent results, and to investigate whether the global modes of instability, found by Robinet (2007) for the shock-wave impinging case, are also present for ramp or jet-in-crossflow configuration.

• To study the final breakdown to turbulence for supersonic ramp flow, using the most unstable mode found in the instability study.

• To carry out a 2D parametric study to determine the effects of jets and cavities on ramp flow separation.

• Based on a practical background, to evaluate narrow cavity effect, the jet strength and orientation effects on ramp flow.

• With turbulent inflow condition, to study a practical ramp flow with/without jet injection and quantify the turbulent upstream flow effect on ramp flow separation.

This thesis is organized as follows. In Chapter 2, technical details related to the methods used in this research are introduced. Base flow and instability analysis of jet in crossflow are presented and discussed in Chapter 3. Simulations of ramp flow for instability and the consequent transition studies are demonstrated in Chapter 4. Parametric studies of flow separation for the ramp flow with/without a jet and with/without a cavity are given in Chapter 5. Evaluations of turbulent inflow and jet effect on practical ramp flow are done in Chapter 6. Conclusions and recommendations for further work are given in Chapter 7.

Chapter 2

Numerical methodology

Different flows have different requirements on the numerical schemes for spatial discretization of the governing equations, boundary conditions, as well as mesh construction and partition. For the sonic jet in supersonic crossflow, supersonic ramp flow, as well as cavity flow studied here, the energy equation is strongly coupled with the momentum equation by pressure and density, and as a consequence, the full unsteady compressible Navier-Stokes (NS) equations need to be solved based on the Newtonian fluid assumption. What is more, because of SWBLI existing in all the cases and leading to complex flowfields with shock-waves and flow separations, high levels of accuracy and shock capturing are essential. Simulations carried out in this thesis solve the unsteady 3D compressible NS equations using an in-house Fortran code, known as the Southampton SBLI code. In this chapter, the numerical tools are introduced. The governing equations are introduced firstly in both dimensional and non-dimensional forms, followed by the grid transformation. Spatial discretization and time marching schemes are then discussed and entropy splitting and shock-wave capture schemes are outlined. Boundary conditions are summarized before the introduction of turbulence inflow generator, DNS setup and mesh generation. Finally code validations are carried out. In this and the following chapters, variables are usually given in non-dimensional form, while an asterisk $*$ is used to denote the dimensional quantities.

2.1 Governing equations

The Navier-Stokes equations are the mathematical expression of the laws of conservation of mass, momentum and energy, which can be written in the following form

$$\frac{\partial \rho^*}{\partial t^*} + \frac{\partial \left(\rho^* u_i^*\right)}{\partial x_i^*} = 0, \tag{2.1}$$

$$\frac{\partial\left(\rho^* u_i^*\right)}{\partial t^*}+\frac{\partial\left(\rho^* u_i^* u_j^*\right)}{\partial x_j^*}=-\frac{\partial p^*}{\partial x_i^*}+\frac{\partial \tau_{ij}^*}{\partial x_j^*} \tag{2.2}$$

and

$$\frac{\partial\left(\rho^* E^*\right)}{\partial t^*}+\frac{\partial\left(\rho^* E^*+p^*\right) u_i^*}{\partial x_i^*}=-\frac{\partial q_i^*}{\partial x_i^*}+\frac{\partial\left(u_i^* \tau_{ij}^*\right)}{\partial x_j^*}. \tag{2.3}$$

The dimensional variables are defined as follows: ρ^* is the density, u_i^* are the velocity components, p^* is the pressure, τ_{ij}^* is the shear stress tensor, q_i^* is the heat flux components and E^* is the total energy. By assuming Newtonian fluid and the Fourier law of heat conduction, the last three parameters are defined as

$$\tau_{ij}^*=\mu^*\left(\frac{\partial u_i^*}{\partial x_j^*}+\frac{\partial u_j^*}{\partial x_i^*}-\frac{2}{3}\delta_{ij}\frac{\partial u_i^*}{\partial x_i^*}\right), \tag{2.4}$$

$$q_i^*=-k^*\frac{\partial T^*}{\partial x_i^*} \tag{2.5}$$

and

$$E^*=(e^*+\frac{u_i^* u_i^*}{2}), \tag{2.6}$$

where δ_{ij} is the Kronecker delta function, k^* is the thermal conductivity, Fourier's law of thermal conduction is assumed to calculate the heat flux, and e^* is the internal energy. The dynamic viscosity μ^* is assumed to follow the Sutherland's law

$$\mu^*=\mu_{ref}^*\left(\frac{T^*}{T_{ref}^*}\right)^{3/2}\frac{T_{ref}^*+S^*}{T^*+S^*}, \tag{2.7}$$

where S^*=110.4 K is used as the Sutherland temperature constant, freestream static temperature T_∞^* is used as the Sutherland reference temprature T_{ref}^*, and freestream dynamic viscosity μ_∞^* is used as the reference viscosity μ_{ref}^*. Non-dimensionalization is based on inflow condition and a characteristic length L^* as

$$\begin{aligned} &t=\frac{t^* u_\infty^*}{L^*}, \qquad x_i=\frac{x_i^*}{L^*}, \quad \rho=\frac{\rho^*}{\rho_\infty^*}, \quad u_i=\frac{u_i^*}{u_\infty^*}, \\ &p=\frac{p^*}{\rho_\infty^* {u_\infty^*}^2}, \qquad T=\frac{T^*}{T_\infty^*}, \qquad \mu=\frac{\mu^*}{\mu_\infty^*} \text{ and } e=\frac{e^*}{{u_\infty^*}^2}. \end{aligned} \tag{2.8}$$

The non-dimensional NS equations are then obtained as

$$\frac{\partial \rho}{\partial t}+\frac{\partial\left(\rho u_i\right)}{\partial x_i}=0, \tag{2.9}$$

$$\frac{\partial\left(\rho u_i\right)}{\partial t}+\frac{\partial\left(\rho u_i u_j\right)}{\partial x_j}=-\frac{\partial p}{\partial x_i}+\frac{\partial \tau_{ij}}{\partial x_j} \tag{2.10}$$

and

$$\frac{\partial(\rho E)}{\partial t} + \frac{\partial(\rho E + p)\,u_i}{\partial x_i} = -\frac{\partial q_i}{\partial x_i} + \frac{\partial(u_i \tau_{ij})}{\partial x_j}, \tag{2.11}$$

where

$$\tau_{ij} = \frac{\mu}{Re}\left(\frac{\partial u_i}{\partial x_j} + \frac{\partial u_j}{\partial x_i} - \frac{2}{3}\delta_{ij}\frac{\partial u_i}{\partial x_i}\right) \quad \text{and} \qquad q_i = -\frac{\mu}{Re\,(\gamma-1)\,M_\infty^2 Pr}\frac{\partial T}{\partial x_i}. \tag{2.12}$$

The Reynolds number is defined by $Re = \rho^*_\infty u^*_\infty L^*/\mu^*_\infty$ and the Prandtl number as $Pr = c^*_p \mu^*/k^*$. For all simulations in this thesis, a constant Prandtl number of 0.72 is used. $M_\infty = u^*_\infty/a^*_\infty$, where a_∞ is the sound speed, is the freestream Mach number used as reference value. Other useful quantities in non-dimensional form can be deduced as internal energy

$$e = E - \frac{1}{2}(u^2 + v^2 + w^2), \tag{2.13}$$

temperature

$$T = e\gamma(\gamma-1)M_\infty^2, \tag{2.14}$$

pressure

$$p = \frac{\rho T}{\gamma M_\infty^2}, \tag{2.15}$$

and sound speed

$$a = \frac{T}{M_\infty^2}. \tag{2.16}$$

2.2 Generalized coordinates

The configuration for numerical simulations varies much with different study objectives. The current study involves ramp and cavity, therefore a more complicated domain is required than a rectangular box. The mesh used also needs to be adapted to the flowfield features like shear layers and shock-waves to get reliable result or to save simulation time. This kind of geometry and the non-uniform mesh required, as shown in figure 2.1(a), will make solving NS equations more difficult. With the help of grid transformation from Cartesian coordinates to general coordinates, a rectangular orthogonal uniform mesh is obtained as shown in figure 2.1(b). However, a change to the generalized NS quations should also be done. In the current 3D studies, meshes are always extruded from a 2D mesh in the spanwise direction, although sometimes a stretched mesh is used in the spanwise direction. Therefore, mesh transformation is only carried out in the streamwise and the wall-normal directions. The non-dimensional NS equations of equation (2.9) to equation (2.11) can be written in conservation form as (Anderson, 1995)

$$\frac{\partial U}{\partial t} + \frac{\partial F}{\partial x} + \frac{\partial G}{\partial y} + \frac{\partial H}{\partial z} = 0, \tag{2.17}$$

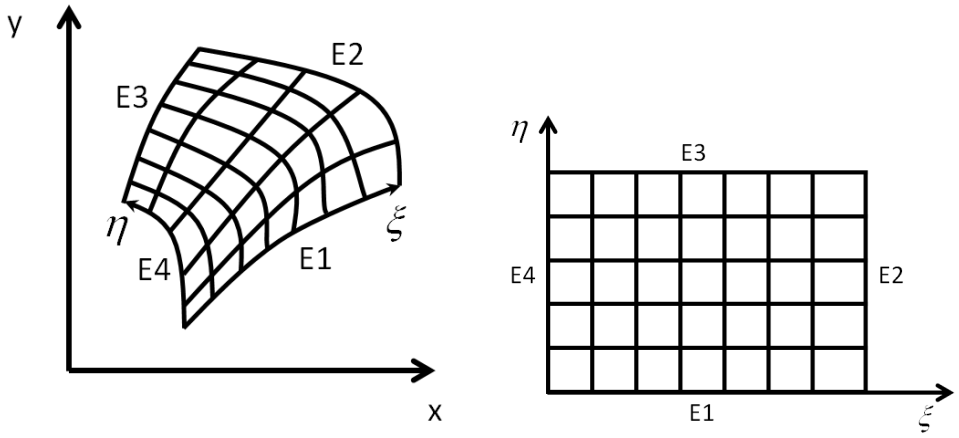

(a) (b)

FIGURE 2.1: Mesh transformation from Cartesian coordinates (x, y) to general coordinates (ξ, η).

where U is a column vector of the conservative variables and F, G, H are column vector of the flux terms in the three coordinate directions. Details can be found in many CFD text book, for example Anderson (1995). Based on a 2D transformation of

$$\xi = \xi(x, y), \tag{2.18}$$

and

$$\eta = \eta(x, y), \tag{2.19}$$

equation (2.17) is expressed in the following form

$$\frac{\partial U}{\partial t} + \frac{\partial F}{\partial \xi}(\frac{\partial \xi}{\partial x}) + \frac{\partial F}{\partial \eta}(\frac{\partial \eta}{\partial x}) + \frac{\partial G}{\partial \xi}(\frac{\partial \xi}{\partial y}) + \frac{\partial G}{\partial \eta}(\frac{\partial \eta}{\partial y}) + \frac{\partial H}{\partial z} = 0. \tag{2.20}$$

By multiplying equation (2.20) with the Jacobian metrics J given by

$$\begin{bmatrix} \frac{\partial x}{\partial \xi} & \frac{\partial y}{\partial \xi} \\ \frac{\partial x}{\partial \eta} & \frac{\partial y}{\partial \eta} \end{bmatrix}, \tag{2.21}$$

rearranging the terms and substituting the relationships for the direct Jacobian metrics with the inverse metrics in the following form,

$$\frac{\partial \xi}{\partial x} = \frac{1}{J}\frac{\partial y}{\partial \eta}, \tag{2.22}$$

$$\frac{\partial \eta}{\partial x} = -\frac{1}{J}\frac{\partial y}{\partial \xi}, \tag{2.23}$$

$$\frac{\partial \xi}{\partial y} = -\frac{1}{J}\frac{\partial x}{\partial \eta} \tag{2.24}$$

and

$$\frac{\partial \eta}{\partial y} = \frac{1}{J}\frac{\partial x}{\partial \xi}, \tag{2.25}$$

we can get the conservation form of the NS equations in (ξ, η, ζ) space as

$$\frac{\partial U_1}{\partial t} + \frac{\partial F_1}{\partial x} + \frac{\partial G_1}{\partial y} + \frac{\partial H_1}{\partial z} = 0, \tag{2.26}$$

where

$$U_1 = JU, \tag{2.27}$$

$$F_1 = F\frac{\partial y}{\partial \eta} - G\frac{\partial x}{\partial \eta}, \tag{2.28}$$

$$G_1 = -F\frac{\partial y}{\partial \xi} + G\frac{\partial x}{\partial \xi} \tag{2.29}$$

and

$$H_1 = JH. \tag{2.30}$$

2.3 Spatial discretization and time marching schemes

2.3.1 Spatial discretization

Simulations in this thesis use an in-house high-order finite-difference code, SBLI. A fourth-order central difference scheme is employed for the spatial discretization at internal points (Lawal, 2002). The first ($\dot{U}_i$) and second ($\ddot{U}_i$) order derivative operators are given by

$$\dot{U}_i = \frac{-U_{i+2} + 8U_{i+1} - 8U_{i-1} + U_{i-2}}{12h}$$

and (2.31)

$$\ddot{U}_i = \frac{-U_{i+2} + 16U_{i+1} - 30U_i + 16U_{i-1} - U_{i-2}}{12h^2},$$

where h is the grid spacing and i is the grid index in the discretization direction. For points close to non-periodic boundaries, some of the information required by the central difference scheme is not available, therefore the fourth-order stable boundary treatment proposed by Carpenter et al. (1999) is applied.

2.3.2 Time marching scheme

The low-storage third-order compact Runge-Kutta method by Wray (1986) is used for time marching the independent variables $(\rho, \rho u, \rho v, \rho w, \rho E)$. Two storage locations, Q_1

and Q_2, are allocated for each time-dependent variable and updated at each of the three substeps as follows

$$Q_m^{new} = a_{lm}\Delta t Q_1^{old} + Q_2^{old} \qquad (m = 1,\ 2;\ \ l = 1,\ 2,\ 3), \tag{2.32}$$

where l is the substep number. The constants a_{lm} are

$$a_{l1} = (\frac{2}{3},\ \frac{5}{12},\ \frac{3}{5}), \qquad a_{l2} = (\frac{1}{4},\ \frac{3}{20},\ \frac{3}{5}). \tag{2.33}$$

Time step Δt is tested before each simulation to make sure that it is well within the stability limit of Δt and also keeps simulation efficiency high. A smaller time step is needed for flowfields with finer grids or dramatic local changes like jet injection.

2.4 Entropy splitting and shock-wave capture scheme

2.4.1 Entropy splitting

In consideration of the non-dissipation character of the central difference scheme involved in the code and damping the numerical disturbance, the entropy splitting method used by Sandham et al. (2002) is applied to the non-linear term to improve the numerical stability of the code. This method splits the inviscid flux derivatives into conservative and non-conservative parts for stability improvement. The Euler equations, if still in the form of equation (2.17), can be rewritten in the entropy split form as

$$\frac{\beta}{\beta+1}\frac{\partial U}{\partial t}+\frac{\beta}{\beta+1}U_W\frac{\partial W}{\partial t}+\frac{\beta}{\beta+1}(\frac{\partial F}{\partial x}+\frac{\partial G}{\partial y}+\frac{\partial H}{\partial z})+\frac{1}{\beta+1}(F_W\frac{\partial W}{\partial x}+G_W\frac{\partial W}{\partial y}+H_W\frac{\partial W}{\partial z}) = 0. \tag{2.34}$$

The parameter β was introduced in Yee et al. (2000), while W, F_W, G_W and H_W are given in Sandham et al. (2002). In the present work we take β=4.0.

2.4.2 TVD

The total variation diminishing (TVD) scheme of Yee et al. (1999) for shock-wave capture and the artificial compression method (ACM) by Harten (1978) are used in the code to treat flow discontinuities. They are applied at the end of each Runge-Kutta time marching step for regions around shock-waves only, to preserve the non-dissipative properties of the central difference schemes elsewhere and to achieve low overall numerical dissipation. The TVD/ACM procedure is based on a standard TVD scheme where the modified form of the numerical flux term can be expressed as

$$\tilde{F} = \frac{1}{2}B\tilde{\Phi}, \tag{2.35}$$

where B represents the eigenvector of the flux Jacobian. $\tilde{\phi}^l$ are components of $\tilde{\Phi}$ and given by the ACM as

$$\tilde{\phi}^l = \kappa L \vartheta^l \phi^l, \tag{2.36}$$

where κ is a constant with a standard range from 0.0 to 0.7, ϕ^l is a standard TVD 'limiter'. ϑ^l is the ACM sensor and L represents an additional sensor which turns off the shock capturing in vortical flow regions such as boundary layer. In the code, the sensor proposed by Ducros et al. (1999) and modified by De Tullio (2013) is programmed. The L is defined by

$$L = \frac{(\nabla \cdot u)^2}{(\nabla \cdot u)^2 + \omega^2/a + \epsilon}, \tag{2.37}$$

where ω is the vorticity and ϵ is a small positive real number, chosen to prevent numerical divergence in regions where both $\nabla \cdot u$ and ω equal zero. This function varies from zero in weakly compressible vortical regions (such as within boundary layers) to near one in shock regions. Simulation tests show that the modified Ducros sensor (with a=10 used in the current work) led to a better resolution of contact discontinuities while not introducing noticeable numerical dissipation in regions of turbulent flow.

2.5 Boundary conditions

Five different kinds of boundary conditions are used in this study. They are the no-slip isothermal wall condition, an integral method for filtering outgoing waves, characteristic boundary conditions, an inflow extrapolation method and periodic boundary conditions. For simulations with complex geometry, different conditions may be applied on the surface such as a slot jet on the wall, for which a detailed specification of the boundary condition is deferred to the next chapter.

The lower walls in the simulation setup are always specified as a no-slip isothermal wall. Density at the wall is allowed to float, while all the velocity components are set to zero.

An integrated characteristic method is used at the upper boundary, while characteristic boundary condition is used on the outflow boundary. They both use a characteristic decomposition of the Euler terms in the NS equations and get 5 eigenvalues as characteristic velocity, i.e. $u - c$, u, u, u and $u + c$. For the subsonic area, taking the flow in the boundary layer of the outflow as an example, the $u - c$ term is less than zero and the subsequent incoming characteristic needs to be set to zero to prevent the downstream flow contaminating the flow in the simulation domain.

An extrapolation method is always used as the inflow boundary condition. In supersonic regions of the inflow boundary, flow parameters are set equal to the inflow condition, while in subsonic regions of the inflow boundary, pressure is obtained from extrapolating the pressures on the second and third layers of mesh in the streamwise direction and then used to update density and other parameters.

For periodic conditions, the mesh setup, including first and second order derivatives on both sides of the boundaries should be the same. Correct specification of values at so-called 'halo zone' of each side of periodic boundary is required to make sure of the periodicity.

The laminar inflow profile is generated from solutions of the compressible laminar flow similarity solution by White (1974). Depending on the wall condition as adiabatic or isothermal, different initial guesses of $\partial u/\partial y$ and T_w, or $\partial u/\partial y$ and $\partial T_w/\partial y$ using shooting method are carried out to get the inflow profile.

2.6 Turbulent inflow generator

A synthetic turbulence approach (Sandham et al., 2003; Touber, 2010) is used here to prescribe an artificial incoming flow field and mimic streaks in turbulent boundary layer. The flow recovers to equilibrium further downstream. This allows a turbulent boundary layer to be generated within a short distance compared to natural transition for laminar flow.

In the study here, streaks are added to the base laminar inflow condition. They are close to the wall at inflow boundary and expressed in the following divergence-free form to generate turbulent flow further downstream.

$$v' = cy^2 e^{-(\frac{y}{d})^2} \sin(\omega t) \cos(\frac{2\pi N}{L_z} z), \tag{2.38}$$

$$w' = -2cye^{-(\frac{y}{d})^2}(1 - (\frac{y}{d})^2) \sin(\omega t) \sin(\frac{2\pi N}{L_z} z) \frac{L_z}{2\pi N}, \tag{2.39}$$

where C, d and ω are coefficients, wavenumber N is carefully chosen according to test for the most preferred spanwise wavelength. To break the added periodicity in the spanwise direction, a small amplitude sub-harmonic is added in the w-velocity component as

$$\rho w = \rho w(1 + 0.05 \cos \frac{2\pi z}{L_z}). \tag{2.40}$$

2.7 DNS case setup

For the simulation setup, the domain is chosen as only part of the whole flowfield. This domain should not be too large, in consideration of mesh size, but should include the important features of interest. The plate leading edge is not included in the chosen domain, since a large number of grid points would be necessary in the boundary layer to reach the required resolution. What is more, the hypersonic flow around a leading edge becomes more complicated with the presence of a shock-wave. To make the flowfield simple and the calculation more efficient, it is beneficial to use velocity and temperature

profiles downstream of the leading edge as the inlet condition for the computational domain. A schematic of the computational domain is shown in figure 2.2. It is noted that in this and the following chapters of simulations, non-dimensionalized variables are used with the inflow displacement thickness δ_0^* as their reference length and inflow temperature, velocity, density and dynamic viscosity as corresponding reference values.

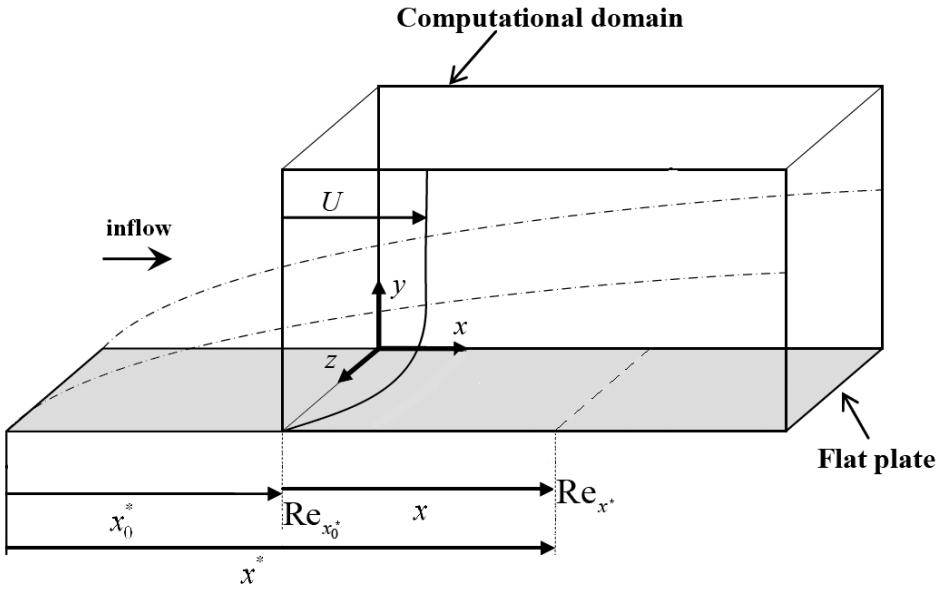

FIGURE 2.2: Sketch of the computational domain from Sandham et al. (2011).

In the simulation, we need to specify the Reynolds number to be consistent with the experiment. If we relate the x-coordinate, non-dimensionalized by the inflow displacement thicknesses and the distance measured from the computational domain inlet as shown in figure 2.2 to the Reynolds number based on the distance from the plate leading edge (Re_{x^*}), we have

$$Re_{x^*} = Re_{x_0{}^*} + xRe, \tag{2.41}$$

where Re is the Reynolds number used in the calculation, based on the inflow properties and inflow displacement thickness. $Re_{x_0{}^*}$ is the Reynolds number based on the inflow properties and distance from the plate leading edge to the start of the computational domain. If we assume that the laminar boundary layer similarity solution applies from the leading edge to the computational inflow, $Re_{x_0{}^*}$ can be obtained from compressible laminar flow similarity solution as (Sandham et al., 2011)

$$Re_{x_0^*} = \frac{1}{2}(\frac{Re}{\Delta})^2, \tag{2.42}$$

where Δ is a scale factor that is computed during the similarity solution. During the calculation, it equals to the integral part of displacement thickness at the computational

domain inlet which is defined as

$$\Delta = \int_0^\infty (1 - \frac{\rho^* u^*}{\rho^*_\infty u^*_\infty}) \frac{\mathrm{d}\eta}{(\rho^*/\rho^*_\infty)}, \tag{2.43}$$

where

$$\eta = \frac{U^*_\infty}{\sqrt{2\xi^*}} \int_0^{y^*} \rho^* dy^* \text{ and } \xi^* = \rho^*_\infty(x^*)\, U^*_\infty(x^*) \mu^*_\infty(x^*) x^*. \tag{2.44}$$

2.8 Mesh generation

In Computational Fluid Dynamics (CFD), generation of meshes and their quality are of great significance to the simulation result. Smoothness and orthogonality of a mesh are key performance indicators on both mesh continuity and higher order matrix calculation for high order simulations. The meshes for the jet in high speed cross flow are generated from an algebraic method. They are orthogonal, and are stretched in both the streamwise and the wall-normal directions around the slot centre. The streamwise stretching function is defined as

$$x = L_s(1 + \frac{\sinh(a\xi)}{\sinh a}), \tag{2.45}$$

and the wall-normal stretching follows

$$y = L_y \frac{\sinh(b\eta)}{\sinh b}. \tag{2.46}$$

In the expressions above, L_s is the distance from the computational domain inlet to the slot centre. ξ is evenly spaced between (-1, ξ_{max}) for the x-coordinate from the domain inlet (ξ=-1) and outlet ($\xi = \xi_{max}$) with ξ=0 corresponding to the jet slot centre. L_y is the height of the computational domain. The stretching coefficients a and b are adjustable to generate meshes with different grid distribution.

The meshes for the ramp flows with or without a cavity in the simulation are generated by the commercial software GRIDGEN (Pointwise, 2008) because of the more complex configurations. In the software, meshes are generated in three steps, with a check function at the end of each step. A formatted mesh data file can be obtained after these three steps.

2.9 Code validation

SBLI code has been mentioned in many works and been successfully applied in research done by Lawal (2002), Gajbhiye (2010), De Tullio (2013), De Tullio and Sandham (2010), Touber and Sandham (2011), Touber and Sandham (2009a), Touber (2010), Sandham

et al. (2011), Sandham et al. (2003) and Zhang et al. (2012). In this section, code validation works are carried out based on the supersonic flat-plate flows from Katzer (1989) and Powrie (1996), respectively. The shock impingement for Katzer (1989) and jet injection for Powrie (1996) are not concerned here. According to setup of Katzer (1989), flow conditions are listed in table 2.1.

Parameter	Main stream
Mach number	2.0
Static temperature (K)	288
Wall type	Adiabatic
Reynolds number Re_x^*	2.96×10^5 (based on the impingement location)
Simulation Reynolds number Re	950

TABLE 2.1: Flow conditions for the flat plate in Katzer (1989).

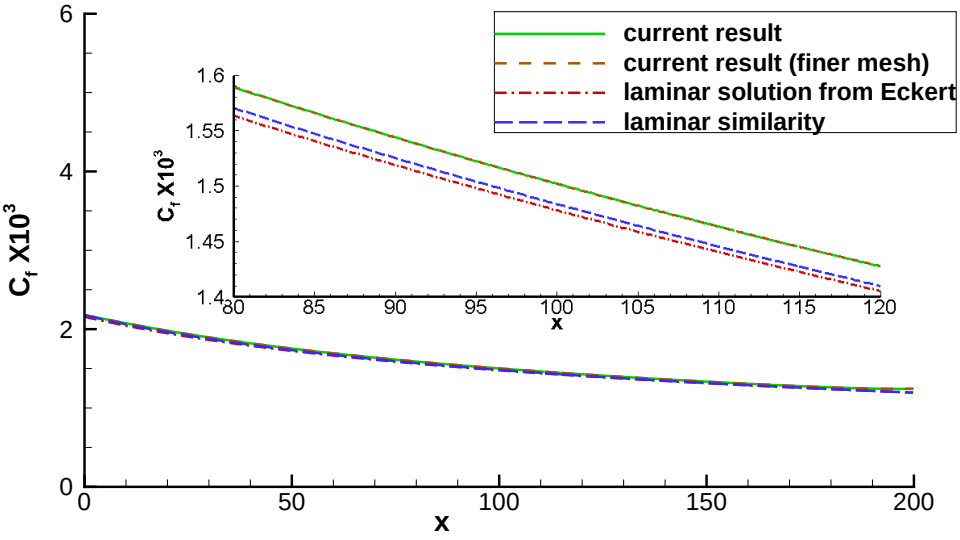

FIGURE 2.3: Distribution of skin friction for the flat plate of M=2 flow.

A rectangular computational domain of size 200 × 80 is used here, which is stretched in both the streamwise and the wall-normal directions. Finer meshes are also applied but do not make any difference to the skin friction coefficient (C_f) curves as shown in figure 2.3 where C_f curve is compared with solution from Eckert (1955) and the laminar boundary layer similarity solution. Good agreement can be observed, showing the flow is resolved well. The zoomed-in figure shows the grid-independency of the result and the difference between the current result to the reference values are 1.6% and 1.2%, respectively. Here the skin friction is defined by non-dimensional quantities and has the form of

$$C_f = \frac{2}{Re}(\mu\frac{\partial u}{\partial t})_w, \tag{2.47}$$

where Re is the Reynolds number used in simulation and the subscript w means the quantity on the wall. The Eckert's solution for laminar flow (Eckert, 1955) is defined as

$$C_f = \frac{0.664}{\sqrt{Re_x^*}} \left(\frac{T^*}{T_\infty} \right)^{\frac{n-1}{2}}, \tag{2.48}$$

where n=0.7 for air, T_∞ is the freestream static temperature. T^* is a reference temperature and defined by

$$T^* = 0.5(T_w + T_\infty) + 0.22(T_r - T_\infty). \tag{2.49}$$

The recovery temperature T_r is defined by

$$T_r = T_e \left(1 + r \frac{\gamma - 1}{2} M_\infty^2 \right), \tag{2.50}$$

where r is the recovery factor with r=$Pr^{\frac{1}{2}}$ for laminar flow. Eckert's solution for turbulent flow (which will be used in Chapter 6)

$$C_f = \frac{T_\infty}{T^*} \frac{0.370}{\left\{ \log_{10}[Re_x^* (\frac{T_\infty}{T^*})^{n+1}] \right\}^{2.584}}, \tag{2.51}$$

where $r = Pr^{\frac{1}{3}}$ for turbulent flow.

The C_f from laminar similarity is defined as

$$C_f = \frac{\sqrt{2}}{\sqrt{Re_x^*}} \frac{\mu_w \rho_w}{\mu_\infty \rho_\infty} \left(\frac{\partial u}{\partial y} \right)_w. \tag{2.52}$$

The term $\left(\frac{\partial u}{\partial y}\right)_w$ in the expression can be obtained from the similarity solution.

Streamwise velocity profiles and temperature profiles at three different locations, x=2.7, 89.8 and 151.2, are plotted in figure 2.4 to compare with the similarity solution at x=0. The wall-normal coordinates for the profiles are scaled by the local boundary layer thickness (at 99% frees tream velocity), and the velocities or temperatures for the profiles are scaled by the freestream values. As observed in both frames, the scaled profiles agree with each other showing the code is reliable for further simulation.

The second case simulated is based on the experimental configuration of Powrie (1996). A flat plate with jet injection based on the same experiment will be studied in next chapter with further grid-dependency studies. The inflow conditions are listed in table 2.2. The freestream Mach number is 6.69 with a unit Reynolds number of 4.27×10^6 m^{-1}. The static freestream temperature is 63.11 K and is used as the reference temperature. The freestream static pressure is 403.7 Pa. The stagnation pressure and stagnation temperature are 1.255×10^6 Pa and 628 K, respectively. The isothermal wall temperature is set to 293 K.

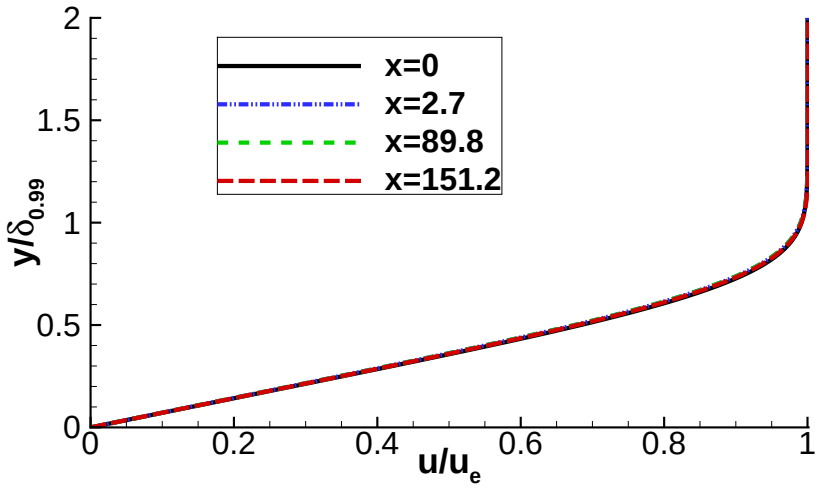

(a)

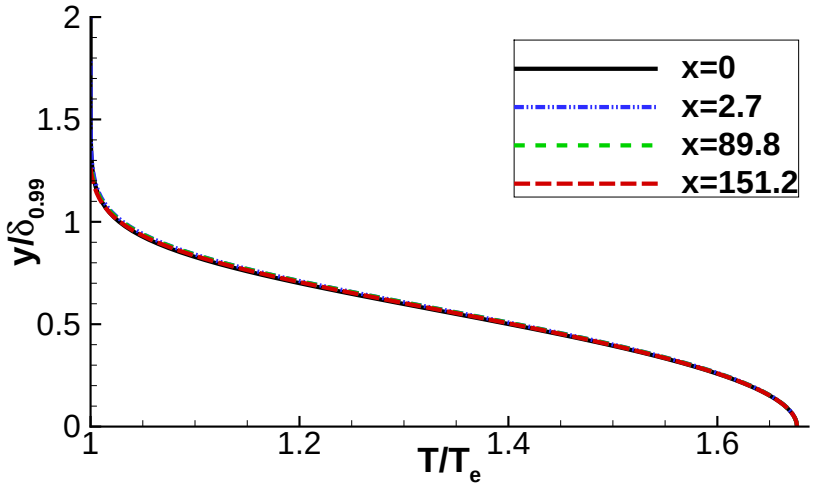

(b)

FIGURE 2.4: Streamwise velocity (a) and temperature (b) profiles at different streamwise locations for the M=2 flow.

In Powrie's experiments, the flat plate is 112.5 mm long. The centre of the slot jet to the leading edge is 74.5 mm. According to equation (2.41) and equation (2.42), a Reynolds number of 2,500 based on inflow displacement thickness is chosen with $Re_{x_0{}^*}$ of 34,757 and $x_0{}^*$ of 8.31 mm.

Distribution of the boundary layer thickness for the converged flowfield without a jet is plotted in figure 2.5. Thickness of the boundary layer develops smoothly from 1.24 at inflow boundary until 5.44 at exit. The slight jumps are caused by the choice of the 99% velocity among grid points. Vectors of velocity with the flowfield are also plotted as shown in figure 2.6 to give visual impression of the shape of the velocity distribution as a function of the wall-normal coordinate y.

Parameter	Main stream
Medium	Nitrogen
Mach number	6.69
Static pressure (pa)	403.7
Stagnation pressure (pa)	1.255×10^6
Static temperature (K)	63.11
Stagnation temperature (K)	628
Wall temperature (K)	293
Sound speed (m/s)	161.94
Density (Kg/m^3)	0.02155
Unit Reynolds number (/m)	4.27×10^6
Simulation Reynolds number	2,500

TABLE 2.2: Flow parameters for the flat plate used by Powrie (1996).

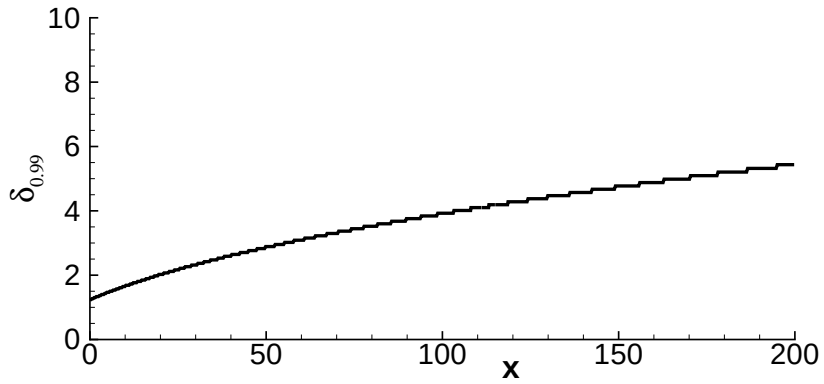

FIGURE 2.5: Development of boundary layer thickness in the streamwise direction based on $u = 0.99$ of free stream velocity.

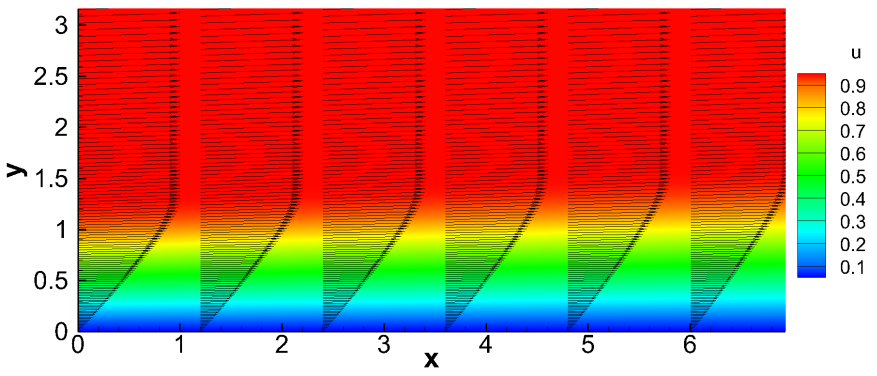

FIGURE 2.6: Flowfield with vectors of streamwise velocity displayed in every 4 grids.

Figure 2.7 shows the calculated skin friction distribution and is compared with similarity solution and Eckert (1955). The obtained result accords with the other two C_f distributions. Compared with the reference curve from laminar similarity, the simulation result is closer to the solution from Eckert especially at the inflow.

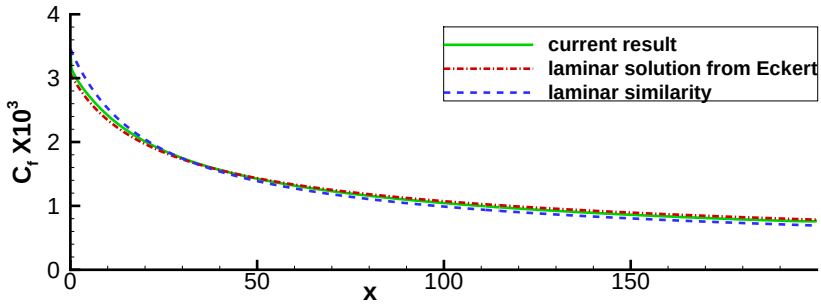

FIGURE 2.7: Distribution of skin friction for the flat plate M=6.69 flow.

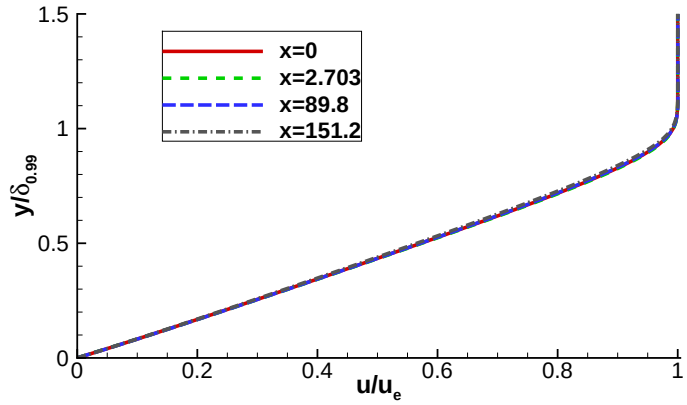

(a)

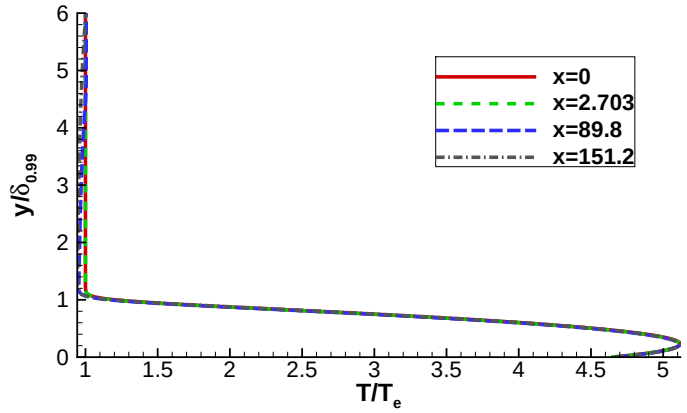

(b)

FIGURE 2.8: Streamwise velocity (a) and temperature (b) profiles at different streamwise locations for the flat plate M=6.69 flow.

Streamwise velocity profiles and temperature profiles are plotted in figure 2.8 at the same locations plotted for the M=2 case with the same scaling method. It can be seen that all the velocity profiles in figure 2.8(a) collapse. For the temperature profiles, there is a slight difference of about 5% just outside boundary layer. With the help of two figures in figure 2.9 showing the temperature contours for the flowfield and close to the inflow boundary, it can be seen that the difference appearing in figure 2.9(b) is caused by a wedge-shape low temperature area. It is believed that this slight difference should be caused by the mismatch of similarity solution and NS solver. However this difference is very small and doesn't affect the downstream flow.

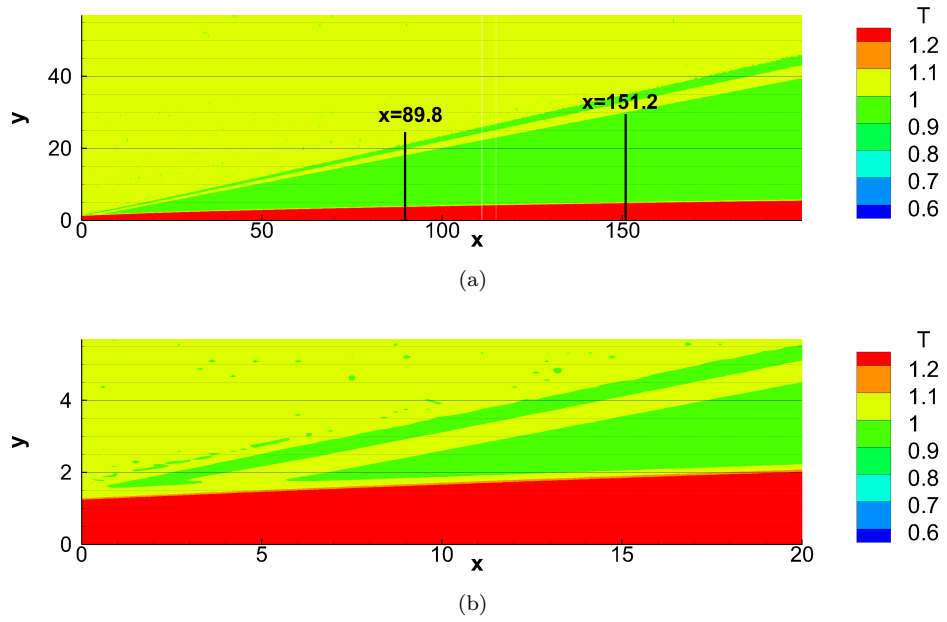

FIGURE 2.9: Temperature distribution for the M=6.69 flowfield (a) and close to its inflow boundary (b).

Chapter 3

Global instability for jet in high speed crossflow*

The code validation work briefly introduced at the end of Chapter 2 was based on the experiments done by Powrie (1996) without jet injection. Simulations carried out here are also based on the experiments of Powrie (1996) but with jet injection. A 2D base flow of a sonic jet in a supersonic crossflow is firstly studied and compared with previous work. The effect of different momentum flux ratio (J_p) is evaluated. Then a 3D instability study is carried out based on different J_p and different spanwise lengths of the computational domain. Finally, the non-linear stage of disturbance growth is studied.

3.1 Simulation setup

Parameter	Main stream	Jet injection
Medium	Nitrogen	Nitrogen
Mach number	6.69	1
Static pressure (Pa)	403.7	§
Stagnation pressure (Pa)	1.255×10^6	§
Static temperature (K)	63.11	244.17
Stagnation temperature (K)	628	293
Wall temperature (K)	293	N/A
Sound speed (m/s)	161.94	318.52
Density (Kg/m^3)	0.02155	§
Unit Reynolds number (/m)	4.27×10^6	N/A
Simulation Reynolds number	2,500	N/A

TABLE 3.1: Inflow parameters for the jet in crossflow (§ means to be determined by J_p, N/A means not applicable).

*Some of the contents of this chapter were presented at the 30th AIAA Applied Aerodynamics Conference, New Orleans, June 2012

The main flow parameters shown in table 3.1 are the same as in the code validation section in last chapter. Additional jet injection parameters are also given in table 3.1. The length of the flat plate is 112.5 mm. Sonic nitrogen with a temperature of 244.17 K is injected from a slot of width w^* =2.24 mm on the bottom wall. The jet centre is located 74.5 mm downstream of the leading edge. In non-dimensional form, w =3.8 and the slot centre is located at x =113. The simulation Reynolds number is $2,500$, $Re_{x_0{}^*}$ here is 34,757 and $x_0{}^*$ is 8.31 mm.

A multi-block rectangular computational domain of 200×80 shown in figure 3.1 is used for 2D base flow, and later 3D instability studies after an extrusion in the spanwise direction. As introduced in Chapter 2, the mesh is stretched in both the streamwise and the wall-normal directions to obtain higher resolution near the wall and the slot as shown in figure 3.1. The stretching coefficients are specified as $a = 3.0$ and $b = 5.5$. Three monitor points at (99.76, 6.19), (114.20, 6.19) and (122.69, 6.19), marked by black spots in figure 3.1, are chosen to get information about the variation of variables with time. The 3D mesh is extruded from the 2D mesh with different L_z, ranging from 3 to 64. For all 3D cases 8 spanwise grid points are adopted. This number is obtained by comparing N_z =8, 16 and 32 with simpler meshes, showing that N_z =8 is sufficient to resolve the exponential stage of growth and get the same growth rate of the 3D instability.

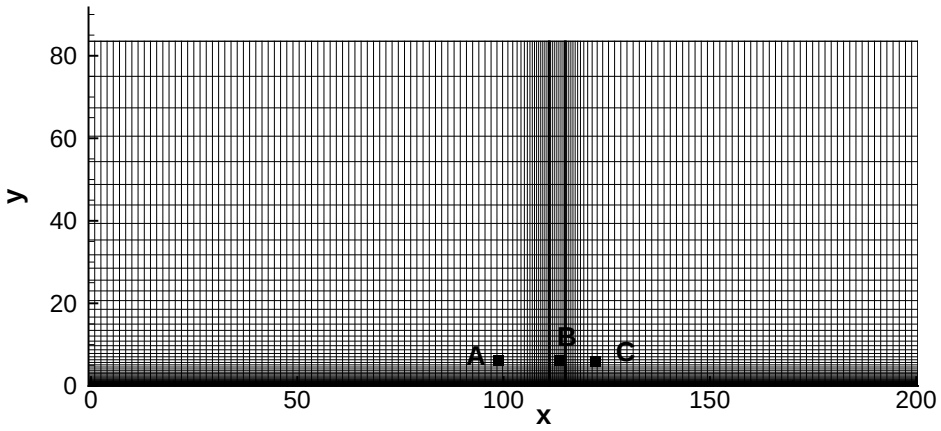

FIGURE 3.1: 2D geometry and mesh displayed in every 5 points for jet in crossflow with three monitor point locations.

The similarity solution for a compressible laminar boundary layer given in White (1974) is used to generate the inflow profiles and initialize the flowfield. Extrapolation and characteristic boundary conditions are used at the inflow and outflow boundaries respectively. An isothermal no-slip wall at room temperature of 293 K is adopted to compare with experiment of Powrie (1996), while an integral characteristic condition is used for the upper boundary. A periodic boundary condition is applied in the z direction for 3D cases.

For the jet in crossflow, an integral characteristic boundary condition is applied across the jet. The jet profiles are defined over the injection slot from $x = 111.1$ to $x = 114.9$ on the wall with a parameter δ which decides the slope of jet velocity and temperature at the edge of the slot with specified centreline values in the following form

$$\begin{aligned} \text{for } (L_s - w/2) < x \leq L_s: \quad & v = v_j \ \tanh(\tfrac{x-(L_s-w/2)}{\delta}) \\ & T = T_w + (T_j - T_w) \ \tanh(\tfrac{x-(L_s-w/2)}{\delta}), \\ \text{for } L_s < x \leq (L_s + w/2): \quad & v = -v_j \ \tanh(\tfrac{x-(L_s+w/2)}{\delta}) \\ & T = T_w + (T_w - T_j) \ \tanh(\tfrac{x-(L_s+w/2)}{\delta}), \end{aligned} \tag{3.1}$$

where x is the non-dimensional x-coordinate, v_j and T_j are the wall-normal velocity and the temperature at the centre of the jet, respectively, and $w = 3.8$ is the slot width. T_w is the wall temperature. A value of $\delta = 0.0717$ is obtained by iteration to achieve 99% of the jet centreline value within 5% of the slot width. Figure 3.2 shows the profiles with different δ values. The profiles are smoother but with the same central-jet value when a larger δ is used.

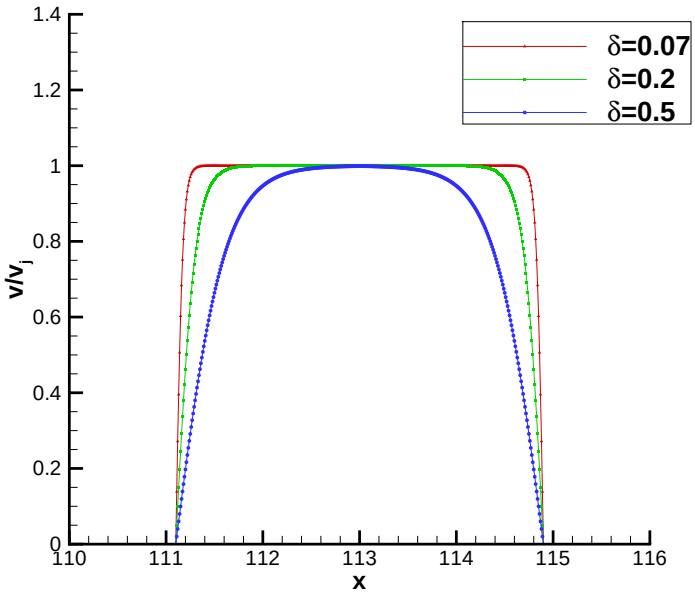

FIGURE 3.2: Velocity distribution across the jet with different δ values.

An important parameter used in jet flow is the momentum flux ratio (J_p) (Powrie, 1996) given by equation (1.1). The pressure across the jet exit is assumed to be constant. In the present study, the ratio of the jet stagnation pressure to the exit pressure is 1.8929 for isentropic flow, and L_s=126.38 in non-dimensional form. By introducing the reference values (w=3.8 in non-dimensional form), equation (1.1) can be used to calculate the

non-dimensional expression for p_j as

$$p_j = 0.280435 J_p. \tag{3.2}$$

The non-dimensional density across the jet inlet can be obtained as

$$\rho = \frac{\gamma {M_\infty}^2 p_j}{T}. \tag{3.3}$$

3.2 Results

The 2D jet-in-crossflow simulation becomes steady after a time length of 12,000 which is about 60 throughflow times for the whole domain. The flowfield at $t = 12,000$ is shown in figure 3.3 by contours of density with superposed streamlines. A typical shock system for jet in crossflow is seen, as observed by Spaid (1975), Qin and Redlich (1999) and Gajbhiye (2010). Flow separations are formed both upstream and downstream of the jet injection, inducing an upstream separation shock and a shear layer, a bow shock above the jet, as well as a recompression shock downstream.

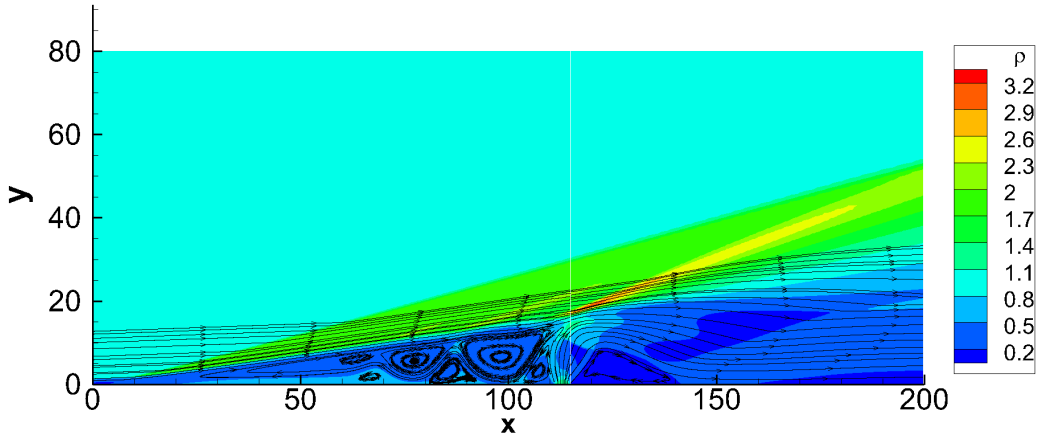

FIGURE 3.3: Density contours for 2D jet in crossflow superposed by streamlines (for J_p=0.3).

3.2.1 Mesh dependency study

A mesh dependency study is carried out for a case with J_p=0.3 based on a computational domain of size 200 × 80. Three different meshes with different streamwise resolutions are used here, denoted as an S mesh (379 × 256 with Δx=1 and 0.5 at the inflow and outflow boundaries, respectively), M mesh (765 × 256 with $\Delta x = 0.3$ at inflow and outflow boundaries) and L mesh (1088 × 256 with $\Delta x = 0.2$ at inflow and outflow boundaries). Δy near the wall and Δx around the slot jet are 0.014 and 0.1 for all three

meshes. Meshes with a higher resolution in the wall normal direction or around the jet area were also tried, but led to small amplitude unsteadiness in the 2D simulation especially above the jet, even with smaller time step. To get a clear observation of the global instability development and eliminate the interference, the resolution in the the wall normal direction and around the jet in the streamwise direction are chosen as N_y =256 ($\Delta y = 0.014$ near the wall) and Δx =0.1. This resolution follows a previous mesh dependency study using a single block mesh where different N_y were tested and N_y =256 was found to be sufficient to generate a mesh-independent solution. The error of skin friction was within 0.52% when the wall-normal mesh was doubled. The Ducros sensor is turned off and there are always more than 65 grid points within the boundary layer in the wall normal direction.

Densities measured from the S, M and L mesh setups at the three different monitor points, lying upstream, above the jet and downstream of the jet, follow the same trend to become steady, though there are oscillations before a non-dimensional time of 10,000. The differences of mean densities from the S, M and L meshes at the same point are within 0.5% after flow reaches steady state.

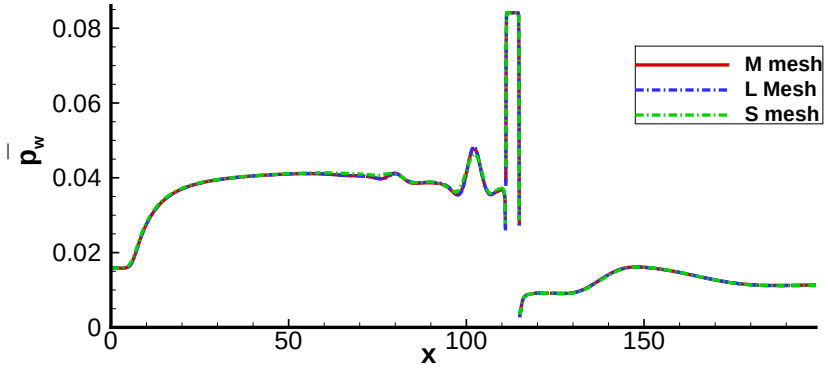

FIGURE 3.4: Distribution of mean wall pressure for different meshes with J_p=0.3 (the gaps in the curves are caused by interfaces between computational blocks).

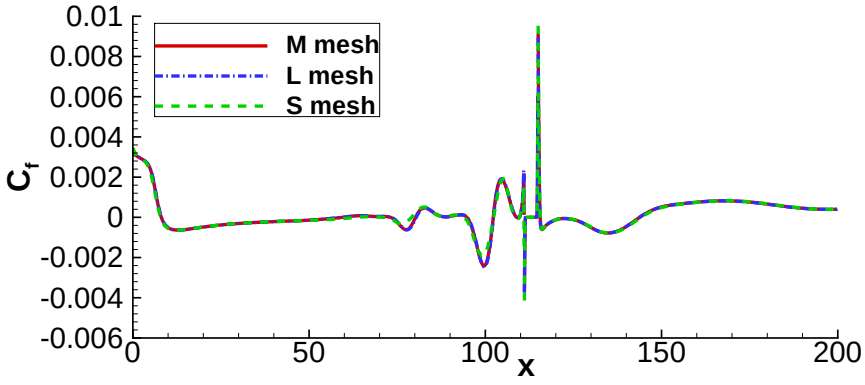

FIGURE 3.5: Distribution of skin friction coefficient for different meshes with J_p=0.3 (the gaps in the curves are caused by interfaces between computational blocks).

Figure 3.4 shows the mean wall pressure distribution based on different meshes. Small differences in distributions of mean wall pressure from different meshes can be observed between results on the S mesh and other meshes. They are mainly focused on the recirculation zone. Figure 3.5 shows the skin friction coefficients based on different meshes. Results from mesh M and mesh L accord with each very well. The overlap of both results mentioned above leads to the conclusion that result from the M mesh is grid-independent.

3.2.2 Validation

Validation is done based on the preferred mesh and the works of Qin and Redlich (1999) and Powrie et al. (1993) where a slot jet of $w^* = 0.075$ mm width was used. The corresponding J_p value is 0.354. This narrow slot would require an extremely highly stretched mesh, however it was observed by Gajbhiye (2010) that as long as J_p was fixed the slot width was not important, so a slot width of $w^* = 2.24$ mm (3.8 in dimensionless variable) is used here. Same J_p value of 0.354 is used as in the experiment with the practical effect of using lower density of injected gas compared with experimental setup.

Figure 3.6 to figure 3.8 show the flowfields development with time. As we are particularly interested in the flow separation length, only upstream flowfields at selected time instants are plotted. From plot 3.6(a) to plot 3.6(f), flow separation spreads upstream as time goes on. Initially there is one upper vortex and one lower vortex as shown at $t = 100$. Another lower vortex appears around $x = 90$ at $t = 200$. We will call this the 1+2 mode, where 1 means the upper vortex number and 2 means the lower vortex number. At $t = 300$, two upper vortices and three lower vortices appear, showing the 2+3 mode. According to the time spent and flow separation point locations from $t = 200$ to $t = 300$, the speed of separation spreading upstream can be calculated to be about 0.2. As flow separation develops further upstream, a 3+3 mode develops at $t = 400$. Then, after experiencing the 3+4 mode at $t = 500$ (we count the lower vortex and the small vortex underneath it around $x = 90$ as one vortex), the flowfield reaches the strongest mode 4+4 at $t = 800$, with flow separation at $x = 9.44$. By multiplying the displacement thickness 0.5855 mm at inflow boundary, the flow separation at t=800 is 59.46 mm upstream of the jet injection, which is in good agreement with the 58.6 mm in Powrie's experimental data and 60 mm obtained by Qin and Redlich (1999).

Figure 3.7 shows the movement of the separation point and a vortex core in the separation region with time. It is observed in figure 3.7(a) that after experiencing a quasi-steady state with minor downstream movement of flow separation from $t = 800$ to $t = 1,000$, flow separation spreads even further upstream at much slower rate and settles down at x=4, which is at least 13 mesh grid points away from inflow boundary. It is observed that the flow becomes steady at $t = 2,000$ when the flow separation is 15 grid points away from inflow boundary. Therefore it is believed that the flow is converged and flow

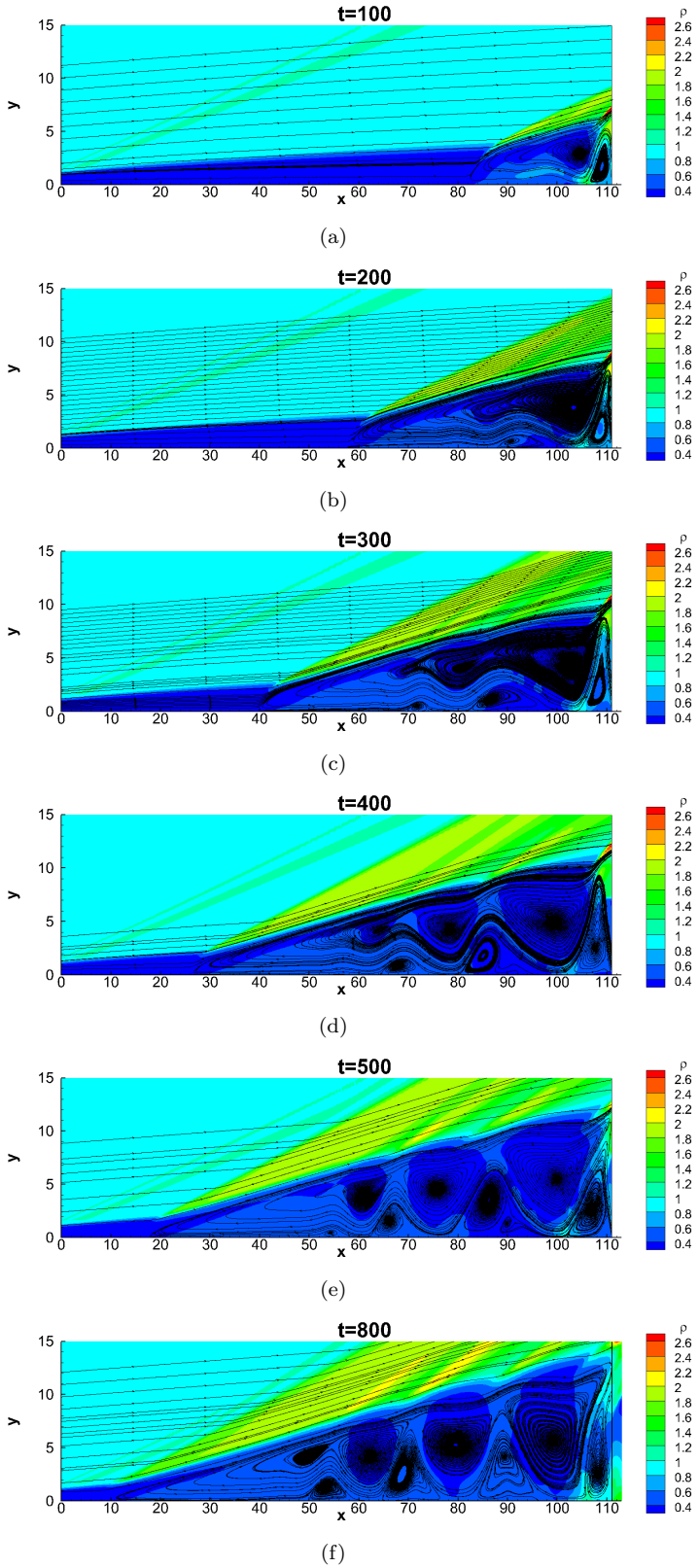

(a)

(b)

(c)

(d)

(e)

(f)

FIGURE 3.6: Flowfields of jet in crossflow at different time instants before $t = 800$ contoured by density and superposed by streamlines.

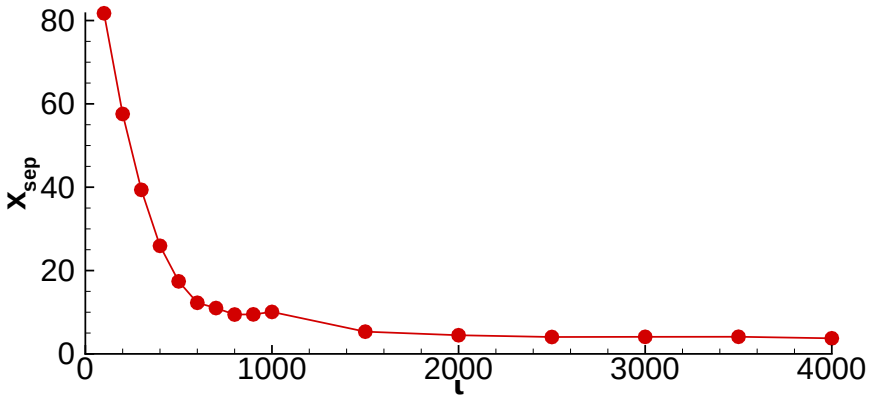

(a)

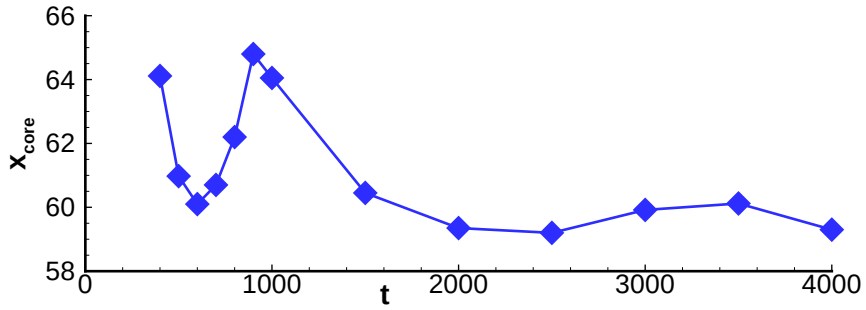

(b)

FIGURE 3.7: Movement of (a) flow separation point and (b) location of the third upper vortex core centre, counted from jet, with time.

separation is not (quite) stopped by inflow boundary condition. The flow separation is no longer spreading upstream, and the computational domain is large enough for the flow separation. Figure 3.7(b) shows the movement of the third vortex core which is counted from downstream jet. The plot starts from $t = 400$ since only two upper vortices are developed before $t = 400$. As seen in the plot, rapid movement of upper third vortex core is observed from $t = 800$ to $t = 1,000$, which means the flow separation oscillation is relevant to the whole flow structure. Some of the corresponding flowfields at different time instants after $t = 800$ are plotted in figure 3.8. It is found that after the 4+4 mode, which lasts from $t = 600$ to $t = 2,000$, the flow reaches a converged 3+3 steady mode as shown in plot 3.8(d). The flow separation length according to the converged 3+3 mode is 62.65 mm, which is 7% larger that observed by Powrie (1996) and obtained by Qin and Redlich (1999).

To further compare with work of Qin and Redlich (1999) and Powrie et al. (1993), figure 3.9 shows the pressure distribution at $t = 800$ rather than $t = 2,500$ from current simulation and that obtained by Qin and Redlich (1999). The streamwise and wall-normal direction coordinates are presented in dimensional form for easier comparison to Qin and Redlich's figure. It should be noted that the simulation of Qin and Redlich is

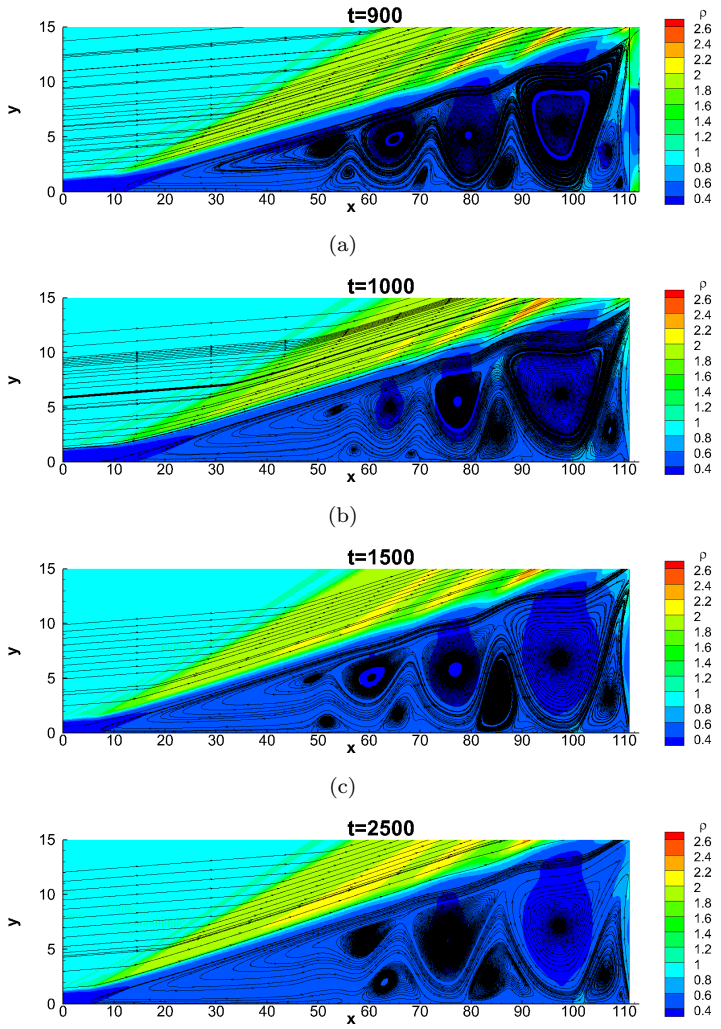

FIGURE 3.8: Flowfields of jet in crossflow at different time instants upto $t = 800$, showing by density contour superposed by streamlines.

based on the whole flowfield from leading edge to the end of the experimental platform, while the current simulation starts downstream of the leading edge. By comparing the two figures, high pressure areas upstream and above the jet after the separation shock and the low pressure areas between the high pressure area, above and downstream of the jet, are obviously seen. With the help of finer mesh in the present work, the low pressure caused by the vortexes upstream jet is better described. Figure 3.10 shows comparison of the wall pressures between current simulations and reference data. As mentioned before, the J_p value for the reference data from Powrie (1996) and Qin and Redlich (1999) is 0.354. Over-estimation on flow separation is observed for the current corresponding result (J_p=0.354 case). The same upstream separation length is observed when reducing the J_p to 0.3 in current simulation. However, over-estimation of wall pressure in the upstream separated flow is observed for all the simulations, including result from Qin and Redlich, compared with the experimental result from Powrie.

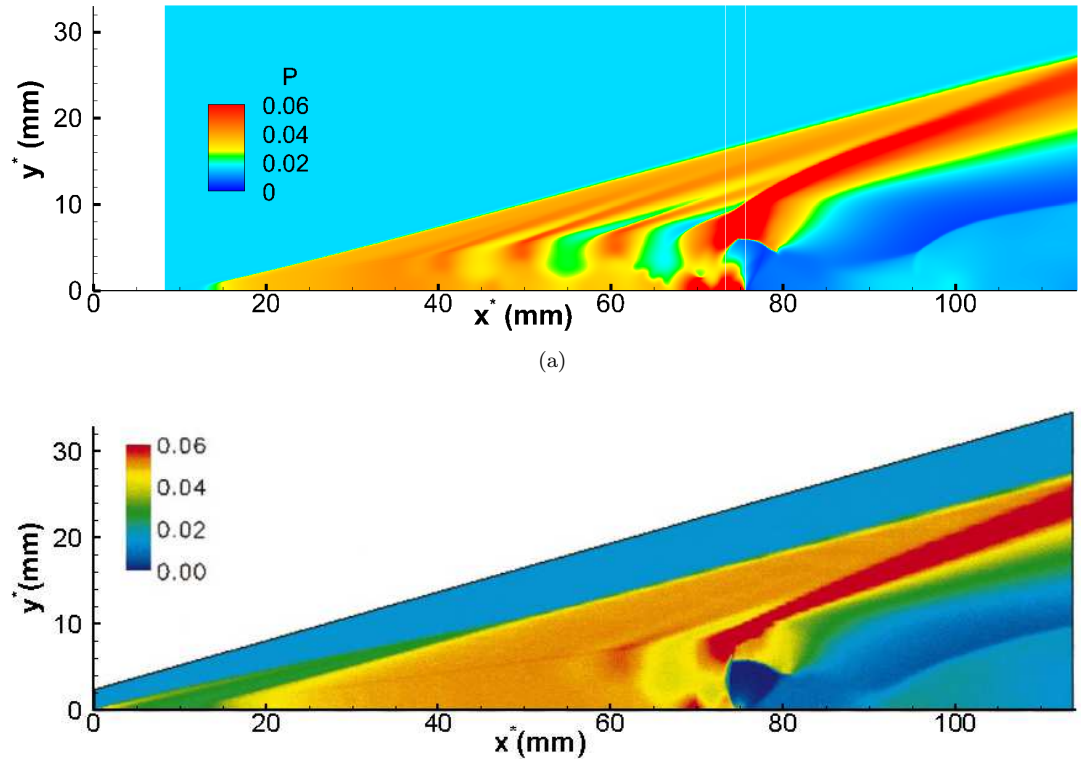

(a)

(b)

FIGURE 3.9: Distribution of pressure for 2D jet in crossflow, (a) simulation result at $t = 800$ with J_p=0.354, (b) result from Qin and Redlich (1999).

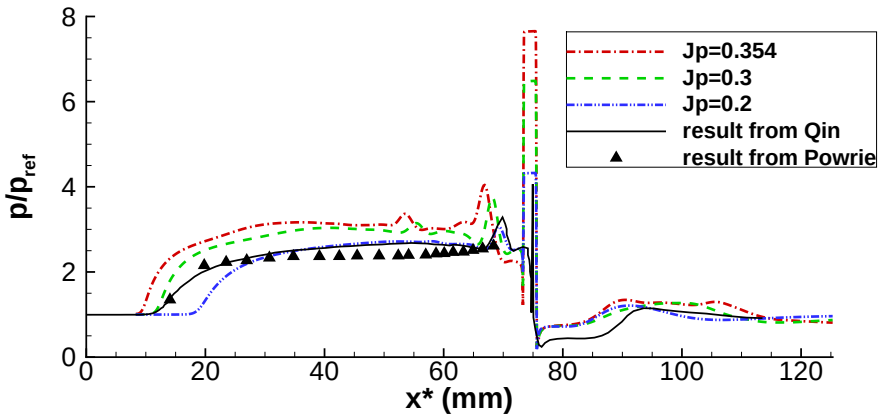

FIGURE 3.10: Comparison of wall pressures with different J_p with that from Powrie (1996) and Qin and Redlich (1999).

As mentioned in separation length comparison, current result is 7% larger that observed by Powrie (1996) and Qin and Redlich (1999). This should be caused by the difference between simulating from the leading edge and from a similarity solution. If examining the flow field carefully, a leading edge shock is observed in figure 3.9(b) which could increase the downstream pressure and help preventing flow separation spreading upstream as the separation point is close to the leading edge. There are also other possible reasons

like the 3D effect in experiments or the influence from the effect of jet width. Although the result with the current method does not predict as well as Qin and Redlich (1999), it does save computational cost and can get better resolved result which is helpful for further 3D simulation. As a conclusion, all the works done above show the reliability and qualification for the current code to carried out further study.

3.2.3 2D flowfield study

As shown by Powrie (1996) and Gajbhiye (2010) the main parameter controlling the separation length is J_p. Figure 3.11 shows the distribution of mean wall pressure ($\overline{p_w}$) for J_p of 0.1, 0.2, 0.3 and 0.4 but with the same δ of 0.0717. The differences between the curves are mainly seen in the amplitude of mean wall pressure at the jet (since the jet pressure is directly proportional to J_p). The variation of mean wall pressure around the jet and the place where mean wall pressure starts to increase, i.e. the upstream separation points. It is observed that mean wall pressure shows stronger variations near the jet and the separation appears closer to the inflow boundary for flow higher J_p. For the jet injection, a larger pressure across the sonic jet exit means a larger mass flow rate, producing larger recirculation zones. When J_p=0.4 the separation region is too large for the current domain to capture, since the separation point reaches the inflow.

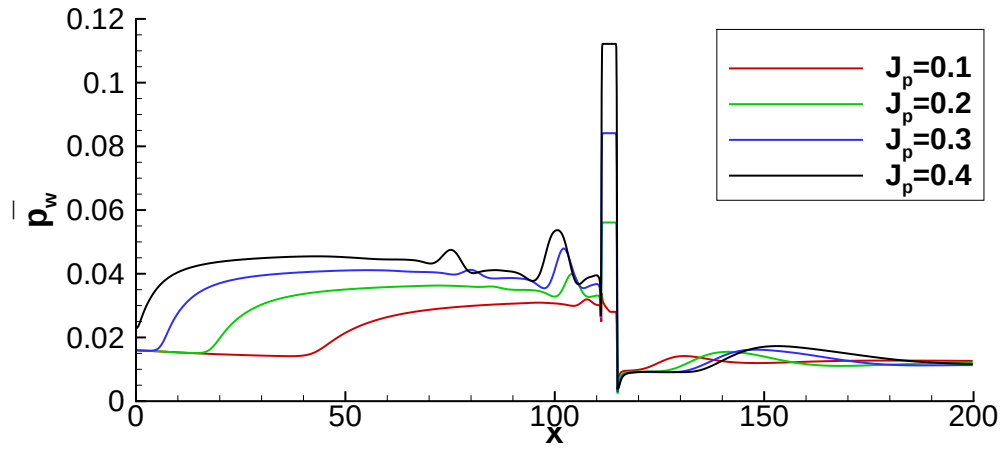

FIGURE 3.11: Distribution of mean wall pressures for flows with different J_p.

Figure 3.12 shows the skin friction distribution for different J_p. The laminar solution from Eckert (1955) is also plotted in the figure shown by the black dashed line. Because of the jet injection, the skin friction deviates away from the laminar solution. The stronger the jet, the earlier and further away is the deviation. However, according to the upstream coincidence between curves with different J_p and the laminar solution curve, it is concluded that upstream flow is laminar. However for the $J_p = 0.4$ case, it is noticed that flow separation reaches to the inflow boundary. To make sure the

separation zone is not affected by the inflow boundary, J_p =0.1 and J_p =0.3 is used in the following study.

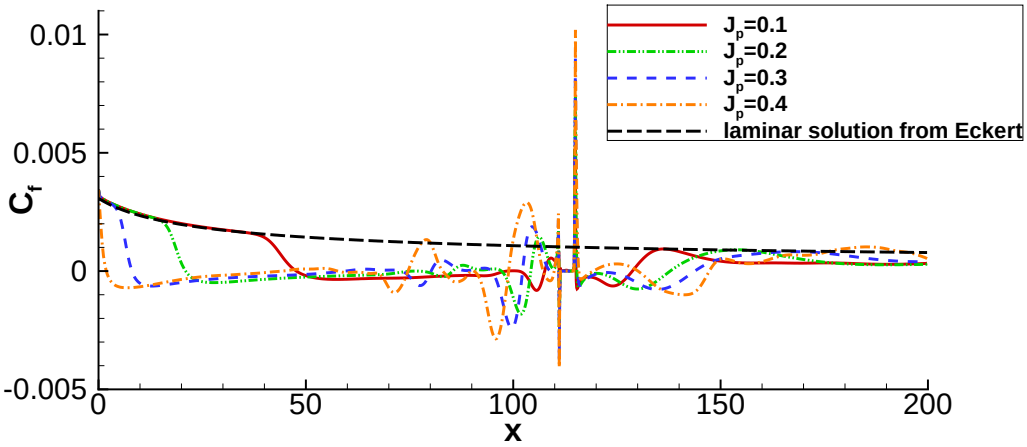

FIGURE 3.12: Distribution of skin friction coefficients for flows with different J_p.

3.2.4 Instability

The converged 2D results are extended in the spanwise direction to form a 3D base flow. Small perturbation is then added to the spanwise velocity component to study the global instability with a Gaussian profile in the $x-y$ plane and a sinusoidal distribution in the spanwise direction. The spanwise wavelength equals to the domain span ($\lambda = L_z$). The perturbation is given by

$$w'(x,y,z) = Ae^{-\frac{1}{4}[(x-x_c)^2+(y-y_c)^2]} \sin\left(\frac{2\pi z}{L_z}\right), \tag{3.4}$$

where A is the amplitude, $A = 3.5 \times 10^{-12}$ is used in all the following simulations for instability study. The centre of the Gaussian profile (x_c, y_c) was chosen right above the jet slot at (113, 6). A parameter $\varepsilon(x,\ y)$, measuring the mean square fluctuation of the spanwise velocity, is used to monitor the development of the 3D flow instability. The parameter is defined by

$$\varepsilon(x,y) = < w(x,y,z)^2 > - < w(x,y,z) >^2, \tag{3.5}$$

where $< . >$ denotes an average in the spanwise direction.

Three-dimensional instability for flows with different J_p are compared. The 3D simulations are carried out based on converged base flows. Figure 3.13 shows the development of the spanwise variation quantified by ε at a monitor point (x=113, y=2.12) above the jet for flows with J_p of 0.1 and 0.3 and L_z (λ) of 6. It is obvious that spanwise fluctuations show a exponential stage of growth for the flow with the stronger jet, while

for the case with weak jet, the spanwise variation grows only slightly. This comparison shows the flow with J_p of 0.3 is strongly globally unstable, while the flow with J_p of 0.1 is slightly unstable. It is also observed that there are periodic-like oscillations for both curves which are caused by the flowfield unsteadiness and flow structures oscillating around the monitor point.

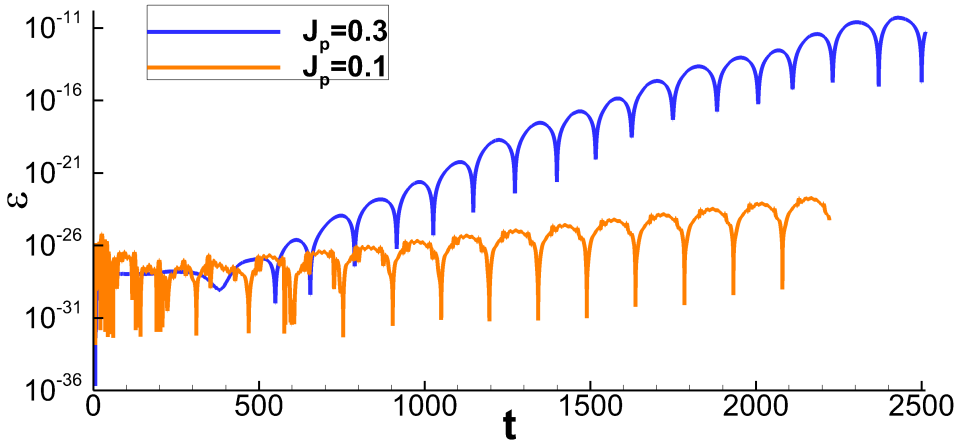

FIGURE 3.13: Growth of spanwise variations for flows with different J_p along time at monitor point (113,2.12).

Based on the above comparison, the case with J_p of 0.3 is used here to study the preferred mode for the global instability. Simulations are run for flows with different spanwise lengths. Spanwise grid point N_z=8 is used for all the cases. As shown in figure 3.14(a), after an initial development of about 300 in non-dimensional time, an exponential growth of spanwise variation appears. The growth rate of the instability varies with the spanwise wavelength. By measuring the slopes of the curves in the exponential stage, the variation of growth rate $\sigma = 0.5\, d\,(\ln \varepsilon)/dt$ as a function of the spanwise wavenumber $\alpha = 2\pi/L_z$ is obtained and plotted in figure 3.14(b) with an estimated error bar to indicate the growth rate range. The error estimations shown in the plot were obtained by calculating the slopes at three different monitor points. The same conclusion can be obtained compared with figure 13 from Robinet (2007). The growth rate is zero or close to zero when the relevant wavelength is either very small or very large. It can be seen that the most unstable mode corresponds to the flow with a forcing wavelength of around 8 times the inflow displacement thickness. This was confirmed by performing a simulation with L_z=64 and N_z =32 as 7 spanwise periodic wave were observed all over the flowfield, corresponding to a most unstable wavelength of about 9.

After increasing exponentially, the instability reaches a saturated state. Figure 3.15 shows the distribution of w-velocity at different stages for a case with L_z=6 and an increased N_z=32. Compared with the w-velocity distribution in the exponential growth stage on figure 3.15(a), the amplitude of the w-velocity increases by a factor of 10^3 in the

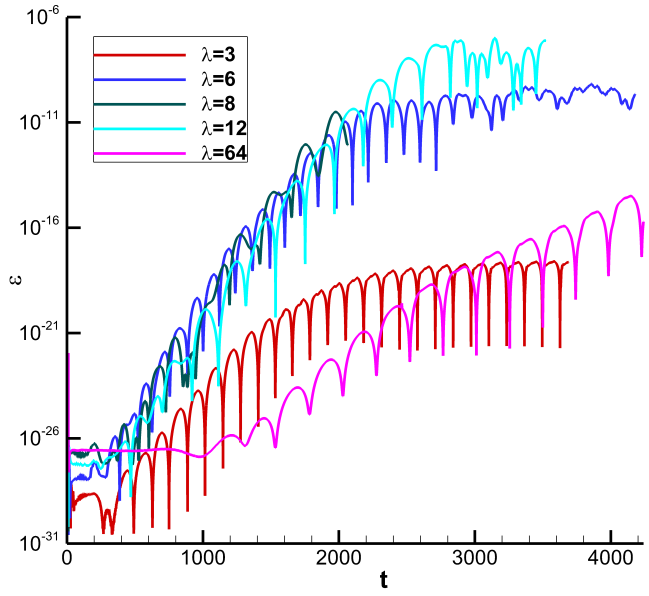

(a)

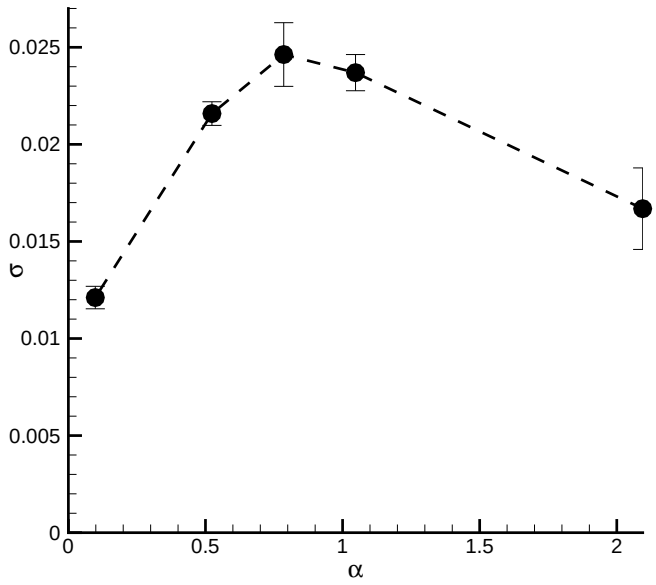

(b)

FIGURE 3.14: Development of stability for the jet case with different spanwise lengths: (a) growth of spanwise variations with time at monitor point (113,2.12), (b) spanwise variation growth rate along wavenumber, with error bars.

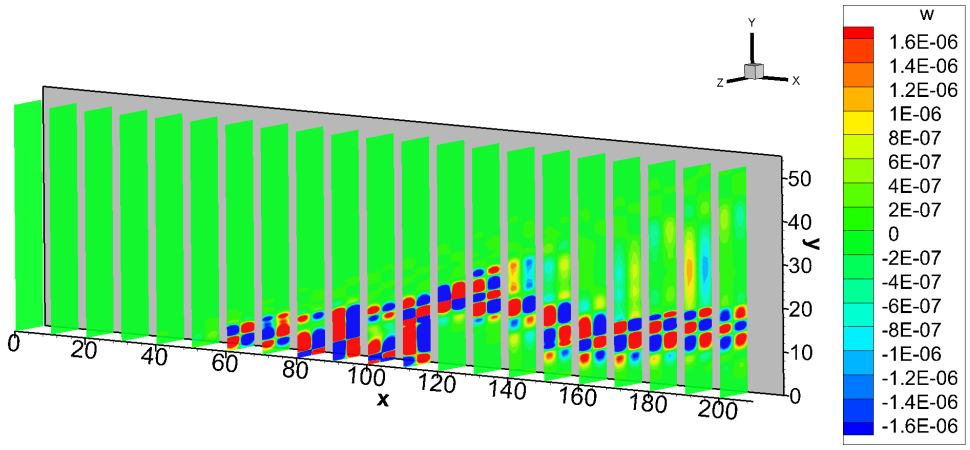

(a)

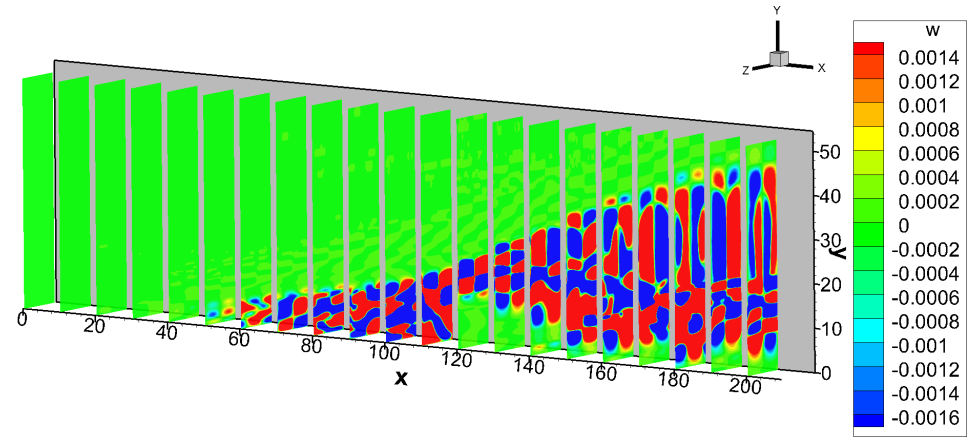

(b)

FIGURE 3.15: Distribution of w-velocity on $y-z$ slices for L_z=6 (a) at t=1,600 in the exponential growth stage, (b) at t=2,400 in the saturated stage.

saturated stage with higher harmonics near the exit as shown in figure 3.15(b). Observations from other cases also show that the single-harmonic structure of the disturbance breaks down at the saturated stage.

Vortical structures at different stages are plotted in figure 3.16 based on streamwise vorticity quantity ω_x ($\omega_x = \frac{\partial w}{\partial y} - \frac{\partial v}{\partial z}$) and contoured by the distance to the wall. The flow structures in the upstream separated region and above jet can be seen in both plots. The streamwise vortices observed in the exponential stage are not as stretched as those observed in the saturated stage. The flow structure in the exponential stage is also smoother than that in the saturated stage, showing the variation of flowfield becomes more intense in the saturated stage.

Compared with the uniform spanwise distribution that would be seen for the streamwise velocity u in the exponential stage (since the disturbances there are much smaller than the mean flow variation), a variation of u-velocity in the saturated stage is observed at x=90 and downstream, showing the presence of streamwise (Görtler-like) vortices

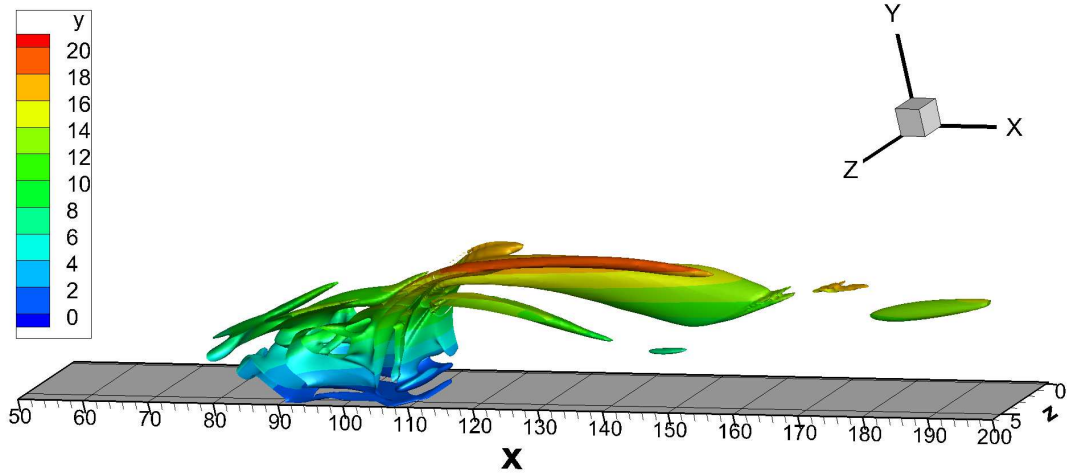

(a)

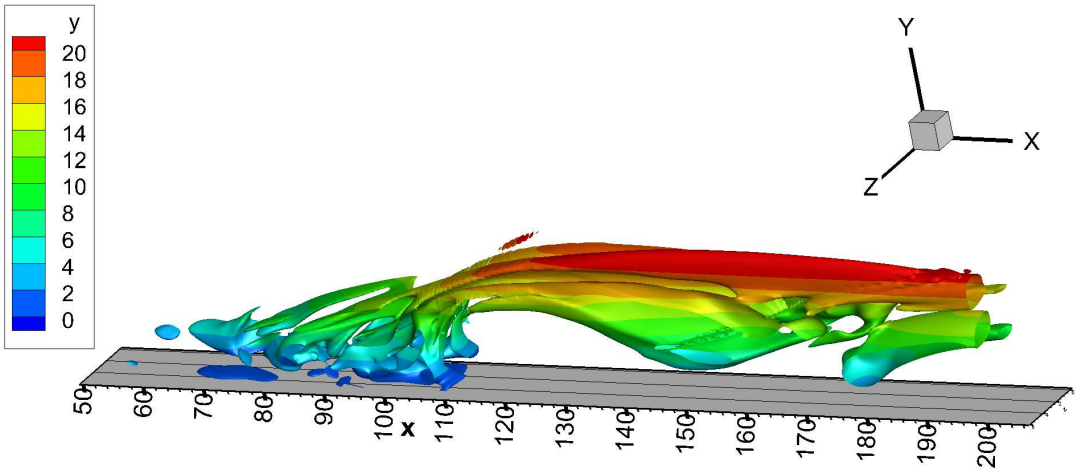

(b)

FIGURE 3.16: Iso-surfaces of ω_x=0.01 at different stages, (a) t=1,200, (b) t=2,400.

as shown in figure 3.17(a). They are formed by the concave shear layer near the flow reattachment point. The vortices develop towards the wall but don't reach it, as confirmed in figure 3.17(b) which shows the contours of u-velocity near the exit superposed by streamlines. Two pairs of counter-rotating vortices are observed above y=10. Flow breakdown to turbulence is not observed in saturated stage even when a mesh with higher spanwise resolution is used. The reason is that in the current computational domain the streamwise streaks are pushed away from the wall by the jet and become weak close to the wall. However, Andersson et al. (2001) stated that a streak amplitude of about 26% of the freestream speed was needed for streak breakdown to occur in incompressible flow. In the current study, streak amplitudes of about 26.2% are observed. In consideration of that the streamwise vorticity is still not far away from the wall in the saturated stage, streak breakdown and flow transition might happen when the computational domain is elongated.

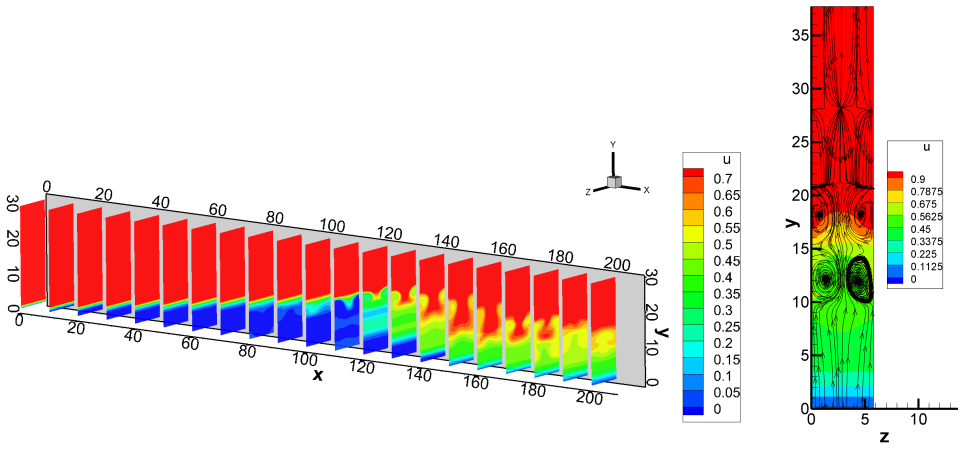

(a) (b)

FIGURE 3.17: Contours of the u-velocity (a) on different $y-z$ slices, (b) on x=199.5 plane.

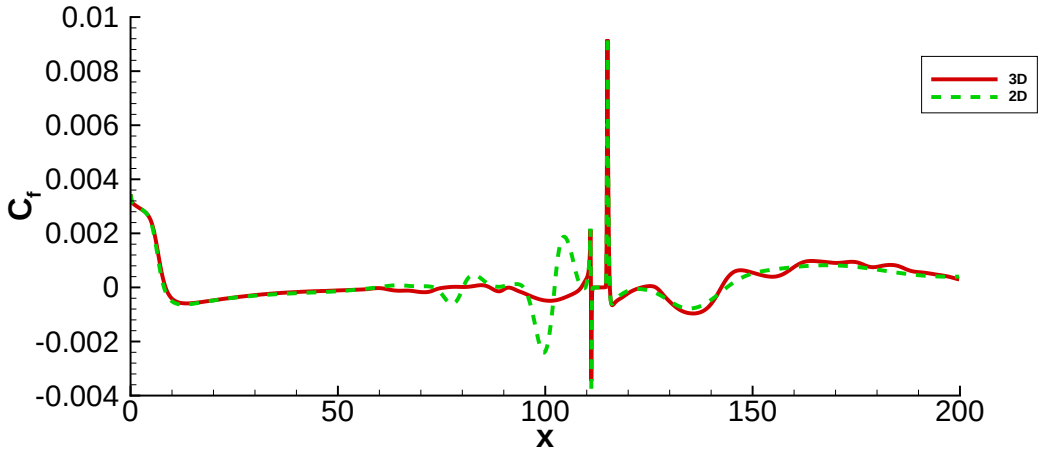

FIGURE 3.18: Comparison of friction coefficient distribution between 2D and 3D.

The effect of the change to a 3D unstable flow is analysed by plotting the skin friction coefficient (C_f) distribution as shown in figure 3.18 for the converged 2D flow at t=1,200 and 3D saturated flow at t=2,400. For the 3D case, C_f is obtained by averaging in the spanwise direction. It is found that the separation point, where C_f=0 firstly appears, is only slightly affected by the 3D instability, leading to a slightly shorter bubble. It can also be seen that the variation in C_f upstream of the jet is smaller than that in the saturated 2D flow. After the jet, the 3D result shows stronger variation than the 2D case.

3.3 Summary

Simulations of a jet in supersonic crossflow have been conducted. Following a grid-independency mesh, 2D base flows with different jet strengths are compared. For the J_p=0.4 case, the flow separation is strong enough to reach the inflow boundary. The jet in crossflow becomes unstable as J_p is increased, with a critical value of J_p below 0.1. Hence flow with J_p=0.3 is used for instability study with different spanwise lengths which is equal to the wavelength of the added disturbance. The most unstable wavelength is found to be 8 based on the incoming boundary layer displacement thickness. A streamwise vortex is observed in the jet case in the saturated state formed after disturbance growth. The vortex is located away from the wall and does not have a strong effect on flow properties at the wall.

Chapter 4

Global instability for high speed ramp flow*

Supersonic flow over a compression ramp is simulated in both 2D and 3D. Code validation and a mesh dependency studies are performed, then 3D instability of flowfield is analyzed at different Reynolds numbers and for disturbances with different spanwise wave lengths. Finally, flow transition to turbulence is studied.

4.1 Simulation setup

Parameter	Main stream
Medium	Nitrogen
Mach number	4.8
Static temperature (K)	55.4
Wall temperature (K)	Adiabatic wall
Simulation Reynolds number	3,422 and 6,843

TABLE 4.1: Ramp flow parameters.

The configuration for the ramp flow used in this chapter comes from Pagella et al. (2004) in their comparison between supersonic ramp and supersonic shock impingement flow, and was also used by Lüdeke and Sandham (2010). The flow conditions are listed in table 4.1. The freestream Mach number is 4.8 and the static temperature is 55.4 K which is used as the reference temperature. The wall is considered to be isothermal with temperature equal to its laminar adiabatic value of $T_{aw} = 4.90$ obtained from the similarity solution. Two cases with Reynolds numbers of 3,422 and 6,843 based on the inflow boundary layer displacement thickness are simulated. If the inflow conditions are fixed, the practical difference between the two simulations is the distance from leading

*Some of the contents of this chapter were presented at the 30th AIAA Applied Aerodynamics Conference, New Orleans, June 2012

edge to the ramp corner. This distance for Re=3,422 case is about half of that for Re=6,843 case.

The ramp angle used here is 12°. The computational domain extends 215.2 and 325 (in non-dimensional unit) before and after the ramp corner respectively, and has a height of 50 in the wall-normal direction. The coordinate system is set to having the $x-$axis parallel to the wall behind the ramp corner, therefore the inflow velocity and the wall before the ramp corner are at an angle of 12° to the $x-$axis. The domain (shown in figure 4.1) is meshed with stretched grids in both the streamwise and the wall-normal directions to better resolve the flow near the corner and the wall.

Meshes for 3D simulations are extruded from the 2D mesh with different spanwise lengths (L_z) ranging from 3 to 24. To resolve the flow in the spanwise direction, a spanwise grid size of N_z =16 is chosen for the study of the exponential stage of 3D global instability. This is considered to be sufficient to resolve the flow at linear growth stage. Finer mesh with Nz=64 is used when flow transition is investigated. The details will be introduced in the section of transition to turbulence.

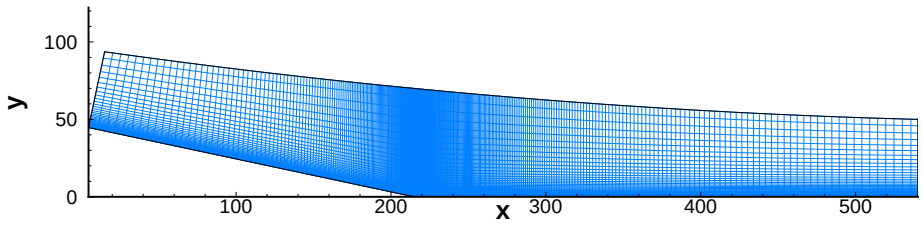

FIGURE 4.1: Two-dimensional mesh used for study of a 12° ramp flow (the grid lines are displayed every 10 points).

The similarity solution for a compressible laminar boundary layer (White, 1974) is used to generate the inflow profiles and initialize the flowfield. Extrapolation and characteristic boundary conditions are used at the inflow and outflow boundaries respectively. A no-slip isothermal wall is adopted. An integral characteristic condition is used for the upper boundary. Periodic boundary conditions are applied in the z direction. The solution procedure then marches forwards in time.

4.2 Results of base flows and 3D instability

To have a qualitative impression of the ramp flow structure, figure 4.2 shows a 2D flowfield plot contoured by density and superposed by streamlines. It is obvious that a shock-wave is formed after the ramp corner. The interaction between the shock-wave and the boundary layer induces flow separation around the corner, causing a weaker upstream separation shock. As shown in the figure, the flow around the ramp corner is complex

and needs to be carefully resolved. To get a reliable flowfield, a mesh-dependency study is firstly carried out.

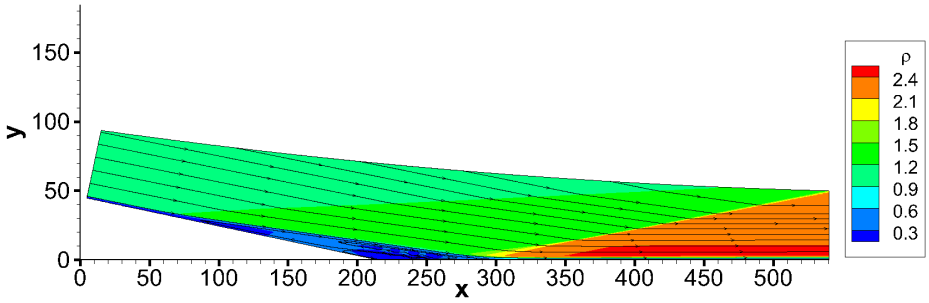

FIGURE 4.2: Density contours for a 12° ramp flowfield superposed by streamlines.

4.2.1 Grid refinement

To check the grid-dependency, simulations based on five meshes with different grid distributions in the streamwise and the wall-normal directions (meshes SX: 800×169, SY: 1,153×109, M: 1,153×169, L: 1,800×250 and XLY: 1,800×376) are performed. Based on a former study, Δx is finally set to be 0.05 around the corner, Δy is set to be 0.01 at the first cell away from the wall. The streamwise grids are stretched both upstream and downstream of the ramp corner. The mesh is stretched in the wall-normal direction (and is uniform in the spanwise direction for 3D cases). All the stretched meshes were generated using a hyperbolic tangent function in Gridgen (Pointwise, 2008). The

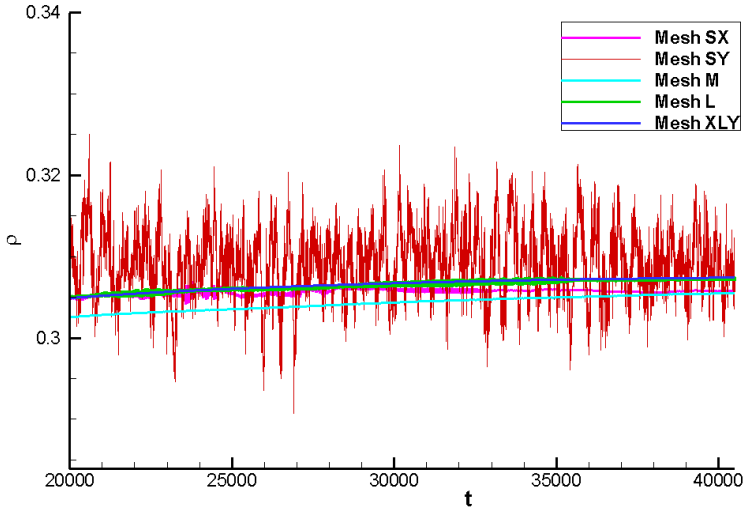

FIGURE 4.3: Time histories of density at (x=196.76, y=6.70) for 2D ramp flows with $Re = 6,843$ from different meshes.

maximum spatial spacing is fixed once the grid point number and the minimum spatial spacing are specified using the method proposed by Vinokur (1980).

The time histories of density at a monitor point (x=196.8, y=6.7) just upstream of the ramp calculated by different meshes are plotted in figure 4.3. Significant differences can be seen between results from meshes SY and M. The result from mesh SY is unsteady with a peak-to-peak amplitude of about 0.03, while the flowfields from meshes SX, M, L and XLY are steady, hence it is believed that the simulation is more sensitive to the mesh in the wall-normal direction. According to the agreement of results from mesh L and mesh XLY, the result from mesh L is considered to be grid-independent. The same conclusion is obtained from the two pressure statistics: the mean pressure and the root-mean-square (RMS) pressure on the wall, as plotted in figure 4.4. It is shown that the mesh in the wall-normal direction is the principal factor influencing the average length of separation obtained from the distribution of the mean pressure. Figure 4.4(b) shows that the flow is steady when the finer meshes are used. Figure 4.5 shows C_f distributions from different meshes. The oscillations near the corner for the result from mesh SY are caused by the lack of grid resolution in the wall normal direction. The shortest separation bubble is also observed for flow using mesh SY. Although the results from SX and M agree well upstream, differences are observed downstream. The downstream oscillation from simulation result using mesh SX is caused by a lack of grid points downstream. Results from mesh L and mesh XLY agree both upstream and downstream and give the largest separation bubble. All of the comparisons mentioned above lead to the conclusion that the results from mesh L are mesh-independent. In the following calculations of this section, mesh L is used for further study. The time step is decided below the stability limit by testing different Δt.

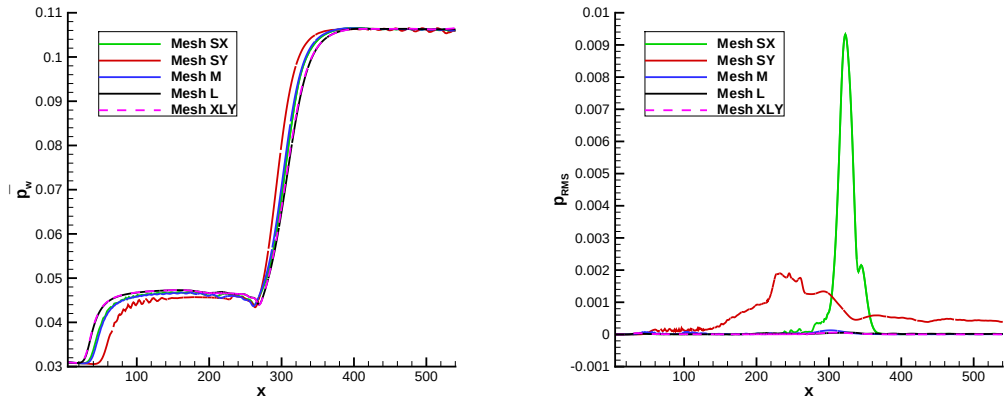

(a) (b)

FIGURE 4.4: Statistic values of pressure on the wall: (a)mean pressure, (b)RMS pressure.

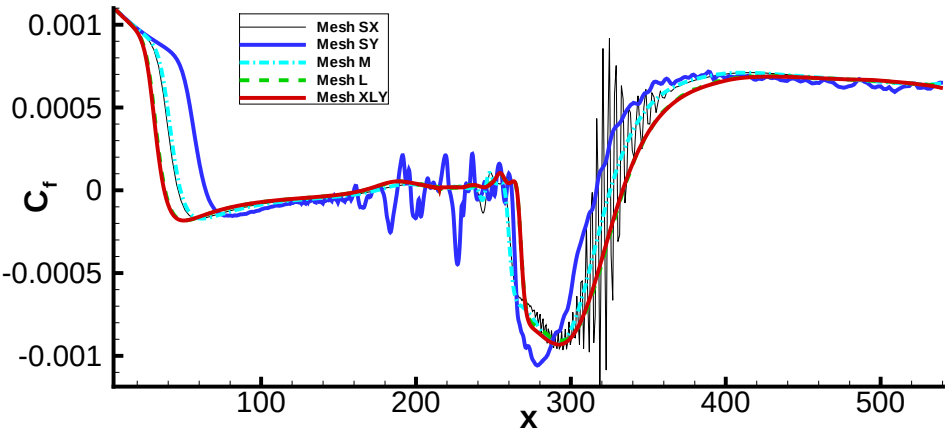

FIGURE 4.5: Distribution of skin friction for simulation using different meshes.

4.2.2 2D flowfield

In this section, simulation of a compression ramp with high speed incoming flow at M=4.8 and Re=6,843 is firstly run in 2D at ramp angle 6° to validate the code by comparing with numerical results from Pagella et al. (2004) and Lüdeke and Sandham (2010). After knowing the mesh requirement of grid independency, 2D simulations based on 12° ramp flow are carried out with different Reynolds numbers (6,843 and 3,422) to evaluate the effect of Reynolds number and get steady base flows for the following 3D simulations.

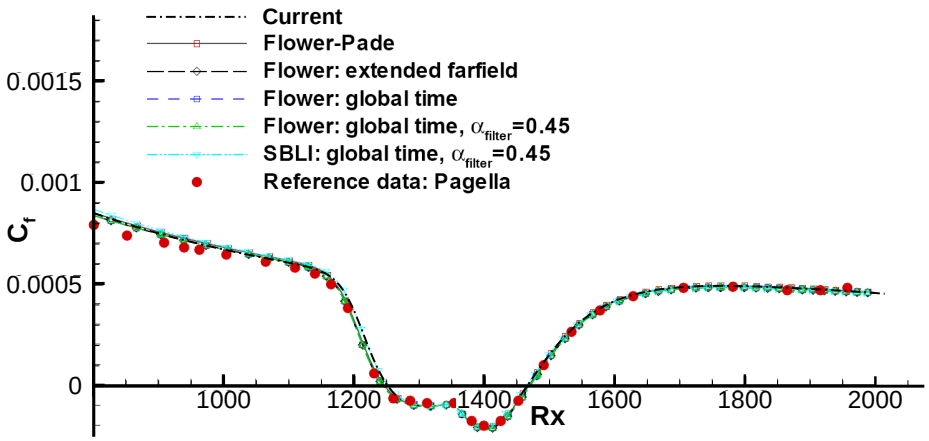

FIGURE 4.6: Comparison of skin friction distribution with data from Pagella et al. (2004) and Lüdeke and Sandham (2010) for 6° ramp flow with $Re = 6,843$ (Current case represents the current result).

Code validation is done by comparing distributions of C_f, plotted as a function of local Reynolds number R_x ($R_x = \sqrt{Re_{x^*}}$), with the result presented by Lüdeke and Sandham (2010) for a ramp angle of 6° and Re =6,843 flow. Lüdeke and Sandham (2010) ran

the case with two Navier-Stokes solvers (Flower developed in DLR (German Aerospace Center) and SBLI from University of Southampton) and found that both of them agreed with reference data (Pagella et al., 2004), with only small differences between the two solvers due to the different discretization methods. As shown in figure 4.6, a good agreement is observed between the current simulation (labelled 'Current' in the figure), the SBLI result obtained by Lüdeke and Sandham (2010) and the published result of Pagella et al. (2004).

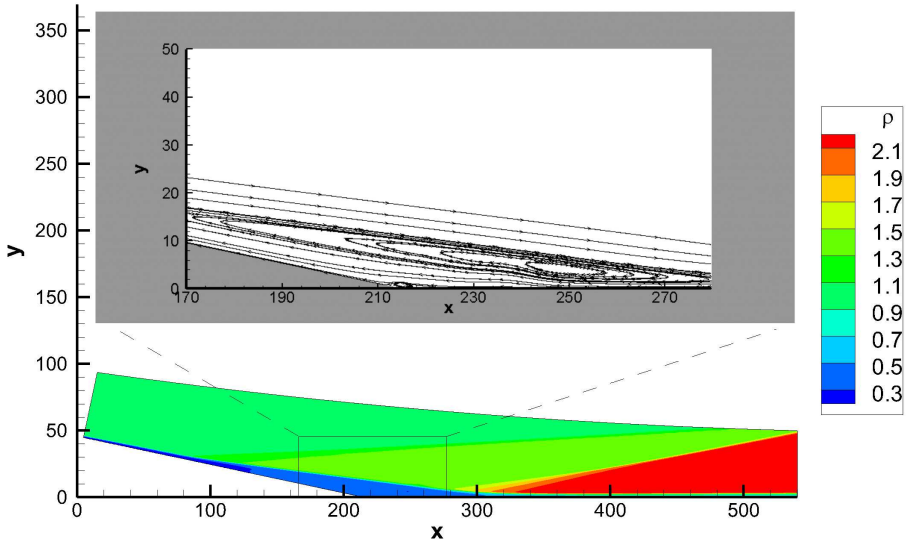

(a)

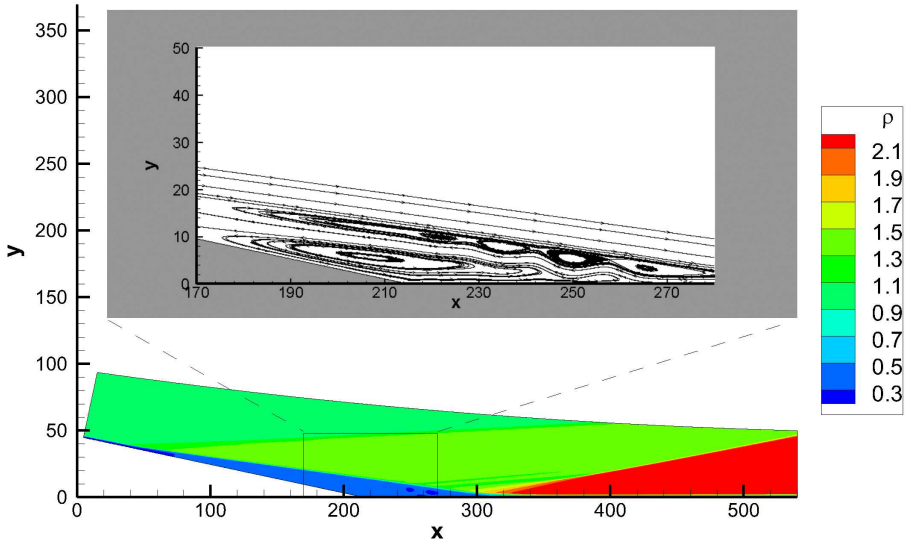

(b)

FIGURE 4.7: The separated flow for the 12° ramp at two different Reynolds numbers (a) 3,422, (b) 6,843.

Flowfields with the same Mach number but different Reynolds numbers are compared in figure 4.7 with the ramp angle of 12°. Recirculation zones are clearly seen in both plots. It is measured that separation region for the low Reynolds number flow extends from x=84 to x=325, while for the high Reynolds number flow, flow separation occurs from x=40 to x=332. Based on the same density contour levels, it can be seen that the recompression shock starts at about x=311 for the low Reynolds number case, while it appears from x=314 for the high Reynolds number case. The highest densities in the low and the high Reynolds number cases are 2.33 and 2.41 respectively, showing the shock for the high Reynolds number flow is stronger than that for the low Reynolds number flow. The flowfield with the high Reynolds number is more complex. At high Reynolds number large secondary recirculation zone is observed as shown in figure 4.7(b), while a comparably small secondary recirculation zone is observed at the low Reynolds number flow as shown in figure 4.7(b).

4.2.3 Instability

Stability study on 3D ramp flow is carried out in this section, following the same procedure used for the jet in Chapter 3. Firstly, 3D simulations are run at the two Reynolds numbers used in the 2D study, 3,422 and 6,843, with the same spanwise length to evaluate the Reynolds number effect on flow instability. Then further studies with Reynolds number of 6,843 are carried out with 3D ramp flow of different spanwise domain lengths L_z. Three monitor points at (196.76, 6.70), (216.10, 2.82) and (246.86, 2.81) are used to collect data for spanwise variation.

To further study the effect of Reynolds number, simulations are run with the spanwise length L_z of 12, and the number of the spanwise grid point N_z=16. Although N_z=8 was capable of studying the 3D instability study in the previous chapter, more spanwise grid points N_z=16 are used here for all the simulations in the linear growth stage in consideration of grid-independency and to prevent simulation failure due of lack of resolution. The 3D initial flowfield is obtained by extending the converged 2D results in the spanwise direction. The same Gaussian pulse perturbations, with a single sinusoidal spanwise variation, as in the jet in crossflow, are used here. The centre of the Gaussian profile is chosen right above the ramp corner at the coordinate of (x_c =234.7, y_c =10.7).

Figure 4.8 compares the growth of ε (defined in equation (3.5)) at the initial growth stage of the small added disturbances for ramp flows with different Reynolds numbers and L_z =12 at monitor point (196.76, 6.70). The y-axis is displayed on a logarithmic scale. It can be seen that the spanwise variation stays at a very low level for the low Reynolds number (Re =3,422) case. For the high Reynolds number (Re=6,843) case, an exponential growth is observed after an initially low growth rate. It appears that there is a threshold in Reynolds number for the development of strong 3D global instability of ramp flow. This threshold lies between the two Reynolds numbers studied. Contours

of ε on the $x-y$ plane are shown in figure 4.9 at an early stage ($t = 900$) of instability development. Streamlines are superposed in the zoomed-in figure to show the position of the recirculation regions. It can be seen that the spanwise variation starts from the centre of a recirculation zone.

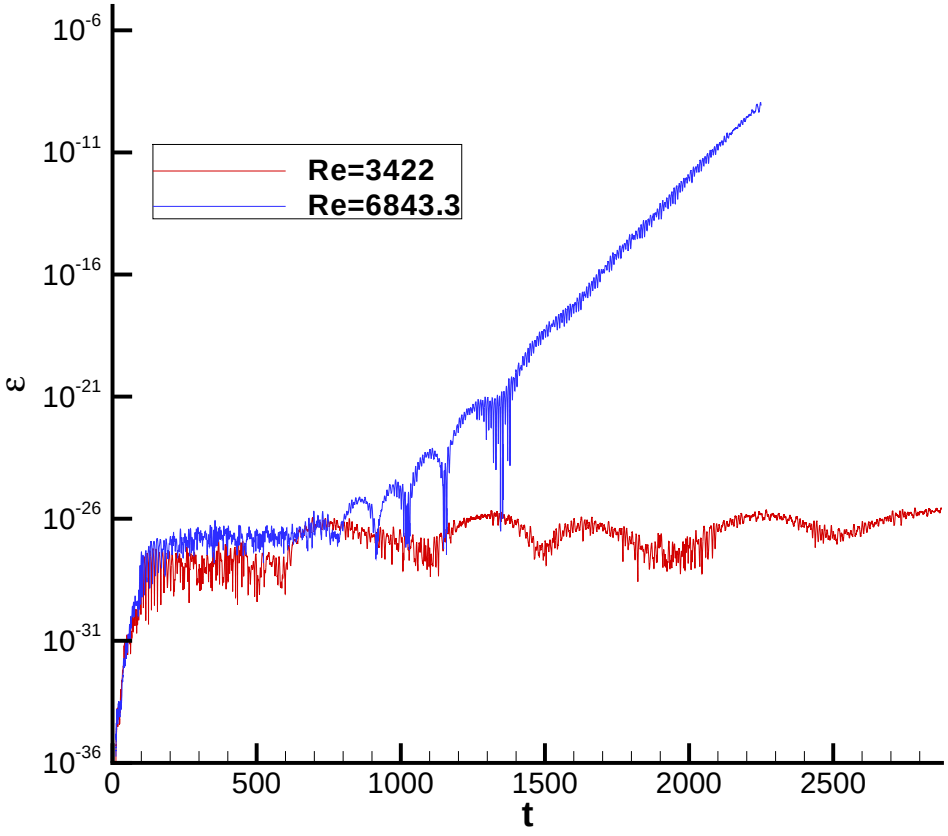

FIGURE 4.8: Growth of ε with time for L_z=12 and different Reynolds numbers at monitor point (196.76, 6.70).

Alam and Sandham (2000) proposed that reverse flow of 15−20% freestream velocity is required for absolute instability. By checking 3D flowfields for Re=6,843 and Re=3,422, the magnitudes of the streamwise reverse flow are 26% and 19.5% of the freestream speed, respectively. So the flow with Re=6,843 is likely to be absolutely unstable, while the flow is neutral or might need more time to become unstable for Re=3,422.

Simulations are then run for 3D flows with different spanwise lengths L_z of 6, 8, 12, and 24 to determine the most unstable mode. It is found that the growth rate varies with the wavelength of the added perturbation. Figure 4.10(a) shows growth of the spanwise variations with time. By measuring the slopes in the exponential stage, a plot of the variation of growth rate with wavenumber is shown in figure 4.10(b). The peak of the curve in figure 4.10(b) corresponds to L_z=12. The error estimations are obtained by

calculating the slopes at three different monitor points. The sizes of error bars for L_z=3, 6, 12 and 24 are dependent on the locations of the monitor point relative to the large recirculation zones.

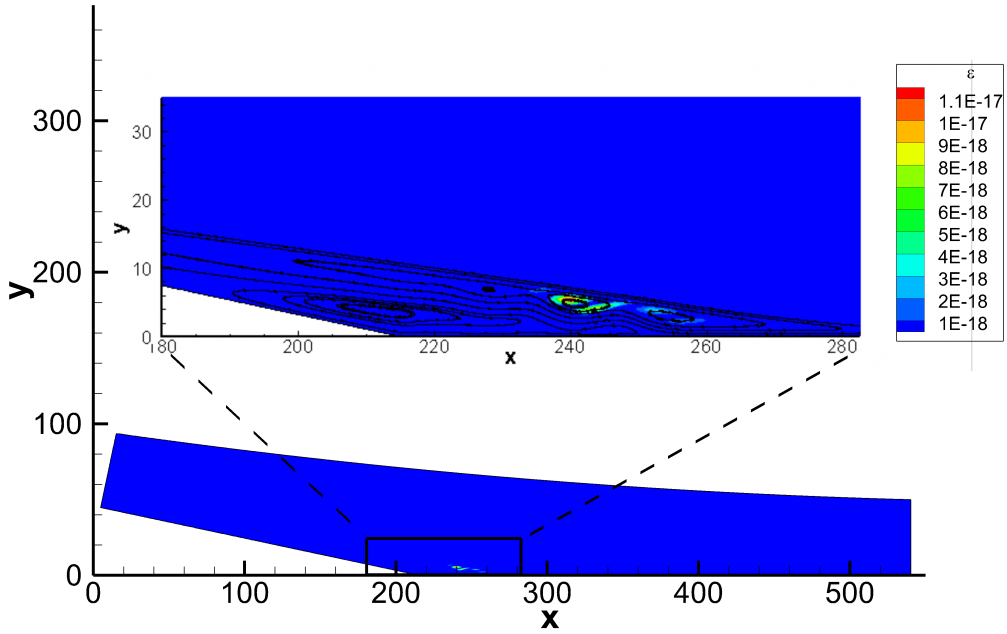

FIGURE 4.9: Distribution of ε on $x-y$ plane for L_z=12, Re=6,843 ramp flow at t=900.

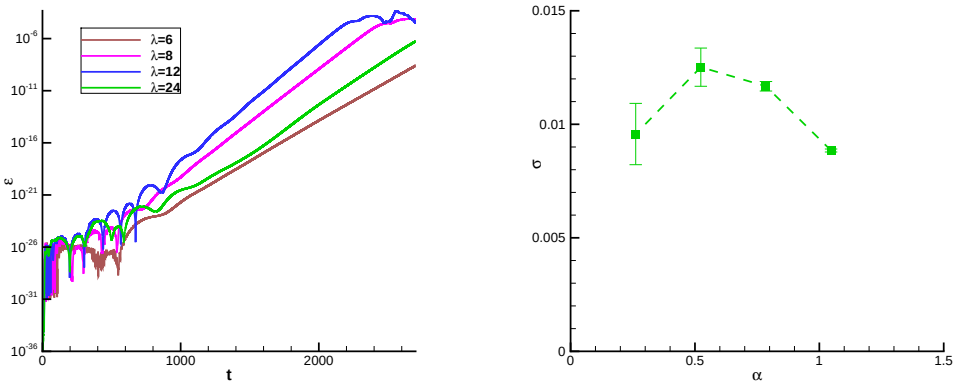

(a) (b)

FIGURE 4.10: Statistical measures of instability for ramp flow with different spanwise lengths: (a) variation of ε, defined by equation (3.5) at monitor point (246.86, 2.81) along with time, (b) spanwise variation growth rate along wavenumber, with error bars.

In the exponential stage of spanwise variation growth, the development of the added w-velocity perturbation still follows the single-spanwise harmonic structure as shown in figure 4.11 with the highest amplitudes appearing in the region x=230 to 320 and y=0 to 20, corresponding to the flow recirculation zone.

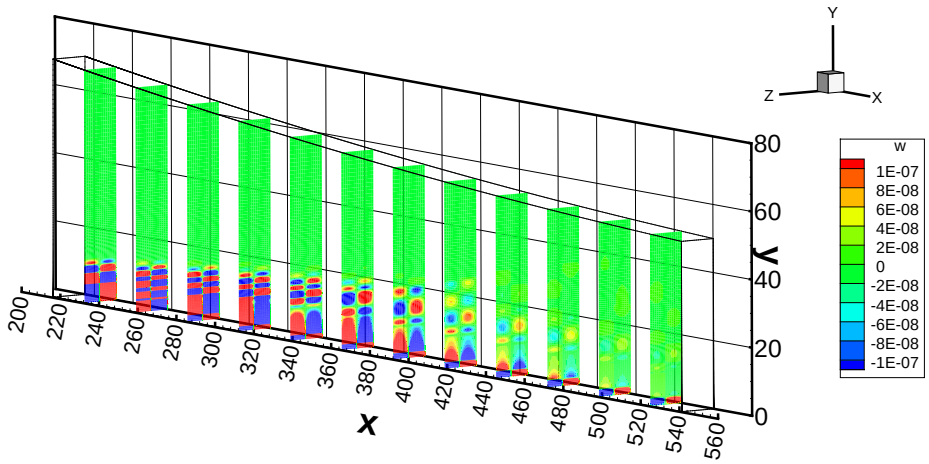

FIGURE 4.11: Spanwise variation of w-velocity visualized on different $y-z$ planes at t=1,800 for L_z=12 and Re=6,843 ramp flow.

4.3 Transition to turbulence

In the last section, variations of the spanwise velocity in a single-spanwise harmonic distribution was observed in the exponential stage of instability growth for the 12° ramp flow with Reynolds number of 6,843. The most unstable mode was found to be the one with a spanwise length of 12 times the inflow boundary layer displacement thickness. Nonlinear effect was observed after the exponential growth stage and in this section, the ramp configuration is further studied for the transition to turbulence.

4.3.1 Simulation setup and validation

The same 12° configuration is used with a spanwise length of 12 times the inflow boundary layer displacement thickness, but the mesh is refined downstream and in the spanwise direction to better resolve the flow during transition. In total, there are 2,452 and 250 grid points in the streamwise and the wall-normal directions respectively, compared with 1,800 and 250 used for the stability study. A spanwise resolution of N_z=64 is finally used after some tests to check the effect of varying N_z. Based on time averaged and spanwise averaged C_f, the maximum values of Δx^+ and Δz^+ is 10 within the whole flowfield, appearing downstream of the ramp corner around x=440. Wall-normal resolution ensures that y^+ is less than 0.5 and at least 80 grid points are within the boundary layer. The ratio of the spanwise grid spacing Δz to the separation length is 1/1392, which is close to the value used by Lüdeke and Sandham (2010) of 1/1536 for their finest mesh.

A converged 2D base flow is obtained with a mesh of $2,452 \times 250$. Then the flowfield is extended in the third direction with addition of the same Gaussian pulse perturbation in Chapter 3. The amplitude of the disturbance is 3.5×10^{-12}. To speed up simulation, a simulation with 16 spanwise grid points is run firstly. At t=1,800, in the exponential stage of instability growth, linear interpolation is used to extend the result from N_z=16 to N_z=64. Then the 3D flow is advanced after the restart.

To check that this strategy has no influence on the final result, development of the spanwise variation expressed by ε based on the finer spanwise mesh is compared with the result from mesh with $2,452 \times 250 \times 16$ grid points. As shown in figure 4.12, they all experienced the same exponential stage for a time period of up to 2,300 before reaching the nonlinear stage. Six different time instants, $t1$ to $t6$, marked in the plot, are used for flowfield analysis later. The interpolated flow follows the same instability growth route after the restart in all the three monitor points: M1 (x=216.10, y=2.82) near the corner, M2 (x=313.22, y=2.66) at the end of the recirculation and M3 (x=425.82, y=2.52) further downstream. The oscillation experienced at monitor M1 after restart is caused by the adjustment from flowfield of N_z=16 to that of N_z=64 within the recirculation zone.

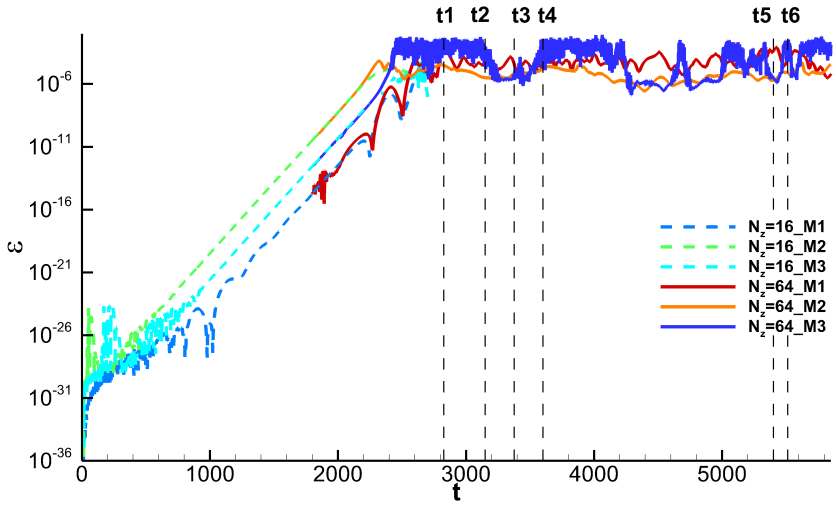

FIGURE 4.12: Growth of ε with time at monitor points M1, M2 and M3 ($t1$=2,925, $t2$=3,150, $t3$=3,375, $t4$=3,600, $t5$=5,400 and $t6$=5,513).

4.3.2 Downstream variation of the flowfield

As seen from figure 4.12, intense oscillations of ε with time in the saturated flow stage are observed at the downstream monitor point M3 compared with the other two upstream monitor points, M1 and M2. To further study the flow in the nonlinear stage, flow data at another 4 downstream monitor points, M4 (x=451.24, y=2.51), M5 (x=490.62, y=2.50) and M6 (x=495.54, y=2.50) in the reattachment zone and M7 (x=539.40, y=2.52) near

the exit, are recorded from t=3,150 with their positions shown in figure 4.13. The five monitor points from M3 to M7 all locate in the downstream disturbed flow observed from x=420 until exit. Developments of the spanwise variation with time at these 5 downstream monitor points are plotted in figure 4.14. The earlier time history of ε at M3 is also plotted to link the comparison with figure 4.12. Intense variations for all the downstream monitor points are observed. Moreover, there are local variations, such as observed from roughly t=3,100 to t=3,600 which obviously exist at monitor M3 and M4, but are not so obvious at M5 and M6 and can not be clearly observed at M7, showing that variation of the flow structure might become weak or not reach the last three downstream monitor points in the time period.

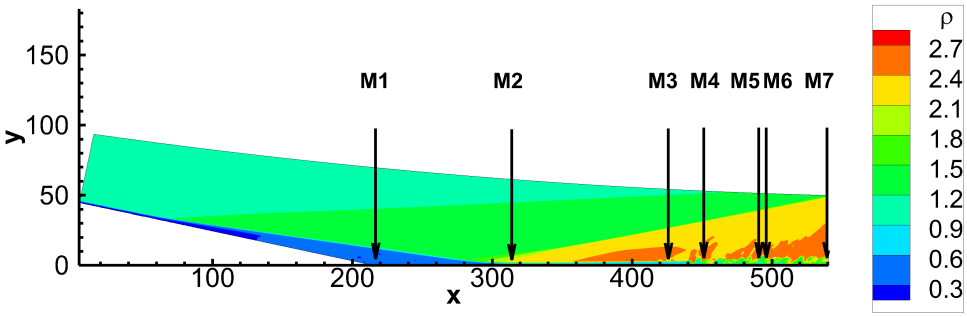

FIGURE 4.13: Position of seven monitor points in the flowfield contoured by density (ρ) at $t = 3,150$.

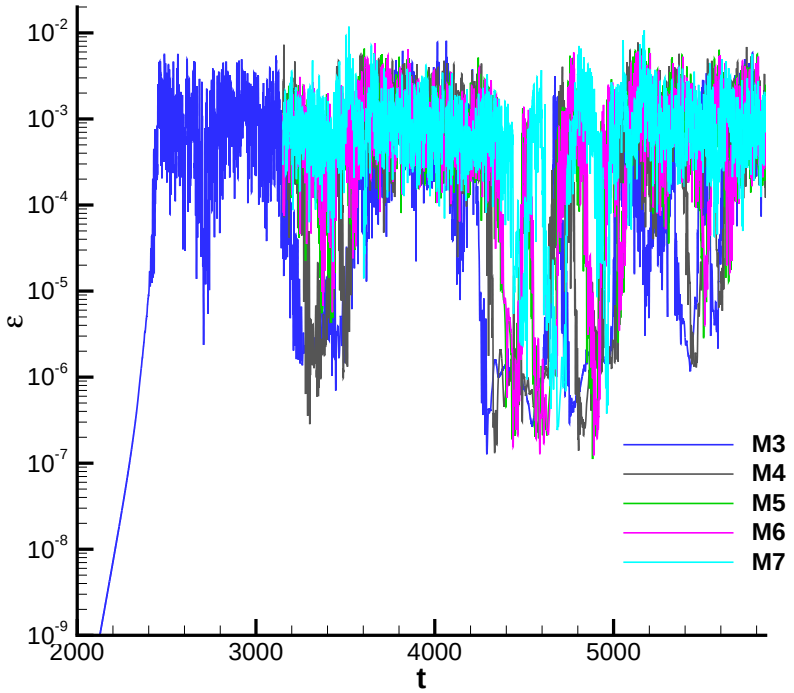

FIGURE 4.14: Growth of ε with time for downstream monitor points.

Density variations with time at two monitor points within the separation bubble (M1 and M2) and for two downstream points (M3 and M7), are plotted in figure 4.15. High frequency variations of density with time are more obvious at the downstream monitor points compared with those within the separation bubble. Low frequency variations with a period of about 1,700 in non-dimensional time are observed at monitor point M2. Intermittent signals are observed at both downstream monitor points, and generally stronger variations are observed downstream of the separation bubble. By comparing the amplitudes of peak-to-peak variation, it is obvious that downstream flow (with amplitude higher than 1.5 at monitor points M3 and M4) varies more greatly than the upstream flow (with amplitude less than 0.12 at monitor points M1 and M2).

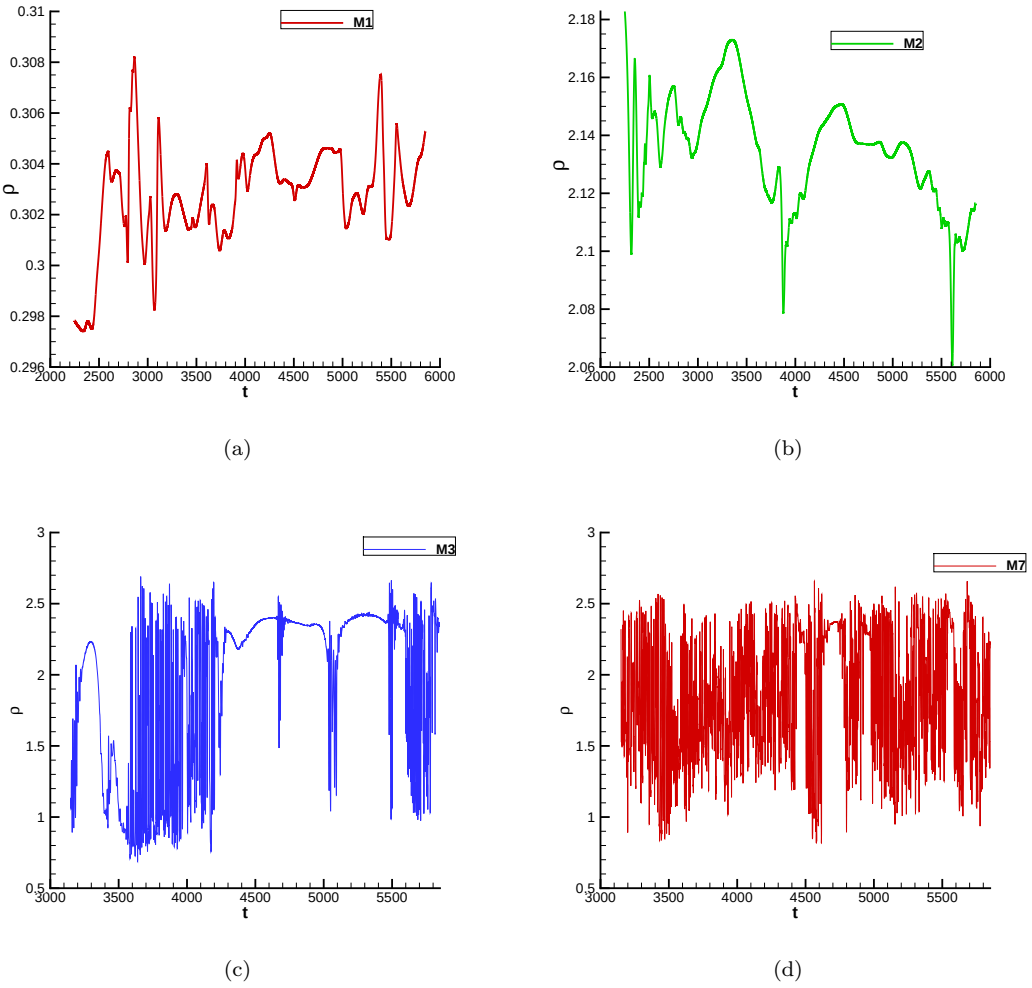

FIGURE 4.15: Density histories at monitor points M1 (a), M2 (b), M3 (c) and M7 (d).

4.3.3 Transition study

Spanwise-averaged skin friction coefficients at six different time instants marked in figure 4.12 are plotted in figure 4.16 with the ramp corner at x=215.2. For comparison, skin friction coefficient distributions at two time instants t=2,025 and t=2,250 in the exponential stage of the spanwise variation growth are plotted in figure 4.16(a) as the red and green curves, respectively, showing that the downstream flow is still laminar at t=2,025 and t=2,250. Distributions of C_f at all the time instants show that the upstream flow is steady. However, as shown by the other six curves for t=2,925 and 5,513 in figure 4.16(a), t=3,150 to 5,400 in figure 4.16(b), the downstream flow seems to be experiencing transition to turbulence with strong oscillations observed downstream from x=360. Distribution of C_f at t=5,513 is plotted in figure 4.16(a) for comparing the largest separation bubble more easily.

It is noted that from t=2,925 to t=3,375 the disturbed area moves downstream with decreased skin friction from ramp corner to the transition area. At t=3,600, the disturbed area starts upstream. Downstream distribution of skin friction coefficient returns with maximum value about 0.0028 at t=5,400. For the distribution of skin friction at t=5,513, the disturbed area is found further upstream. The distributions of skin friction around the ramp corner show that the flow there is also unsteady. At all time instants, in spite of C_f >0 regions around corner, which are caused by the secondary recirculation flow, the recirculation zones can be considered as a single large separation bubble with the upstream separation point around x=60 and the downstream reattachment point around x=300. Both the separation and reattachment points move forwards and backwards with time. It is observed that flow at t=5,513 has the largest separation region, followed by flows at t=2,025 and t=2,250. Flow at t=2,925 has the shortest separation bubble.

According to the locations of the disturbed areas and the separation lengths shown in figure 4.16, it is concluded that from t=2,925 to t=3,375, the separation bubble expands and the reverse flow around x=280 becomes stronger when the disturbed area moves further downstream. The reverse flow becomes weaker and downstream separation point begins to move upstream at t=3,600 and t=5,400 with the upstream separation point moves upstream slightly. The largest separation bubble at t=5,513 goes with the relatively weak disturbance from x=400 to x=460 and the following quiet region from x=460 to x=50 shown in figure 4.16. All the observations mentioned above show the complexity of the flow, which cannot be simply explained and needs further study.

According to work of Dubief and Delcayre (2000), the iso-surface of the second invariant Q is helpful in detecting coherent structures. This invariant is defined by

$$Q = \frac{1}{2}(\Omega_{ij}^2 - S_{ij}^2), \tag{4.1}$$

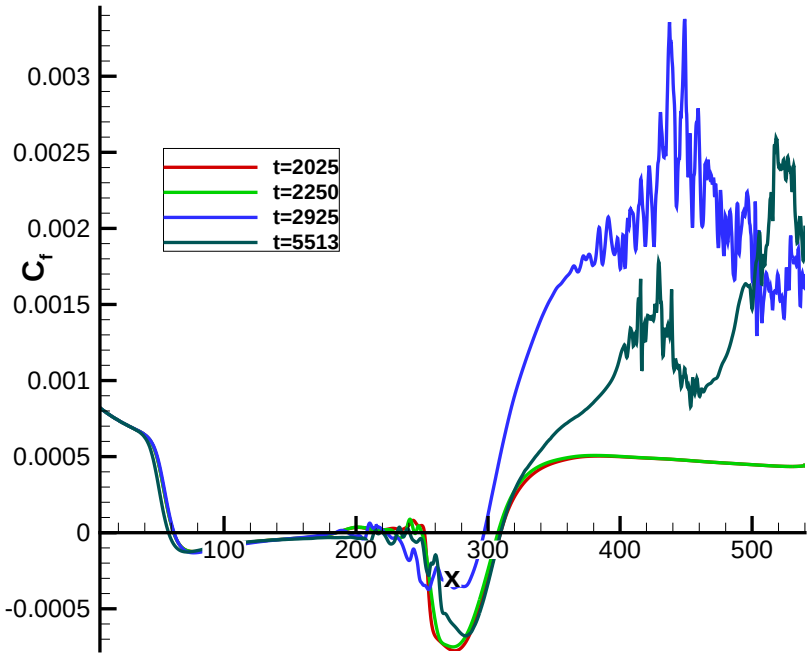

(a)

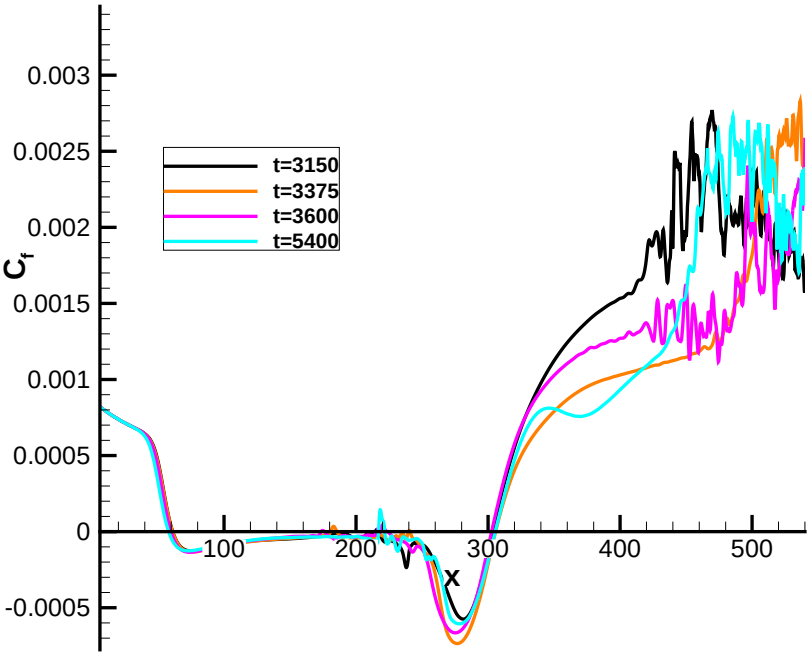

(b)

FIGURE 4.16: Distributions of spanwise averaged skin coefficients at different time.

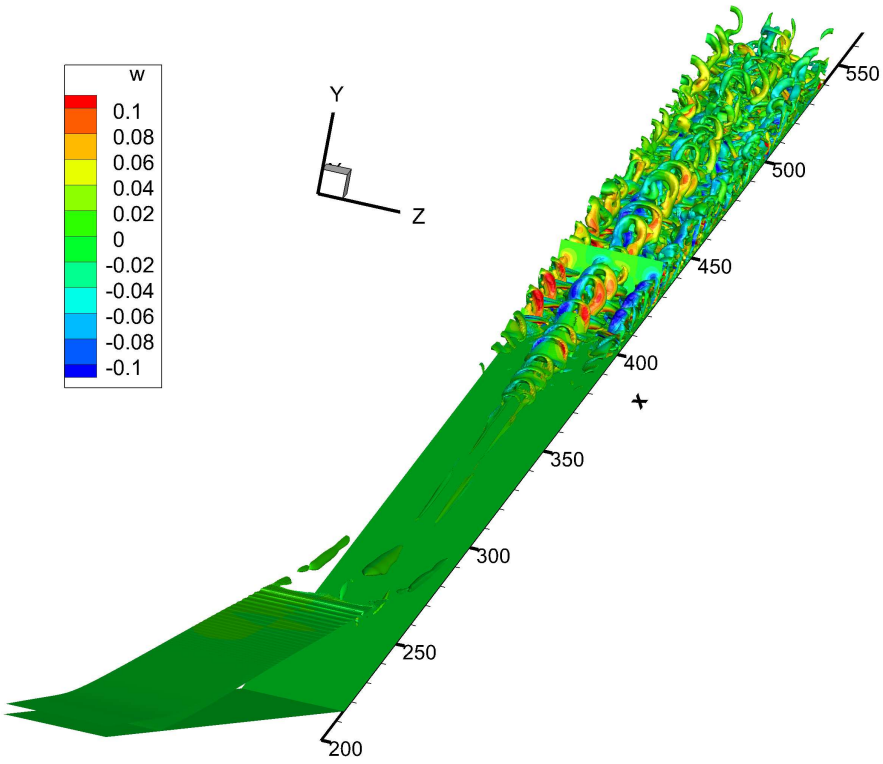
w
0.1
0.08
0.06
0.04
0.02
0
-0.02
-0.04
-0.06
-0.08
-0.1
Y
Z
550
500
450
400
350
300
250
200

(a)

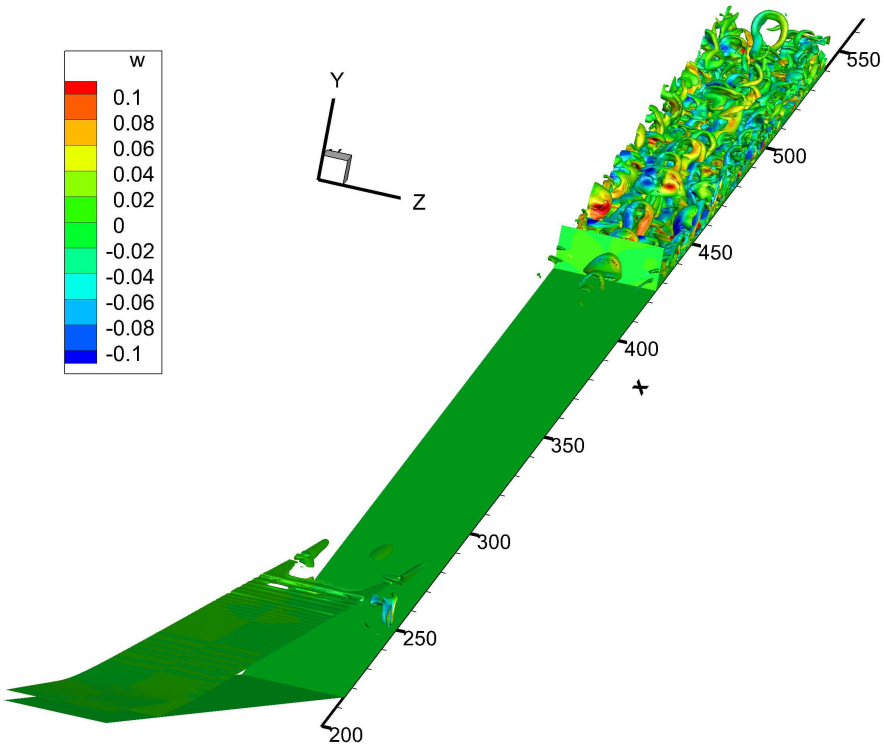
w
0.1
0.08
0.06
0.04
0.02
0
-0.02
-0.04
-0.06
-0.08
-0.1
Y
Z
550
500
450
400
350
300
250
200

(b)

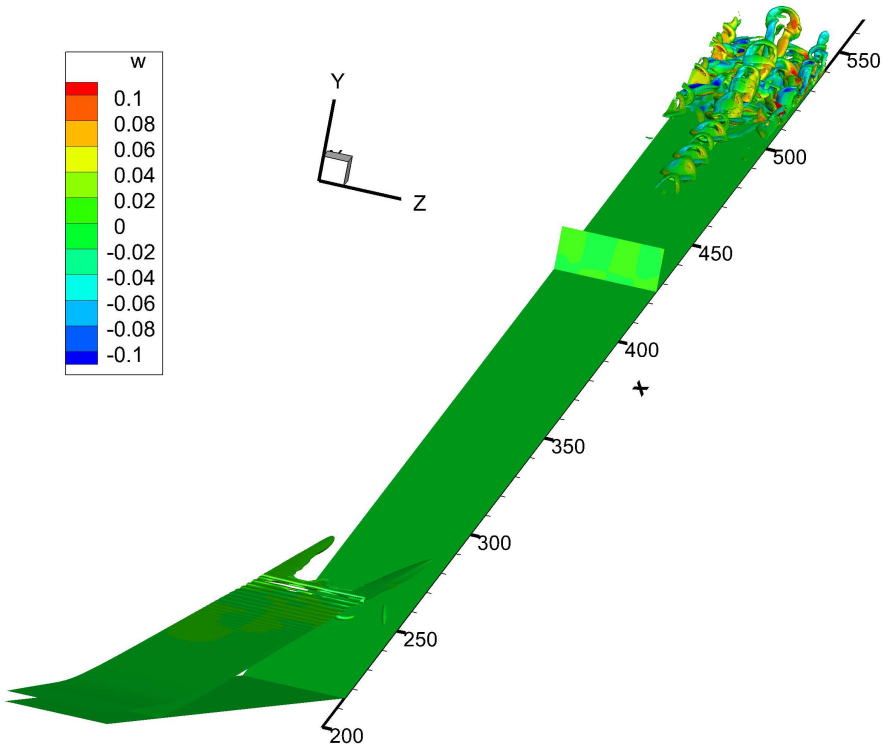
w
0.1
0.08
0.06
0.04
0.02
0
-0.02
-0.04
-0.06
-0.08
-0.1
Y
Z
550
500
450
400
350
300
250
200

(c)

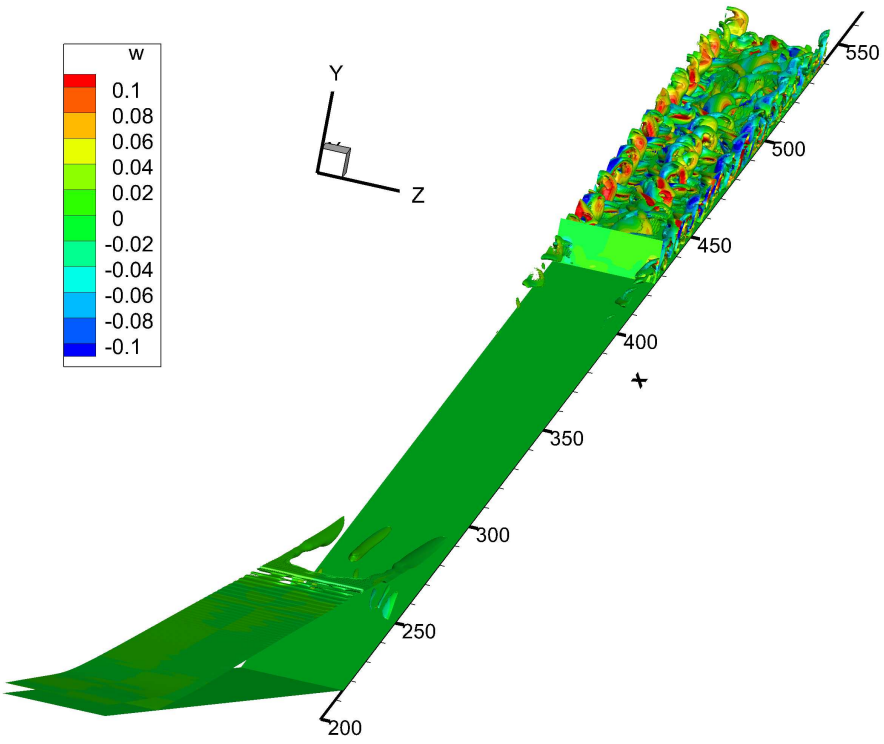
w
0.1
0.08
0.06
0.04
0.02
0
-0.02
-0.04
-0.06
-0.08
-0.1
Y
Z
550
500
450
400
350
300
250
200

(d)

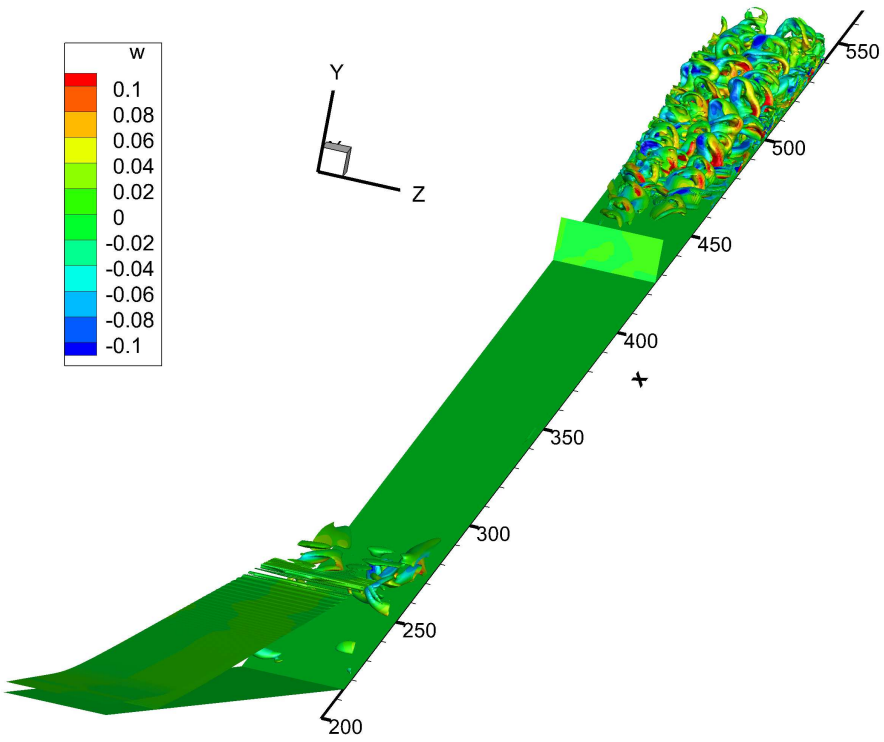

(e)

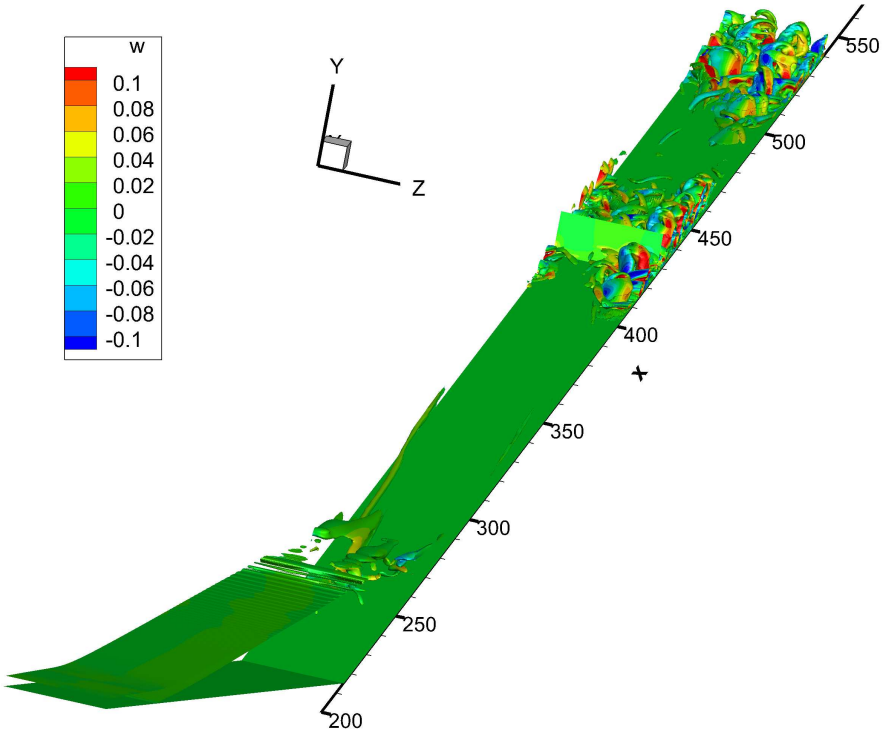

(f)

FIGURE 4.17: Iso-surface of Q=0.01 superposed by spanwise velocity at time instants: (a) 2,925, (b) 3,150, (c) 3,375, (d) 3,600, (e) 5,400, (f) 5,513.

where $\Omega_{ij} = (u_{i,j} - u_{j,i})/2$ and $S_{ij} = (u_{i,j} + u_{j,i})/2$ are the antisymmetric and the symmetric components of ∇u respectively. Spatial distributions of flow structures at t=2,925, 3,150, 3,375, 3,600, 5,400 and 5,513 are plotted in figure 4.17 by iso-surfaces of Q coloured by the spanwise velocity, along with a slice at x=425.82, where monitor M3 is located. The iso-surfaces are mainly visible in the upstream shear layer, the separation bubble with the secondary recirculation zone around ramp corner and the downstream area after reattachment. The transitional and turbulent flow areas are confirmed by the presence of worm-like structures identified by iso-surfaces of Q and can be clearly seen in all the subfigures after the reattachment. It is observed that the flow is unsteady and the iso-surfaces shift downstream and upstream with time. As pointed out in the stability study, the flowfield in the exponential stage follows the single-spanwise harmonic structure, while this structure would breakdown and might develop to turbulent flow. From plots at t=2,925 to 3,600, the single-spanwise harmonic structure of Q criteria is still observed, especially at t =2,925, 3,375 and 3,600 by iso-surfaces of Q and w-velocity contours though in saturated stage. At t=5,400 and 5,513, this structure disappears and seems to breakdown. So it is believed that the flowfield is fully developed by t =5,400.

4.3.4 Transition mechanism

Turbulent flow will exhibit high levels of unsteadiness, leading to high turbulence kinetic energy (TKE) value, compared to zero or low levels in the laminar and transitional region. From instantaneous flow field using span averaging, the TKE is defined by

$$TKE = \frac{1}{2}(\overline{u'^2} + \overline{v'^2} + \overline{w'^2}), \tag{4.2}$$

where

$$\overline{u'^2} = \overline{u^2} - \overline{u}^2, \ \overline{v'^2} = \overline{v^2} - \overline{v}^2 \ \textbf{and} \ \overline{w'^2} = \overline{w^2} - \overline{w}^2. \tag{4.3}$$

Statistics are obtained by averaging in the spanwise direction at each time instant. It is observed in figure 4.18 that TKE is zero both in the upstream laminar region and far away from the wall in the potential flow region as transition to turbulence only happens downstream of the ramp. A smaller selection box as defined in figure 4.18 is chosen to have a better view of the TKE distribution which is displayed in logarithm.

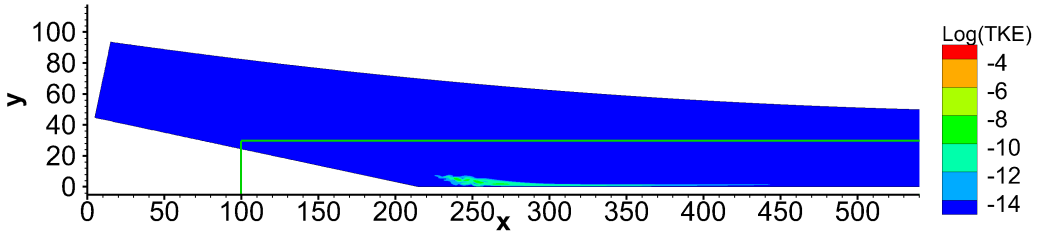

FIGURE 4.18: Distribution of TKE at t=2,025 with selection box.

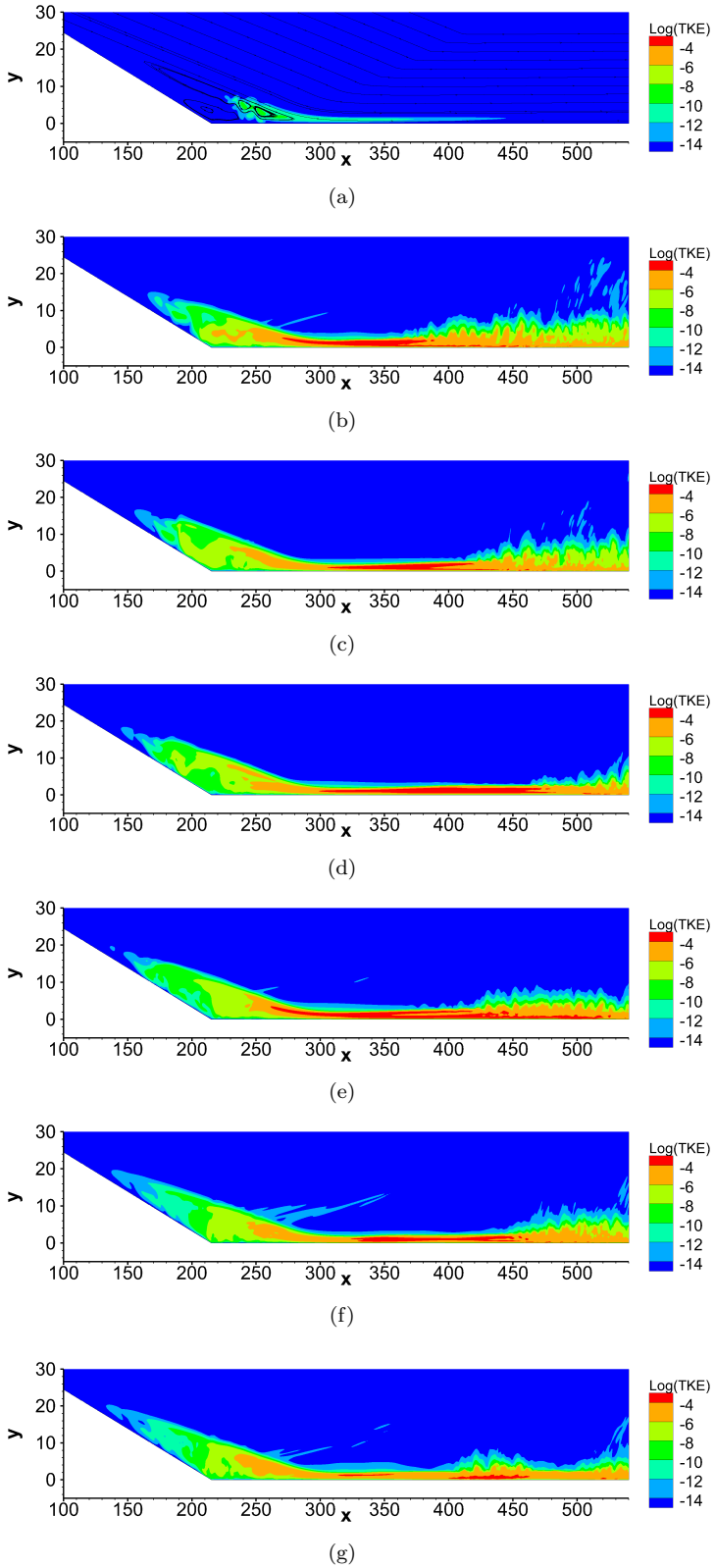

FIGURE 4.19: Distributions of TKE in the selection box shown in figure 4.18 at time instants: (a) 2,025, (b) 2,925, (c) 3,150, (d) 3,375, (e) 3,600, (f) 5,400, (g) 5,513.

TKE distributions at different time instants in the saturated stage are plotted in figure 4.19 to compare with that at t=2,025 in the exponential stage. Streamlines are plotted in frame of t=2,025 to show the flowfield. It can be seen that high TKE is only found in the recirculation zone as well as the following recompression region near the wall in the exponential stage (t=2,025). The areas with high TKE value are always located downstream of the corner. Seen from all the frames, there is no discontinuity for the TKE contours, however the discontinuity of iso-surfaces of Q can be observed such as around x=480 at t=5,513 in figure 4.17(f). It is also seen in figure 4.17 that iso-surfaces of Q always show structures in the flow downstream from x=500 all the way to the exit at different time instants, however, the TKE value near the domain exit as shown in figure 4.19 is relatively small. This can be explained by plotting the downstream u-velocity distribution near the wall in figure 4.20. Streaks of u-velocity are clearly observed from x=320 to x=500 which corresponds to the high TKE regions. In other words, the streak distribution of u-velocity dominates the TKE value as amplitude of spanwise variation for u-velocity is much larger than that for v-velocity and w-velocity, while Q is relevant to velocity derivatives and used as a scale to visualize turbulence. In other word, strong turbulence leads high TKE, but high TKE is not always caused by turbulence.

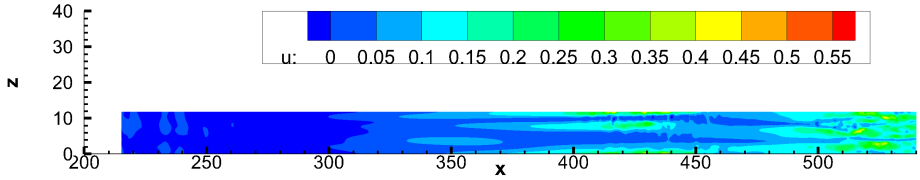

FIGURE 4.20: Distribution of u-velocity on a horizontal ($x-z$) surface 0.069 away from the wall at t=5,513.

At some time instants, no iso-surface of Q can be seen at the locations with high TKE value, for example, in the area from x=300 to x=400 at t=3,150, as shown in figure 4.19(c). However, if the Q is plotted with small value, more flow details such as streaks breaking down into hairpin-shaped structures appears as shown in figure 4.21(a) at t=3,150. The iso-surfaces of vorticity magnitude at t=3,150 are plotted in figure 4.21(b) with stretched streamwise vortices observed before transition. These structures start before x=300, within the recirculation zone, indicating that there is a close relationship between instability within flow recirculation zone and the downstream transition.

The impact of streamwise vortices can be seen in the downstream u-velocity distribution at different $y-z$ slices shown in figure 4.22. From x=220 to x=260, uniform spanwise u-velocity is observed with no obvious streamwise vorticity. Downstream of x=300 until x=420, spanwise variation of u-velocity is observed with one mushroom-shaped vorticity in the center and two half mushroom-shaped vortices on each side at each $y-z$ slice. Downstream of x=420, this spanwise distribution of u-velocity becomes obscure and disappears.

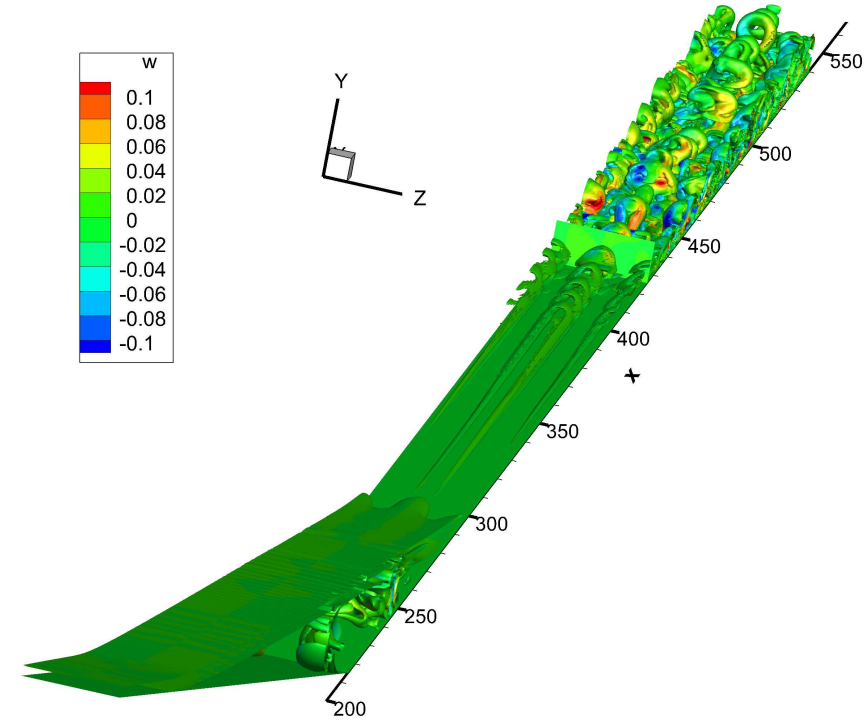

(a)

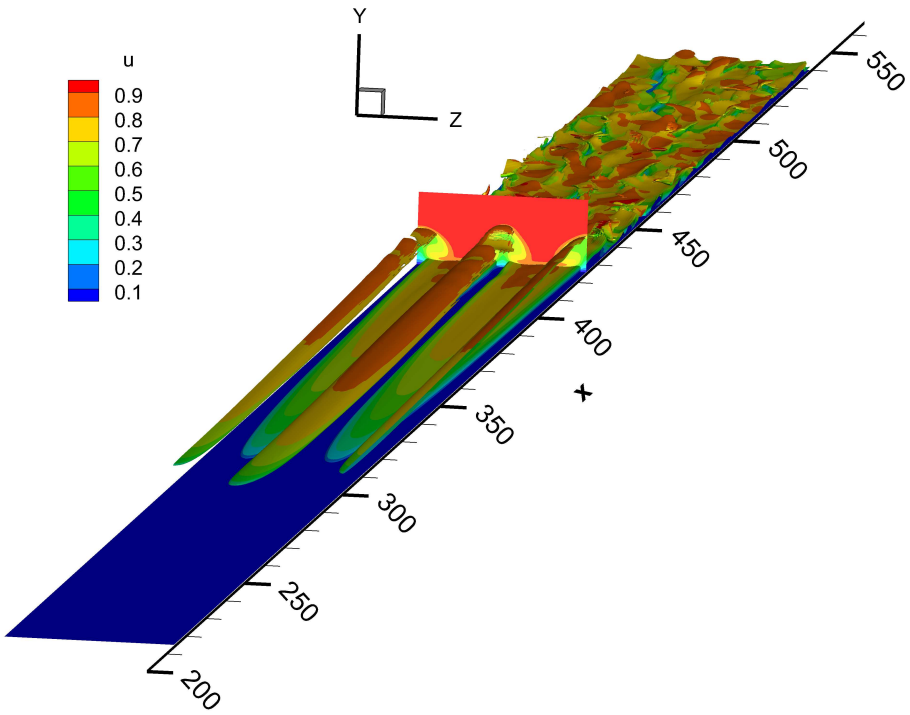

(b)

FIGURE 4.21: Iso-surfaces at at t=3,150 for (a) Q-criteria of 0.001 coloured by the spanwise velocity and (b) vorticity magnitude of 1 coloured by the u-velocity.

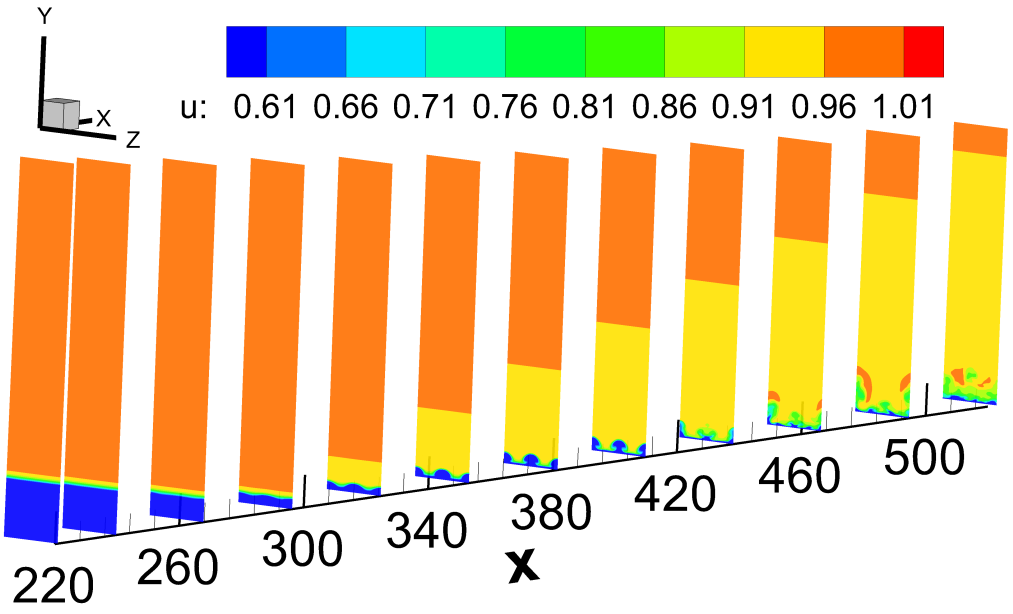

FIGURE 4.22: Distribution of u-velocity visualized on different $y-z$ slices at t=3,150.

Four slices at x=250, x=300, x=400 and x=500 are used to check the flow by streamlines as plotted in figure 4.23. Complex vortical structures are observed in the recirculation zones as shown in figure 4.23(a). The main vortices are centred at about y=2. Streamwise vortices can obviously be seen in figure 4.23(b), with vortices centred at about y=1, and figure 4.23(c), with vortices centred at about y=1.2. Figure 4.23(d) shows that the flow becomes chaotic.

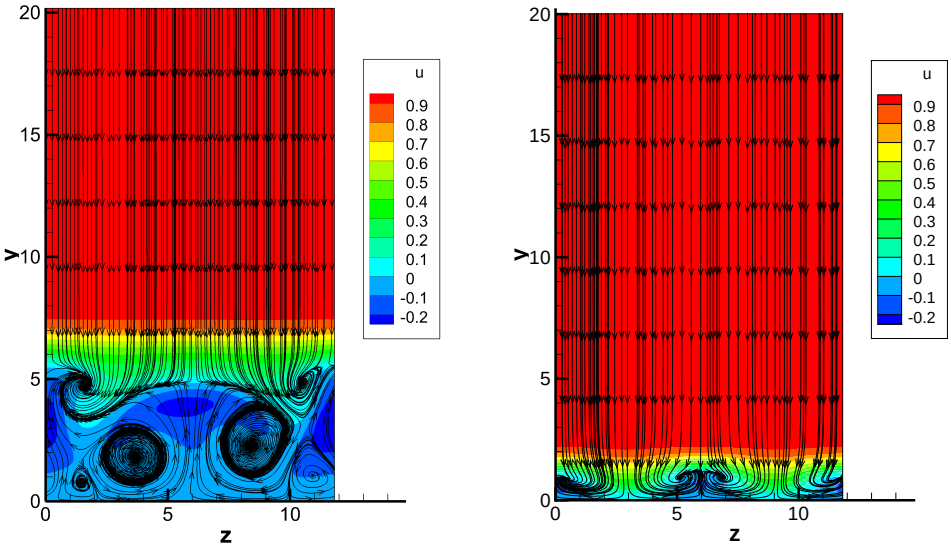

(a) (b)

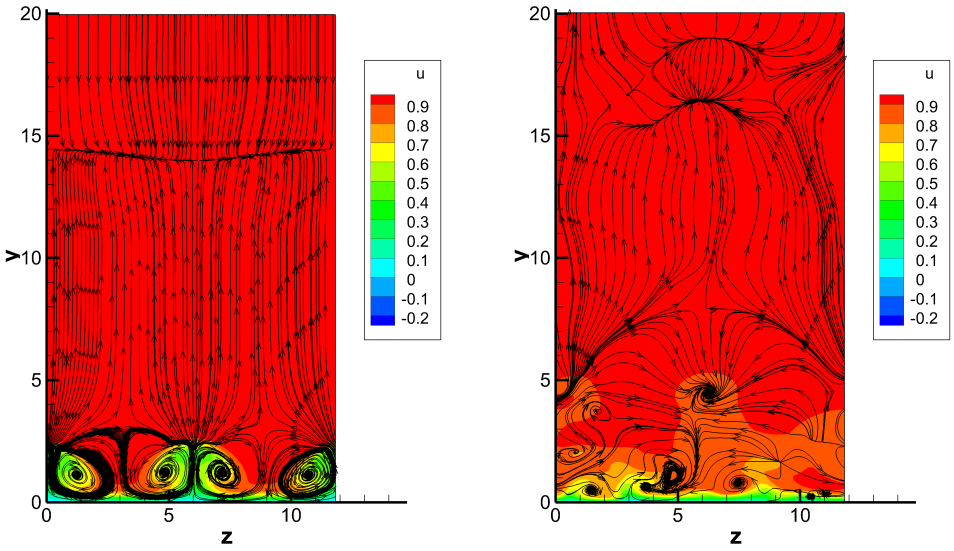

(c) (d)

FIGURE 4.23: Distributions of u-velocity at t=3,150 superposed by streamlines on different $y-z$ slices (a) x=250, (b) x=300, (c) x=400, (d) x=500.

Andersson et al. (2001) stated that an streak amplitude of about 26% of the freestream speed was needed for streak breakdown to occur. In current study, streak amplitudes of more than 29.5% are observed. According to all the analyses done above, it is concluded that the disturbances generated by the recirculation zone do not lead directly to turbulence. Instead, streamwise vortices are formed. Because of the shear flow and reattachment shock, the vortices are pushed gradually near the wall and lead to streamwise velocity streaks. The streaks reach high amplitude and breakdown to turbulence further downstream.

4.4 Comparison of flow separation for ramp and jet in crossflow

Pagella et al. (2004) stated that the SBLI for ramp flow and for an impinging shock were practically identical in two dimensions when the impinging shock angle was set to half the ramp angle. At the low Reynolds number (Re=3,422) used in their study, there was only one recirculation zone with one large vortex for both the 6° ramp and the shock impingement with impinging shock angle of 14°. For the ramp flow and the jet in crossflow studied here, higher Reynolds number (and also larger J_p values for jet injection) is used, inducing large recirculation zones with a series of vortices. The recirculation zone of the jet in crossflow is divided into two regions by the jet, but similar recirculation zones with ramp flow can still be observed. The recirculation zone

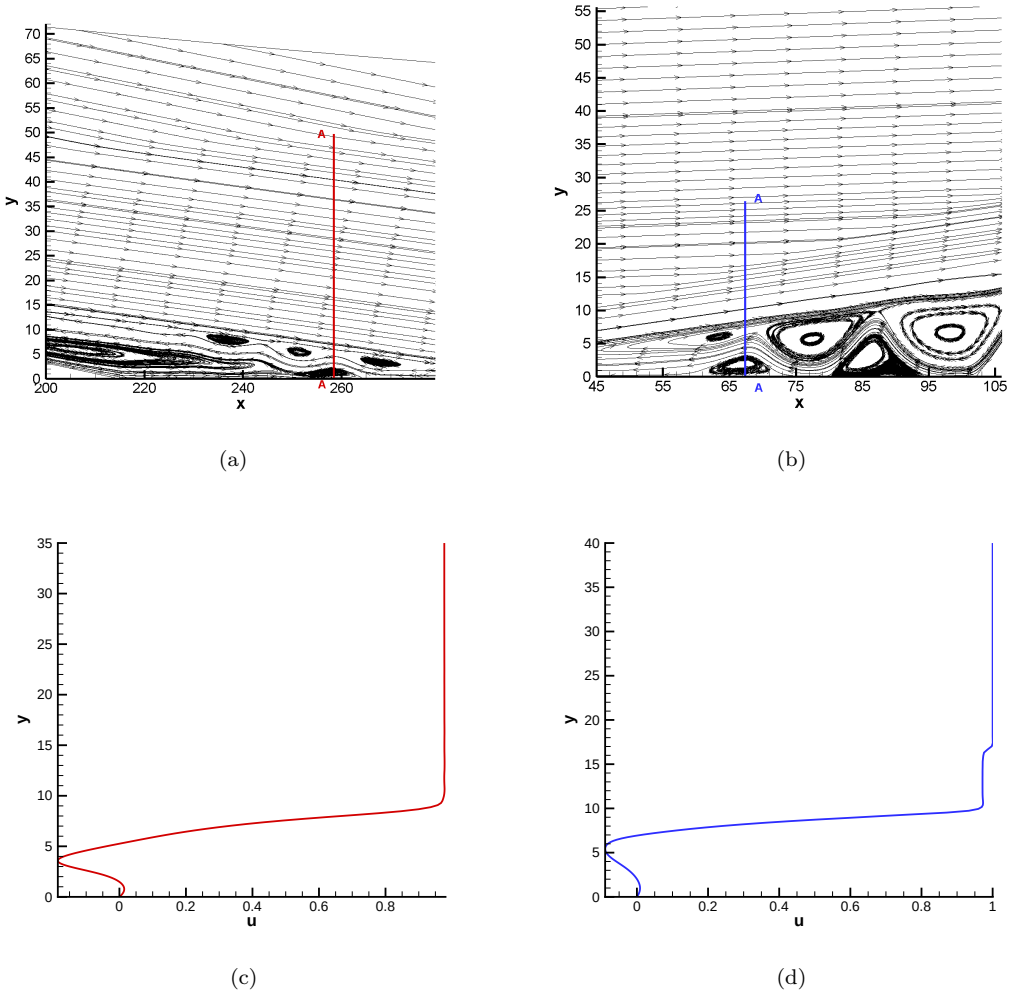

FIGURE 4.24: Comparison of the flow separations in the ramp and the jet cases: (a) recirculation zone in ramp case, (b) recirculation zone for jet case, (c) profile of tangential velocity on AA line in ramp case, (d) u-velocity profile on AA line in jet case.

for the 2D ramp flow with a 12° wedge angle for Reynolds number of 6,843 and the 2D jet in crossflow with J_p of 0.3 are compared in figure 4.24(a) and figure 4.24(b). The recirculation zones in both flows are found to be similar at the top of the recirculation zones. Velocity profiles, extracted at the A-A sections shown in plots 4.24(a) and 4.24(b) for ramp and jet cases respectively, are compared in plots 4.24(c) and 4.24(d), showing the same trend within the boundary layer. The jump at y=15 in figure 4.24(d) is caused by the separation shock.

Table 4.2 compares all the relevant data from the two cases, including the wavelengths of most unstable mode, flow separation lengths for both upstream and downstream flow, the height of the flow separation region, boundary thickness at jet injection or ramp corner if there is no jet injection or ramp corner recompression, and the Reynolds number at injection or ramp area. Among all the collected data, upstream separation length is observed to be directly related to the most unstable mode. However, the

upstream separation length measured in the shock impingement flow (Robinet, 2007) is 0.6 and the wavelength corresponding to the most unstable mode is about 0.8. If comparing the ratio of most unstable wavelength with the upstream separation length for shock impingement (Robinet, 2007), it is found that the ratio for jet and ramp case is 0.078 compared with 1.333 for the shock impingement case.

Parameter	Jet in crossflow	Ramp flow
Wavelength of most unstable mode	8	12
Upstream separation length	103	153.59
Downstream separation length	28.88	94.61
Height of the separation region	10.13	9.05
δ_{99} at jet or ramp area if without jet or ramp	3.7	2.95
Reynolds number at injection or ramp area (Re_{x^*})	318,115	1808,043

TABLE 4.2: Comparison of flow parameters for jet and ramp cases.

4.5 Summary

Simulations of a supersonic ramp flow have been performed to investigate the flow stability and the subsequent transition to turbulence. Ramp flow is found to be globally unstable when a Reynolds number of 6,843 is used, compared to the ramp flow at Re =3,422 which is only convectively unstable. The most unstable mode for the ramp flow has a wavelength of 12 times the incoming boundary layer displacement thickness. Fed by the instability of the recirculation zone near the ramp corner, flow transition to turbulence is observed.

Chapter 5

Effect of cavity and jet on 2D laminar supersonic ramp flow

5.1 Introduction

Ramps, jets and cavities are configurations that commonly appear on high speed aircraft, rockets and reusable spacecraft. Differences in geometries can induce significant changes in flow structures including flow separation, shock-waves and aerothermodynamic load distributions. In this chapter we look at combinations of elementary ramp, jet and cavity flows.

The three sketches in figure 5.1 show the typical flow characteristics for high speed ramp flow with a cavity, with a jet, and with both a cavity and a jet, respectively. The main flow structures of ramp flow, as seen in Chapter 4, include flow separation around the ramp corner, a separation shock upstream and a recompression shock downstream of the corner. With a cavity added at the ramp corner, as shown in figure 5.1(a), it is interesting to see whether a separation can be trapped with such a configuration. In this and the following chapter, high speed ramp flow with jet injection is also computed, as shown in figure 5.1(b). The jet is injected downstream of the ramp corner in the high density region formed by the recompression shock, forming its own bow shock, upstream and downstream separations, upstream separation shock and downstream recompression shock. The upstream separation may merge with the separation bubble caused by the ramp corner. It is also interesting to study the interaction between the shocks caused by the jet and by the ramp and their effect on flow separation. Ramp flow with both jet and cavity is also studied here with the flowfield as sketched in figure 5.1(c).

In the first part of this chapter, the $M = 4.8$ ramp flow with a low Reynolds number $Re = 3,422$ studied in Chapter 4 is used to evaluate the sonic jet and cavity effects on ramp flow. Flowfields with different configurations are compared. The location of

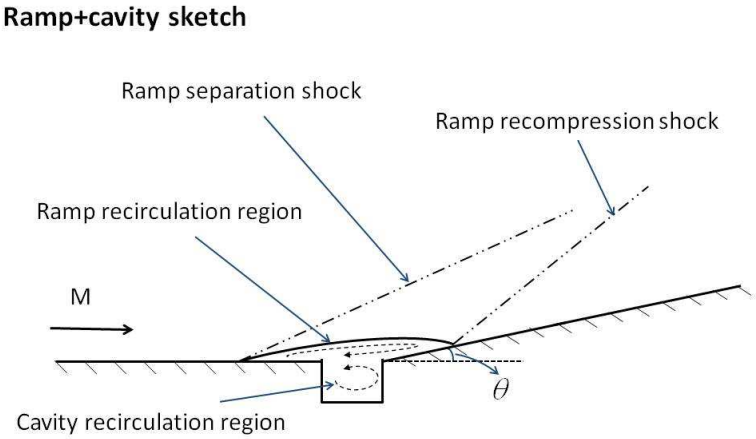

(a)

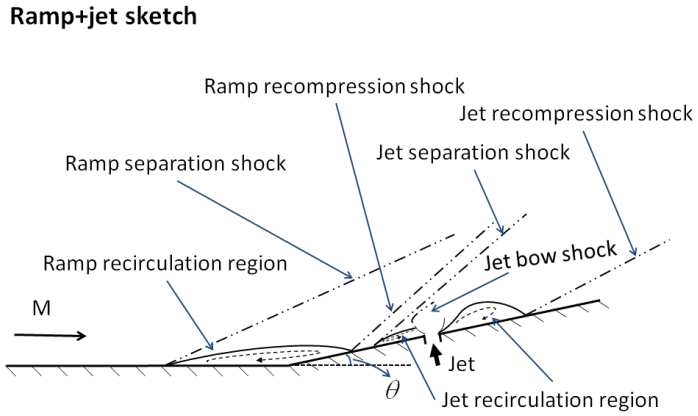

(b)

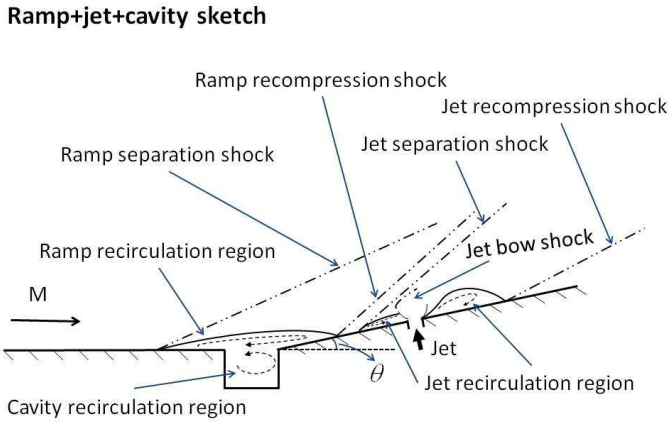

(c)

FIGURE 5.1: Sketches of ramp flowfields (a) with cavity, (b) with jet, and (c) with combined cavity and jet.

the upstream flow separation point relative to the inflow boundary ($x_{\text{sep}} - x_{\text{inflow}}$) is monitored to study the influence on the upstream progress of the separation.

All these configurations can appear in practical aerospace applications such as a rocket. Figure 5.2 shows the configuration of an axisymmetric rocket in a DLR wind tunnel model based on a VEGA rocket (Gallucci et al., 2012; Bianchi, 2008; Camussi et al., 2007). There is a axisymmetric gap between the first and second stage, forming a gap on the rocket surface. Supersonic retro jets are used to separate the first stage from the upper stage, leading to an enlarged gap that can be treated as a cavity. For practical application, heat transfer is vital and is closely related to flow separation and transition which varies with flow configuration. So it is important to evaluate the flow separation and to study the flow structure in different working conditions. Cavities with different length/depth ratios (L/D), as well as jets with different strengths are compared here. The orientation of jet injection is also studied.

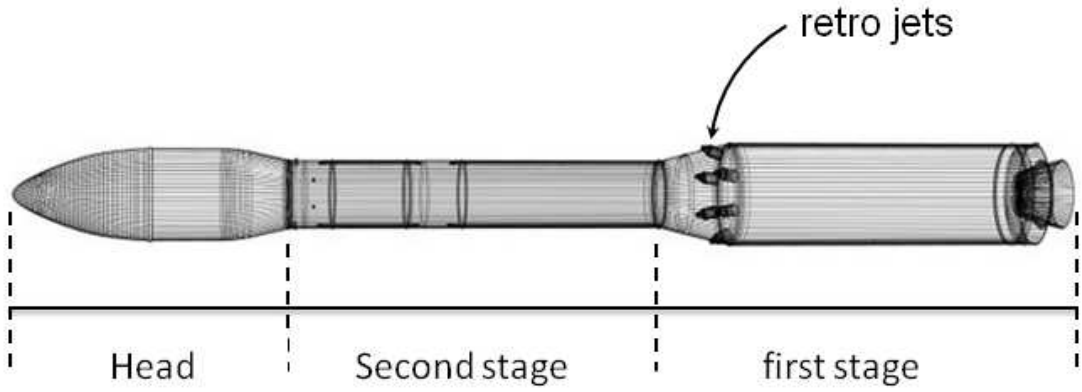

FIGURE 5.2: Rocket configuration from DLR wind tunnel model based on VEGA from IceAspen (2012).

5.2 High speed separated flow over ramp at M=4.8

Parameter	Main stream	Jet injection
Medium	Nitrogen	Nitrogen
Mach number	4.8	1
Static pressure (p_a)	p_∞(unspecified)	$6.32p_\infty$
Static temperature (K)	55.4	244.17
Stagnation temperature (K)	-	293
Wall temperature (K)	Adiabatic wall	N/A
Sound speed (m/s)	-	318.52
Simulation Reynolds number	3,422	N/A

TABLE 5.1: Inflow parameters for the 12° ramp flow with a jet injection.

As shown in table 5.1 the inflow condition in this section is the same to the ramp flow case studied in Chapter 4. The Reynolds number is 3,422 based on the inflow boundary layer displacement thickness. The ramp angle used here is 12°. A nitrogen sonic jet with a stagnation temperature of 293 K is used with specified J_p of 0.045 after numerical tests.

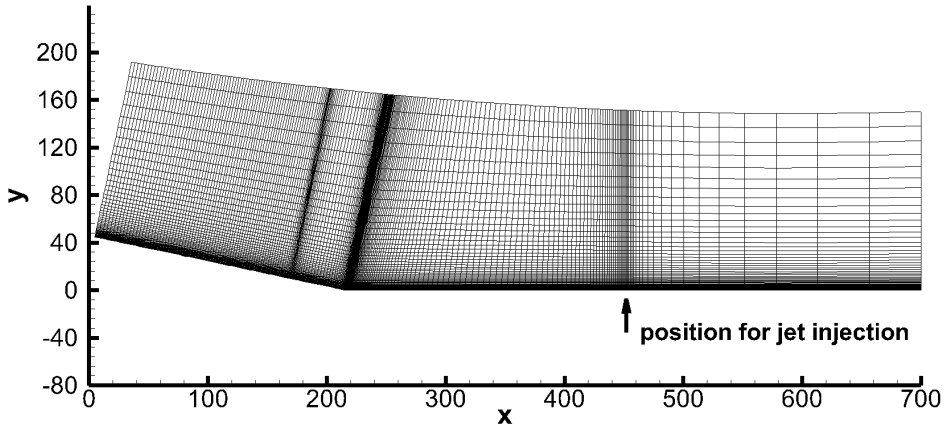

(a)

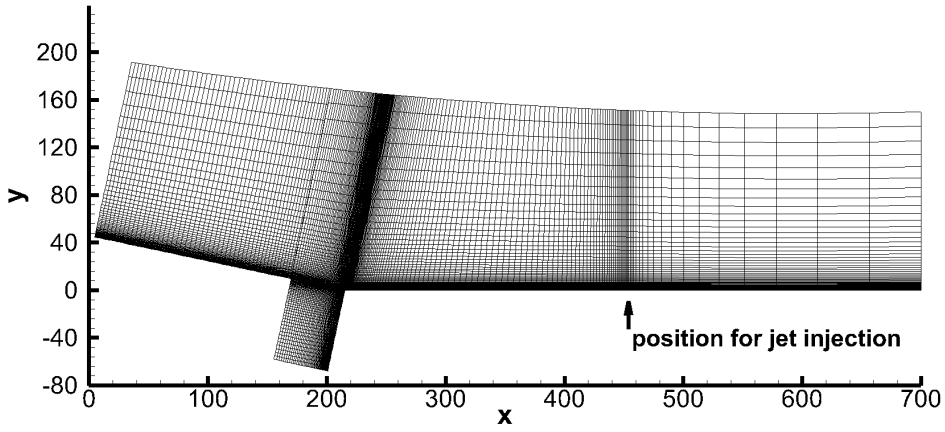

(b)

FIGURE 5.3: Computational meshes to study: (a) a M=4.8 ramp flow with/without a jet, (b) a M=4.8 ramp flow with cavity with/without jet (grid lines are shown every 5 grid points).

The computational domain used here is elongated compared with what is used in Chapter 4, both downstream of the corner in the streamwise direction and in the wall-normal direction to accommodate the jet and for the flowfield to develop, as shown in figure 5.3. The computational domain is 700 long and 150 high. A rectangular cavity is arranged upstream of the ramp corner to investigate the possibility of trapping the flow separation. The length and depth of the cavity are 46.48 and 68.35 respectively, giving a ratio L/D of 0.68. The slot jet is 1.8 wide and injected at x=450.9 downstream of the ramp corner. Two meshes are generated for the cases with and without a cavity, and used to study

the effects of the jet and cavity separately. Finer meshes are used around the corner and slot jet areas. Mesh (a) is used to compare the effect of the jet to the ramp flow. The size of the mesh is $2,347 \times 600$. For cases with a cavity, the same number of grid points are used over the ramp. However, the mesh is more stretched near the ramp corner to resolve the cavity and ramp flow. The cavity is meshed with 634×499 grid points to keep the same resolution in the x-direction. The mesh in the wall-normal direction is stretched, with a finer mesh near the interface of the cavity and the main flow to make sure of the same Δy and its derivative at both sides of the cavity-mainflow interface as shown in mesh (b). For mesh (b), the mesh size is $2,347 \times 600 + 634 \times 499$ (634×499 is the mesh within the cavity). All the jets simulated in this section are sonic and injected normal to the wall. All the flowfields are initialized according to the similarity solution of a compressible laminar boundary layer (White, 1974).

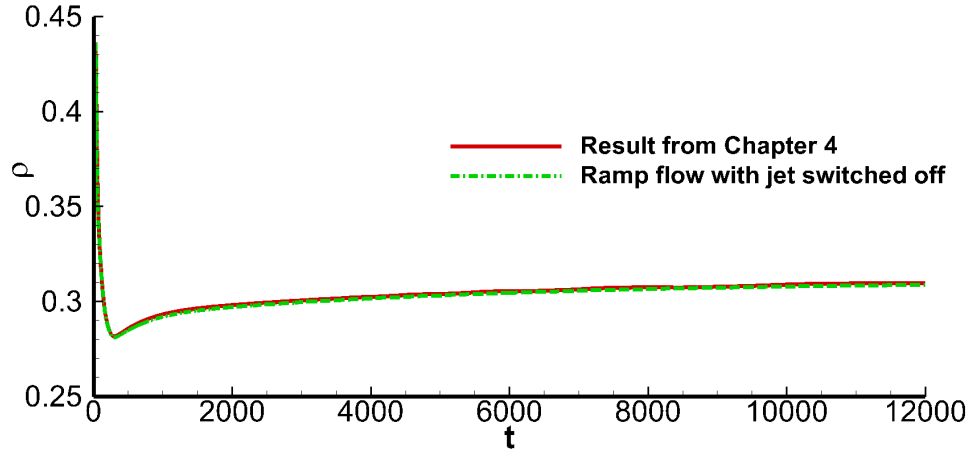

FIGURE 5.4: Density variations with time at monitor point ($x = 216.10, y = 2.82$) for current setup and that at monitor point ($x = 216.16, y = 2.82$) from Chapter 4.

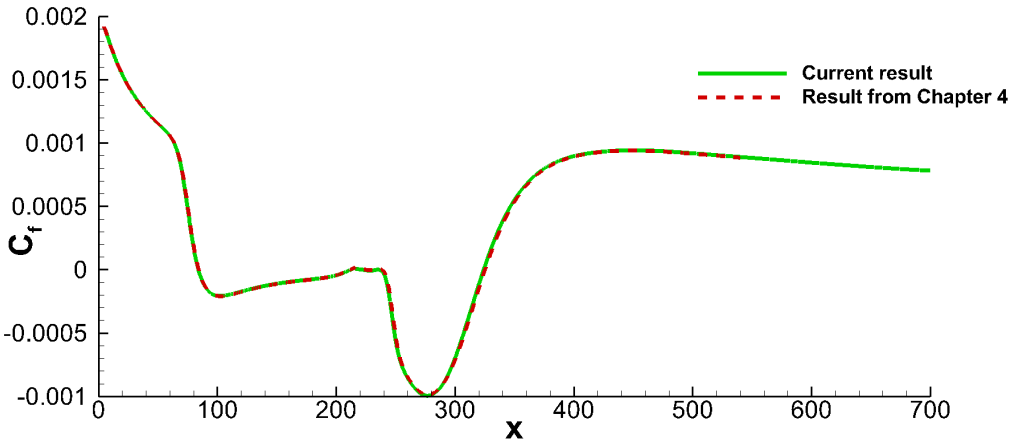

FIGURE 5.5: Distributions of skin friction coefficient for current setup and that from Chapter 4 at time instant: $t = 12,000$.

Four sets of simulations comprising (a) ramp flow alone, (b) ramp flow with a jet, (c) ramp flow with a cavity and (d) ramp flow with a jet and a cavity, are studied here. A mesh-dependency study is carried out for the ramp configuration by comparing the density time history at specified monitor points and skin friction coefficients with results already obtained in Chapter 4. Figure 5.4 shows the density variations with time at a monitor point just downstream of the ramp corner around (x=216, y=2.82). Because of the mesh elongation and the grid stretching, the difference of x- and y-coordinates between corresponding monitor points in the two meshes are $\Delta x \leqslant 0.06$ and $\Delta y \leqslant 0.003$, respectively. Good agreement is observed. The 0.34% difference appeared for the two curves can be explained by the slightly difference in the monitor point locations. It can be seen that the flow is reasonably well converged by $t = 12,000$ (results for longer runs will be shown later). Skin friction coefficients for the current setup and that obtained in Chapter 4 at $t = 12,000$ are plotted in figure 5.5. The curve corresponding to the current result is longer due to the elongated streamwise domain. The good agreement between the two curves shows that the laminar flow separation and reattachment points for both 2D setups happen at the same streamwise locations. According to the comparison above, we can say that the mesh is sufficient for simulation and the setup is correct.

5.2.1 Instantaneous flowfield comparison

Figure 5.6 shows the instantaneous flowfields for (a) ramp flow, (b) ramp flow with a jet, (c) ramp flow with a cavity and (d) ramp flow with a jet and a cavity at the same time instant t=9,000, respectively. The time t=9,000 corresponds to approximately 13 throughflows of the computational domain. Contours are shown with same levels of density superposed by streamlines.

The flowfields are not completely converged at t=9,000, but the separation for the case of a ramp with a jet has been restricted by the inflow boundary and is no more than 10 grid points away from inflow boundary, so this simulation has to be stopped. The other simulations are run further in time and results will be shown later. All the four cases show the general features of supersonic ramp flow, including flow separations, recompression shocks caused by the ramp corner and separation shocks.

For the ramp-only flow, a shock is formed when the freestream confronts a compression ramp corner as shown in figure 5.6(a). The high pressure after this shock causes flow separation from x=88 to x=320, forming a separation shock near the upstream separation point and a recompression shock near the downstream reattachment point.

Ramp flow with a jet injected downstream of the ramp recirculation zone is shown in figure 5.6(b). The jet imposes a strong influence on increasing flow separation and pushes the upstream separation point to the inflow boundary at time t=9,000. The large recirculation zone formed extends all the way from the inflow boundary to the jet

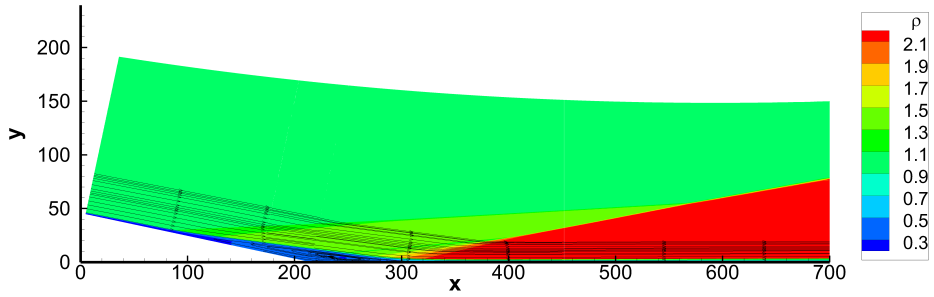

(a)

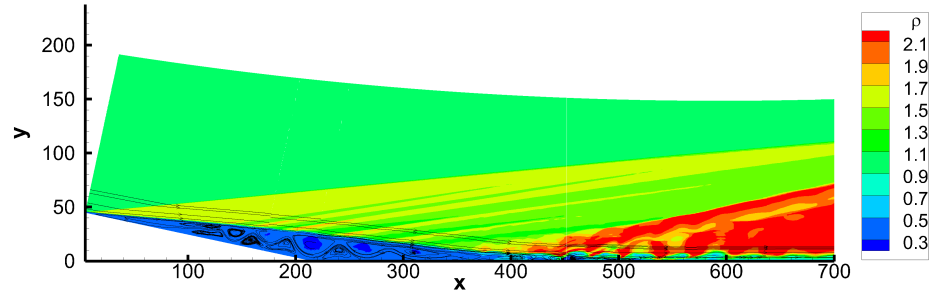

(b)

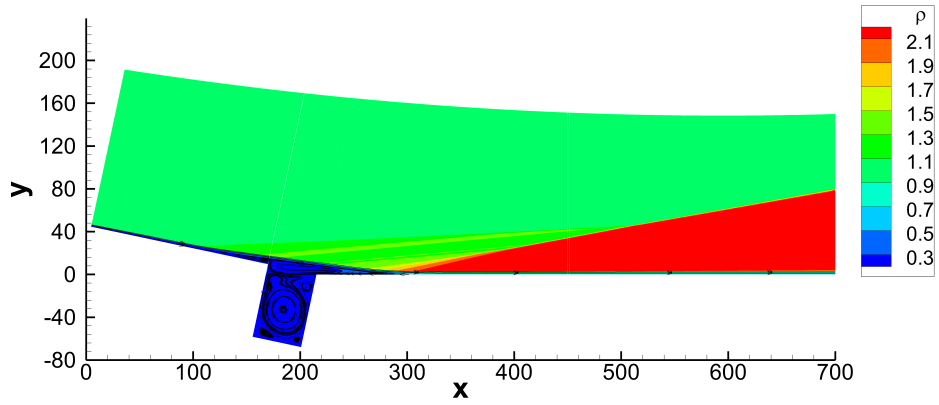

(c)

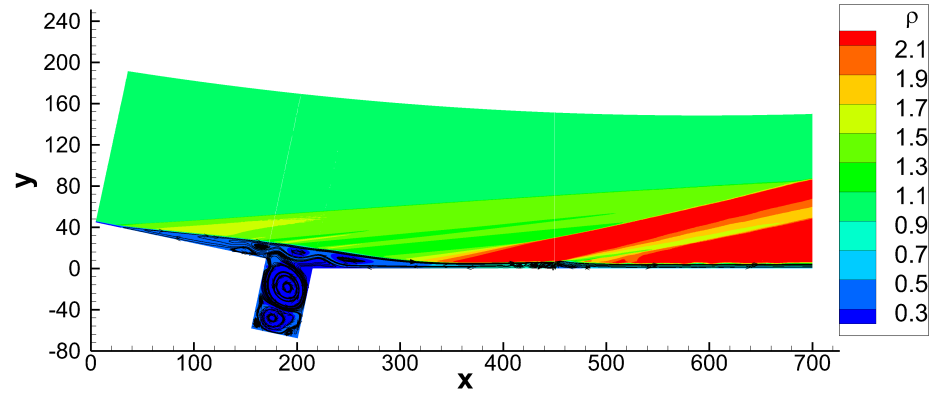

(d)

FIGURE 5.6: Density contours superposed by streamlines for (a) a ramp flow, (b) a ramp flow with a jet,(c) a ramp flow with a cavity and (d) a ramp flow with a jet and with a cavity at t=9,000 (cases at M=4.8).

location (illustrated by the low density contours coloured in dark blue), which means the separation zones formed by the ramp corner and the jet have merged into one. Secondary recirculations appear in the large separation bubble. The injected jet introduces both upstream and downstream shocks, making the flow more complex and forming higher density regions (the highest density of ρ=4.56 appears above the jet and is much higher than that of ρ=2.36 found downstream of the recompression shock in the ramp flow case). The reattachment point for the ramp only flow is at x=320, while in ramp flow with a jet case the separated flow does not realize reattachment before jet injection. A more detailed comparison will be presented later.

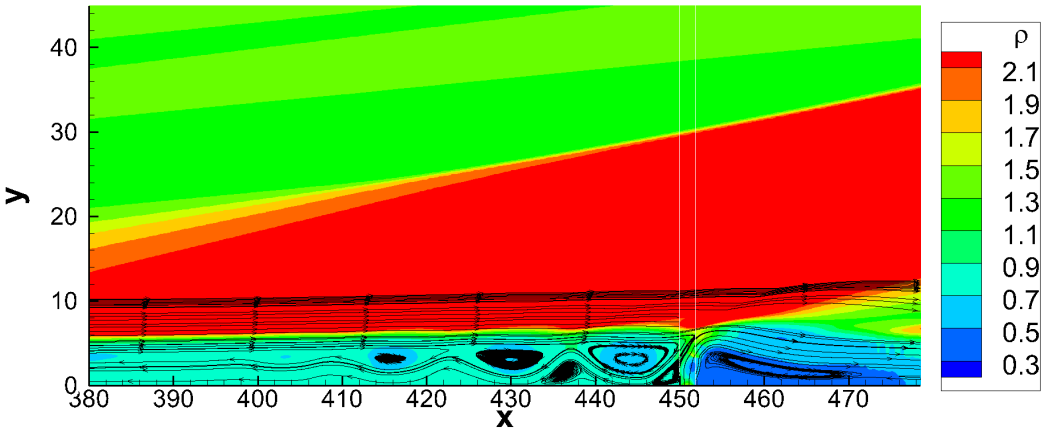

FIGURE 5.7: Density contours around jet injection from plot 5.6(d) superposed by streamlines.

Compared with the ramp flow case, there is little change in the flowfield for the ramp flow with a cavity (figure 5.6(c)), except for the vortex within the cavity, and an additional weak shock observed outside the boundary layer above the cavity caused by the small change in flow direction. For the ramp flow with a cavity and a jet (figure 5.6(d)), a large separation region with secondary recirculation is formed, which is similar to the ramp flow with a jet case, but there is still distance between the flow separation and the inflow boundary, indicating a slower growth of the upstream separation. Flow downstream is quieter compared with the ramp flow with a jet case, which is explained by the upstream available space for further expansion of the flow separation. Associated with the recirculation zones within the separation bubble, a series of compression shocks are observed upstream of the jet because of the series of vortices as shown in the expanded plot of figure 5.7, but they are weak compared with the bow shock above the jet.

By comparing all four sub-figures in figure 5.6, the most obvious conclusion is that the cavity does not have a strong effect on either the length of the separation or the density within the separated flow region, whereas the jet always leads to increased lengths of flow separation.

5.2.2 Effect of jet injection on ramp flow separation

Ramp flow with and without the downstream jet injection is compared in more details in this section. It was seen in figure 5.6(a) that the separation bubble of the basic ramp flow starts from x=88 at t=9,000. However, for ramp flow with a jet injected at $x = 451$, the separation reaches the inflow boundary by $t = 9,000$ as shown in figure 5.6(b). Compared with corresponding ramp flow without jet, appearence of secondary recirculation zone within the separation bubble shows that the flow with jet injection is more unstable. Flow reattachment for the ramp flow with a jet is also observed, but further downstream at x=630.

In the ramp flow, the separation shock and recompression shock can be clearly recognized and appear as straight lines. However, for the ramp flow with jet injection, a series of shocks are observed both upstream and downstream above the separation region because of the secondary recirculation zones as shown in figure 5.6(d) and figure 5.7. Shocks, especially downstream of the jet, are bent because of the downstream recirculation flow and the interactions between the shocks caused by jet and recompression shock.

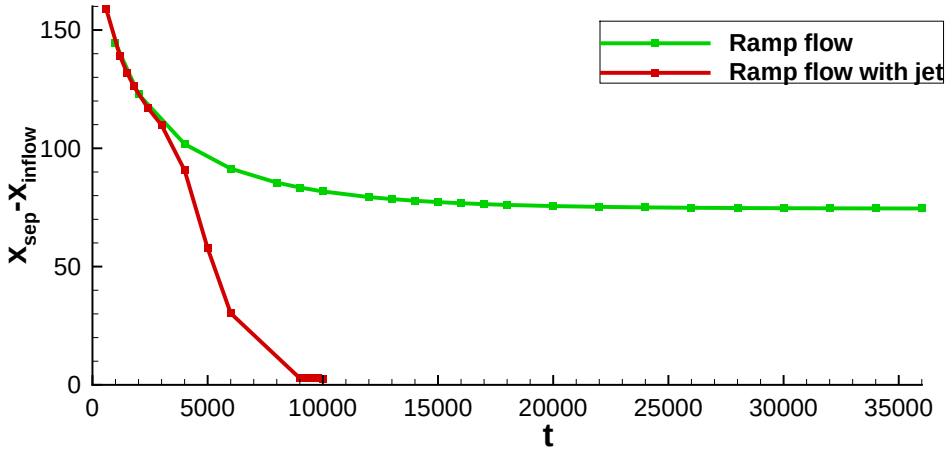

FIGURE 5.8: Developments of flow separation point along with time for ramp flow without/with jet.

To study the flowfield development, the progresses of flow separation with time for the ramp flow without and with a jet are shown in figure 5.8. Because of the rotated computational domain, the streamwise coordinate of the inflow boundary on the wall (x_{inflow}) is at $x = 4.7$. In the plot, by subtracting the x-coordinate of the inflow boundary x_{inflow} from that of flow separation point (x_{sep}), the y-axis shows the distance from the inflow boundary to the flow separation point. It can be seen that ramp flow separation does not reach the inflow. The separation point stabilizes at $x = 80$ when running the simulation much further in time. However, for the case with jet injection, the separation region moves upstream very quickly. The trend of separation point movement upstream suggests that the inflow boundary stops the separation point, and the recirculation region

would further develop upstream had the inflow boundary been further forward. The influence of the jet on the downstream flow is significant. The separation zones caused by ramp corner and jet injection merge and give reattachment further downstream than in the ramp-only case.

It can be concluded that jet injection has a very strong effect on the ramp flow separation. It pushes the separation region both further upstream and further downstream, reaching the current inflow boundary. Later on different jet strengths will be tested, based on the practical background of a rocket stage separation problem.

5.2.3 Effect of cavity addition on ramp flow separation

Ramp flow with a cavity is studied here with two different setups, with a jet and without a jet, and compared with the flow results without a cavity given in the last section. To make comparison of the cavity effect more easily, the flow without a jet is also calculated further, up to a non-dimensional time of 36,000.

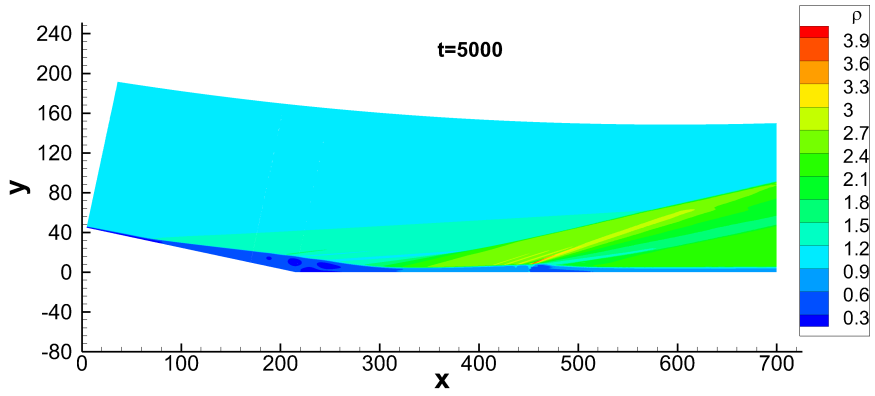

(a)

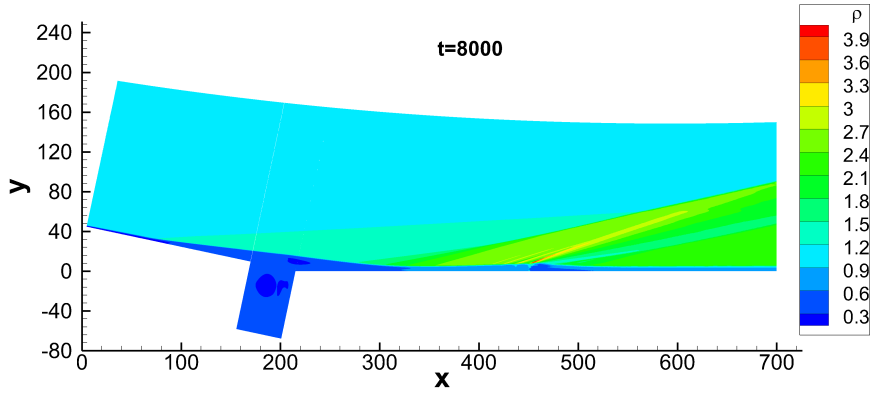

(b)

FIGURE 5.9: Instantaneous flowfields of (a) the ramp flow with a jet at t=5,000 and (b) the ramp flow with a jet and a cavity at t=8,000.

Figure 5.9 shows density contours with the same levels for ramp flow with a jet with-/without a cavity. The flowfields, including flow separation shock, ramp recompression shock and shock caused by jet injection, are quite similar except in the cavity area. The two flows have a similar separation length after running for different time (8,000 and 5,000 respectively). With consideration of the same initial flowfield except cavity area, this figure hints that the cavity might delay flow separation.

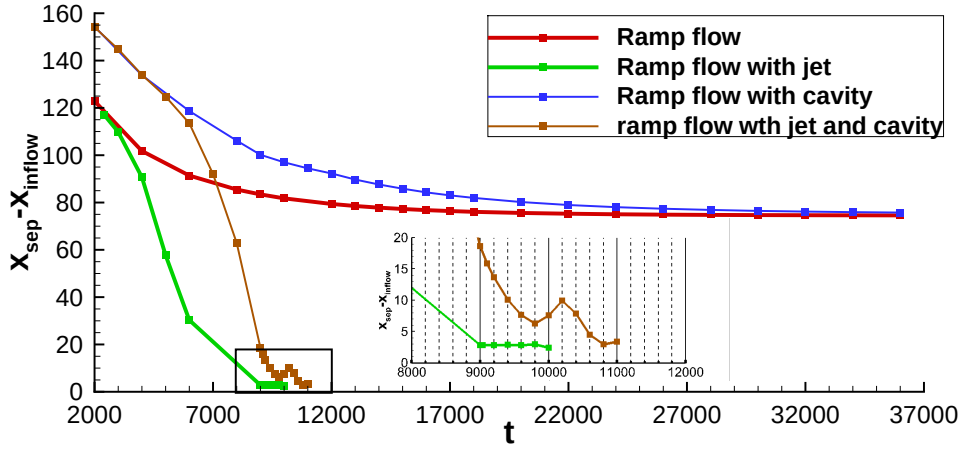

FIGURE 5.10: Variations of flow separation point with time for M=4.8 cases. The inset shows the behaviour as the separation point reaches the inflow boundary.

Movements of the flow separation point with time, as well as a zoom-in showing an oscillation in the separation region development which will be discussed later, are illustrated in figure 5.10 for the four cases, i.e. the ramp flow with (thick green curve) and without a jet (thick red curve), the ramp flow with a cavity with (thin brown curve) and without a jet (thin blue curve). In the cavity cases for t <2,000 the separation point is within or downstream of the cavity. It can be seen that at t=2,000, when the cavity cases have separation at the cavity lip (x=160), the cases without a cavity already have separation points located further upstream (near x=120), hence the cavity reduces the initial development of the separation zone. For the ramp case, the separation point moves rapidly upstream, and finally converges 80 downstream of the inflow boundary. The same separation location is reached, albeit more slowly, for the case with a cavity. However, for the ramp flow with a jet injection, the separation reaches the inflow boundary by t=9,000 as shown infigure 5.6(b). For the case with a jet and a cavity the separation point reached the inflow at around t=10,000, i.e. slightly later than that when the cavity was not present.

Based on the analysis above, converged flowfields for ramp flow cases with and without the cavity are compared at t=36,000 in figure 5.11. By comparing the shock position, the high density area in red and the separation area in blue based on the same density levels, it is found that the flowfields are very similar except in the cavity area.

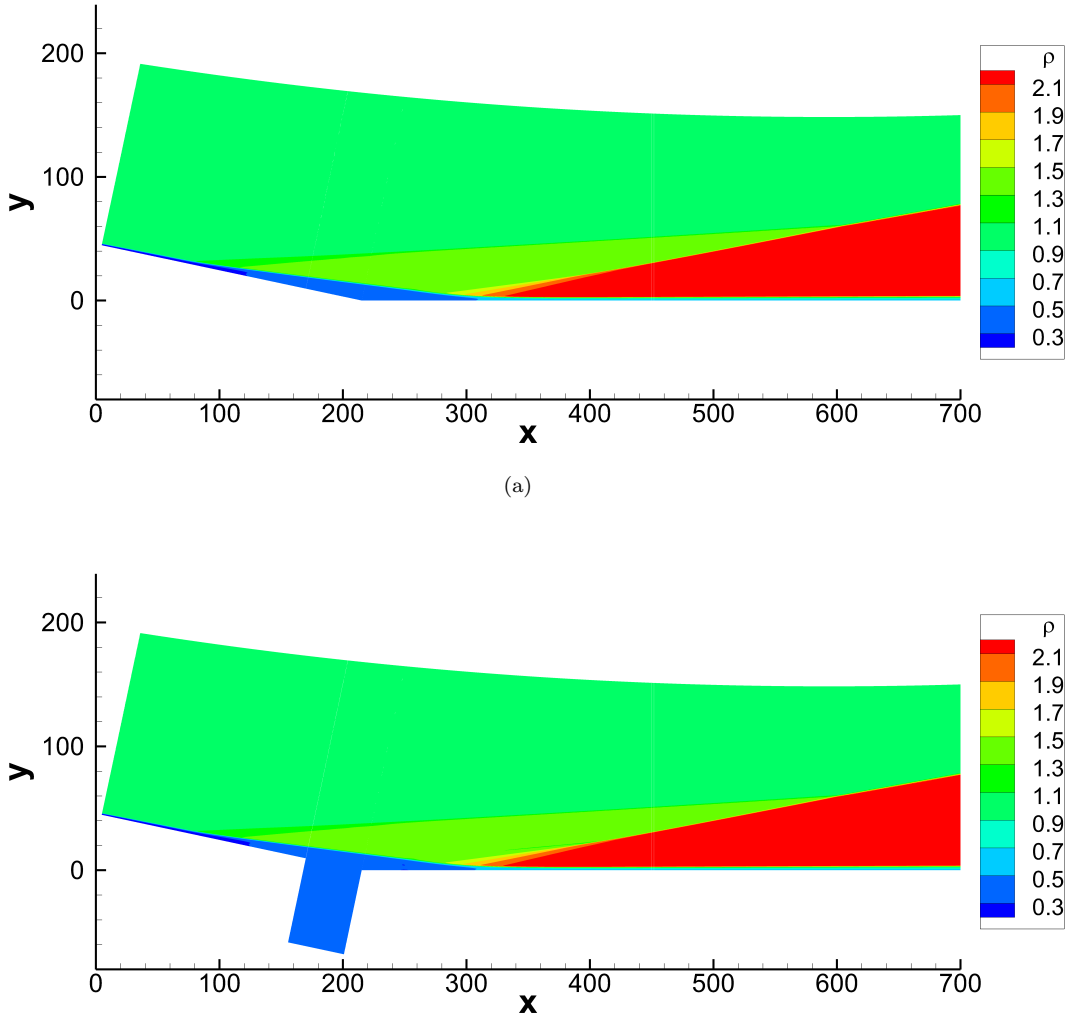

(a)

(b)

FIGURE 5.11: Instantaneous flowfields of M=4.8 ramp flow (a) without and (b) with a cavity at $t = 36,000$.

Figure 5.12 shows the skin friction for ramp flow and ramp flow with a cavity at t=36,000. The skin friction coefficient upstream is determined by both u-velocity and v-velocity derivatives because of the upstream inclined wall. The flow separation points for the converged ramp flow without and with a cavity are at x=79.23 and x=80.24 respectively. The corresponding reattachment points for the two flows are at x=329.1 and x=327.6, meaning that the separation bubble for ramp with cavity is slightly smaller. The distributions of skin friction coefficient for ramp flow with a cavity (in green) and ramp flow (in red) are very close. The low values of C_f seen between x=240 and x=330 are caused by the downstream recompression shock pressing the large vortex inside the separation bubble towards the wall as displayed in figure 5.13. A small secondary recirculation zone is seen near the ramp corner. The most obvious differences of the two C_f curves are around $x = 169$ and $x = 215$ where there are small departures with more than 10 grid

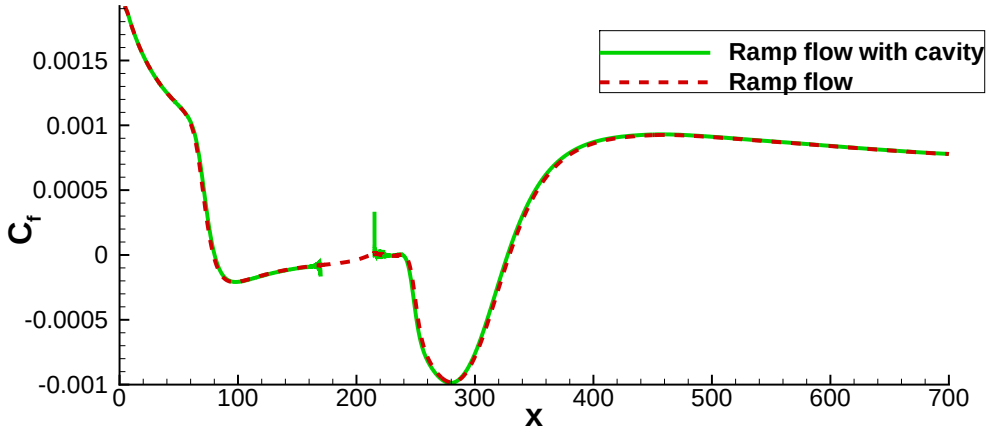

FIGURE 5.12: Skin friction comparison between ramp flow with/without a cavity at t=36,000.

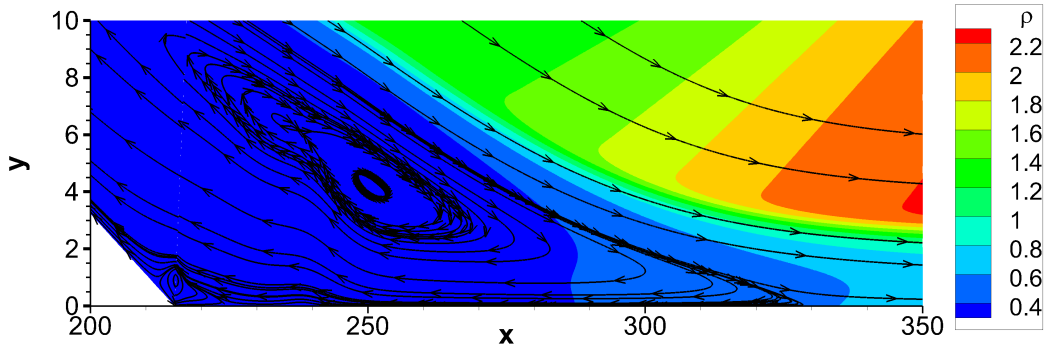

FIGURE 5.13: Density contours near the ramp corner superposed by streamlines for the ramp flow at t=36,000.

points each, corresponding to the leading and trailing edges of the cavity. The drop of the C_f curve for ramp flow with cavity around x=169 is caused by the intensive flow variation at the leading edge of the cavity as shown in figure 5.14. The flowfield is shown by contours of v-velocity superposed by streamlines. Two vortices above and within the cavity are observed. The cores of these vortices are steady by checking flowfields at different time instants. Due to the interaction of two vortices above and within the cavity, u-velocity and v-velocity experienced intense variations which will not happen for the ramp flow without a cavity. It is the variations that cause the departure of C_f distribution at the leading edge of the cavity.

A similar interaction of vortices is observed near the trailing edge of the cavity as shown in figure 5.15(a), as well as in the zoomed-in plot 5.15(b). Both figures show contours of u-velocity and are superposed by streamlines. As the zoomed-in figure is only used to describe the detailed flow, narrow u-velocity contour levels are used. Two vortices are observed with their core locations stabilized with time. One is inside the cavity and the other one is within the boundary layer downstream of the cavity. The vortex inside

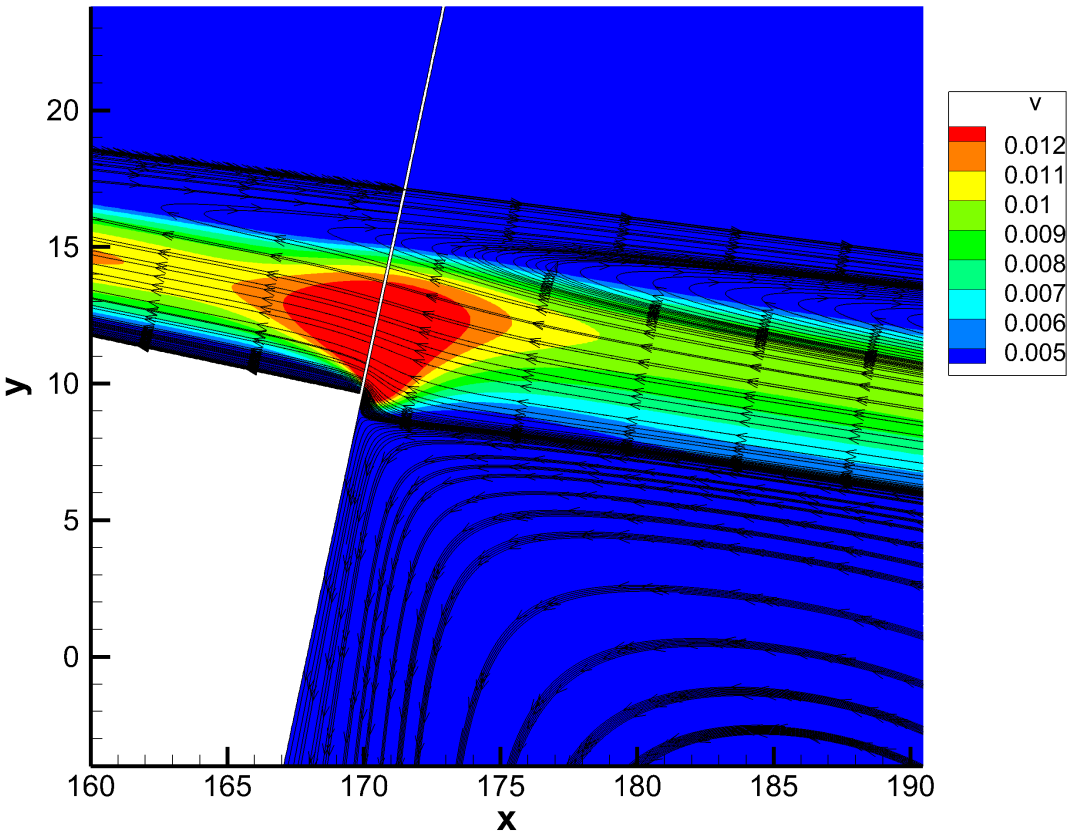

FIGURE 5.14: Contours of v-velocity near the upstream cavity lip for the ramp flow with a cavity at t=36,000.

the cavity tends to expand downstream in opposition to the downstream vortex. The interaction of the two vortices forms a small recirculation zone close to the trailing edge of the cavity from x=215 to x=223 as shown in figure 5.15(b). This recirculation region is the reason for the drop of skin friction curve from x=215.2 in figure 5.12 for ramp flow with a cavity.

Figure 5.16 shows the RMS of pressure fluctuation on the wall for ramp flow with/without cavity. The data are obtained based on the same time length of $5,000$ from t=32,000. The value for the ramp flow with a cavity is much larger than that for the ramp flow, showing that the addition of a cavity makes the flow more unsteady, although the levels are still small. The two main peak locations at x=75.6 and x=303 for the two cases are in agreement with each other. They are located at the edge of separation shock or reattachment shock, where interactions between the shear layer and shock-wave exist.

It was earlier remarked that an oscillation appears at $t = 10,000$ for the flow separation development of the ramp flow with a jet and a cavity case as shown by the enlarged plot in figure 5.10. This oscillation is caused by the movement of the recirculation zone

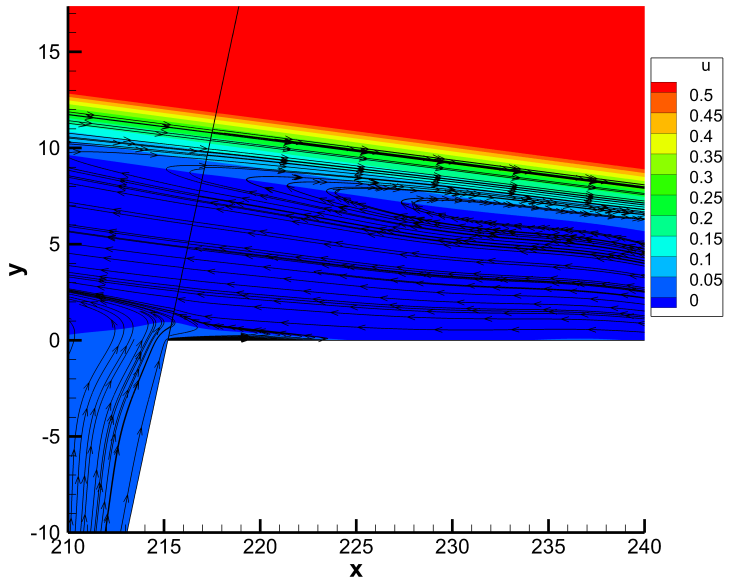

(a)

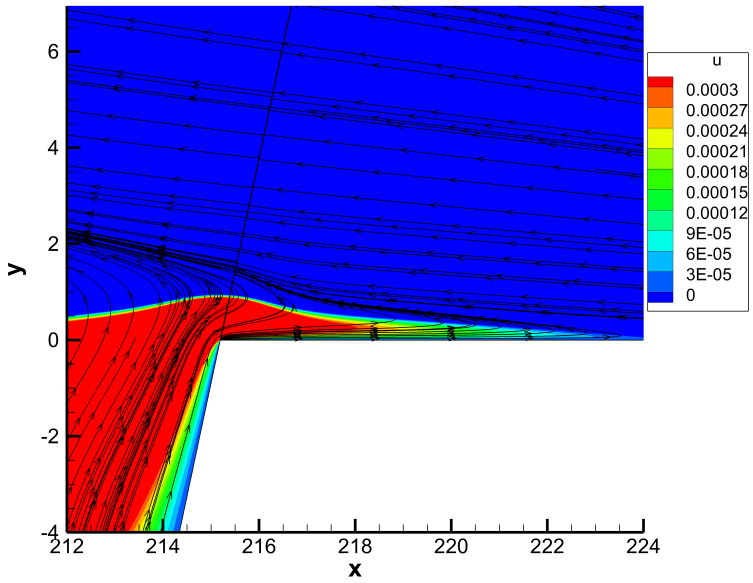

(b)

FIGURE 5.15: Contours of u-velocity near the trailing edge of the cavity in different scales for the ramp flow with a cavity at t=36,000.

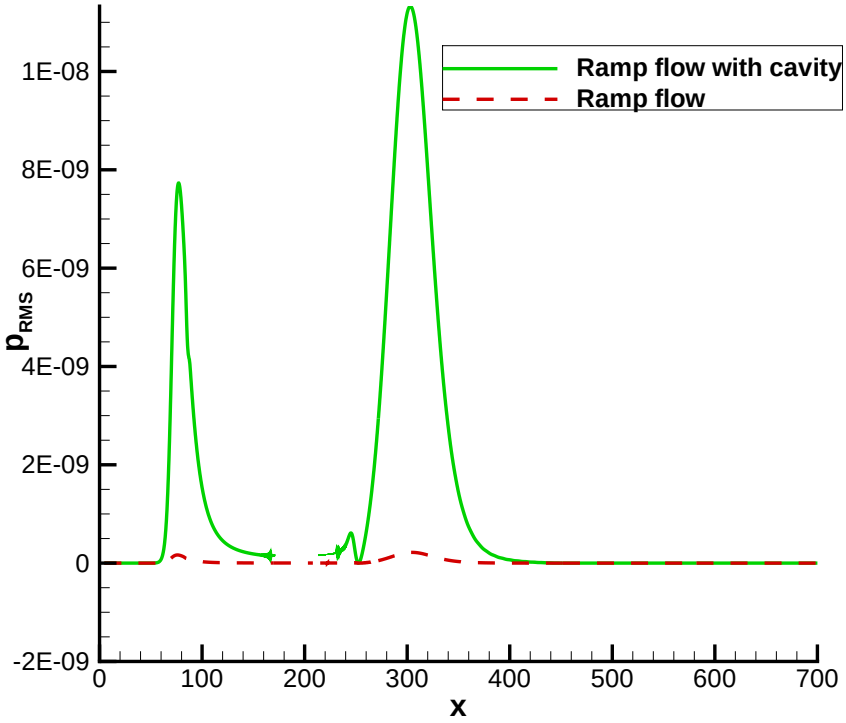

FIGURE 5.16: RMS wall pressure for ramp flow with/without cavity.

within the boundary layer when the separation bubble arrives at the inflow boundary as shown in figure 5.17. Plots 5.17(a), 5.17(b), 5.17(c) and 5.17(d) show the flowfield at four consecutive time instants, which are picked according to the sub-figure in figure 5.10. The vortex marked by the white arrow is observed to move downstream after the flow separation arrives at the inflow boundary (at t=9,800). After flow separation is stabilized at t=10,200, the vortex starts to expand which can be seen by comparing the core locations of the lower vortex within the cavity. From t=9,600 to t=10,600, the location of the core of the upper vortex in the cavity develops from y=-13.3, y=-12.5, y=-9.6 and until y=-11.3. This causes unsteadiness of the flow separation after the separation reaches the inflow boundary. Compared with the separation curve of ramp flow with jet, it is believed that the flow unsteadiness is caused by the cavity.

The main conclusions from the 2D study at M=4.8 are that the jet has a significant effect on the flowfield, with the separation point moving all the way to the inflow boundary even at small jet momentum flux. The cavity (in this case with L/D of 0.68) hardly has any effect on the final location of the separation point, but does slightly delay the upstream travel of the separation point. Further study will be carried out based on a practical case for a rocket.

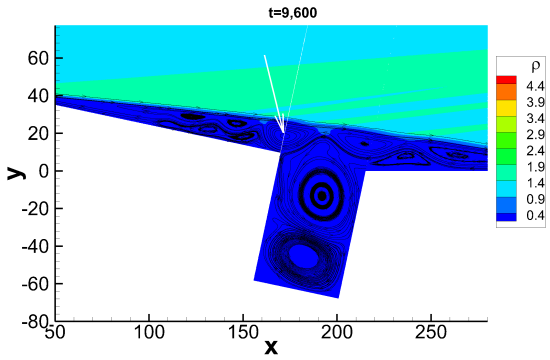

(a)

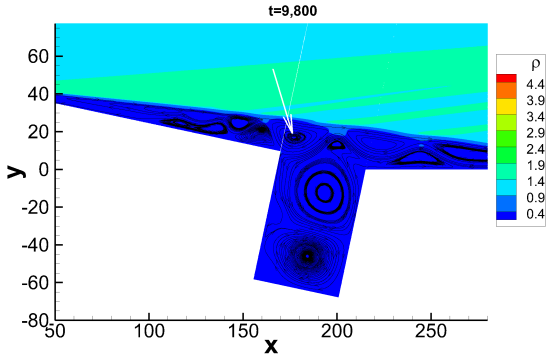

(b)

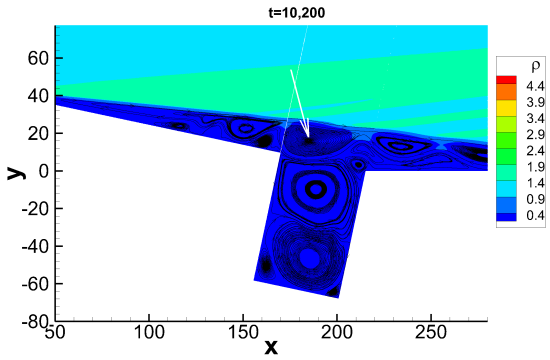

(c)

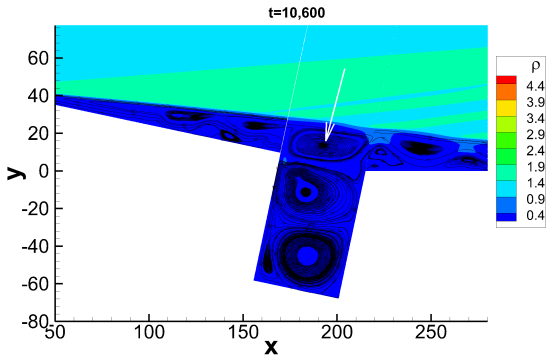

(d)

FIGURE 5.17: Comparison of flowfields with a cavity and a jet near the ramp corner at different time instants for the ramp flow.

5.3 2D study of a rocket case

Simulations presented in this section are based on the DLR wind tunnel tests used to study stage separation (based on the VEGA rocket design), as shown in figure 5.2. The length of the second (top) stage is 47.09 cm. The first and second stages are separated by a 5 mm gap, so that the forces on the second stage could be measured with strain gauges. Six retro flush-mounted nozzles are located on the first stage along the azimuthal direction with equal distances between jets to help force the first stage away from the second stage when needed. The ramp angle formed between the first and second stages is 14.75°. The jet is injected upstream with angle of 26.16° to the first stage (11.41° to the second stage). The work here is to further evaluate the cavity effect (due to the separation between the stages) on the flowfield and to study a 2D jet with different strengths and orientations.

Parameter	Main stream	Jet injection
Medium	Air	Air
Mach number	5.3	3.6
Static pressure (Pa)	400	§
Stagnation pressure (Pa)	0.3×10^6	§
Static temperature (K)	58.9	80.73
Stagnation temperature (K)	390	290
Wall temperature (K)	298	N/A
Sound speed (m/s)	153.85	180.13
Density (Kg/m^3)	2.37×10^{-2}	§
Unit Reynolds number (/m)	4.74×10^6	N/A
Simulation Reynolds number	6,000	N/A

TABLE 5.2: Inflow parameters used in DLR wind tunnel for rocket stage separation study (§ means to be determined by J_p, N/A means not applicable).

The flow conditions used in DLR wind tunnel for the rocket separation study are listed in table 5.2. The freestream Mach number is 5.3 with a unit Reynolds number of 4.74×10^6 m^{-1} and a static temperature of 58.9 K as the reference temperature. The wall temperature is set to the room temperature of 298 K. Mach 3.6 air with a stagnation temperature of 290 K is injected through the six nozzles with a diameter of 3.25 mm used in this section (from an earlier version of the experimental configuration, compared to 3.7 mm for the 3D cases shown in the next chapter).

In this section the results from a 2D study based on a simplified configuration are presented in figure 5.18. The flat plate before the gap is used to replace the axisymmetric head and second stage of rocket shown in figure 5.2. The first stage is modelled by a ramp with a slot jet. The width of the slot is set equal to the retro-jet diameter. Different jet strengths (J_p) are tested, with a maximum J_p of 3.492 used, which is 1/6.7 of the slot jet momentum flux ratio equivalent to the practical retro jet. For the current

flow conditions, the J_p values used here is much higher than described in the previous sections.

The distances are scaled with the boundary layer displacement thickness at the inflow, which is δ_0^*=1.266 mm. Between the the stages, the 3.95 width gap represents the 5 mm gap for the experimental model. The Reynolds number based the displacement thickness and the free-stream properties is Re=6000. The computational domain starts at 48.6 mm downstream of the notional launcher tip (corresponding to the leading edge of the flat plate).

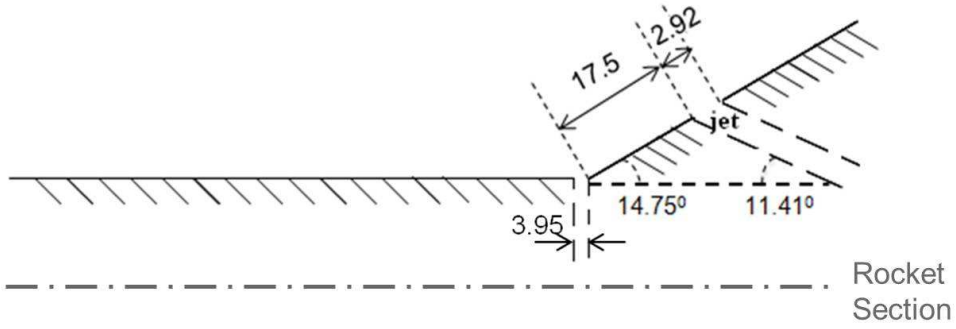

FIGURE 5.18: 2D simplified rocket configuration (with dimensions normalised with the inflow boundary layer displacement thickness δ_0^*=1.266 mm).

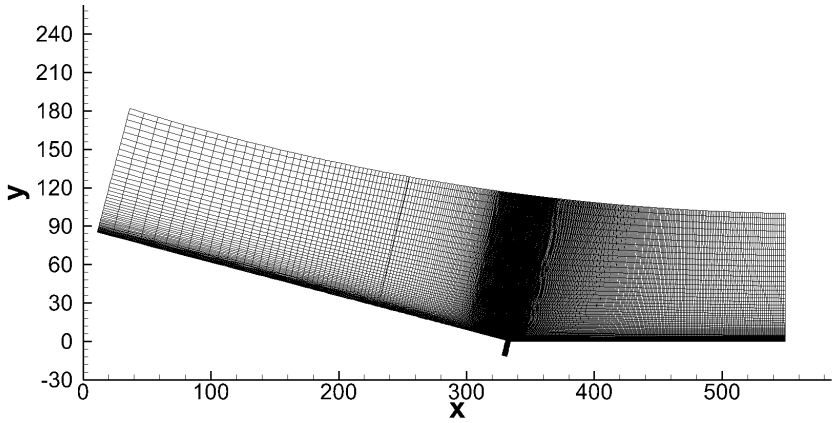

FIGURE 5.19: 2D mesh for the rocket with a narrow (5 mm) gap based on the simplified configuration.

With the similar rotation discussed in the previous section, a 2D mesh is obtained as shown in figure 5.19. A length of 334.42 including the 3.95-width cavity is used before the corner. The length/depth (L/D) ratio of the cavity is 0.3. The jet is injected from a slot of width w=2.6 centred at x=348. A multi-block mesh is used, which is stretched in both the streamwise and wall-normal directions. To study cavity effects another two meshes, one without a cavity, as shown in figure 5.20(a), and the other with a wider and deeper cavity (with L=38.17 and L/D=0.7), as shown in figure 5.20(b), are used.

The cavity upstream and downstream side walls are set normal to the upstream surface (representing the rocket second stage). The mesh for the cavity is stretched to ensure the same mesh spacing and continuity of its derivative on both sides of the cavity-mainflow interface. The same upstream length, including the cavity, before the ramp corner is used. The only difference between the three meshes is the mesh for the cavity. The grid size for the main domain is 4291×300. The narrow and wide cavity cases have added blocks of 396×89 and $2,516 \times 241$, respectively, with very fine grids needed to resolve the flow near the cavity corners using the current high-order code.

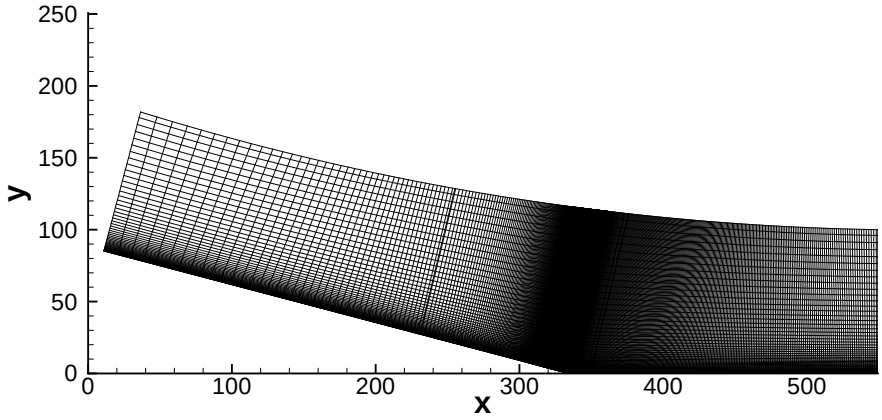

(a)

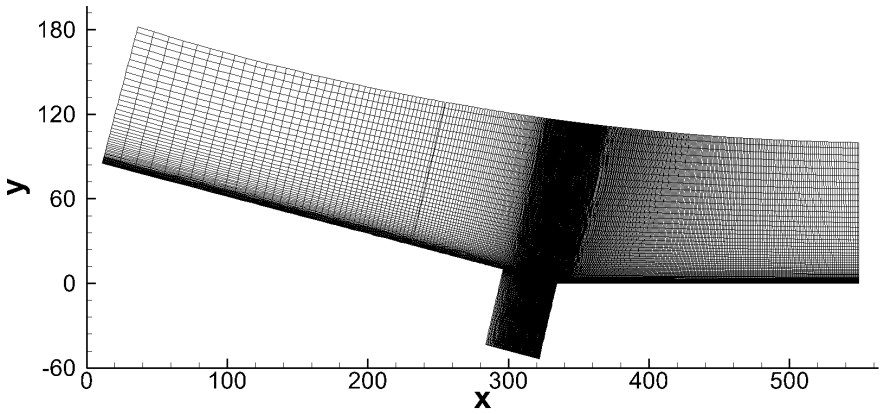

(b)

FIGURE 5.20: Meshes for M=5.3 ramp flows (a) without a cavity and (b) with a wide cavity.

Non-slip wall condition is used here, with extrapolation and characteristic conditions applied at the inflow and the outflow boundaries. An integral characteristic condition is used for both the upper boundary and jet area. The jet is imposed over the range from x=346.7 to 349.3 as a slot jet with fixed T_{0j} and M_j but variable static pressure so that different jet strengths can be compared. For jet injection study, a jet normal to the surface is firstly studied, then an upstream pointing jet with an angle of 26.16°

obtained from the rocket configuration is used. The jet profiles are prescribed using a hyperbolic tangent profile as given in equation (3.1) with δ=0.2 to give 'top-hat' profiles for velocity and temperature. A jet pressure parameter p_j is programmed in the code and defined as the constant pressure across the jet normalised by the free-stream density and velocity, which is proportional to the J_p parameter used before, with the relationship $J_p = 23.28p_j$. Three different normal jets with $p_j = 0.05$, $p_j = 0.1$ and $p_j = 0.15$ are considered in the following simulations with jet injection firstly. The upstream inclined jets with strength of $p_j = 0.1$ and $p_j = 0.15$ are then presented.

5.3.1 Further study of cavity effects

Figure 5.21 shows instantaneous flowfields of ramp flow, ramp flow with a narrow cavity and ramp flow with a wide cavity at the same time instant t=10,000 during the initial flowfield development. Contours are shown for density, superposed with streamlines. A separation shock, recirculation zone and reattachment shock are observed in all the three plots. The ranges of density variations are similar for all the three flows. However, a larger separation zone is observed for the ramp flow with a narrow cavity whereas the separation lengths for the ramp flow case and the ramp flow with a wide cavity case are similar. The separated region is from $x = 20$ to $x = 494.5$ for the ramp flow with a narrow cavity case, from x=108 to x=448 for the ramp flow case, and from $x = 108.5$ to $x = 446$ for the ramp flow with a wide cavity case. At the same streamwise location (x=230), the boundary layer is thicker for the ramp flow with a narrow cavity case than for other two cases. Secondary recirculation zones are observed in all the three flows. By comparing their distributions, it is noticed that vortex structures are similar for the ramp flow and the ramp flow with a narrow cavity cases, except that there is one more upper vortex and one more lower vortex within the boundary layer upstream of the ramp corner around x=230 for the ramp flow with a narrow cavity case. A third vortex around $x = 343$ close to the wall is also observed for the ramp flow with a narrow cavity. Similar vortex distributions are observed for the cases of ramp flow and the ramp flow with a wider cavity however the lower vortices in the boundary layer above the cavity merge with the vortices in the cavity for the case of ramp flow with wide cavity.

Figure 5.22 shows the time development of the flow separation point (x-coordinate) relative to the domain inflow boundary (x-coordinate of inflow boundary is 11.02). It can be seen that flow separation for the ramp flow with a narrow cavity case (green curve) arrives at the inflow boundary by t=10,000, while flow separations stop moving upstream until t=40,000 around x=70 (59 downstream of the inflow boundary) for both ramp flow (blue curve) and ramp flow with a wide cavity (black curve). The oscillations on the black curve are due to significant unsteadiness in the flow which is introduced by the wide cavity. Figure 5.23 shows the RMS distribution for ramp flow with and without the L/D=0.7 cavity. The statistic data are collected from t=90,000 to t=110,000. The

overlapped and mismatched curves for the flow with the wide cavity at the leading and trailing edges of the cavity are because of the inclined cavity walls. It is clearly seen from the plot that the flow becomes unsteady when adding the L/D=0.7 cavity.

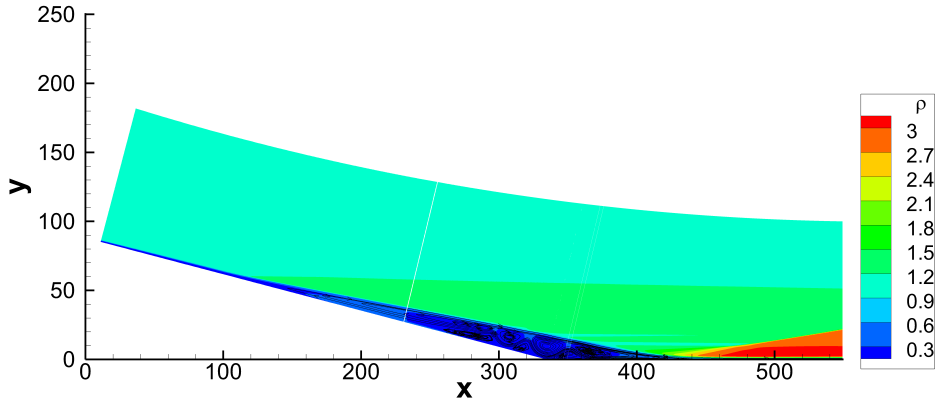

(a)

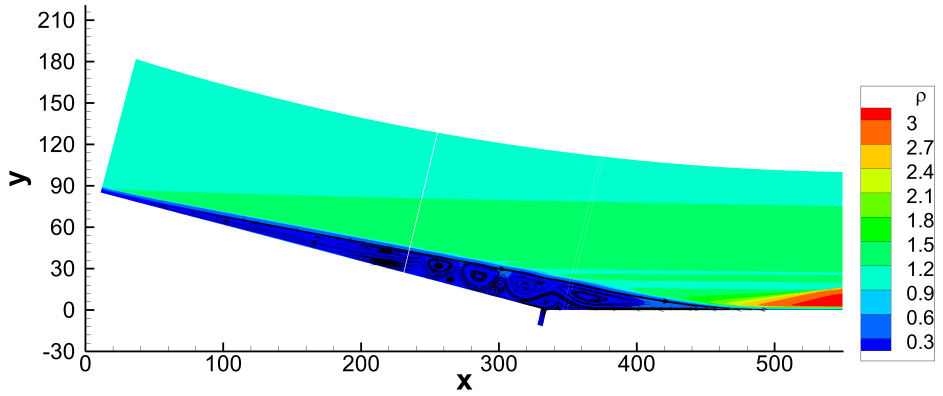

(b)

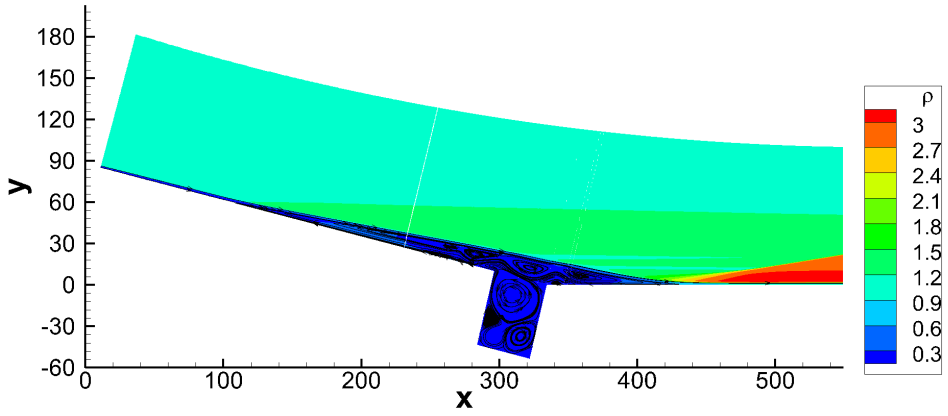

(c)

FIGURE 5.21: 2D flowfields for different ramp flows at $t = 10,000$ (M=5.3).

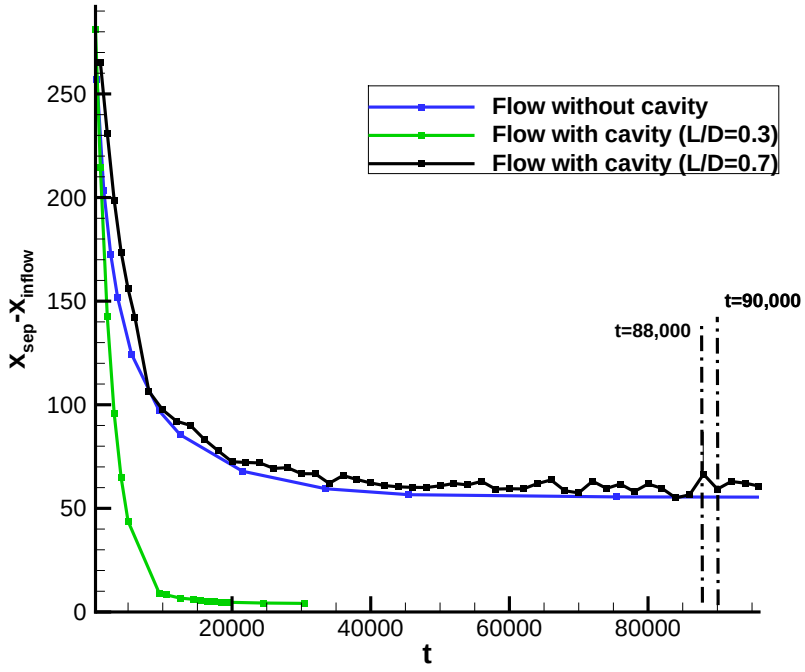

FIGURE 5.22: Flow separations with different cavity arrangements at M=5.3.

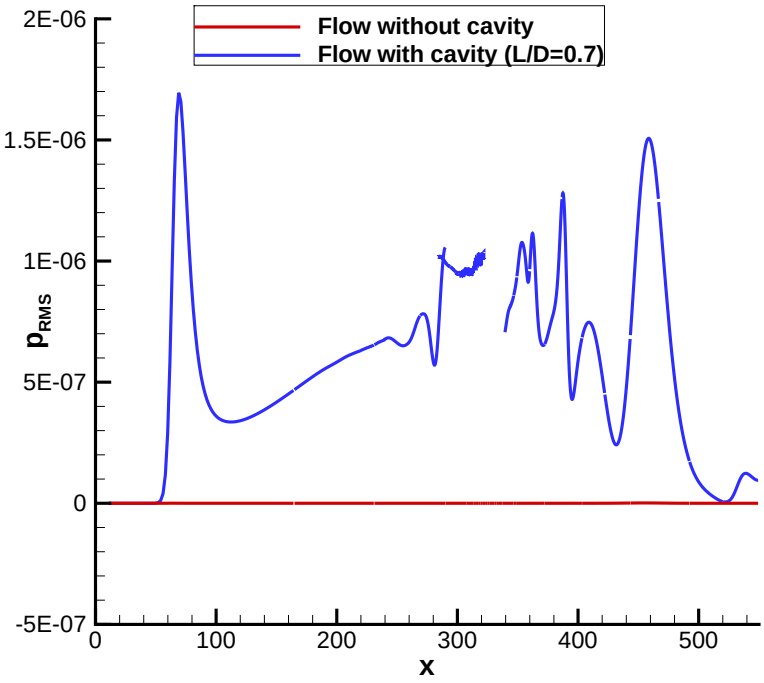

FIGURE 5.23: RMS of wall pressure for ramp flow with/without L/D=0.7 cavity at M=5.3 in a period of t=20,000.

As introduced in Chapter 1, there are four different modes of mechanism for cavity flow unsteadiness. To study the unsteadiness confronted here when adding a cavity upstream a ramp flow, the contours of Mach number for both the Mach 4.8 ramp flow with cavity studied in former section and the Mach 5.3 ramp flow with a wide cavity are illustrated in figure 5.24. It is observed that although both inflows are supersonic, the local flows for both cases around the cavities are subsonic. Reverse flow and vortex above the cavities are observed for both flows. The Mach number around the cavity for the Mach 4.8 case is around 0.1, while more complex flow full of vortices with Mach number changing from Mach 0.1 to about 0.5 is observed for around the cavity for the Mach 5.3 case. These reverse flows and vortices make it difficult to study the mode which causes the unsteadiness of the flows.

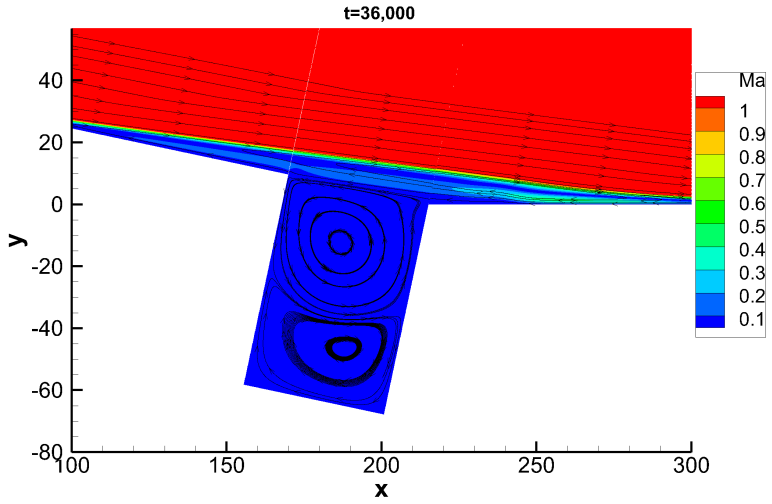

(a)

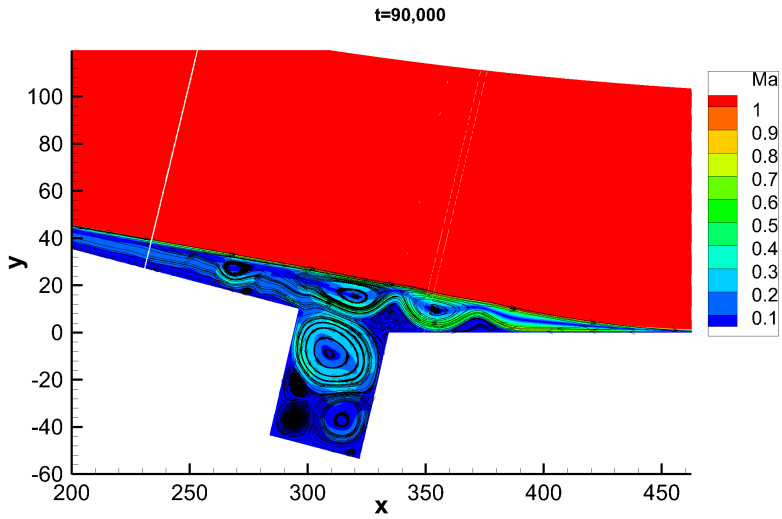

(b)

FIGURE 5.24: Contours of Mach number for the (a) Mach 4.8 flow and (b) Mach 5.3 flow with a wide cavity, superposed by streamlines.

Flowfields around the wide cavity at two time instants, $t = 88,000$ and $t = 90,000$, as marked in figure 5.22, are plotted in figure 5.25, where contours of v-velocity are superposed with streamlines. As can be seen in figure 5.22, the separation point is further upstream at $t = 90,000$ than that at $t = 88,000$. By comparing the flowfields at the two instants in figure 5.25, it can be seen that the upper vortex within the cavity expands at $t = 90,000$, with its vortex edge higher than the cavity rim, while the downstream vortex stays nearly in the same place. Hence the recirculation zones above the cavity and upstream are compressed and pushed upstream, making the flow separation move upstream. The place of the large downstream vortex remains the same (only half of the vortex is visible in the figure from $x = 340$ to $x = 350$) at the two time instants, and the rear reattachment point always occurs at $x = 477$.

It have been seen that the cavity has little effect on flow separation but makes the flow more unstable, which was also found for the M=4.8 case shown in the last section. However the narrow cavity has a great effect in pushing the flow separation upstream as shown by green curve in figure 5.22. This strong effect of a narrow gap is believed to be consistent with DLR experimental results based on the 5 mm gap between the two stages of a rocket. The big separation disappeared when a 75 mm-wide gap was tested. Attempts here are made to explain the phenomenon based on the detailed numerical results.

Figure 5.26 shows a series of instantaneous flowfields at t=4,000, t=4,500 and t=5,000 around the narrow cavity. At these time instants the separation has not reached the inflow boundary, but is moving rapidly upstream (as shown by the green curve in figure 5.22). Streamwise velocity contours are used here to show the flow details around the cavity, with streamlines superposed. A large upstream vortex is observed to expand both upstream and downstream with its measured core location changing from 11.3 to 11.71, and 12.07 in the wall-normal direction, corresponding to the three time instants. The vortex within the cavity close to the rim is pushed towards the bottom of the cavity by comparing the red contour regions and the streamlines. Because of the concave curvature of the flow structure shown by the streamlines formed at the rim of cavity, the downstream vortex moves from x=342.1 to x=342.7 then x=343.2, with its core lifted from y=1.74 to y=1.96 and y=2.11, making the recirculation region thicker. This strong local distortion of the flow field and the resulting strong recirculation zones appear to cause the downstream movement of the reattachment point and the upstream movement of the separation point.

Figure 5.27 shows a blow-up of the flowfield around the interface of the cavity and the main flow from plot 5.26(c). It is clear that the cavity is always fully sealed by the vortex above. Moreover, the vortex tends to crowd into the cavity. This is the most obvious difference compared with ramp flow and ramp flow with a wide cavity. This concave structure makes the circulation region thicker compared with both the ramp flow and the ramp flow with a wide cavity. This thicker recirculation region pushes the

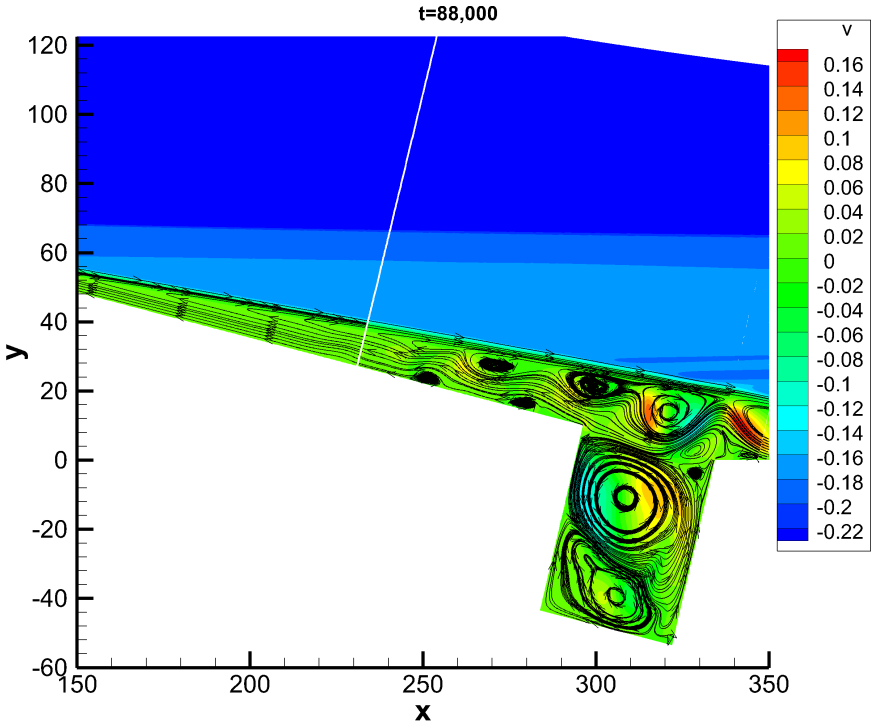

(a)

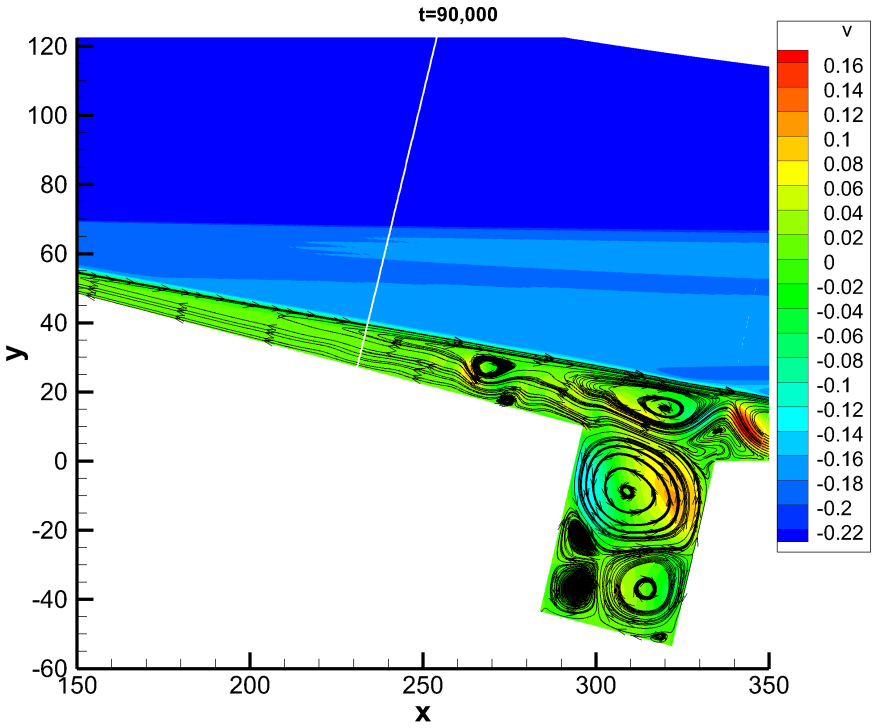

(b)

FIGURE 5.25: Contours of v-velocity near the corner at time: (a) $t = 88,000$, (b) $t = 90,000$ (M=5.3 case).

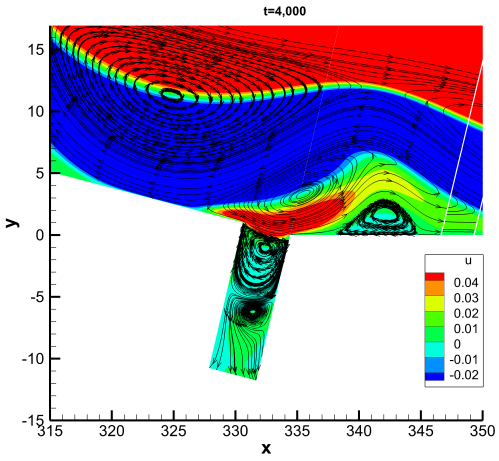

(a)

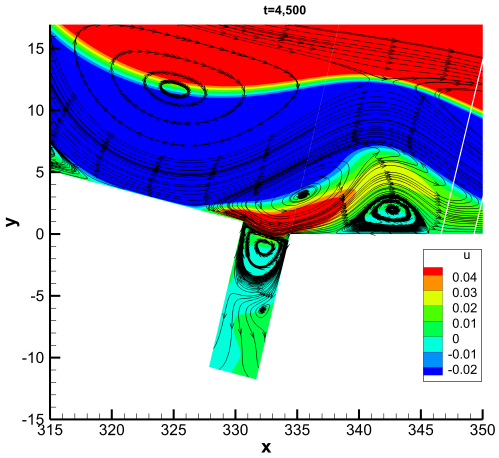

(b)

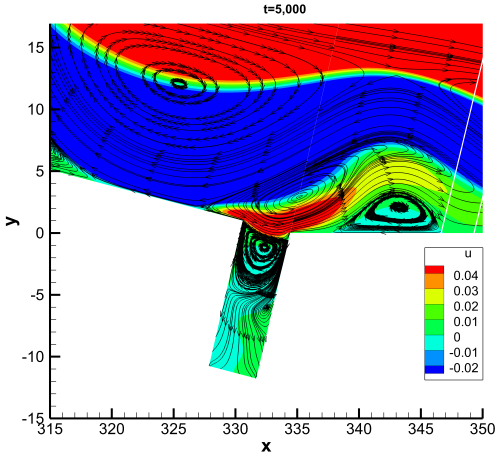

(c)

FIGURE 5.26: Contours of v-velocity near the ramp corner at time: (a) $t = 4,000$, (b) $t = 4,500$ (c) $t = 5,000$ (M=5.3 case).

separation both upstream and downstream. For the ramp flow, vortices cannot easily expand into the main flow, while for the ramp with a wide cavity flow, as we discovered before, the vortex in the main flow merged with the vortex in the cavity so that the flow in the cavity could exchange with the main flow, making the flow in the cavity cannot be depressed too much. As a conclusion, the existence of a vortex at the narrow cavity rim, sealing the whole cavity width and forming a concave structure, is the main reason for the extraordinary large separation length. Ramp flow with a narrow cavity leads to large separation region, while the wide cavity has little influence on the flow separation. This shows that the location and width of cavities are factors that cannot be neglected for aerodynamic design.

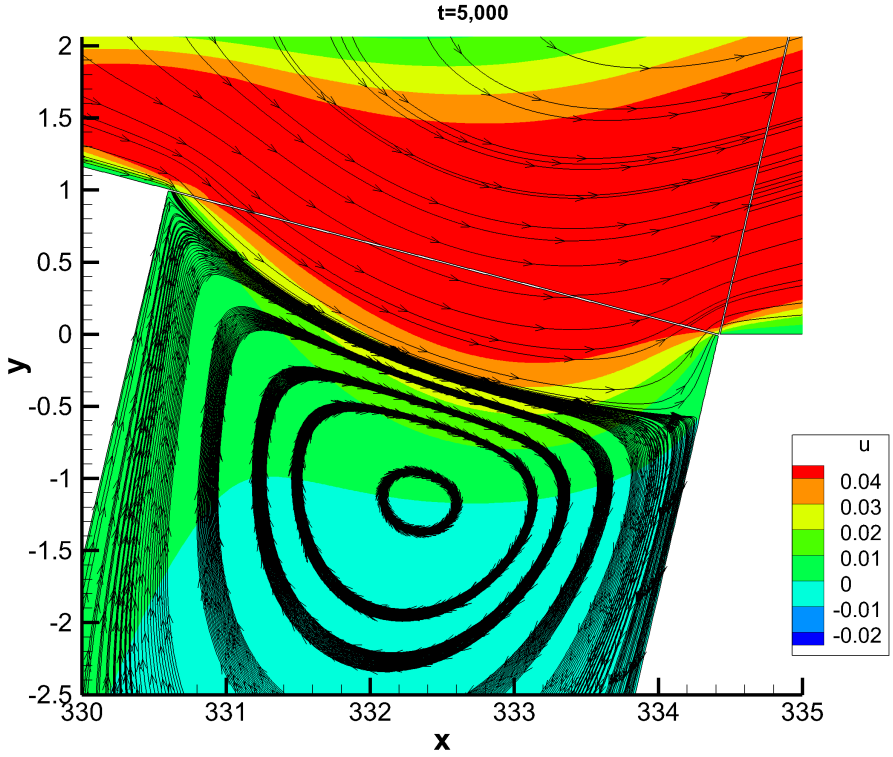

FIGURE 5.27: Partial zoomed-in of plot 5.26(c).

5.3.2 Further study of jet effect

Simulations with M_j=3.5 jets presented in this section are based on the mesh shown in figure 5.20(a). As seen in the previous chapter, a jet can greatly increase the extent of the separation zone for a ramp flow. Here we will first consider jets issued normal to the wall and then study the effect of jet orientation. Ramp flow is firstly run to get a converged flow. Then, the time is reset to t=0 and the simulations are continued with jets of different strengths switched on.

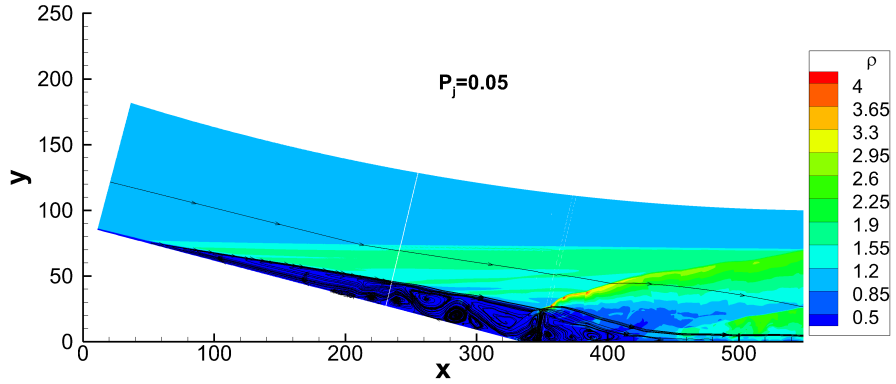

(a)

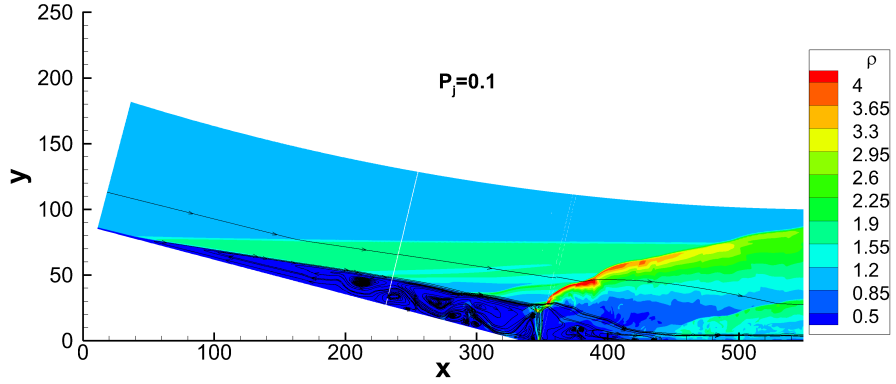

(b)

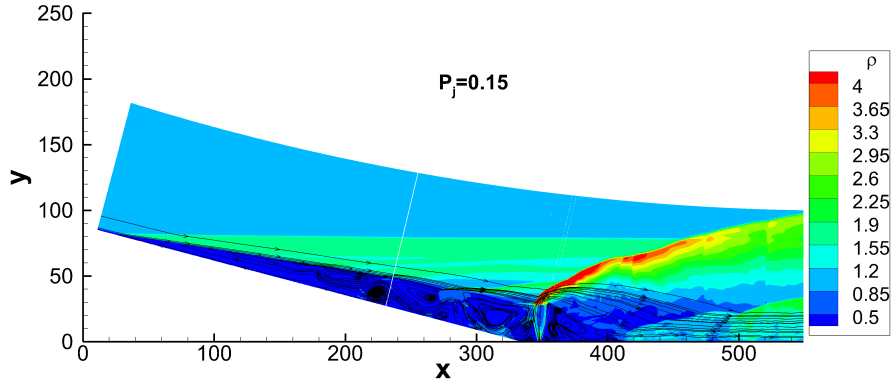

(c)

FIGURE 5.28: Ramp flow with wall-normal jets of different strengths: (a) $p_j = 0.05$, (b) $p_j = 0.1$, (c) $p_j = 0.15$ at $t = 900$ (M=5.3).

Figure 5.28 shows the ramp flowfields with different jet strengths at $t = 900$ after the jet is switched on. Three different jet strengths are compared, namely $p_j = 0.05$, $p_j = 0.1$ and $p_j = 0.15$. All the three jets here are injected normal to the wall. The flowfields are shown by the same contour levels of density and superposed by streamlines. Complex flowfields, with a series of recirculation zones and strong interactions between the jet and the separation bubble, are observed for all cases. Although all the flowfields are taken at the same time, it can be seen that ramp flow with $p_j = 0.15$ jet has the largest separation zone and the strongest bow shock formed by jet injection seen from the area of red contours. The location of the jet-induced shock at the outflow boundary is also the highest for the p_j=0.15 case. The ramp flow with p_j=0.05 jet has the smallest separation zone and the weakest bow shock. The location of the jet-induced shock at outflow boundary is also the lowest.

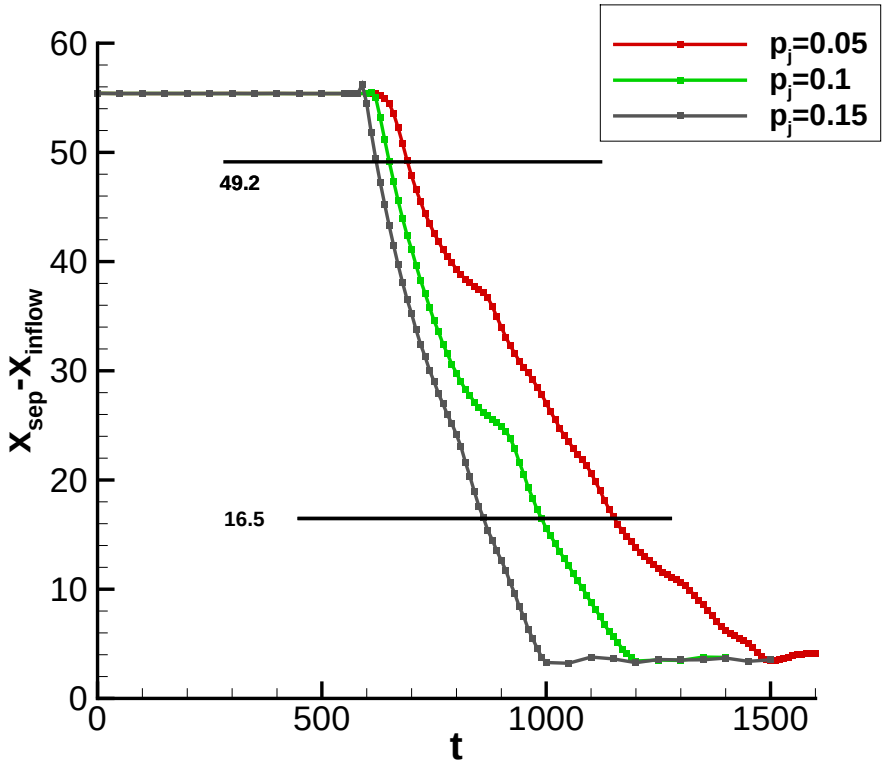

FIGURE 5.29: Flow separations for ramp flow with different jet strengths (M=5.3 case).

Figure 5.29 shows the upstream development of the separation point. It can be seen that the upstream separation point is stationary up to around t=600 (varies slightly for different jet strengths) before starting to move upstream. Flow separations reach the inflow boundary for all the tested jet strengths, but with an increase of p_j the movement of upstream separation point is more rapid. It is noticed that the rate at which the separation point moves upstream changes with time for all the cases, especially for the two lower p_j cases. The weaker of the jet strength, the greater of the variation of the

separation rate. This should be caused by the kick when the flow separation moves upstream.

As the separation points for flows with different jets all reach the inflow boundary, it is not possible to get converged statistical result. Here studies on skin friction and heat transfer distributions are based on a statistical collection over a short time period of 20 around the specified time instants. Flowfields with different jet strengths are compared at the time instants when they have the same upstream separation points 49.2 away from the domain inlet. The corresponding time instants are t =690 (p_j=0.05), t =650 (p_j=0.1) and t =620 (p_j=0.15). Further upstream after change of the rate at which the separation point moves upstream for different p_j, flowfields with same separation point 16.5 away from the inflow boundary are also studied, with the corresponding time instants of t =1,150 (p_j=0.05), t =990 (p_j=0.1) and t =860 (p_j=0.15).

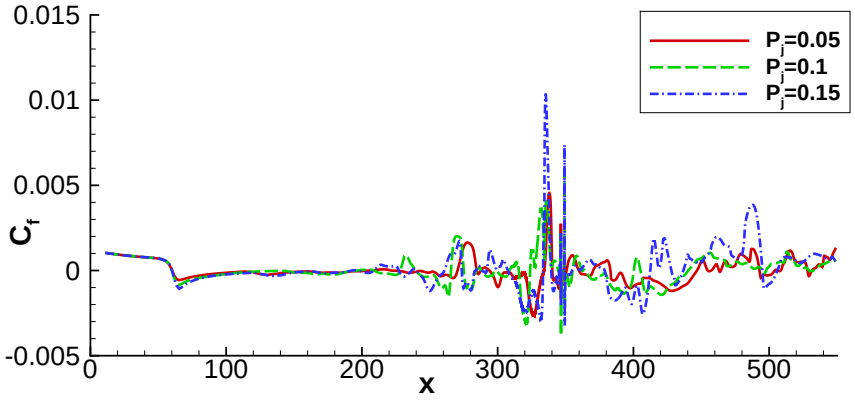

(a)

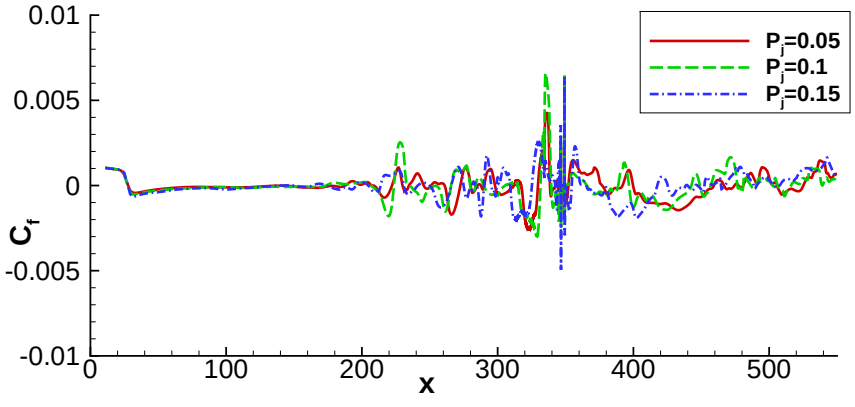

(b)

FIGURE 5.30: Skin friction coefficient distributions for flows with different jet strengths when the same upstream separation points are (a) 49.2 and (b) 16.5 away from the inflow boundary (M=5.3).

Figure 5.30 compares C_f for flows with different jet strengths when they have the same upstream separation points. In both frames, a steady upstream flow with a disturbed

downstream flow is observed for all the cases. Although with different jet strengths, the upstream C_f distributions accord with each other until secondary recirculation zone appears at x=200, making the flow more complex. Two distinct peaks are observed corresponding to the ramp corner at x =334.42 and the jet injection area (C_f here actually shows the gradient of u-velocity in the wall-normal direction at the jet exit). At the early stage, it is found that the amplitude of the C_f fluctuation increases when stronger jet (p_j=0.15) is applied. Amplitude of the peak for p_j=0.15 case is two times the amplitudes of both peaks for p_j=0.1 and p_j=0.05 cases. Later in the flow developments when the separation points move to 16.5 away from the inflow boundary, amplitude of C_f variation for p_j=0.15 is reduced especially obvious at ramp corner and downstream at x=490. For both p_j=0.05 and 0.1 cases, not much difference appears between C_f distributions corresponding to the separation points 49.2 and 16.5 away from the inflow boundary. This shows that the strong C_f variation appeared at early stage becomes weak in the later stage, while nearly no change appears on other distributions of C_f with weak variations.

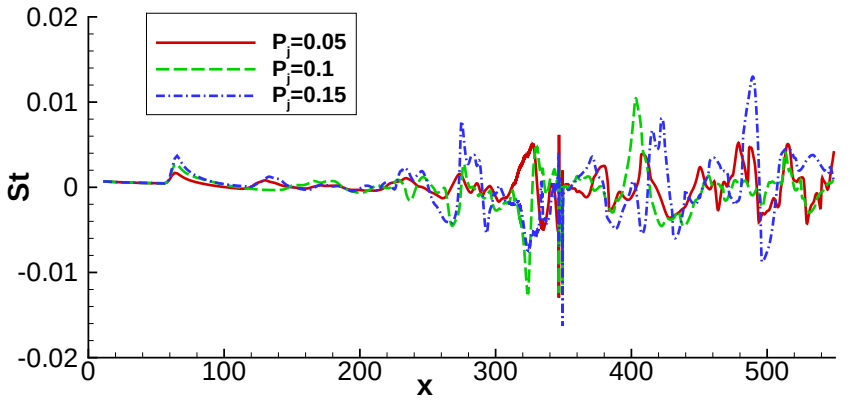

(a)

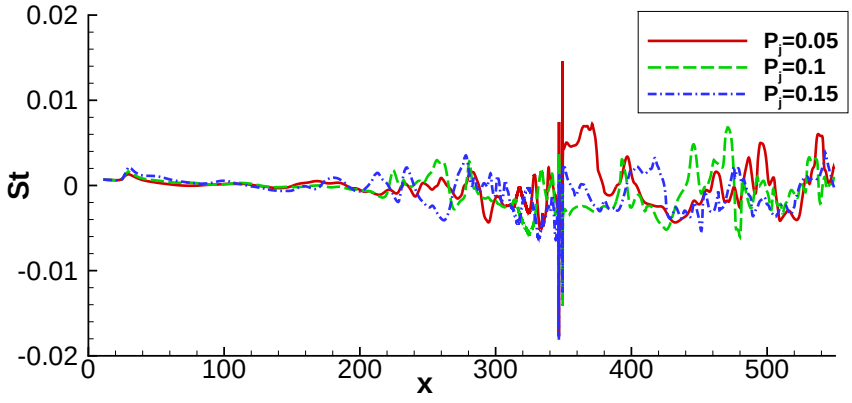

(b)

FIGURE 5.31: Heat transfer comparisons between flows with different jet strengths when the same upstream separation points are (a) 49.2 and (b) 16.5 away from the inflow boundary (M=5.3).

A Stanton number is a parameter charactering the heat transfer and is defined as (Bedarev et al., 2002)

$$St = \frac{q_w^*}{\rho_e^* u_e^* C_p^* (T_r^* - T_w^*)}, \tag{5.1}$$

where $q_w = -k^*(\partial T^*/\partial y^*)_w$ is the heat flux at the wall, ρ_e^* and u_e^* are density and velocity in the potential flow and C_p^* is the specific heat capacity of the gas at constant pressure. The recovery temperature T_r^* is obtained from a laminar flow assumption, $T_r^* = (1 + \frac{\gamma-1}{2} Pr^{1/2} M^2) T_\infty$.

Figure 5.31 shows the Stanton number distributions at the two separation positions discussed earlier. At the earlier stage when the separation point is at 49.2 away from the inflow boundary, cases with strong jet strengths (p_j=0.1 and p_j=0.15) correspond to higher amplitudes of St variation, while in the late stage when the separation point moves to 16.5 downstream the inflow boundary, amplitudes of St peaks are reduced. A high heat transfer region is observed just downstream of the jet injection for the case with the weakest jet. This region is formed by the interaction between different vortices. Figure 5.32 shows temperature field superposed by streamlines. The high Stanton number region found in figure 5.31(b) corresponds to the high temperature area caused by the flow hitting the wall around x=360. As a conclusion, flowfield both upstream and downstream of the ramp and jet is influenced by the increase of the jet strength. The amplitudes of C_f and St variations are increased when stronger jet is applied. However, after the changes of the rate at which the separation point moves upstream, the high amplitudes of C_f and St variations seem to be reduced.

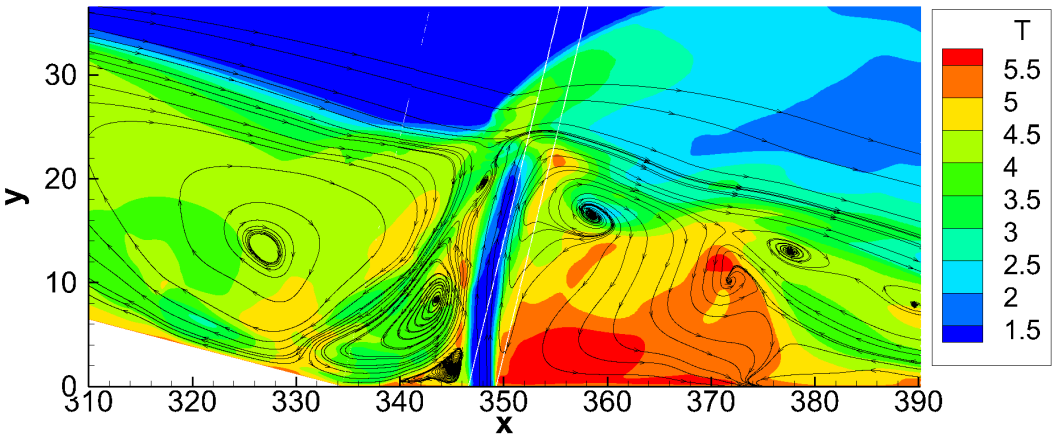

FIGURE 5.32: Temperature field around the ramp corner and the jet for the $p_j = 0.05$ case at t =1,150 (M=5.3 case).

To evaluate the effect of jet injection orientation, another case with jet injection of $p_j = 0.1$ is studied. In this case the jet is injected at 11.41° to the freestream parallel to the wall upstream the ramp corner, equivalent to 26.16° to the x-axis ($\alpha_0 = 26.16°$) which comes from the wind tunnel model shown in figure 5.18. Figure 5.33 shows the

flowfield with contours of density, superposed by streamlines. Although the time run here is short (t=700), the separation bubble is larger than that of all the ramp flow cases with a normal jet at $t = 900$, showing that the separation point moves upstream at a higher rate at which the separation point moves upstream. The bow shock here appears further upstream around x=320 compared with $x = 350$ for normal jet injection.

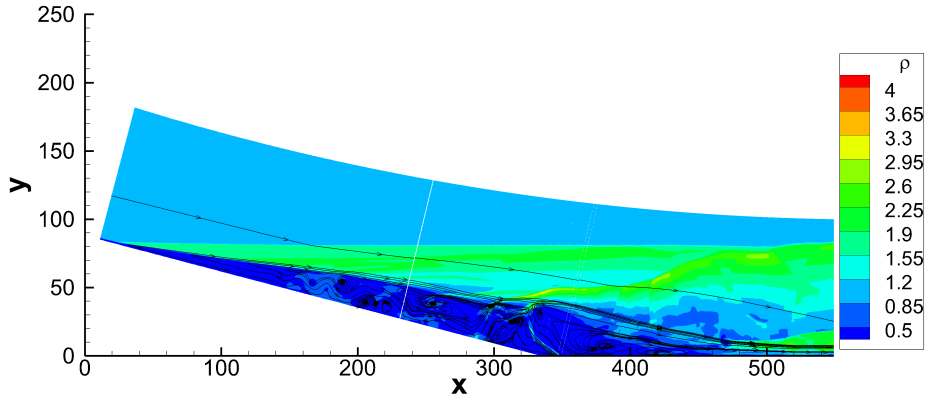

FIGURE 5.33: Ramp flow with $p_j = 0.1$ jet facing upstream ($\alpha_0 = 26.16°$) at $t = 700$ (M=5.3 case).

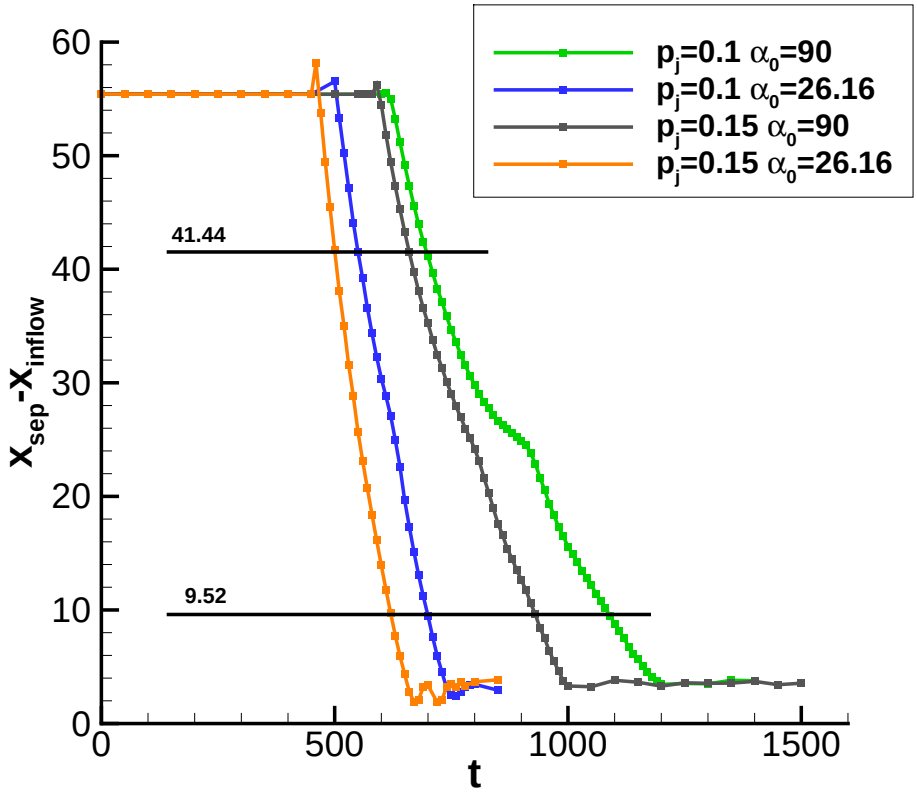

FIGURE 5.34: Development of flow separations with different jet strengths and injection angles (M=5.3 case).

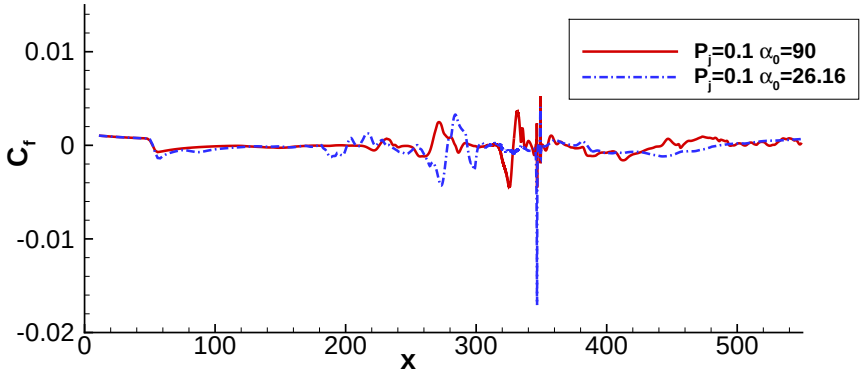

(a)

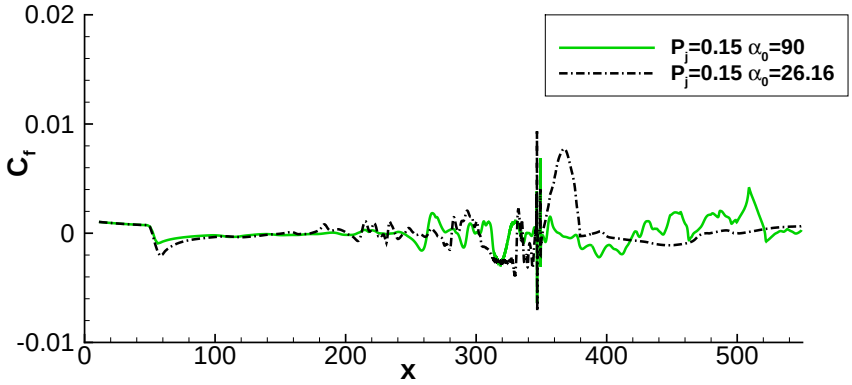

(b)

FIGURE 5.35: Skin friction coefficient distributions for flows with different jet orientations and strengths of (a) 0.1 (b) 0.15 when the same upstream separation points are at $x_{\text{sep}} - x_{\text{inflow}}$=41.44 ($M$=5.3).

Figure 5.34 shows the development of upstream separation point in time for jet cases with same strengths of 0.1 and 0.15 but different injection angles, $\alpha_0 = 90°$ and $\alpha_0 = 26.16°$. At t=0 different jets are added to the converged flow. It can be seen that the separation points start to move upstream earlier for the inclined jet cases. By dividing the whole distance of the separation movement with the time interval spent, approximate average rates of upstream movement of the separation point are obtained as shown in table 5.3. By comparing upstream movement rate of flow separation, it is found that when the jet is pointed upstream, the flow separation spreads upstream more than two times faster for both jet strengths than using the wall-normal pointing jets. It is also noticed that the faster the separations spread upstream (the orange and blue curves), the higher the peaks appear for the curves before they start to decline (i.e. flow separation start to move upstream), which corresponds to the cases with upstream inclined jets.

Based on skin friction and Stanton number distributions, flowfields for cases with different jets but the same upstream separation points 41.44 and 9.52 downstream the inflow

Jet strength (p_j)	Inclined angle (α_0)	Movement rate of separation
0.05	90	0.061
0.1	26.16	0.222
	90	0.088
0.15	26.16	0.278
	90	0.127

TABLE 5.3: Rates of the separation point moves upstream for different jet strengths and injection angels.

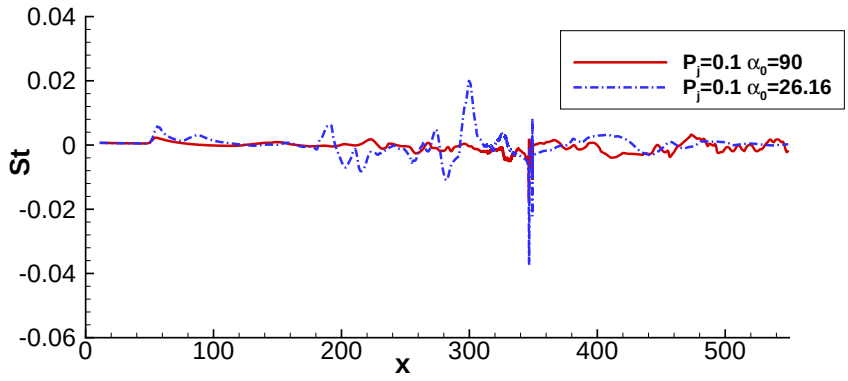

(a)

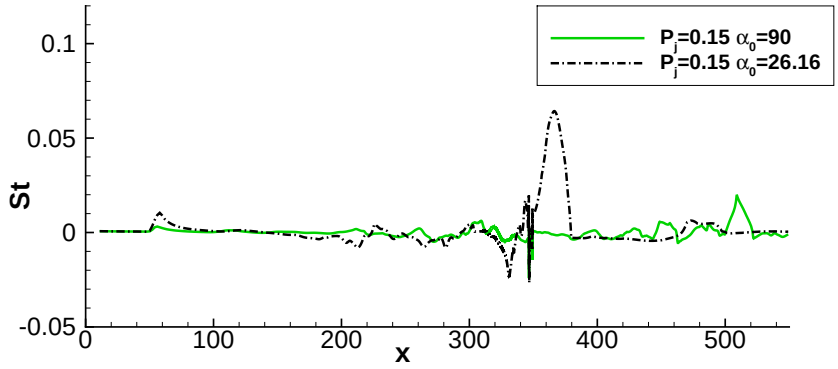

(b)

FIGURE 5.36: Heat transfer comparisons between flows with different jet orientations and strengths of (a) 0.1 (b) 0.15 when the same upstream separation points are at $x_{\text{sep}} - x_{\text{inflow}}$=41.44 ($M$=5.3).

boundary are used to evaluate effects of the jet injection orientation. The two separation lengths locate in regions of different rates at which the separation points move upstream. Figure 5.35 and figure 5.36 show C_f and St distributions for p_j=0.1 and 0.15 with different orientations, when the separation points are at $x_{\text{sep}} - x_{\text{inflow}}$=41.44. The difference between inclined/normal jets is mainly observed upstream of the jet injection for p_j=0.1 cases (case with inclined jet shows stronger heat transfer peaks), while for the p_j=0.15 cases the difference is obviously seen downstream close to the jet. A peak at about x=370 is observed for the case with inclined jet in both C_f and St distributions.

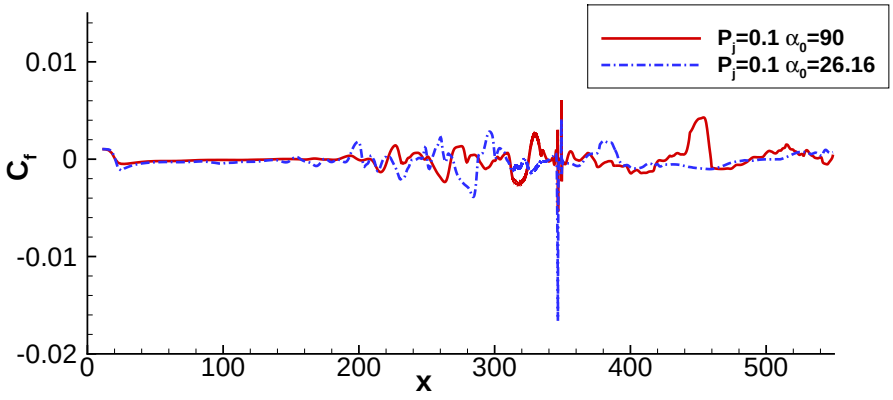

(a)

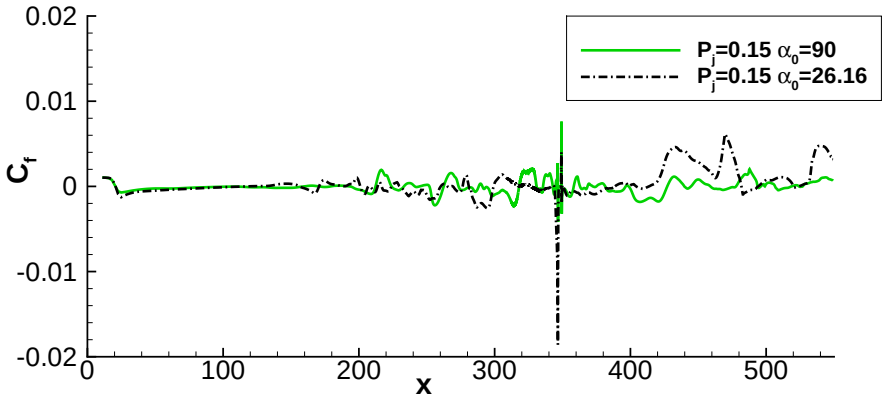

(b)

FIGURE 5.37: Skin friction coefficient distributions for flows with different jet orientations and strengths of (a) 0.1 (b) 0.15 when the same upstream separation points are at $x_{\text{sep}} - x_{\text{inflow}}$=9.52 ($M$=5.3).

Distributions of both C_f and St are shown in figure 5.37 and figure 5.38 respectively, when the upstream separation point is at $x_{\text{sep}} - x_{\text{inflow}}$=9.52 . It is noticed that the most obvious differences for both C_f and St are located downstream of the jet, which is different to the flowfield when the separation point is at $x_{\text{sep}} - x_{\text{inflow}}$=41.44. For flows with separation points at x=41.44, an inclined jet generates stronger C_f and St variations than a normal jet. The peak value of St which is about 0.07 for the case with p_j=0.15 and upstream inclined jet as shown in figure 5.36(b) disappears, and effect of inclined jet becomes hard to recognize after the change of the rate at which the separation point moves upstream.

All the comparisons on C_f and St done above show that after the changes of the rate at which the separation point moves upstream, the highest amplitudes of C_f and St variations (corresponding to the flow with the strongest jet) are reduced. The effect of inducing strong variations of C_f and St for a inclined jet becomes obscure after the change of the rate at which the separation point moves upstream.

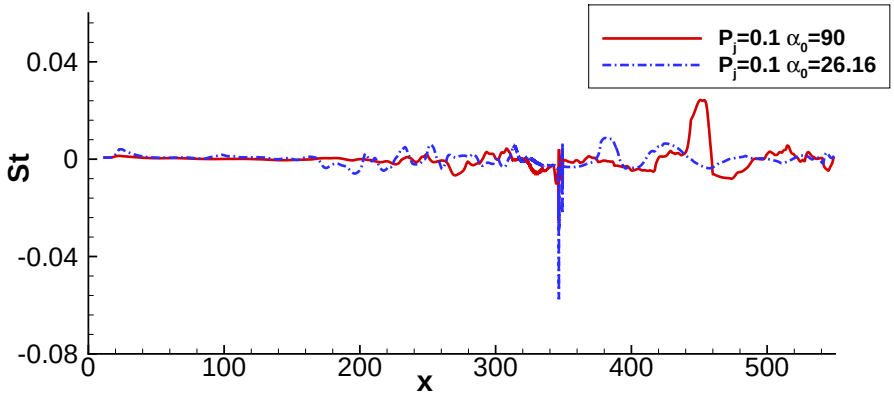

(a)

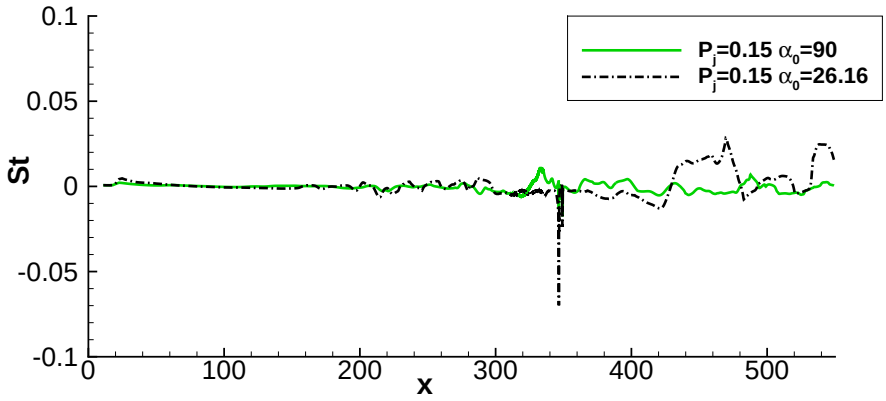

(b)

FIGURE 5.38: Heat transfer comparisons between flows with different jet orientations and strengths of (a) 0.1 (b) 0.15 when the same upstream separation points are at $x_{\text{sep}} - x_{\text{inflow}}$=9.52 ($M$=5.3).

5.4 Summary

Based on the study in this chapter, it is discovered that for the jet strengths and flow conditions used for the wind tunnel model of rocket stage separation, the action of the jets is to completely separate the upstream flow, in a very short timescale (for example a time of 400 in the simulation for the separation to move to the inflow boundary would correspond to 0.6 ms in the experiment). The rate of upstream motion increases when the jets are pointed upstream or when a stronger jet is applied. An anomalously large upstream separation is found for the narrow cavity case due to the local flowfield distortion near the cavity. The L/D=0.7 cavity studied here, does not influence the separation of the ramp flow except for an increase in the flow unsteadiness. All the cases with jet injection studied have separation developed to the inflow for the laminar boundary layer. It is possible that some experimental cases are transitional or turbulent,

hence in the next chapter we attempt to repeat a ramp and jet simulation for fully three-dimensional flow, where transition to turbulence is captured within the computational domain.

Chapter 6

Three-dimensional study of supersonic ramp flow with jet

6.1 Introduction

This chapter is a continuation of the third part of Chapter 5, where simplified rocket configurations with slot jets and cavities were studied in two dimensions. The case is further investigated here for 3D flow. Results from these 2D simulations showed that a ramp flow with a wide cavity would be similar to a ramp flow. Hence the cavity is not included in the current study. A 3D ramp flow is firstly studied with disturbances applied at the inflow to trigger transition to turbulence. After the flowfield is fully developed, slot jet is turned on to study the rate of upstream movement of separation, for comparison with the laminar cases presented in Chapter 5.

6.2 Simulation setup

To simplify the problem, a flat plate with a ramp corner and no cavity is adopted here. One sixth of the rocket circumference across the retro-jet centre at $x = 353.38$ is used as the spanwise length ($L_z = 24.8$). The same simulation Reynolds number of $6,000$ as used for 2D cases is used, which means the inflow boundary of the computational domain is located 48.6 mm downstream of the rocket tip. The inflow Mach number is 5.3 with a Mach 3.6 jet injection. The rocket front stage is again simplified to a flat plate for comparison purposes. A larger computational domain is used here compared with that used in the 2D study of Chapter 5. The length of the downstream domain after the corner is extended from 216 to 416, with the same ramp corner located at $x = 334.42$. The height of the computational domain is extended from 100 to 150 to allow flowfield

development. As in the previous cases, geometrical units are non-dimensionalized by the inflow boundary layer displacement thickness.

The slot jet is injected from $x = 351.92$ to $x = 354.84$ across the span downstream of the ramp corner. It is noted that the slot width and jet injection location are slightly different from the 2D rocket case (based on an updated experimental configuration), as shown in table 6.1. The slot width here is 2.92 (3.7 mm in dimensional form) while that used in 2D rocket study is 2.6 (3.25 mm in dimensional form). The square jet is injected from $x = 351.92$ to $x = 354.84$ and from $z = 10.95$ to $z = 13.85$ in the spanwise direction.

Parameter	2D setup	3D setup
Slot width (mm)	3.25	3.7
Slot jet area	[346.7, 349.3]	[351.92, 354.84]
δ for jet profile	0.2	0.2
p_j	0.05, 0.1, 0.15	0.15
J_p	1.16, 2.33, 3.49	3.87
Jet injection direction	90°, 26.16°	26.16°

TABLE 6.1: Differences between 2D and 3D jet setups for a rocket.

The same freestream conditions as introduced in Chapter 5 are applied here. The freestream Mach number is 5.3. The static temperature of 58.9 K is used as the reference temperature. The wall temperature is set to room temperature at 298 K. Mach 3.6 air with a stagnation temperature of 290 K is injected facing upstream through the slot or square jet inclined at 26.16° to the first stage (or horizontal direction) or normal to the wall.

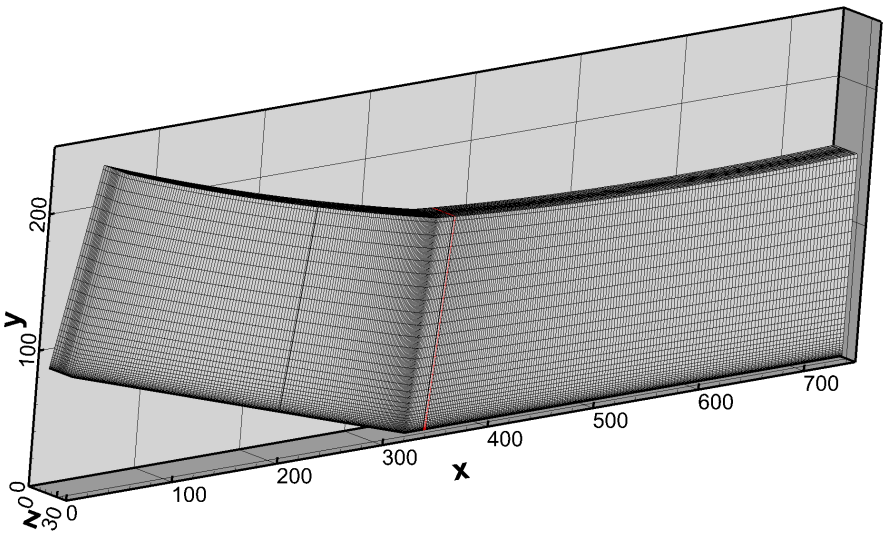

FIGURE 6.1: Three dimensional mesh for the rocket configuration.

The 3D mesh here has grid points $N_x \times N_y \times N_z$=5061 × 450 × 170, giving a total of 387 million grid points. Figure 6.1 shows the 3D mesh setup. The mesh is stretched

in the streamwise, wall-normal and spanwise directions to resolve upstream transition, flow around the corner and the downstream square jet injection. The slot jet injection area is shown in red in figure 6.1.

For the benefit of future work with a square jet injection, a non-uniform gird distribution is used in the spanwise direction. The spanwise mesh in the centre of the span from $z = 10.95$ to z =13.85 is uniform with a fine resolution of Δz=0.1, while on both sides of this area it is stretched in the z-direction with spatial spacing changing smoothly from 0.1 in the centre area to 0.2 at the spanwise edge. The distribution of derivatives of z-coordinate in the stretched area is expressed as

$$\Delta z = 0.05 \tanh(\frac{-15 + k \times \frac{30}{N_z^*}}{2}) + 0.15, \tag{6.1}$$

where k is the spanwise uniform coordinate used in computational domain ($k \in [-1, N_z^* + 2]$ in the stretched region). N_z^* is half of the total stretched spanwise grid number. A hyperbolic tangent function is used here to generate a smooth connection between the uniform mesh in the central region and the spanwise boundary regions as plotted in figure 6.2.

As seen on figure 6.2(a), to resolve a possible square jet flow, the spanwise mesh has a finer uniform mesh across the central area. The mesh near both boundaries in $z-$direction is coarser but uniform. First derivatives of the coarse mesh at both boundaries are set to be the same to allow the periodic boundary condition to be applied at the spanwise boundaries. The second derivative, as shown in figure 6.2(b) is also smooth, with enough grid points distributed in the relatively intense variation area.

The topology of the 3D mesh according to the geometry and jet setup is introduced here as shown in figure 6.3. The 3D computational domain is divided into seven blocks based on the streamwise and spanwise mesh. There is no block-division in the wall-normal direction. Two blocks (Block 1 and Block 2) are distributed upstream of the ramp corner. Three blocks (Block 4, 6,and 7) are used for slot jet injection across the span, while only Block 6 would be used for a possible square jet injection. Block 3 is located between the slot jet region and ramp corner, while Block 5 is downstream of the jet to cover the recovery zone.

Periodic boundary conditions are applied on each side of spanwise boundaries for Block 1, 2, 3 and 5. An interface boundary condition is applied on the streamwise boundaries between the neighbouring blocks and also on the spanwise boundaries of Block 4, 6 and 7. A non-slip isothermal wall condition is applied at the bottom surface of the mesh except for Blocks 4, 6 and 7 for the slot jet (or only Block 6 for the square jet), where an integral characteristic boundary condition is applied. The integral characteristic boundary condition is also applied on the upper surface for all the seven blocks. Extrapolation

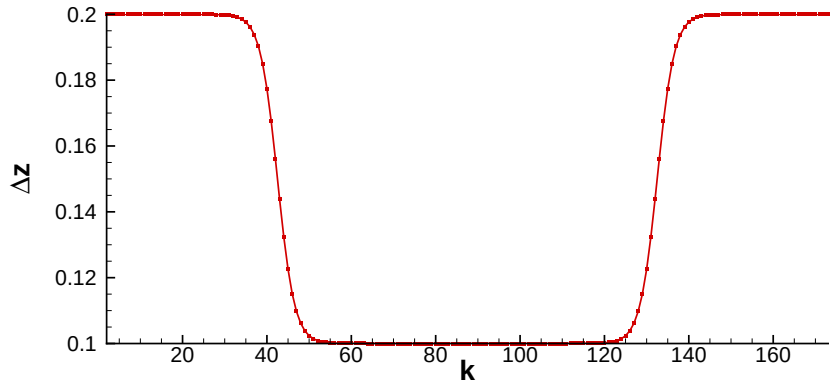

(a)

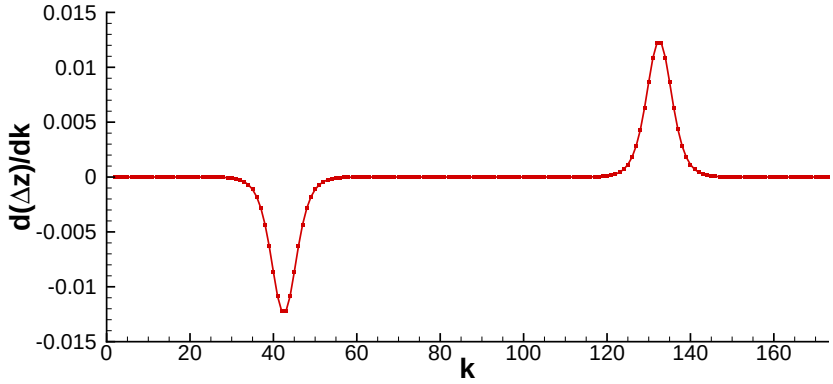

(b)

FIGURE 6.2: (a) First and (b) second derivatives of z-coordinate for spanwise grids.

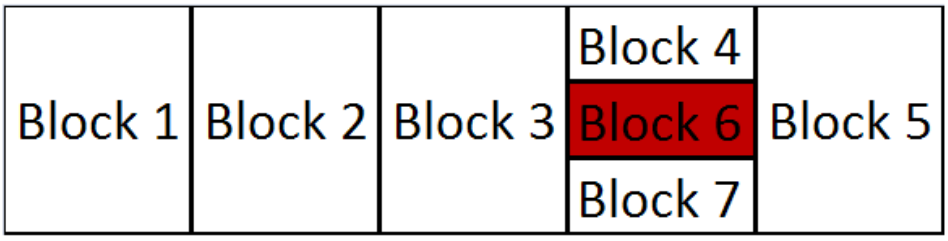

FIGURE 6.3: Block division of the mesh in the streamwise and spanwise direction.

inflow and characteristic outflow boundary conditions are applied at Block 1 and Block 5, respectively.

Streaks are added at the inflow to the flowfield initialized by the laminar similarity flow. They are introduced by adding fluctuations to velocities at different wall normal positions as given by equation (2.38) to equation (2.40) with coefficients C=0.5, d=1.0 and ω=0.2. The wavenumber N is set to be 7, corresponding to the most unstable mode after test. The added velocity components are plotted in figure 6.4. As we can see, the

u'-velocity is zero, while the peak of the v'-velocity is at y=1. This prescription follows the typical lift-up mechanism whereby streamwise vortices rapidly generate low-speed streaks, which at high-enough amplitude are susceptible to instability and subsequently breakdown to turbulence. To prevent a simple repetition of this disturbance periodically across the span, the w-velocity component is modified by adding a z-dependence as described in Chapter 2. The time step used here is Δt=0.004, however it is reduced to Δt=0.0005 after the jet is switched on.

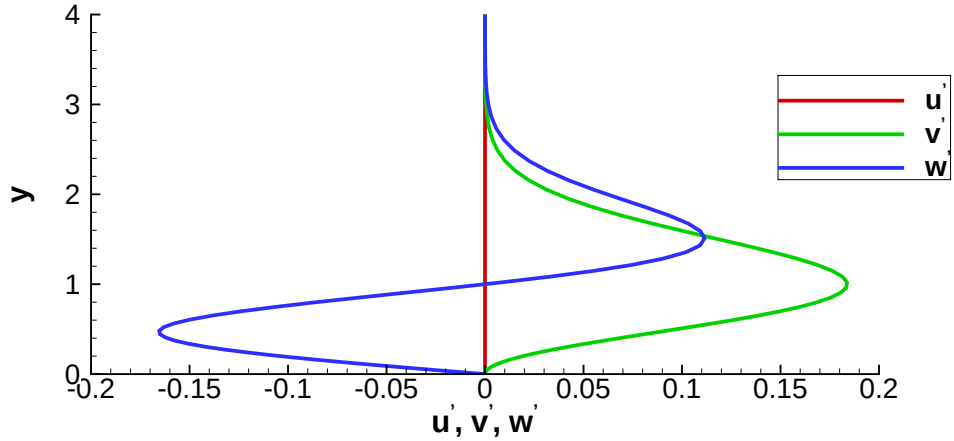

FIGURE 6.4: Velocity added at the inflow boundary.

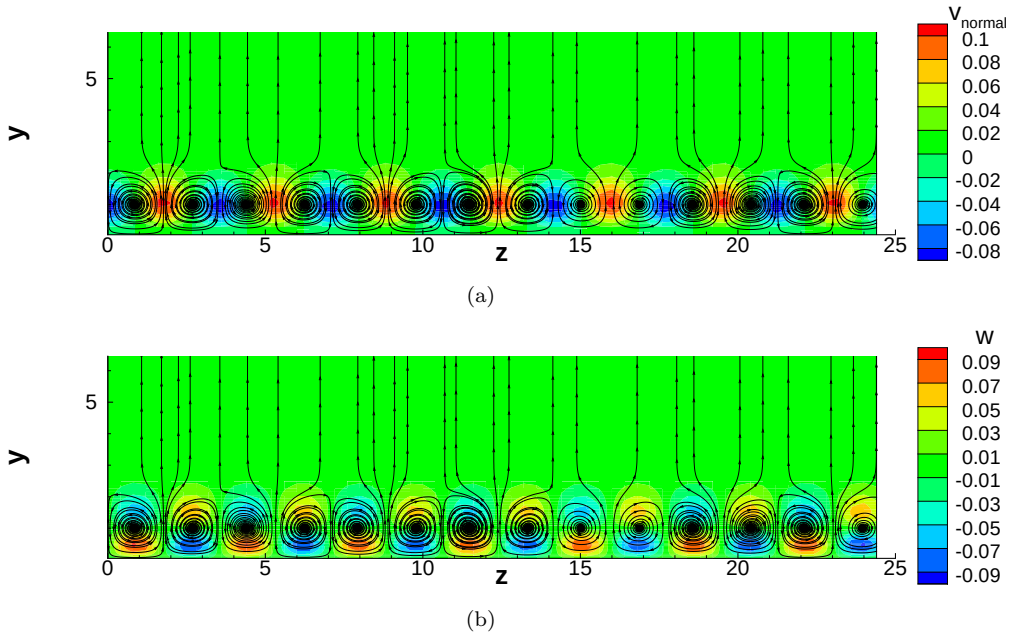

(a)

(b)

FIGURE 6.5: Velocity normal to the upstream wall and w-velocity contours at inflow boundary superposed by streamlines.

Since in the current simulations the upstream wall is not horizontal, the streamwise and wall-normal velocities based on the corresponding flat plate need to be rotated to make the inflow still parallel to the upstream wall. The streaks added based on a flat plate also need to be rotated to make it work for current simulations with inclined upstream

wall. Contours of the velocity normal to the inclined wall, $v_{normal} = v\cos\theta + u\sin\theta$, which is different to the v-velocity, and the w-velocity added at the inflow boundary are shown in figure 6.5 superposed with streamlines. Clear counter-rotating vortices are observed. Seven periods are quite clearly seen for both the wall-normal velocity and spanwise velocity (The additional w-velocity that breaks the periodicity is at low amplitude and not easy to observe in this figure).

6.3 Flat plate transition process

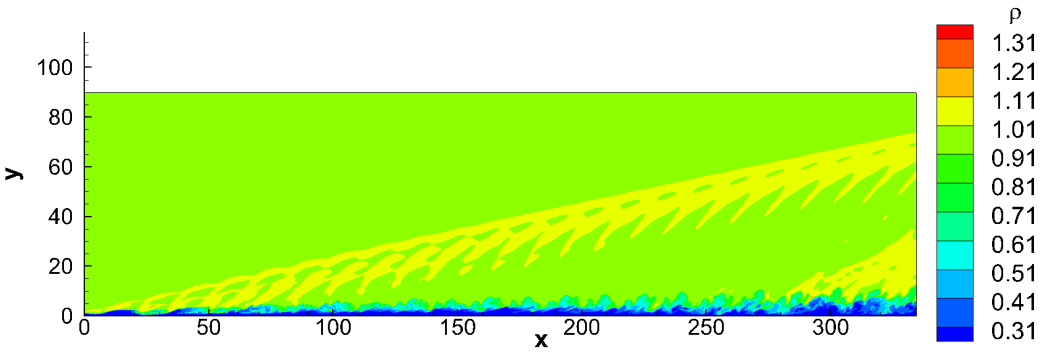

FIGURE 6.6: Slice of flat-plate flowfield at $z = 20$ contoured by density.

In spite of the inclined wall and the rotations for velocity and added streaks, a flat plate case for validation is first run. This case employs the same flat plate as used in the main simulation before the ramp corner. Same mesh resolutions are used here in all the three directions. Figure 6.6 shows the flowfield of the flat plate on an $x - y$ slice contoured by density. It is clear seen that the flow becomes unsteady and irregular as the flowfield develops further downstream. Turbulent-like structures are observed downstream, especially after x=300. The added perturbations are not divergence-free, therefore also generate sound waves as illustrated by the yellow regions developing from the inflow boundary close to the wall in the plot.

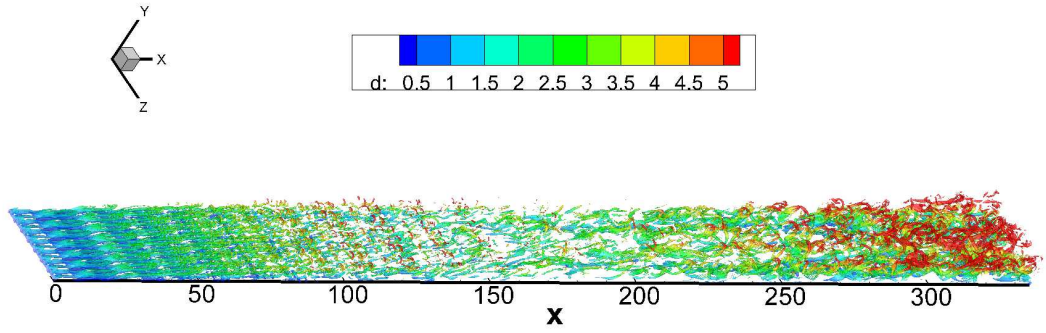

FIGURE 6.7: Iso-surfaces of Q=0.05 contoured by distance to the nearest wall.

To study the 3D flowfield, iso-surfaces of the second invariant Q coloured by distance to the wall are shown in figure 6.7. Seven periodic waves are clearly seen at the inflow as well as in the upstream flow until x=150. Worm-like structures are observed downstream of x=200 after the development of the artificially-added streaks at the inflow boundary.

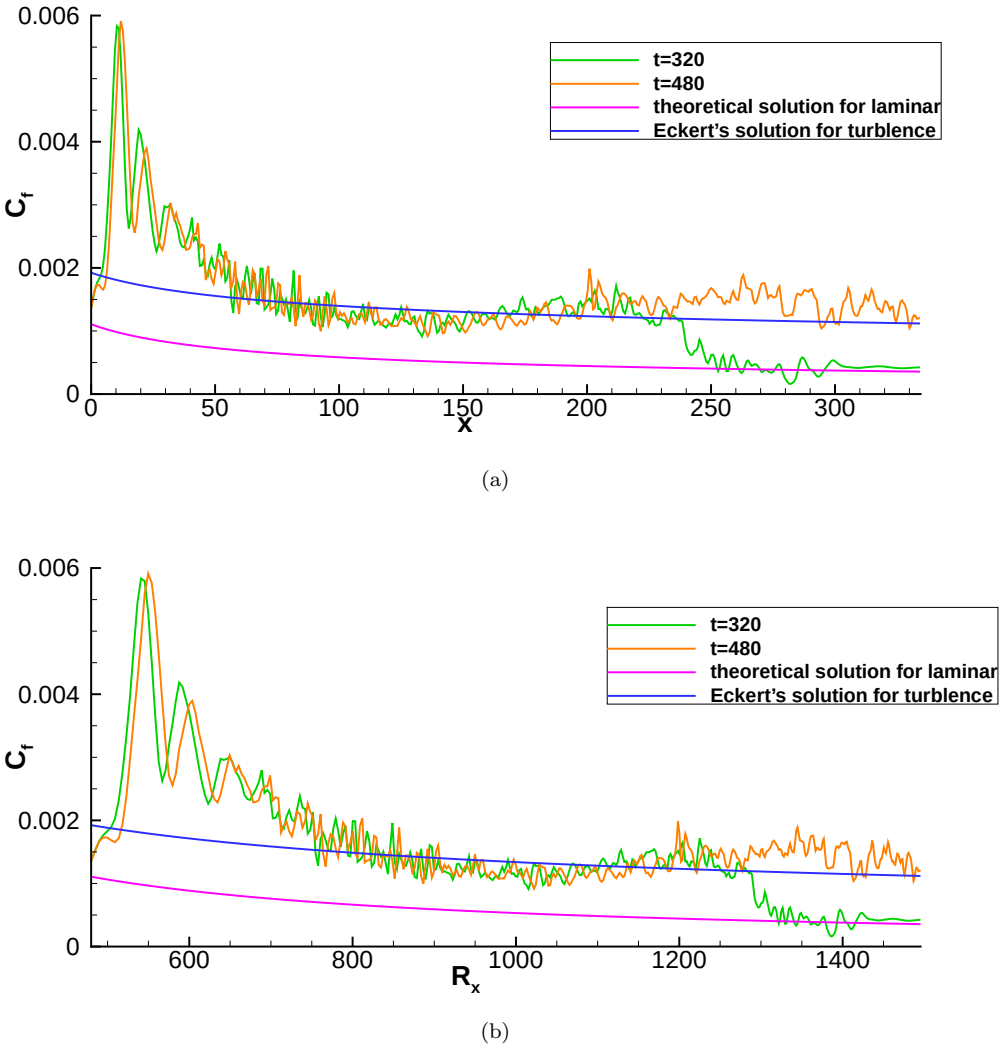

FIGURE 6.8: Spanwise averaged skin friction comparisons with theoretical results at different time with different x-axis: (a) x, (b) R_x.

Spanwise-averaged skin friction coefficient for the flat plate flow at different time instants are compared with the laminar theoretical solution defined in equation (2.48) and the turbulence correlation from Eckert (1955) defined in equation (2.51) in figure 6.8(a). Because of the streaks added at the inflow boundary, there are jumps for the calculated C_f compared with laminar theoretical solution and the turbulence correlation from Eckert (1955). For potential comparison with experiments, the same data are also plotted against R_x in figure 6.8(b). The definition of R_x used in 2D ramp flow validation in Chapter 4 is used here ($R_x = \sqrt{Re_{x^*}}$). Taking figure 6.8(a) as an example, it is obvious that at $t = 320$ the turbulence has not reached downstream of $x = 250$, where the skin

friction coefficient still follows the laminar skin friction curve. At $t = 480$, the whole flowfield is turbulent with transition happening quite early, before $x = 80$. An overshoot of the skin friction distribution is observed at $t = 480$ and x >200. This kind of overshoot was also observed by Franko and Lele (2013), and could be caused by the higher levels of fluctuations in the immediate post-transitioned boundary layer, compared to the equilibrium turbulent boundary layer that would develop further downstream.

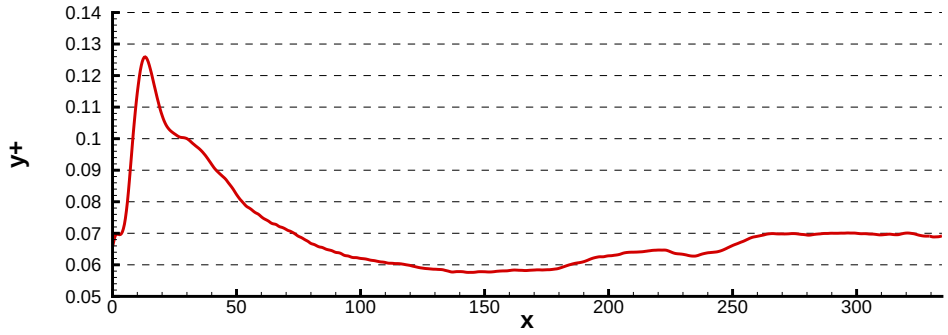

FIGURE 6.9: Distribution of spanwise averaged y^+ based on the mean velocity, temperature and density for the flat plate flow.

With the non-dimensional scheme used in the thesis, the non-dimensional quantity, y^+ can be calculated by

$$y^+ = \frac{\rho y \sqrt{\frac{C_f}{2\rho_w}}}{\mu} Re, \tag{6.2}$$

where the non-dimensional local dynamic viscosity μ can be obtained from Sutherland's law

$$\mu = T^{\frac{3}{2}} \frac{1 + S/T}{T + S/T}, \tag{6.3}$$

where S is the Sutherland temperature and T is the non-dimensional temperature.

The corresponding y^+ (i.e. y^+ at the first grid point away from the wall) is shown in figure 6.9. The peak value of y^+ of about 0.126 is located at $x = 13$ (corresponding maximum x^+ and z^+ are less than 2.5), as shown in the figure which is well below the value of 1 that is normally expected in DNS, hence the flat plate is significantly over resolved. However this is necessary as this grid will be used later for the ramp flow study, it will ensure that the flow around the ramp and further downstream in the separated region is properly resolved.

Figure 6.10 shows the distribution of the spanwise averaged TKE at t=480. The y-axis is scaled to have a much clearer view of the distribution of TKE. The large TKE area is mainly located upstream near the inflow boundary and downstream after x=150. The upstream large value is caused by the artificially added streaks with organised structures seen in the region from x=50 to x=150, which is also caused by the artificial streaks added. These transitional structures disappear further downstream.

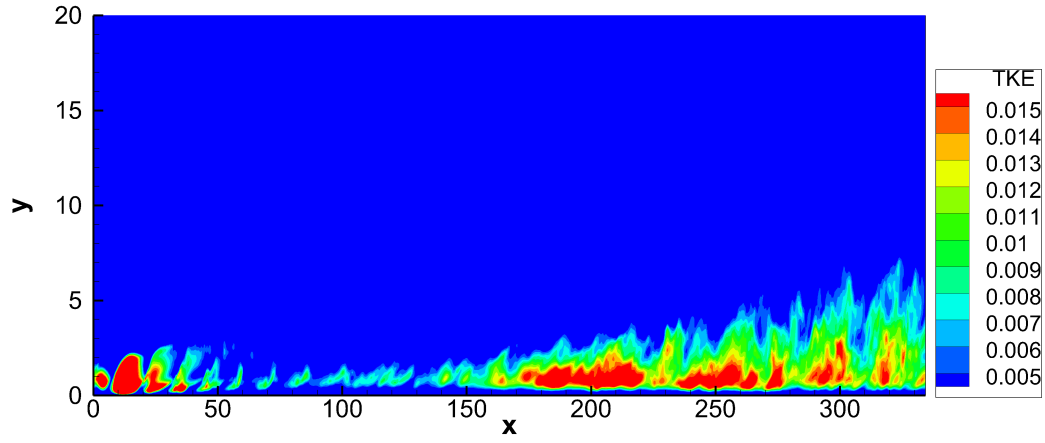

FIGURE 6.10: TKE of the flat plate corresponding to the second stage at t=480.

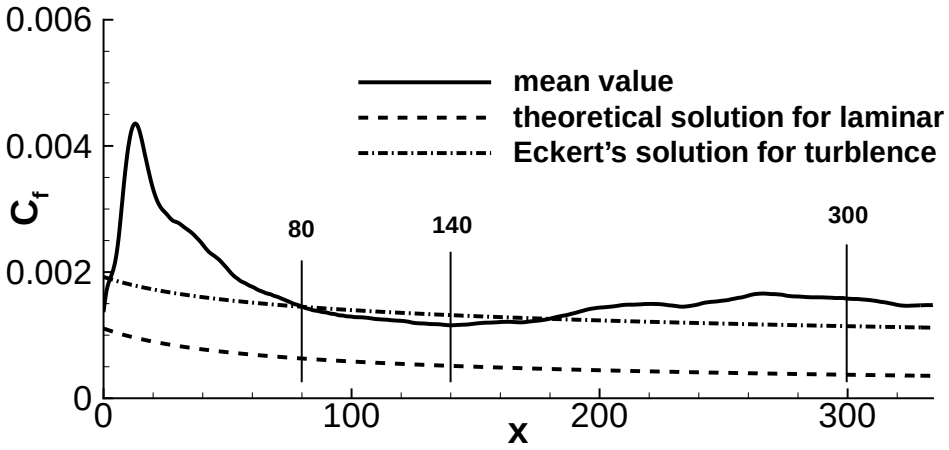

FIGURE 6.11: Distributions of spanwise-averaged mean skin friction collected in a time length of 120.

Statistics are accumulated based on a time length of 120 from t=1,000 to t=1,120 after about 3 throughflow times to clear the transient behaviour. The skin friction is plotted in figure 6.11 together with the laminar theoretical solution and the turbulence correlation from Eckert (1955). The mean skin friction coefficient is observed 33% larger than the reference value from Eckert (1955), indicating that the flow has not reached equilibrium after transition. Flows at three streamwise locations, x=80, x=140 and x=300, as plotted in figure 6.11, corresponding to different relations between the obtained mean C_f and the reference values, are studied.

Figure 6.12 shows the mean streamwise velocity distributions near the wall at the three locations marked in figure 6.11. At x=80 the skin friction recovers to the turbulent boundary layer value given by Eckert's solution, but the velocity profile has irregular variations, suggesting the flow is still severely affected by the artificial streaks added at the inflow. The non-dimensional boundary layer profiles in inner scale are plotted

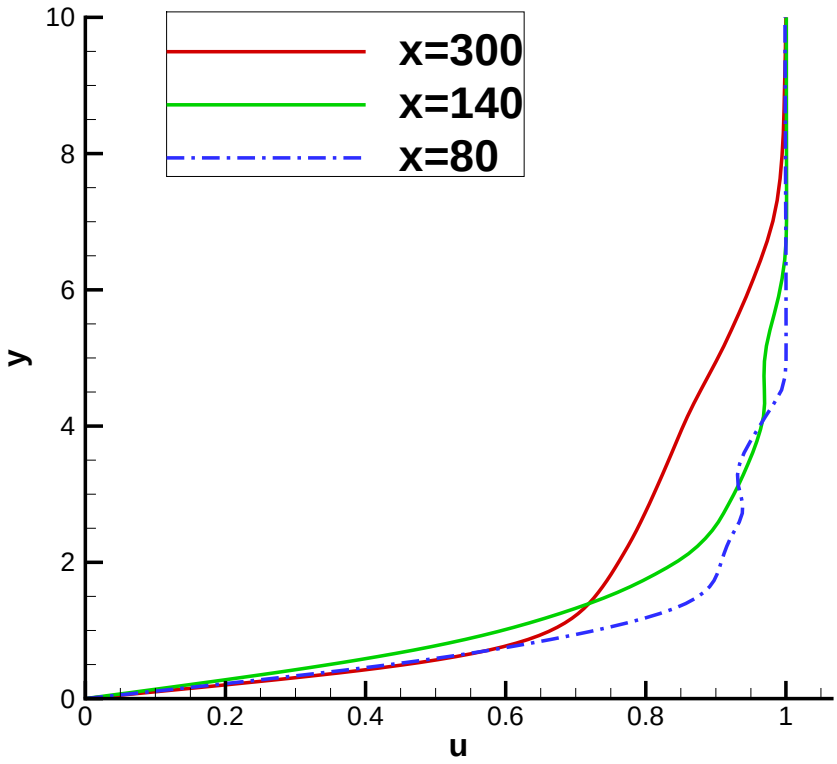

FIGURE 6.12: Distributions of mean u-velocity at different streamwise locations.

in figure 6.13 at the three streamwise locations. Their distributions are compared with the turbulent boundary layer profiles for the sublayer and logarithm region which are defined by

$$u^+ = y^+ \quad \text{for sublayer,} \tag{6.4}$$

and

$$u^+ = \frac{1}{0.41} ln(y^+) + 5.25 \quad \text{for logarithm region.} \tag{6.5}$$

As shown in figure 6.13, the profiles compare well in the viscous sublayer with the theoretical values, however differences are observed in the buffer-layer and the log-law region. These comparisons of the u^+ profiles with theoretical values accord with the relationships between the obtained C_f and the Eckert's solution. The u^+ profile goes better with theoretical value at x=80 with the help of C_f recovery. It is overestimated at x=140 as corresponding C_f is lower than Eckert's solution so that more wall-normal space is required before reaching the log-law region. In contrast, it is underestimated at x=300 as less wall-normal space is required.

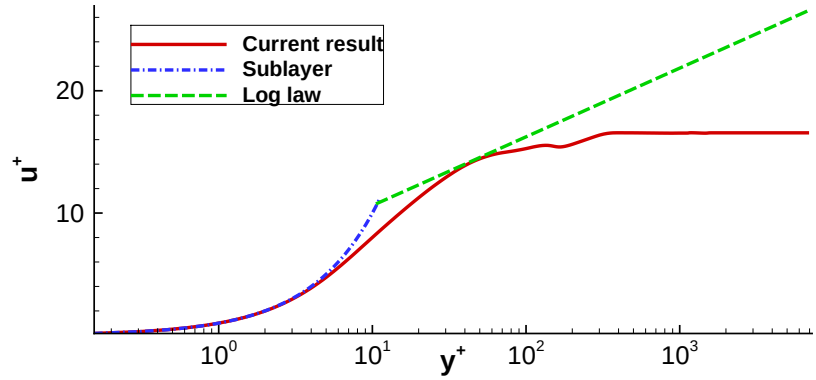

(a)

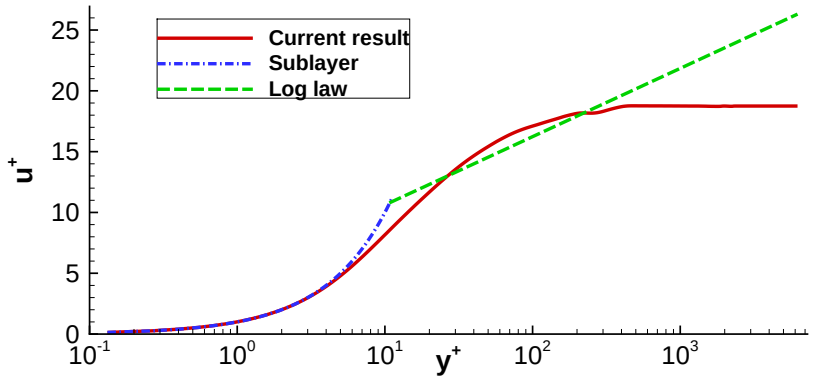

(b)

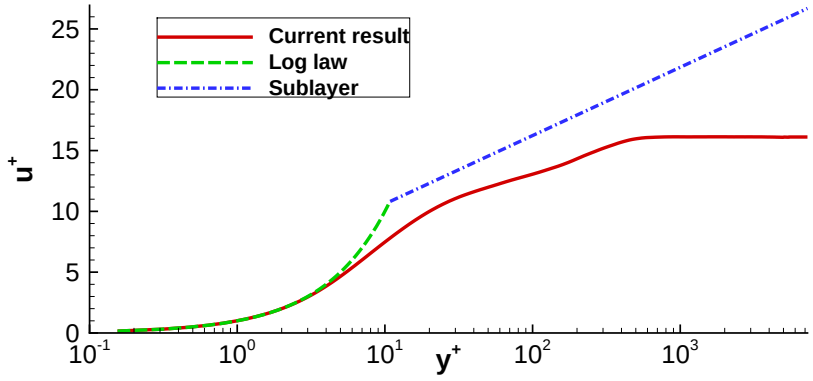

(c)

FIGURE 6.13: Distributions of u^+ in y^+ direction at different streamwise locations: (a) x=80, (b) x=140, (c) x=300

6.4 3D ramp flow result

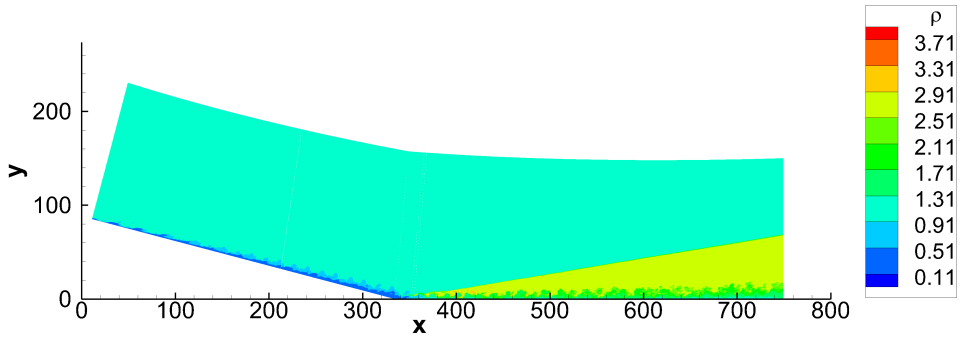

FIGURE 6.14: Contours of density of M=5.3 ramp flowfield at t=2,360.

Figure 6.14 plots the density contours at t=2,360 on an spanwise slice at $z = 0$. Disturbed flow can be seen both upstream and downstream of the ramp corner. Enhanced turbulence is observed after the ramp corner. It can be seen that the separation region is very small (from 334.1 to 335) compared with the 378 long separation length for laminar ramp flow as shown in figure 5.21(a) and figure 5.22 in Chapter 5.

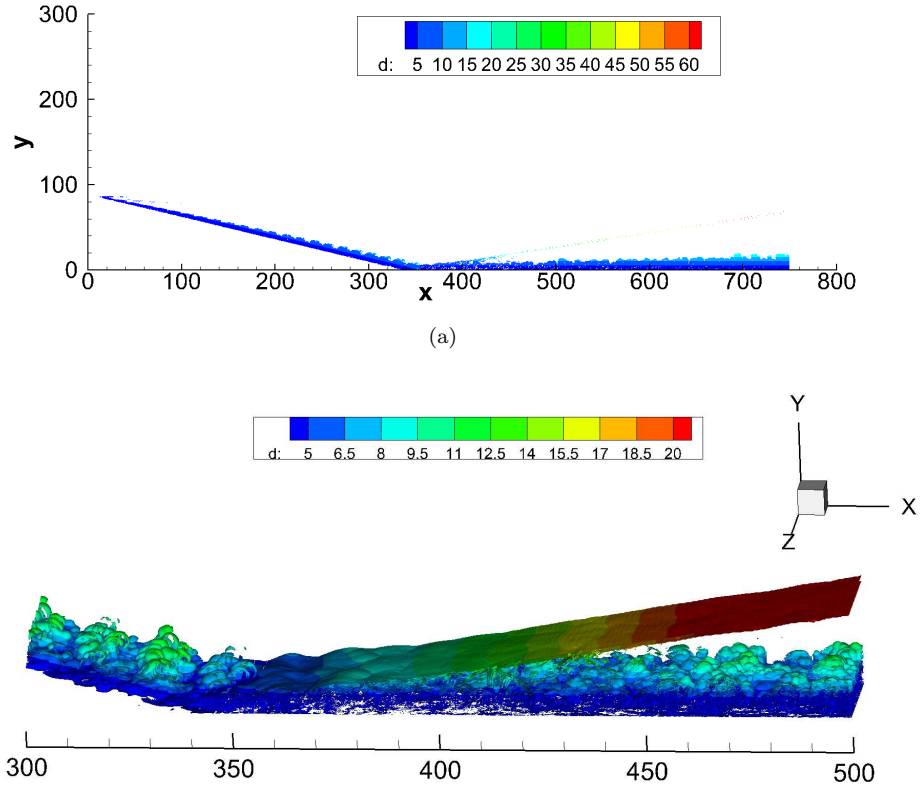

(a)

(b)

FIGURE 6.15: Iso-surfaces of $\nabla\rho\delta/\rho_\infty$=2.5 at $t = 2,360$ (a) on a 2D $x - y$ plane and (b) around corner in 3D (displayed every two grids).

Figure 6.15 shows iso-surfaces of magnitude for density gradient which are defined by $|\nabla\rho| = \sqrt{(\partial\rho/\partial x)^2 + (\partial\rho/\partial y)^2 + (\partial\rho/\partial z)^2}$. A 2D plot of the spanwise averaged 2D values for the whole flowfield is displayed in figure 6.15(a), and a 3D iso-surface near the corner is plotted in figure 6.15(b). The same $|\nabla\rho|$ value ($|\nabla\rho|\delta/\rho_\infty$=2.5) is used here compared with a plot by Priebe and Martin (2012) in figure 1 and figure 3 of their paper on M=2.9 flow passing a ramp corner. The δ used by them was 99% the boundary layer thickness at the inflow and their computational domain upstream of the corner was 7.9δ. In consideration of the long computational domain length upstream of the corner (334.42) in the present simulation, after calculating the boundary layer thickness δ at different streamwise locations, the streamwise location with 7.9 times its boundary layer thickness upstream the ramp corner is identified to be at x=271.5. So the boundary layer thickness at x=271.5 is used to calculate the value of $|\nabla\rho|$. Both of the plots in figure 6.15(b) are coloured by the distance to the closest wall. From the upper frame, the regions with strong density variation are mainly close to the wall, around and downstream the recompression shock. In the lower frame, compared with upstream flowfield, smaller flow structures are seen downstream of the ramp corner and the spanwise non-uniform shock, as also observed by Priebe and Martin (2012).

Iso-surfaces of the second invariant Q are shown in figure 6.16, coloured with distance to the closest wall. To have a clear view of the flow structures, the whole flowfield is displayed in four sections with the top plot showing the initial flow development near the inflow to the bottom frame showing the flow near the outflow boundary. Near the inflow it can be seen in the top plot how the forcing produces seven quasi-streamwise vortices near the inflow. These generate unstable low speed streaks and the flow undergoes transition to turbulence, with the most intense transitional structures halfway along this frame. The second frame covers the relaxation of the post-transitional boundary layer towards a fully-developed turbulent boundary layer and includes the start of the ramp, at which there is a change in flow structure, as seen in the third frame. Here much more intense structures with a wide range of scales are formed. New large-scale structures appear in the outer part of the boundary layer and smaller-scale structures form near the wall, which is consistent with the reduction in the viscous length scale ν/u_τ in the region after the ramp, where the skin friction is expected to be the highest. Near the exit it can be seen in the last frame that there is a slow return to equilibrium of the boundary layer downstream of the ramp, but with much smaller scale structures compared to the turbulent boundary layer upstream of the ramp seen in the second frame.

Spanwise-averaged skin friction coefficients for the flat plate flow with ramp at different time instants are compared with the laminar theoretical solution and Eckert (1955)'s empirical relation for turbulent flow at various times during the ramp simulation in figure 6.17. Mean C_f based on a time length of 160 after t=2,480 is also plotted in the figure. All the instantaneous C_f obtained after t=880 goes well with the mean

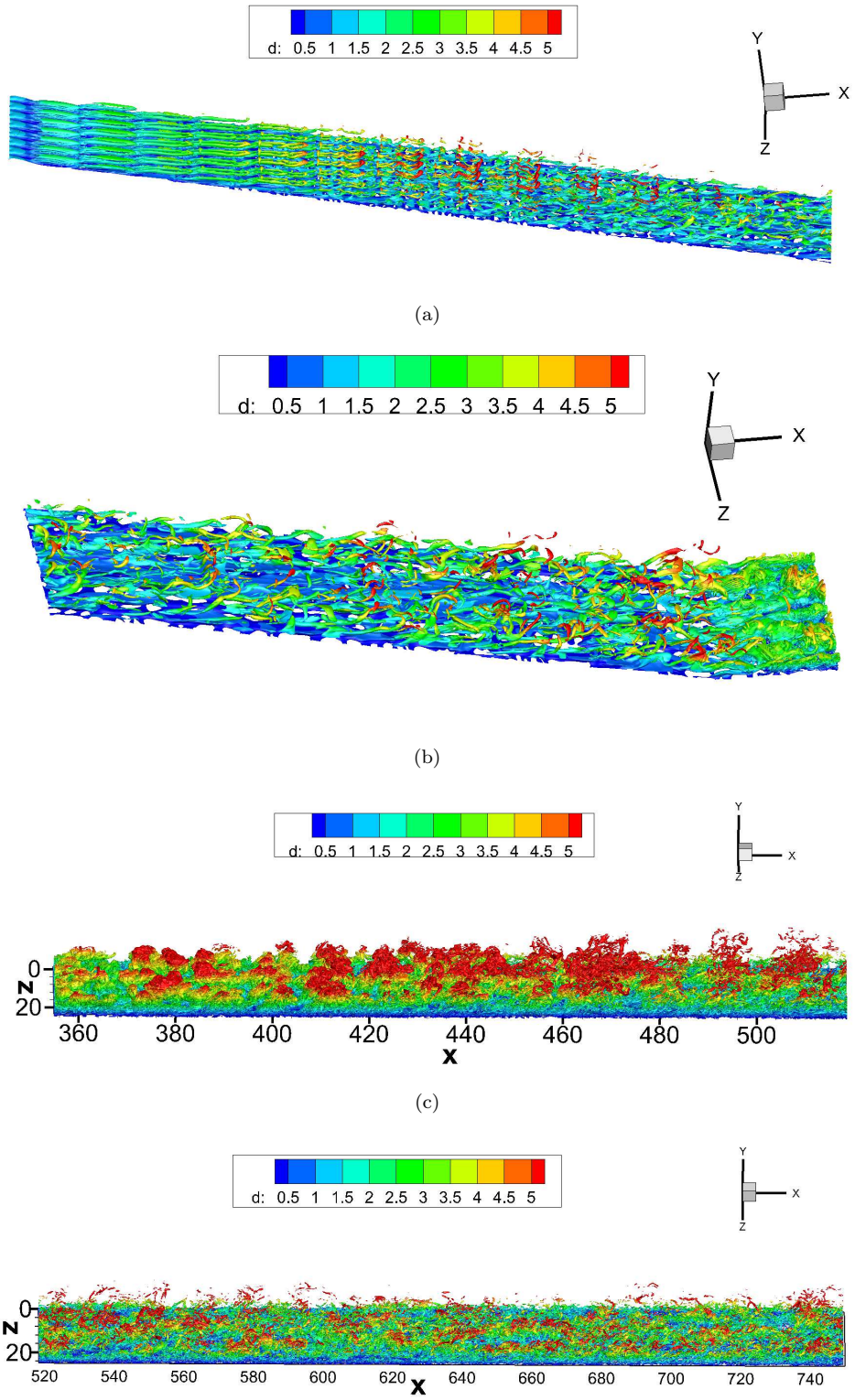

FIGURE 6.16: Iso-surfaces of Q=0.05 contoured by distance to the nearest wall at $t = 2,360$.

C_f, showing the the flow is converged after t=880. Four streamwise locations of x=253, x=371, x=478 and x=663 noted on the figure are identified according to the skin friction distribution. Flows at these locations will be compared later. The flow illustrates convergence towards a turbulent solution, with curves starting from t=160 up to t=2,360. The initial flow is fixed from the flat plate similarity solution, which is not a correct solution near the ramp corner. The disturbance caused by this mismatch has travelled to x=480 by t=160. At the same time the inflow condition is already triggering large values of skin friction as the introduced quasi-streamwise vortices move high momentum fluid towards the wall. By t=880 (corresponding to only just over one throughflow time) the flow has settled down to a well-defined turbulent state. The short time for the flow to achieve a steady state here, compared to the previous laminar flow simulations, is due to the absence of a large separated flow region. Here the separation is tiny and located near x=330. The large laminar separations converge on a viscous timescale, which at high Reynolds number takes a long time to achieve a steady state, resulting in very long run times.

Figure 6.17 shows that a reasonably well-developed turbulent boundary layer is achieved upstream of the ramp, indicated by the good correspondence in C_f to the Eckert level around C_f=0.0012. If comparing with figure 6.11, it is found the C_f curve here agrees better with the Eckert's solution, which may be explained that the flow separation and high pressure around the ramp corner make the upstream flow fully developed earlier. After the ramp there is a rise in C_f by a factor of 5, with the peak observed at x=380. The large increase in C_f is caused by the ramp angle for the high Mach number and the high Reynolds number, chosen to match the experiments. The turbulent upstream flow impinges on the ramp surface, thinning the boundary layer near the wall as well as pushing turbulent eddies towards the wall. Clearly this has implications for the numerical resolution. After the peak C_f there is a slow relaxation of the flow towards a new equilibrium state, reducing to $C_f = 0.004$ by the end of the computational domain.

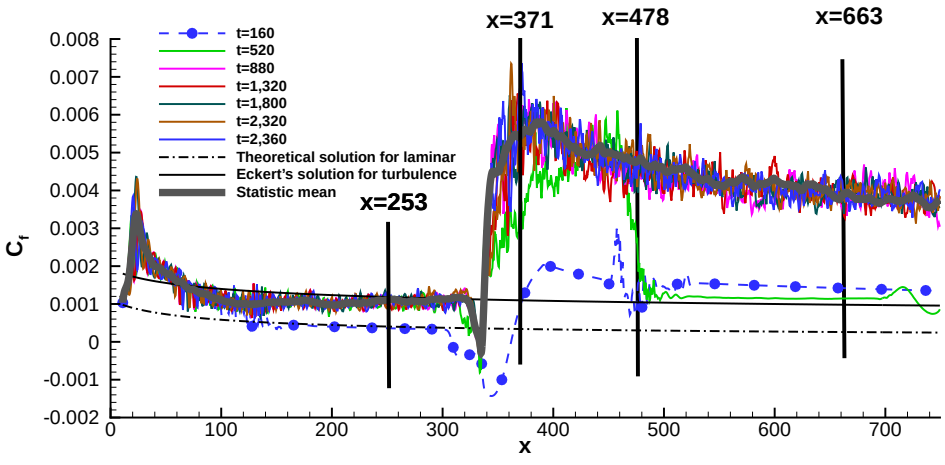

FIGURE 6.17: Instantaneous and mean skin friction coefficients averaged in the spanwise direction.

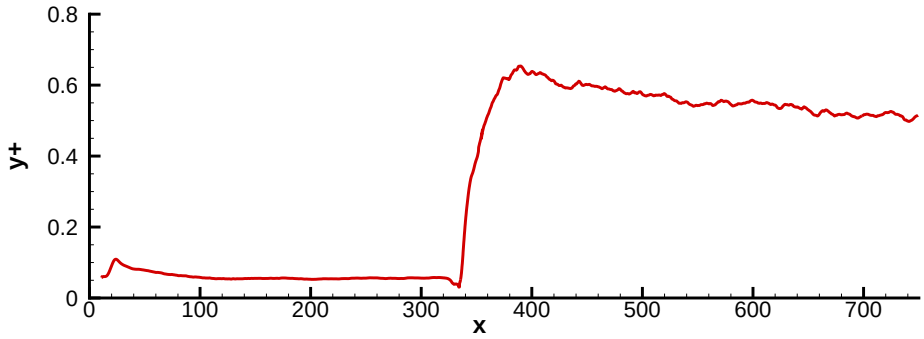

FIGURE 6.18: Distribution of spanwise averaged y^+ based on mean velocity, temperature and density.

All the statistic variables in the following part of this section are collected for a time length of 160 after t=2,480. Figure 6.18 shows the distribution of y^+ for the converged flow. The worst-case y^+ appears downstream of the ramp corner, with a value of around 0.65. At this position, both Δx^+ and Δz^+ are still below 13. Upstream of the interaction at x=300 we have Δx^+=1, Δz^+ =1$\sim$2 and the first off-wall grid point is at y^+=0.1. At x=380 near the maximum in C_f, the equivalent values are Δx^+=7.6, Δz^+=6.5$\sim$13 due to mesh stretching in the spanwise direction and y^+=0.65. Given that for DNS of flows with strong streamwise variations we would like to achieve Δx^+ <5, Δz^+ <5 and y^+ <1 for the first off-wall point, it is clear that, although the upstream turbulent boundary layer is well resolved, the simulations are slightly under-resolved in x and z, based on this rough estimation along the ramp part of the flow.

Flows at the four streamwise locations marked in figure 6.17 are compared here. It should be noted that the spanwise mesh is stretched and special attention should be paid in averaging in the spanwise direction. There are two approaches to do spanwise average, either treating value at each spanwise grid point equally or giving different weighting to the values at different grid points according their spacing. Any spanwise inhomogeneity, for example persistence of the inflow forcing would lead to a difference between the two approaches.

In the following plots, both weighted and non-weighted averages are computed, for example for the Reynolds stress terms shown in figure 6.19. The Reynolds stresses and density are collected over a time period of t=160 and averaged in the spanwise direction. It can be seen that results from both weighted spanwise average approach and regular average approach agree with each other. They follow the same trend and with roughly the same magnitude in the wall-normal direction, which means that the method of computing spanwise averages does not affect the comparison of Reynolds stress terms at different streamwise locations. It also proved the homogeneity of the flow at these locations. The differences between the results obtained with the two approaches are more obvious at the -10.8δ upstream location and 4.8δ downstream close to the ramp corner as the downstream turbulence has longer distance to develop.

Components of Reynolds stress at different streamwise locations are then compared, referring again to figure 6.19. It is seen that all the components of Reynolds stress are amplified downstream of the ramp corner, which was also found by Wu and Martin (2007). This is consistent with the distribution of C_f and hints that the most intensive turbulence events happen just downstream of ramp corner.

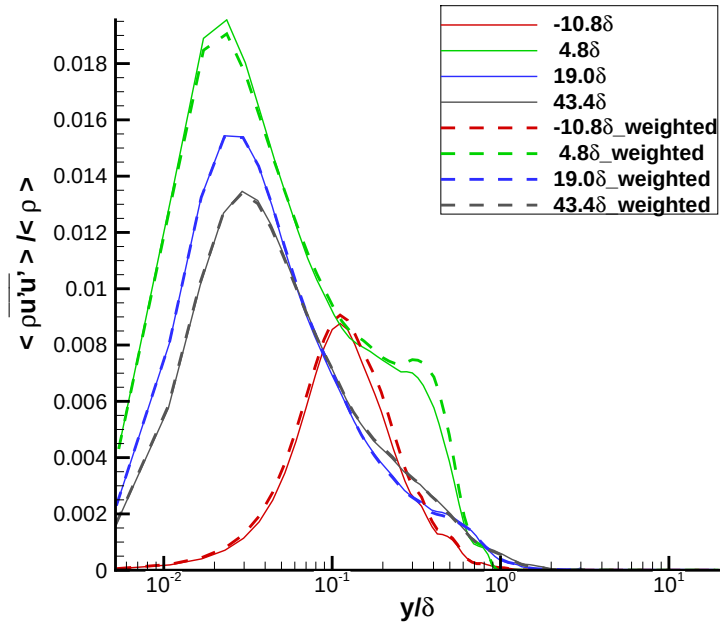

(a)

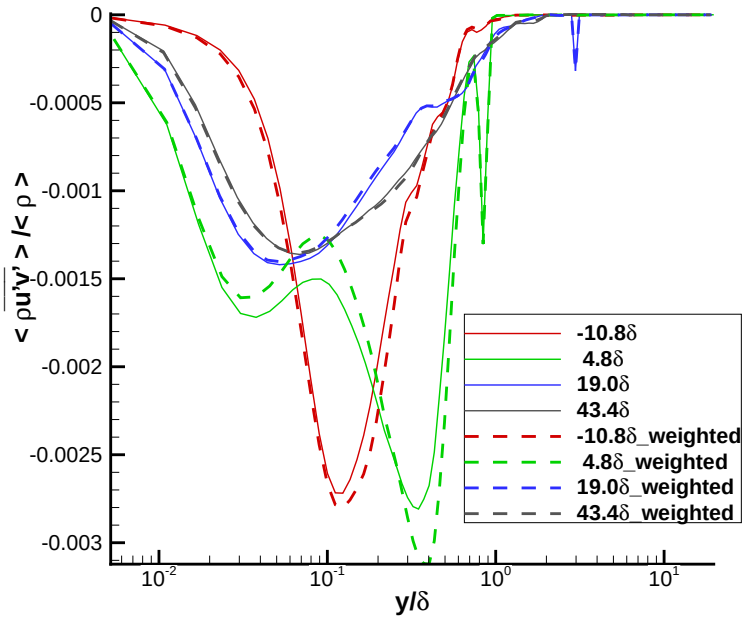

(b)

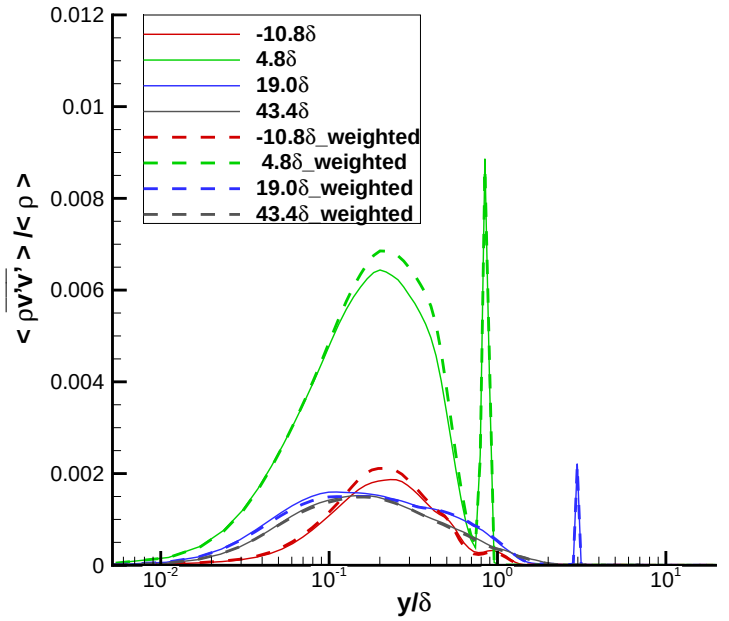

(c)

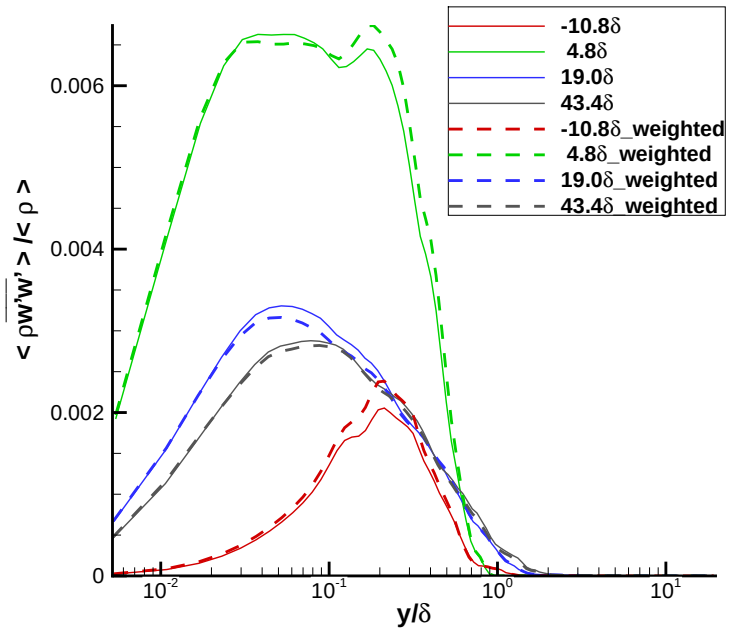

(d)

FIGURE 6.19: Distributions of spanwise averaged Reynolds stresses in wall normal direction.

Wu and Martin (2007) performed numerical simulations for a Mach 2.9 inflow over a 24° ramp corner. Their freestream temperature is 107 K with an isothermal wall at 307 K. The Reynolds number they used based on inflow momentum thickness is 2,300. The incoming boundary layer thickness δ_{99} (the ramp corner is 9 δ downstream in their case) was used to scale the coordinate. Although the conditions are very different to the present case, it is useful to make a comparison to find the magnitude of the differences. To compare with their results, the wall-normal distance here is divided by the boundary layer thickness δ_{99} at x =264.06 which is 1/9 of the distance to the ramp corner. The locations of x = 253, x=371, x=478 and x=663 correspond to distances of -10.8δ, 4.8δ, 19.0δ and 43.4δ to the ramp corner.

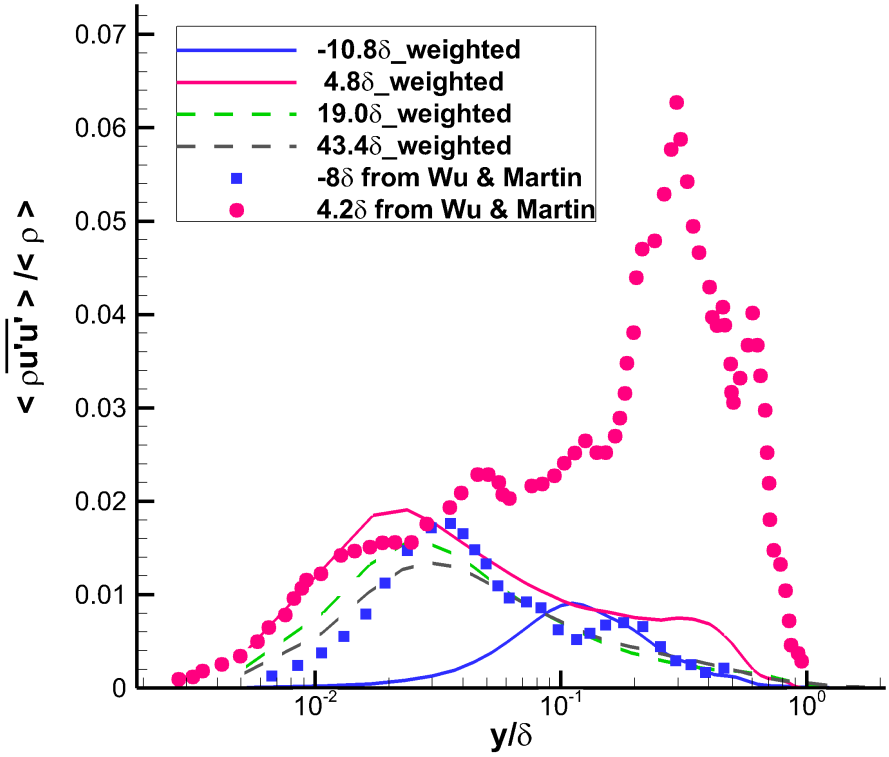

FIGURE 6.20: Comparison of Reynolds stress term $< \rho u'u' >$ in current result and from Wu and Martin (2007).

Taking Reynolds stress term $< \rho u'u' > / < \rho >$ as an example, figure 6.20 rescaled figure 6.19(a) and compared with the data from Wu and Martin (2007) at upstream 8 times and downstream 4.2 times the inflow boundary layer thickness, away from the corner, displayed in blue and pink spots, respectively. Though the comparison setups are similar, obvious differences are observed at both comparable streamwise locations of -10.8δ and 4.8δ due to the distinct differences on flow condition shown in table 6.2. Amplitude of the Reynolds stress variation downstream the ramp corner (at 4.2δ) is 3.5 time that upstream the ramp corner (at -8δ), while this value is about 2 evaluated

from values at 4.8δ and -10.8δ, showing the impingement of upstream turbulent flow is stronger for the 24° ramp flow of Wu and Martin (2007). It is noticed that the Reynolds stress term -8δ upstream from Wu and Martin (2007) is comparable with the current downstream Reynolds stress term, which means the turbulent flows in these regions might be similar.

Flow condition	Current 3D	From Wu and Martin
Ramp angle (°)	14.75	24
Inflow Mach number	5.3	2.9
Free stream temperature (K)	58.9	107
wall temperature (K)	298	307
Reynolds number	6,000	2,300

TABLE 6.2: Differences between current 3D flow condition and flow condition of Wu and Martin (2007).

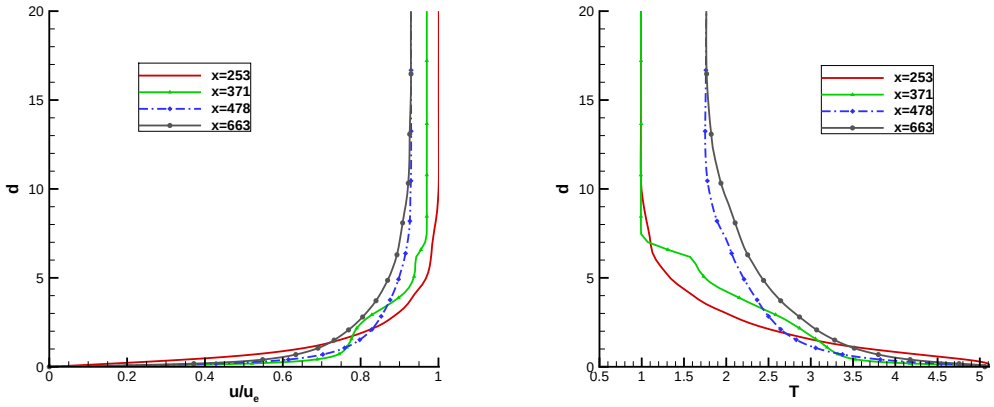

(a) (b)

FIGURE 6.21: Distributions of spanwise averaged (a) mean velocity parallel to the wall and (b) mean temperature at different streamwise locations.

Figure 6.21 shows the mean tangential velocity and temperature distribution in the wall-normal direction at the four different streamwise locations. In consideration of the inclined upstream wall, distance to the wall (n) rather than y-coordinate is used in the plot. Mean velocity and temperature become 1 at d=20 for x=253 curve, however it is noticed that mean velocity and temperature are not equal to 1 at d=20 for curves at x =371, 478 and 663, caused by the downstream recompression shock. After the recompression shock, the temperature increases while the streamwise velocity reduces. Fuller mean velocity and temperature profiles within the boundary layer are observed downstream the corner, showing that the turbulent flow downstream of the ramp corner seems to be more developed compared with upstream flow at x =253. Intense variations of the mean flowfield are observed at x =371 suggesting the complex flow around the corner.

Figure 6.22 shows the time and spanwise-averaged mean and RMS wall pressures as a function of x. Both of the statistic values show steady distribution upstream of the ramp corner as shown in figure 6.22(a) and figure 6.22(b). Upstream of the ramp corner, the mean wall pressure maintains a constant level until experiencing a sharp increase at the ramp corner. After the ramp corner, the mean wall pressure maintains another constant level. The highest RMS pressure (figure 6.22(b)) appears just after the ramp corner from x=355 to x=370. After this unsteady area, the flow tends to become less disturbed but still more unsteady than the upstream flow.

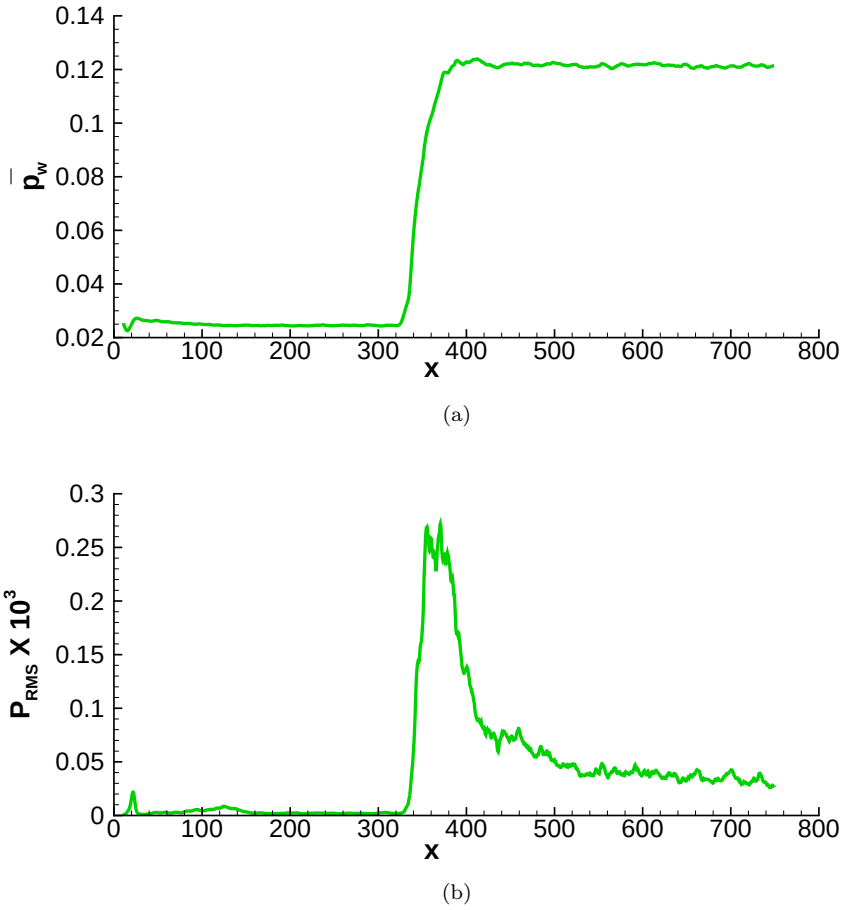

FIGURE 6.22: Pressure statistics on the wall (a) mean pressure, (b) RMS pressure for the Mach 5.3 ramp flow.

Figure 6.23 shows the Stanton number (defined in equation (5.1) in Chapter 5). Here the recovery temperature T_r^* was obtained assuming the flow is fully turbulent from $T_r^* = (1 + \frac{\gamma-1}{2} Pr^{1/3} M^2) T_\infty$. After the initial peak caused by the artificial streaks, the Stanton number keeps around 0.0005 until the location with very high heat transfer just downstream of the corner. Further downstream, the Stanton number keeps on the same level around 0.0017 which is about three times the upstream value. This implies the strongest heat transfer appeared just close downstream the ramp corner.

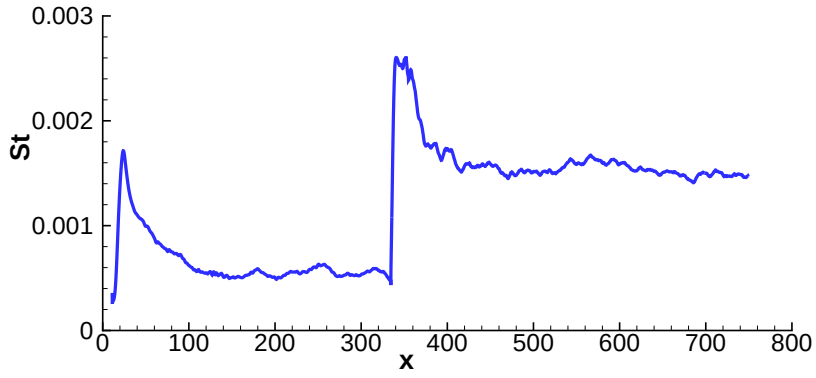

FIGURE 6.23: Distribution of Stanton number for the Mach 5.3 ramp flow.

6.5 Slot jet injection

A slot jet with p_j=0.15, inclined at an angle of 26.16° to the upstream wall, is switched on at t=2,360 after the turbulent flow is fully developed. A local increase in the numerical dissipation (through the TVD scheme built into the code) near the jet was applied to help stabilize the simulation. Difficulties of resolving the narrow jet are exacerbated here, since the jet is injected shortly after the ramp where the highest values of C_f appear and the boundary layer flow is least resolved. Figure 6.24 shows the flow pattern near the jet injection. There is a strong interaction between the jet fluid and the separation zone, and the high jet momentum pushes the separation shock further away from the wall. Recirculation zones are seen both upstream and downstream of the jet injection.

To have a clear view of the flow structure, iso-surfaces of Q-criteria are plotted in four sections in figure 6.25 as did for the ramp flow case in figure 6.16. In the top frame seven quasi-streamwise vortices starting from the inflow and the intense transitional structures are still observed halfway along this frame. In the second frame, flow with intense variation develops upstream along with flow separation shown in figure 6.24(b). The intensely varying flow extends in the third frame with a break at around x=440. By comparing with figure 6.16, it is observed that the iso-surface is lifted higher. In the final frame the flow returns to equilibrium, and structures become comparable to the turbulent boundary layer upstream of the ramp seen in the second frame.

The injected jet clearly has a substantial influence on the upstream boundary layer, even when the boundary layer is fully turbulent. The upstream progress of the separation point is shown on figure 6.26 (note that the time axis here is from the start of the jet injection). The separation point is determined from the span-averaged C_f distribution to find points with C_f=0. As seen in the figure, flow separation point keeps moving upstream until it converges at x_{sep}-x_{inflow}=230 at t=350 after turning the jet on. After this time the flow separation point remains approximately constant. The separation point moves upstream at a rate of 0.284 which is close to the value of laminar flow at

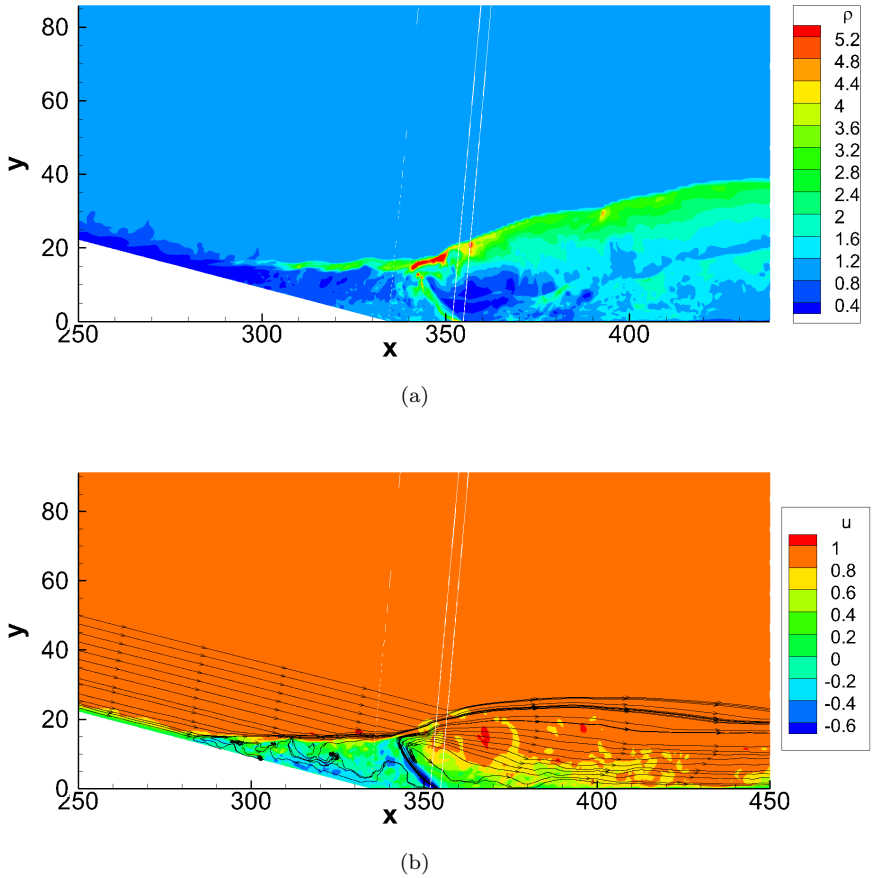

FIGURE 6.24: Jet injection region from 3D simulation 155 non-dimensional time units after turning on the jet at M=5.3, illustrated (a) with contours of density and (b) with u-velocity contours and streamlines.

0.278 at the same jet strength and the same jet angle, as shown in table 5.3 in Chapter 5. However in the current turbulent case the separation does not reach the inflow boundary. Nevertheless, it appears that even with an upstream turbulent boundary layer substantial separated flows would be observed on the launcher upper stage during the stage separation process.

Contours of both density and the streamwise velocity superposed with streamlines are plotted in figure 6.27 from the converged flowfield at t=410 after turning on the jet injection. The jet injection region, the ramp corner and the upstream separation point are all included in the figure. By comparing to the density plot in figure 6.24, it can be seen that the separation shock is further upstream, while the jet shock is further away from the corner. With the help of streamlines in figure 6.27(b), separation bubble is found to increase with complex recirculation regions. Figure 6.28 shows a close-up view for figure 6.27(b) in the flow separation point. Unlike the separation observed for the laminar cases, the separation point is still far away from the inflow boundary, flow recirculation zones in different size are observed.

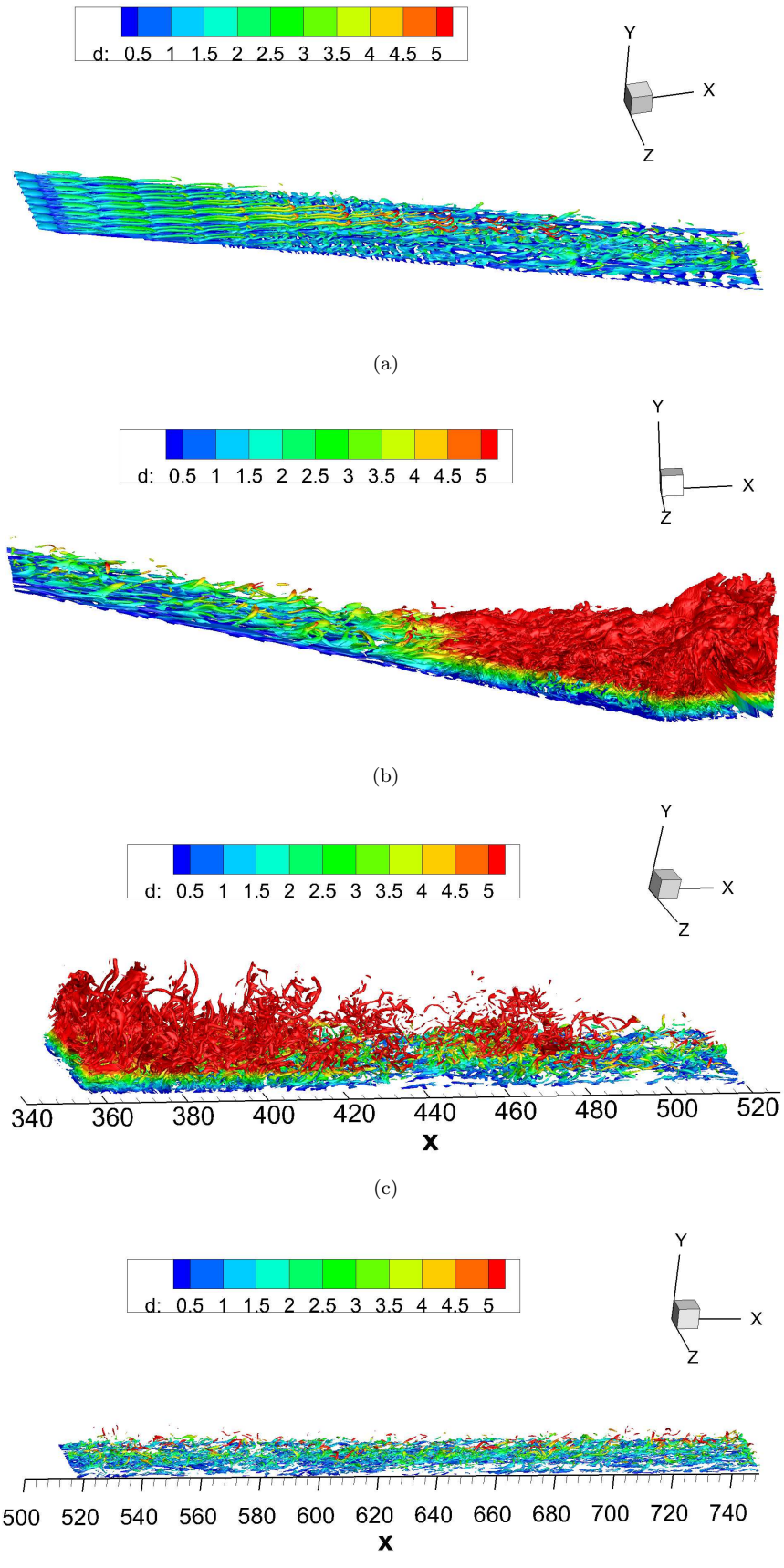

FIGURE 6.25: Iso-surfaces of Q=0.05 for the flowfield at t=175 after the slot jet was turned on.

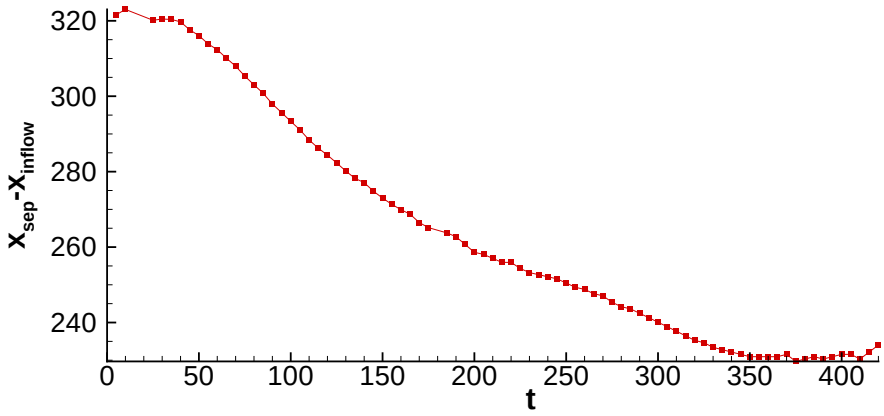

FIGURE 6.26: Movement of the upstream separation point with time after the slot jet is turned on.

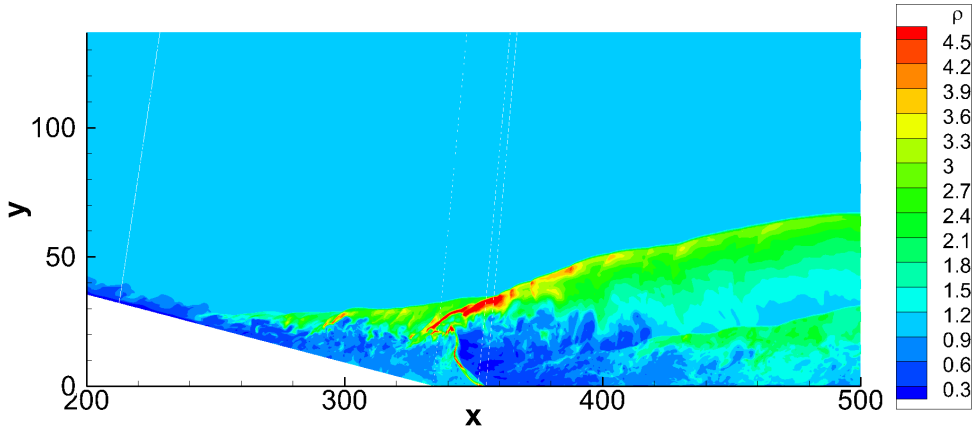

(a)

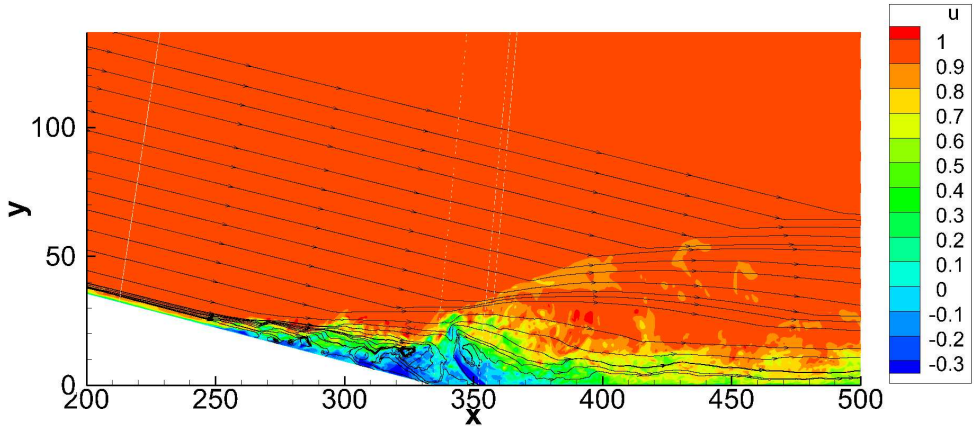

(b)

FIGURE 6.27: Converged flow around ramp and jet injection region on z=0 slice, 410 non-dimensional time units after turning on the jet at M=5.3, illustrated (a) with contours of density and (b) with u-velocity contours and streamlines.

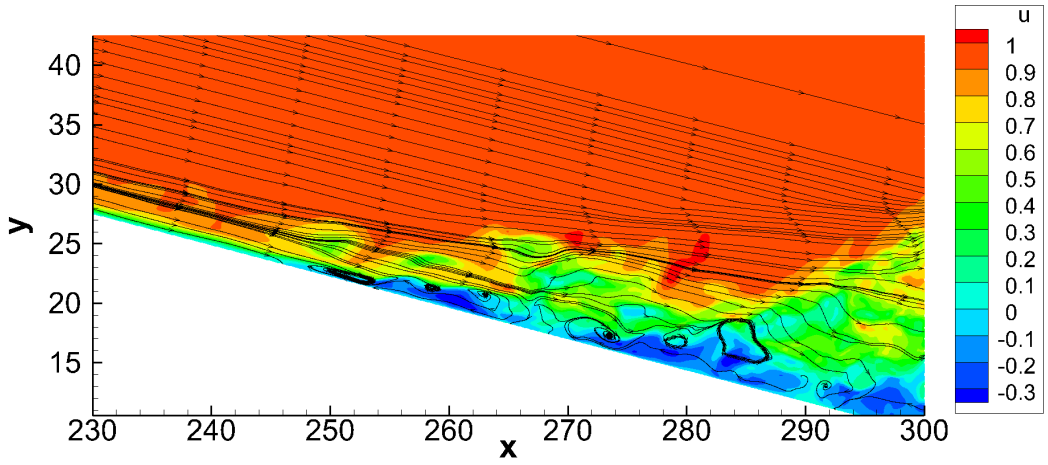

FIGURE 6.28: Flow separation on z=0 slice for converged flow at t=410.

Flowfields before jet injection, at t=155 and t=410 after jet switched on are compared in figure 6.29 through contours of the density gradient magnitude ($|\nabla(\rho)| = \sqrt{(\partial\rho/\partial x)^2 + \partial\rho/\partial y)^2}$) in z=0 slice. Shocks are clearly seen in all the three cases. As shown in figure 6.29(a), turbulence flow structures are observed both upstream and downstream of the ramp corner. Value of $|\nabla(\rho)|$ is higher for the downstream flow. Straight recompression shock above the downstream turbulence flow is observed. It interacts with boundary layer near the corner. At t=155 after turning on the jet as shown in figure 6.29(b), the interaction of the separation shock and the bow shock of the jet injection pushes the ramp recompression shock away from the boundary layer, forming a clear bent shock. Complex flow is observed within the boundary layer. The flowfield with jet injection is converged at t=410, a larger proportion of the straight recompression shock is bent, and the recompression shock downstream the jet injection is observed as shown in figure 6.29(c).

Iso-surface of Q for the converged flowfield at t=410 is plotted in figure 6.30 with four frames. Same Q value and same frame arrangement are used here for easier comparison. Flow structures with a wide range of scales are observed. Compared with figure 6.25, the iso-surfaces far away from the wall in red colour around the ramp corner and jet injection expands both upstream and downstream seem from the second and the third frames compared with those in figure 6.25. This intense varying flow even develops downstream to x=550 in the fourth frame.

Statistics are accumulated from t=350 to t=410. Mean C_f and St curves are plotted in figure 6.31 by also averaging in the spanwise direction. The mean C_f curve shown in figure 6.31(a) is compared with the reference value from figure 6.17 before switching on the jet injection. It can be seen that a substantial separation zone is created both upstream and downstream of the ramp with a length of about 130 compared to 1.8 of ramp flow without jet injection. A side effect of the jet injection is the decrease in the

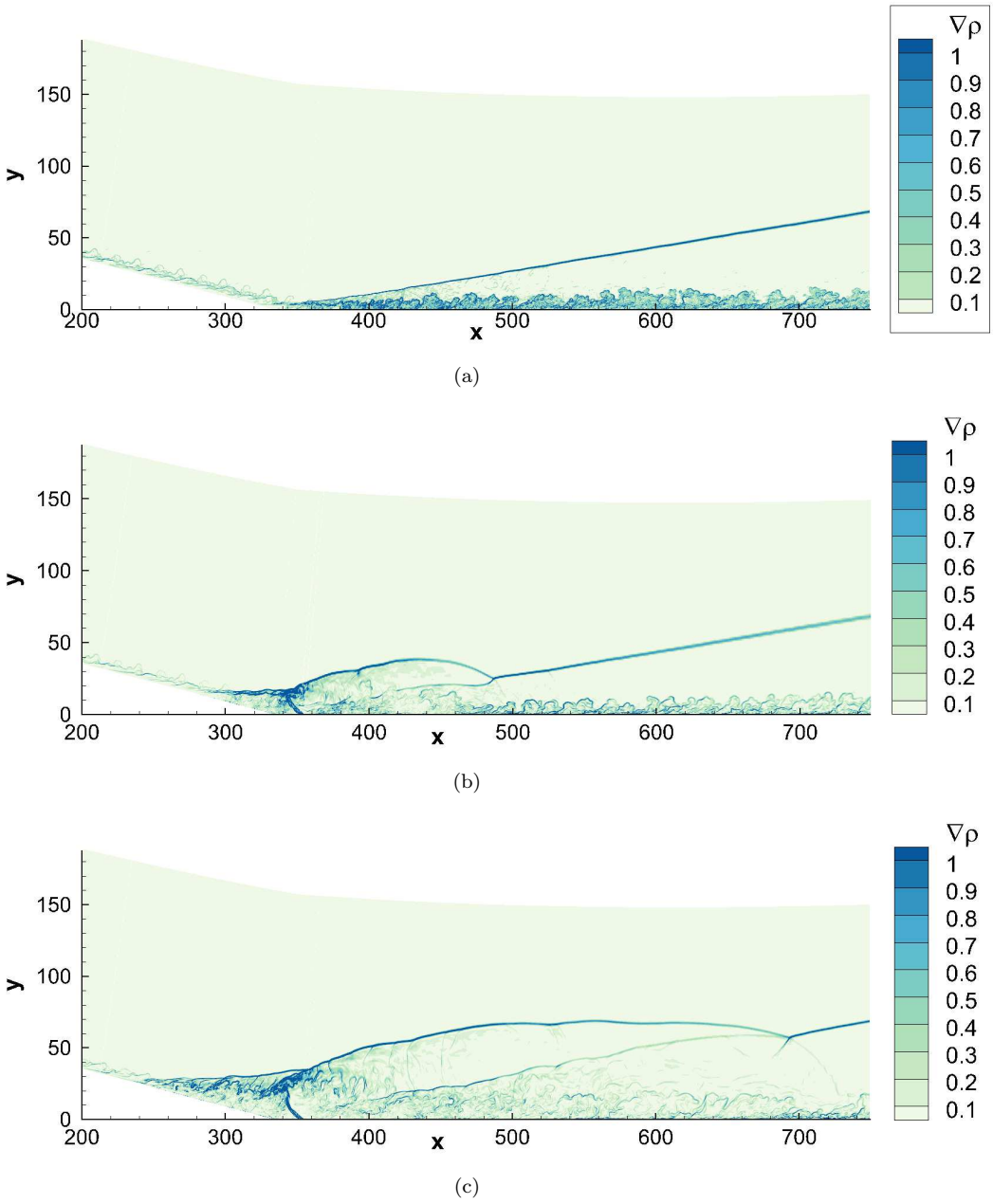

FIGURE 6.29: Distributions of density gradient on z=0 slice for (a) converged ramp flow without jet injection, and at non-dimensional time (b) 155 and (c) 410 after turning on the jet at M=5.3.

maximum skin friction seen on the ramp surface. The maximum value of C_f is 0.006 appearing just downstream of the ramp. When the jet is injected the skin friction near the ramp corner in the separated region is reduced greatly. The maximum value appears down stream in the attached region with a value of C_f=0.0034 which is comparable with the case without jet injection. Within the separation region, the peaks of C_f distribution appear upstream the corner and upstream the jet injection, respectively.

The distribution of St is shown in figure 6.31(b) and compared with St for the flow without jet injection. Except for the jet injection area, the maximum heat transfer

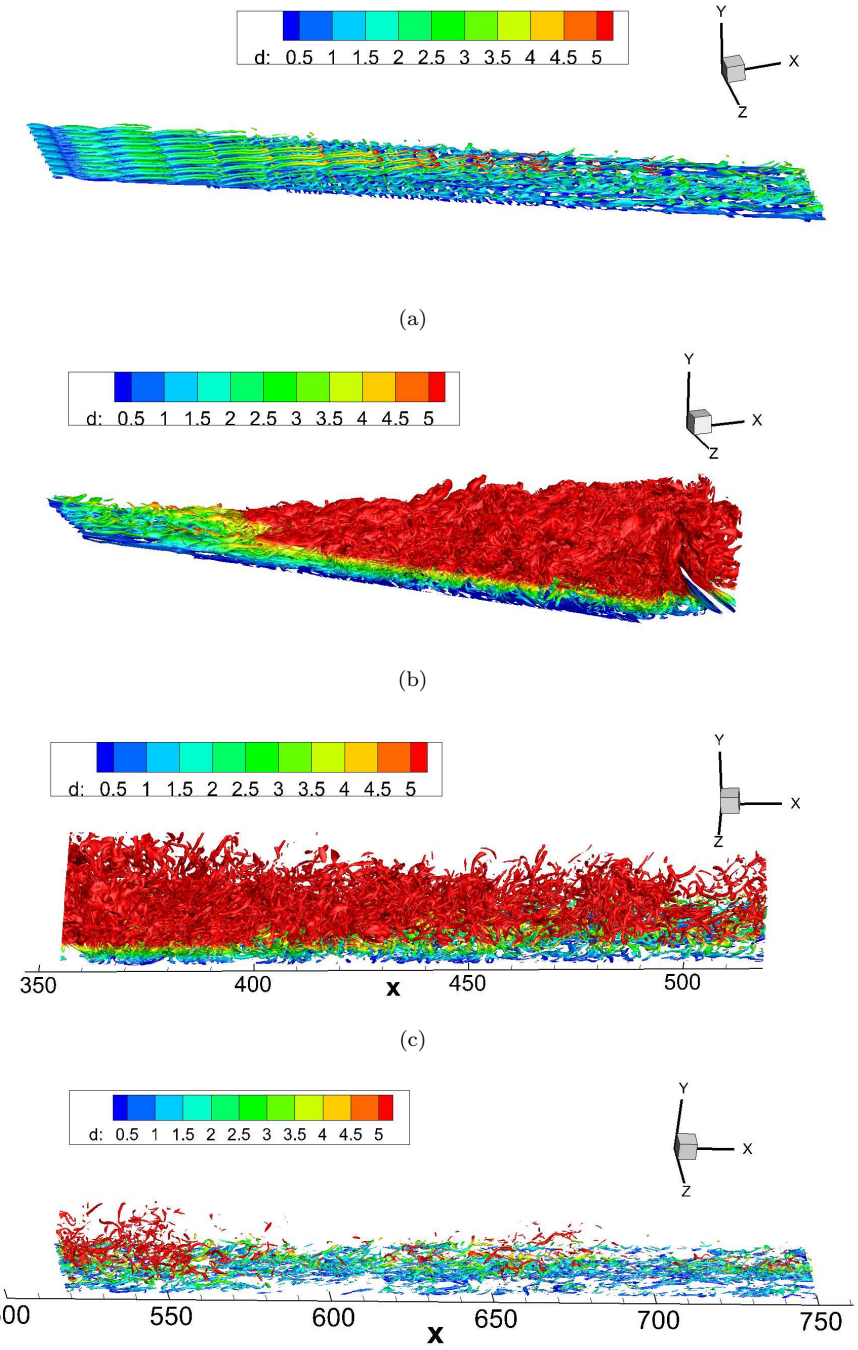

FIGURE 6.30: Iso-surfaces of Q=0.05 for the converged ramp flowfield at t=410 after the jet was turned on.

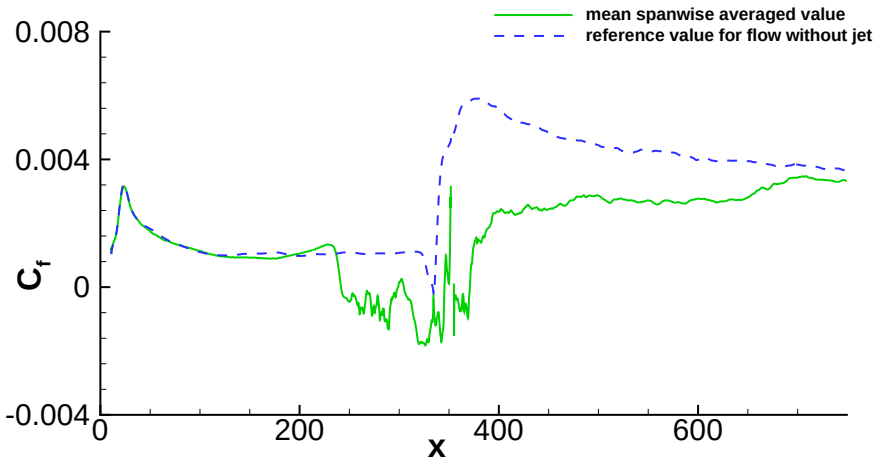

(a)

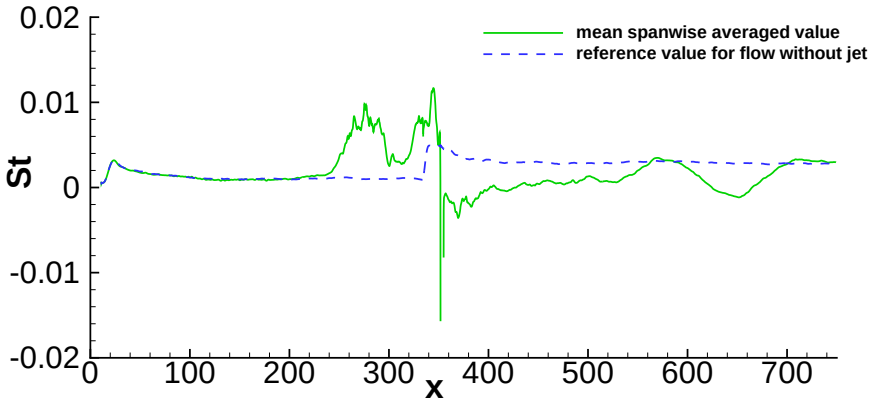

(b)

FIGURE 6.31: Distributions of (a) mean C_f and (b) mean St (discontinuities correspond to the jet location) for the converged flow with jet injection.

value is increased from 0.005 to 0.011 with the same location just downstream of the corner. However another high heat transfer region with a peak value of 0.01 at x=276 is observed upstream the corner from x=241 to x=300, which corresponds to the upstream separation bubble. With the help of C_f distribution above, it can be seen that both of the two upstream peaks for heat transfer are within the flow separation bubble. Because of the jet injection, the heat transfer downstream varies considerably compared to the smoother distribution of heat transfer for the flow without a jet.

Figure 6.32 plots the temperature contours for the flow. A region with high temperature is observed between the upstream separation point and the jet injection. Temperature is increased by both the upstream separation shock and downstream upstream inclined jet.

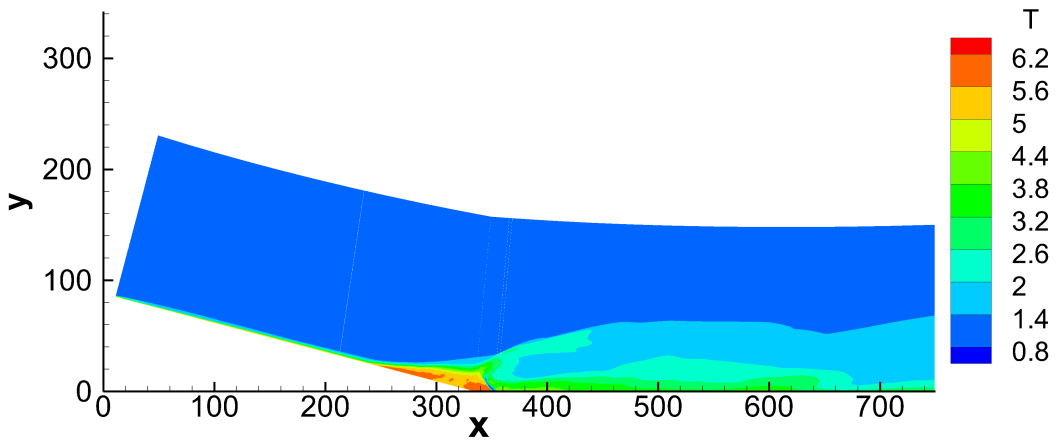

FIGURE 6.32: Mean spanwise averaged temperature distribution.

6.5.1 Square jet injection

An attempt was made to simulate the rocket jet using square jet instead of the slot jet used earlier. A wall-normal jet with strength of $p_j = 0.2$ (equivalent to a same-width slot jet with p_j=0.023) was switched on after the turbulent ramp flow was fully developed at t=1,850. As can be seen in figure 6.17, the jet is centred at x=353.38 in an area with high skin friction just downstream of the ramp corner, which makes the square jet simulation even harder as more interface and more complex boundary are confronted. Figure 6.33 shows flowfield slice across the centre of square jet injection area around the ramp corner superposed with streamlines at time t=10 after jet injection. Recirculation zones are observed both upstream and downstream of jet.

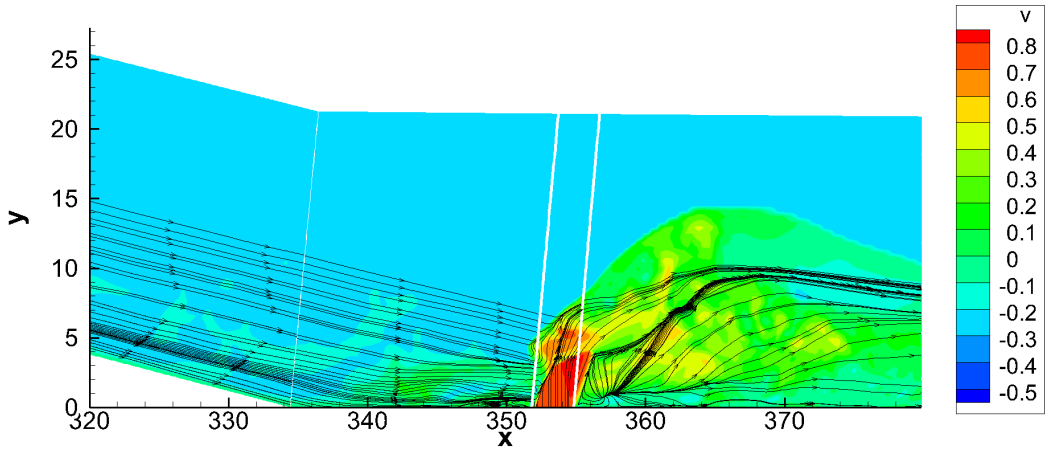

FIGURE 6.33: Flowfield slice around corner across jet centre contoured by v-velocity.

Figure 6.34 plots iso-surfaces of Q for the flow with square jet injection divided into three frames. The corresponding Q value is reduced from 0.05 to 0.01 to have a better view of flow structures, as the flow only developed for a time length of t=10 after the square

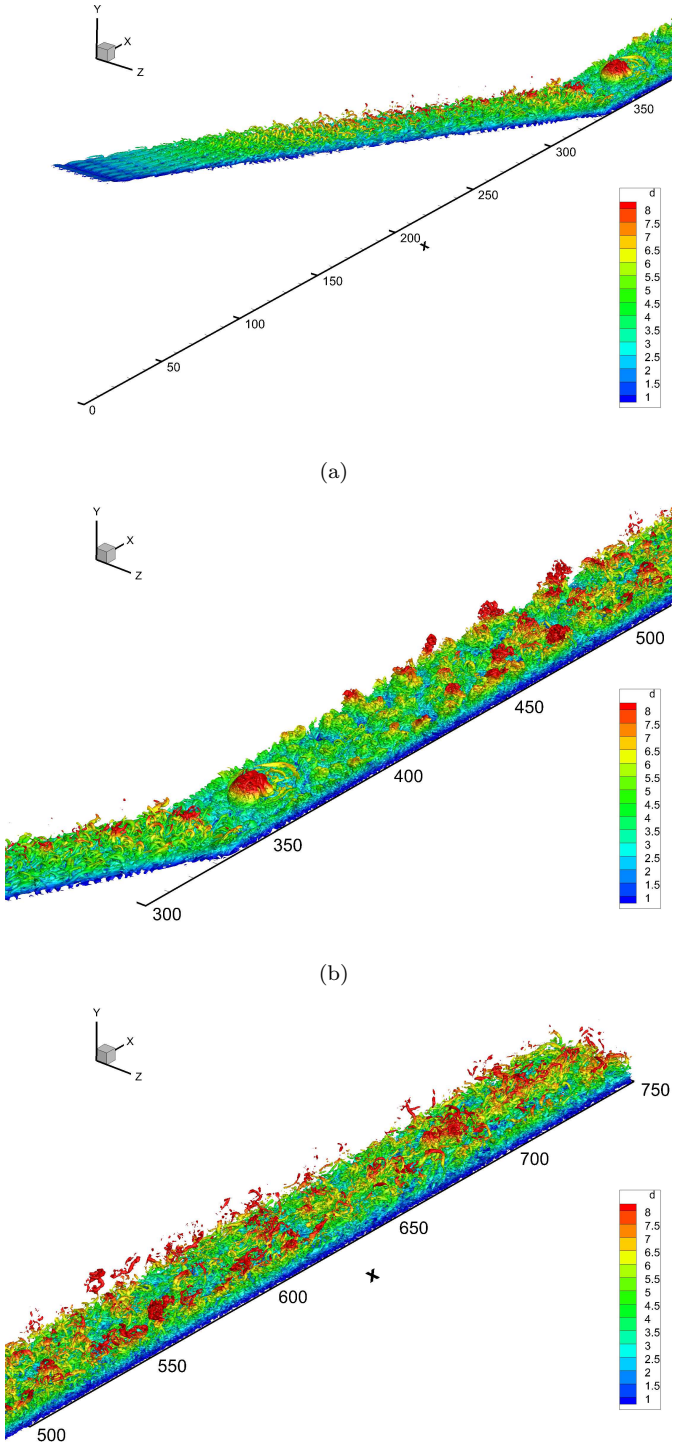

FIGURE 6.34: Iso-surface of Q=0.01 for the flowfield at t=10 after square jet turned on.

jet is activated. As shown in the figure, the most remarkable flow area is above the square jet injection and the close downstream flow. Upstream streaks breakdown, flow transition and downstream larger flow structures, as discussed in the slot jet section, are observed. However, soon after this time, the simulation failed in the vicinity of the square jet. Smaller time step and other numerical treatments, such as increasing the local viscosity, using a local averaging method, and locally increasing the numerical dissipation (which was successful for slot jet injection) near the jet, were tried but none the these treatment worked. To solve this problem, a finer mesh and a smaller time step Δt probably are required, which is beyond our current computational capacity. On the other hand, the equivalent momentum flux ratio for the square jet of $p_j = 0.2$ is 8.55 times smaller for a slot jet of $p_j = 0.2$. To study flow separation with jet relevant to the practical configuration, the slot jet is preferred.

6.6 Summary

In this chapter, 3D ramp flows with and without jet injection, based on a DLR wind-tunnel model, have been simulated. Streaks are added in the inflow to get turbulent flow. A small separation region, with high skin friction just downstream of the corner are observed for the turbulent ramp flow without jet. After turning on the jet, flow separation develops upstream with the rate at which the separation point moves upstream of 0.284, which is comparable to 0.278 for corresponding 2D laminar flow with the same jet strength and inclined angle. The maximum skin friction is reduced after the jet is turned on, but the maximum heat transfer is doubled accompanied with a high temperature region between the upstream separation point and the jet injection. The flow separation point finally settles down well downstream of the inflow boundary, compared with always reaching inflow boundary for 2D laminar cases, showing a large effect of turbulent flow.

Chapter 7

Conclusions and future work

7.1 Conclusions

Simulations have been performed for 2D and 3D high speed separated flows in different configurations, using a high-order code. Firstly, flow stabilities were studied for a sonic jet in high speed crossflow and for a supersonic ramp flow. The jet in crossflow is marginally unstable at the momentum flux parameter J_p=0.1 and becomes more unstable as J_p is increased, suggesting a critical value of J_p below but close to 0.1. Ramp flow is found to be globally unstable at Reynolds number 6,843. A critical Reynolds number for the 3D ramp flow to become globally unstable exists between $3,422$ and $6,843$. For the unstable cases, the most unstable mode has a wavelength of 8 for jet in crossflow, while the most unstable mode for the ramp flow has a wavelength of 12, based on the incoming boundary layer displacement thickness in both cases. Similar recirculation zones and boundary layer velocity distributions were observed in flows based on these two configurations.

Streamwise vortices were observed in the jet case in the saturated state formed after the exponential growth of the added disturbance. The vortices were located away from the wall and did not have a strong effect on flow properties at the wall or lead to transition immediately downstream of the jet injection. In contrast, transition to turbulence occurred for the ramp flow with Reynolds number of 6,843. Streaks, flow intermittence and transition to turbulence were observed. It is believed that transition to turbulence is caused in this case by the instability of the streamwise streaks, and fed by a global instability in the recirculation zone around the ramp corner. This suggests that transition might also be observed in the 3D jet case if the downstream length is long enough and the Reynolds number is higher.

Based on a stage separation model of a rocket, 2D and 3D simulations have been conducted to study laminar and turbulent separations on model problems, considering geometrical features of ramp, and cavity, together with jet injection. A ramp flow case,

previously ran at M=4.8, was firstly extended to include jets and cavities. It is found that while the cavity has little effect, apart from a slight delay in the upstream propagation of the separation point, the jet has a major influence on upstream separation, leading to a large region of separated flow. The flow separation point moves all the way to the inflow for the incoming laminar boundary layer.

Simulations are also carried out for flow conditions corresponding to the wind tunnel tests, with M=5.3 and matched the Reynolds number, ramp angle and jet location. The simulations are run in a planar geometry with an inflow boundary downstream of the rocket tip with profiles from a laminar similarity solution. Based on the 2D parametric studies with this configuration, a wide cavity is found to have little influence on the flow field, but a narrow cavity (corresponding to a 5 mm gap in the experiment) substantially increase the size of the separation zone. A close examination of the flowfield shows that the small cavity produced a large local perturbation in the flow, acting as an increased blockage that then increased the separation length. Jets with M_j=3.6 and different strengths and inclinations were then tested. All cases showed large increases in the separation length, moving the separation point upstream to the inflow boundary. The rate of upstream movement increases for stronger jets and for jets that inclined upstream.

Three-dimensional simulations were run with a forced inflow condition to trigger transition to turbulence, followed by a turbulent ramp interaction. For the case with no jet injection, only a very small separation bubble was observed near the ramp corner. However, when the jet is turned on, the separated flow expands rapidly, but unlike the laminar case, is still restrained within the domain. This suggests that all cases with retro-jets operational are likely to be affected by large separated flow regions on the upper rocket stage. The maximum rate of separation spreading upstream was found to be comparable between laminar and turbulent cases.

7.2 Principal achievements of the research

• Several different configurations of high speed separated boundary layer flows have been modelled numerically with a high-order code.

• Thresholds have been identified for global instability, the momentum flux ratio of jet for sonic jet in high speed crossflow and Reynolds number for supersonic ramp flow.

• Flow instability studies have been extended into jet in crossflow and ramp flow cases, confirmed substantially the generality of the work of Robinet (2007) for shock impingement configuration.

• A breakdown mechanism for ramp flow has been elaborated, with downstream streak breakdown fed by the global instability within the separation bubble identified to be the main mechanism.

• Influences of cavity on ramp flow have been studied. the strong effect of a narrow cavity was observed on ramp flow, suggesting that extreme care is needed in experiments when gaps are incorporated between elements to allow for a measurement.

• Generally separation region in a turbulent boundary layer is much smaller compared to laminar flow. However, large separations were observed for a practical ramp flow with jet injection suggesting that these are hard to avoid in the stage separation problem.

7.3 Future work

• It would be necessary to do simulations of rocket stage separation in a curvilinear reference frame to compare with the planar results obtained in Chapter 6.

• Numerical problems were confronted when trying to simulate a square jet for the M=5.3 rocket-separation study, which was especially due to the small area of the jet and the high momentum flux ratio of jet. Improved resolution in both space and time might help to solve the problem but would greatly increase the computing-hour consumption, which would only be feasible for future work.

• The current code is based on CPU and works well but needs to be updated to be compatible with the GPU in the future to go with the development of high performance computers.

With the development of technology, more complex flows will be solved based on extension of the simulations presented here.

Bibliography

Adams, N. A. Direct numerical simulation of turbulent compression ramp flow. *Theoretical and Computational Fluid Dynamics*, 12:109–129, 1998.

Adams, N. A. Direct simulation of the turbulent boundary layer along a compression ramp at M=3 and Re_θ=1685. *Journal of Fluid Mechanics*, 420:47–83, 2000.

Alam, M. and Sandham, N. D. Direct simulation of 'short' laminar separation bubbles with turbulent reattachment. *Journal of Fluid Mechanics*, 403:223–250, 2000.

Anderson, J. D. Jr. *Computational Fluid Dynamics*. McGraw-Hill, 1995.

Andersson, P., Brandt, L., Bottaro, A., and Henningson, D. S. On the breakdown of boundary layer streaks. *Journal of Fluid Mechanics*, 428:29–60, 2001.

Andreopoulos, J. and Rod, W. Experimental investigation of jets in a crossflow. *Journal of Fluid Mechanics*, 138:93–127, 1984.

Araya, G. and Castillo, L. Direct numerical simulations of turbulent thermal boundary layers subjected to adverse streamwise pressure gradients. *Physics of Fluid*, 25:095107, 2013.

Arnal, D. and Délery, J. Laminar-turbulent transition and shock wave/boundary layer interaction. Technical report, 2001a. Critical technologies for hypersonic vehicle development.

Arnal, D. and Délery, J. Laminar-turbulent transition and shock wave/boundary layer interaction Part B. Shock wave/boundary layer interaction. Technical report, 2001b. Critical technologies for hypersonic vehicle development.

Balakumar, P., Zhao, H., and Atkins, H. Stability of Hypersonic Boundary Layers over a Compression Corner. *AIAA Journal*, 43:760–767, 2005.

Bedarev, I. A., Maslov, A. A., Sidorenko, A. A., Fedorova, N. N., and Shiplyuk, A. N. Experimental and numerical study of a hypersonic separated flow in the vicinity of a cone-flare model. *Journal of Applied Mechanics and Technical Physics*, 43:867–876, 2002.

Benay, R., Chanetz, B., Mangin, B., Vandomme, L., and Perraud, J. Shock wave/ transitional boundary-layer interactions in hypersonic flow. *AIAA Journal*, 44(6): 1243–1254, 2006.

Bianchi, S. VEGA, the European small launcher: Development status, future perspectives, and applications. *ACTA Astronautica*, 63:416–427, 2008.

Bonelli, F., Viggiano, A., and Magi, V. Large eddy simulation of high-density ratio hydrogen jets. In *11th International Conference of Numerical Analysis and Applied Mathematics*, 2013.

Bono, G., Awruch, A. M., and Popiolek, T. L. Computational study of laminar shock-/boundary layer interaction at hypersonic speeds. *Mecánica Computacional*, XXVII: 3135–3150, 2008.

Bower, K. V. William W., Cary, A. W., Alvi, F. S., Raman, G., Annaswamy, A., and Malmuth, N. M. High-frequency excitation active flow control for high-speed weapon release (HIFEX). AIAA 2004-2513, 2004.

Brès, A. G. and Colonius, T. Three-dimensional instabilities in compressible flow over open cavities. *Journal of Fluid Mechanics*, 599:309–339, 2008.

Camussi, R., Guj, G., Imperatore, B., Pizzicaroli, A., and Perigo, D. Wall pressure fluctuations induced by transonic boundary layers on a launcher model. *Aerospace Science and Technology*, 11(5):349–359, 2007.

Carpenter, M. H., Nordström, J., and Gottlieb, D. A stable and conservative interface treatment of arbitrary spatial accuracy. *Journal of Computational Physics*, 148(2): 341–365, 1999.

Chanetz, B., Benay, R., Bousquet, J.-M., Bur, R., Pot, T., Grasso, F., and Moss, J. Experimental and numerical study of the laminar separation in hypersonic flow. *Aerospace Science and Technology*, 2(3):205 – 218, 1998.

Chapman, D. R., Kuhen, D. M., and Larson, H. K. Investigation of separated flows in supersonic and subsonic streams with emphasis on the effect of transition. Technical report, NACA TN-3869, 1957.

Coenen, W. *Absolute instability in the near field of low-density jets*. PhD thesis, Universidad Carlos III de Madrid, 2010.

Cubbison, R. W., Anderson, B. H., and Ward, J. J. Surface Pressure Distributions with a Sonic Jet Normal to Adjacent Flat Surfaces at Mach 2.92 to 6.4. Technical Report NASA TN D-580, 1961.

Das, R. and Kurian, J. Supersonic flow over three dimensional cavities. *The Aeronautical Journal*, 117:175–191, 2013.

De Tullio, N. *Receptivity and transition to turbulence of supersonic boundary layers with surface roughness*. PhD thesis, University of Southampton, 2013.

De Tullio, N. and Sandham, N. D. Direct numerical simulation of breakdown to turbulence in a Mach 6 boundary layer over a porous surface. *Physics of Fluid*, 22: 4105(1)–4105(15), 2010.

Defoort, S., Serre, L., Grenon, R., Varnier, J., Carrier, G., Scherrer, D., and Narmada. ZEHST: environmental challenges for hypersonic passenger transport. AIAA 2012-5873, 2012.

Dolling, D. S. Fifty years of shock-wave/boundary-layer interaction research: What next? *AIAA Journal*, 39(8):1517–1531, Aug 2001.

Drazin, P. G. *Introduction to hydrodynamic stability*. Cambridge University Press, 2002.

Dubief, Y. and Delcayre, F. On coherent-vortex identification in turbulence. *Journal of Turbulence*, 1:1–22, 2000.

Ducros, F., Ferrand, V., Nicoud, F., Weber, C., Darracq, D., Gacherieu, C., and Poinsot, T. Large-eddy simulation of the shock/turbulence interaction. *Journal of Computational Physics*, 152(2):517– 549, 1999.

Eckert, E. Engineering relations for friction and heat transfer to surfaces in high velocity flow. *Journal of the Aeronautical Sciences*, 22:585–587, 1955.

Ferri, A. Experimental results with airfoils tested in the high speed tunnel at Guidonia. Technical report, 1940.

Franko, K. J. and Lele, S. K. Breakdown mechanisms and heat transfer overshoot in hypersonic zero pressure gradient boundary layers. *Journal of Fluid Mechanics*, 730: 491–532, SEP 2013.

Fric, T. and Roshiko, A. Vortical structures in the wake of atransverse jet. *Journal of Fluid Mechanics*, 279:1–47, 1994.

Gajbhiye, R. R. Unsteady aspect of control jets for high speed applications. Master's thesis, School of Engineering Sciences, University of Southampton, 2010.

Gallucci, F. S.and Battie, Volpi, M., Fossati, T., and Curti, G. Vega launch vehicle first flight mission analysis - VV01. In *IEEE First AESS European Conference on Satellite Telecommunications (ESTEL 2012)*, 2012.

Genito, M., Paglia, F., Mogavero, A., and Barbagallo, D. 1st stage separation aerodynamics of vega launcher. In *Proceedings of the 7th European Symposium on Aerothermodynamics*, page 6, 2011. 7th European Symposium on Aerothermodynamics, 9-12 May 2011, Brugge, Belgium.

Grewe, V., Plohr, M., Cerino, G., Muzio, M. D., Deremaux, Y., Galerneau, M., de Saint Martin, P., Chaika, T., Hasselrot, A., Tengzelius, U., and Korovkin, V. D. Estimates of the climate impact of future small-scale supersonic transport aircraft - results from the HISAC EU-project. *The Aeronautical Journal*, 114:199–206, 2010.

Grilli, M., Schmid, P. J., Hickel, S., and Adams, N. A. Analysis of unsteady behaviour in shockwave turbulent boundary layer interaction. *Journal of Fluid Mechanics*, 700: 16–28, 2012.

Hadjadj, A. and Dussauge, J.-P. Shock wave boundary layer interaction. *Shock wave*, 19(6):449–452, 2009.

Harten, A. The artificial compression method for computation of shocks and contact discontinuities. III. Self-adjusting hybrid schemes. *Mathematics of Computation*, 32 (142):363–389, 1978.

Hollo, S. D., McDaniel, J. C., and Hartfield, R. J. Quantitative investigation of compressible mixing: stagged transverse injection into Mach 2 flow. *AIAA Journal*, 32: 528–534, 1994.

Hombsch, M. and Olivier, H. Film cooling in laminar and turbulent supersonic flows. *Journal of Spacecraft and Rockets*, 50(4):742–753, 2013.

Huang, G. *An interactive design enviroment for coal piping system.* PhD thesis, Iowa State University, 2006.

Huerre, P. and Monkewitz, P. A. Local and global instabilities in spatially developing flows. *Annual Review of Fluid Mechanics*, 22:473–537, 1990.

IceAspen. Vega Rocket. http://www.turbosquid.com/3d-models/vega-rocket-3d-max/655678, Feb. 2012.

Ilak, M., Schlatter, P., Bagheri, S., and Henningson, D. S. Bifurcation and stability analysis of a jet in cross-flow: onset of global instability at a low velocity ratio. *Journal of Fluid Mechanics*, 696:94–121, 2012.

Jones, W. P. and Wille, M. Large-eddy simulation of a plane jet in a cross-flow. *International Journal of Heat and Fluid Flow*, 17(3):296–306, 1996.

Katzer, E. On the lengthscales of laminar shock/boundary-layer interaction. *Journal of Fluid Mechanics*, 206:477–496, 1989.

Kaufman, L. G. R. Hypersonic flows past transverse jets. *Journal of Spacecraft*, 4(9): 1230–1235, 1967.

Kawai, S. and Lele, S. K. Mechanisms of jet mixing in a supersonic crossow: a study using large-eddy simulation. Technical report, Center for Turbulence Research, 2007.

Kawai, S. and Lele, S. K. Dynamics and mixing of a sonic jet in a supersonic turbulent crossflow. Technical report, Center for Turbulence Research, 2009.

Kelsot, R. M., Lim, T. T., and Perry, A. E. An experimental study of round jets in cross-flow. *Journal of Fluid Mechanics*, 306:111–144, 1996.

Khoury, G. K. E., Schlatter, P., Noorani, A., Fischer, P. F., Brethouwer, G., and Johansson, A. V. Direct numerical simulation of turbulent pipe flow at moderately high Reynolds numbers. *Flow Turbulence Combustion*, 91:475–495, 2013.

Kim, C.-K., Yu, S.-T. J., and Zhang, Z.-C. Cavity flow in scramjet engine by spacetime conservation and solution element method. *AIAA Journal*, 42:912–919, 2004.

Kim, S.-W. and Benson, T. Calculation of a circular jet in crossflow with a multiple–time-scale turbulence model. *International Journal of Heat and Mass Transfer*, 35 (10):2357 – 2365, 1992.

Krishnamurty, K. *Sound radiation from surface cutouts in high speed flow.* PhD thesis, California Institute of Technology, 1956.

Larchevêque, L., Sagaut, P., Lê, T.-H., and Comte, P. Large-eddy simulation of a compressible flow in a three-dimensional open cavity at high Reynolds number. *Journal of Fluid Mechanics*, 516:265–301, 2004.

Lawal, A. A. *Direct numerical simulation of transonic shock/boundary-layer interactions.* PhD thesis, University of Southampton, 2002.

Lee, C. C. and Barfield, B. F. Interaction of sonic transverse jets with supersonic external flows. *AIAA Journal*, 9(2):304–308, 1971.

Lees, L. and Lin, C. C. Investigation of the stability of the laminar boundary layer in a compressible fluid. Technical report, NACA TR-1115, 1946.

Li, W., Nonomura, T., and Fujii, K. On the feedback mechanism in supersonic cavity flows. *Physic of Fluids*, 25(5):1–15, May 2013.

Loginov, M. S., Adams, N. A., and Zheltovodov, A. A. LES of shock wave/turbulent boundary layer interaction. *High Performance Computing in Science and Engineering*, 3:222–234, 2006.

Lüdeke, H. and Sandham, N. D. Direction numerical simulation of the transition process in a separated supersonic ramp flow. AIAA Paper 2010-4470, 2010.

Mack, L. M. Boundary-layer linear stability theory. Agard 709, Califcrnia Institute of Technology, 1984.

Marini, M. Analysis of hypersonic compression ramp laminar flows under sharp leading edge conditions. *Aerospace Science and Technology*, 5(4):257–271, 2001.

Moin, P. and Mahesh, K. Direct numerical simulation: a tool in turbulence research. *Annual Review of Fluid Mechanics*, 30:539–578, 1998.

Navarro-Martinez, S. and Tutty, O. Numerical simulation of Görtler vortices in hypersonic compression ramps. *Computers and Fluids*, 34(2):225–247, Feb 2005.

Orlebar, C. *The Concorde story*. Osprey Publishing, 2004.

Pagella, A., Babucke, A., and Rist, U. Two-dimensional numerical investigations of small-amplitude disturbances in a boundary layer at Ma=4.8: Compression corner versus impinging shock wave. *Physics of Fluids*, 16(7):2272–2281, 2004.

Pagella, A., Rist, U., and Wagner, S. Numerical investigations of small-amplitude disturbances in a boundary layer with impinging shock wave at Ma=4.8. *Physics of Fluid*, 14:2088–2101, 2002.

Papamoschou, D. and Hubbard, D. G. Visual observations of supersonic transverse jets. *Experiments in Fluids*, 14:468–471, 1993.

Peterson, D. M., Subbareddy, P. K., and Candler, G. V. Assessment of synthetic inflow generation for simulating injection into a supersonic crossflow. AIAA Paper 2006-8128, 2006.

Pointwise, I. *Gridgen 15.13 User Manual*, November 2008.

Powrie, H. E. G., Ball, G. J., and East, R. A. Comparison of the interactions of two and three dimensional transverse jets with a hypersonic free stream. Technical report, AGARD CP-534, 1993.

Powrie, H. *A study of the interaction between an underexpanded normal jet and a hypersonic freestream*. PhD thesis, School of Engineering Sciences, University of Southampton, 1996.

Priebe, S. and Martin, M. P. Low-frequency unsteadiness in shock wave-turbulent boundary layer interaction. *Journal of Fluid Mechanics*, 699:1–49, 2012. ISSN 0022-1120.

Qin, N. and Redlich, A. Massively separated flows due to transverse sonic jet in laminar hypersonic stream. *Shock Waves*, 9:87–93, 1999.

Reshotko, E. Boundary-layer stability and transition. *Annual Review of Fluid Mechanics*, 8:311–349, 1976.

Rizzetta, D. P. and Visbal, M. R. Large-eddy simulation of supersonic cavity flowfields including flow control. *AIAA Journal*, 41:1452–1462, 2003.

Roberts, G. T., Schuricht, P. H., and Mudford, N. R. Heating enhancement caused by a transverse control jet in hypersonic flow. *Shock Waves*, 8:105–112, 1998.

Roberts, G. T. and East, R. A. Liquid crystal thermography for heat transfer measurement in hypersonic flows: A review. *Journal of Spacecraft and Rockets*, 33:761–768, 1996.

Robinet, J.-C. Bifurcations in shock-wave/laminar-boundary-layer interaction: global instability approach. *Journal of Fluid Mechanics*, 579:85–112, 2007.

Rockwell, D. and Naudascher, E. Review: self-sustaining oscillations of flow past cavities. *Journal of Fluids Engineering*, 100:152–165, 1978.

Rogallo, R. S. and Moin, P. Numerical simulation of turbulent flows. *Annual Review of Fluid Mechanics*, 16:99–137, 1984.

Rowley, C. W., Colonius, T., and Basu, A. J. On self-sustained oscillations in two-dimensional compressible flow over rectangular cavities. *Journal of Fluid Mechanics*, 455:315–346, 2002.

Sandham, N., Yao, Y., and Lawal, A. A. Large-eddy simulation of transonic turbulent flow over a bump. *International Journal of Heat and Fluid Flow*, 24:584–595, 2003.

Sandham, N. D., Li, Q., and Yee, H. C. Entropy splitting for high-order numerical simulation of compressible turbulence. *Journal of Computational Physics*, 178(2): 307–322, May 2002.

Sandham, N. D., Roberts, G. T., Surenedra, A., Gajbhiye, R., Zhang, K., and Hu, Z. Calculations of jet injection into a hypersonic crossflow using the TINA and SBLI codes. Technical report, University of Southampton, 2011.

Sarohia, V. Experimental investigation of oscillations in flows over shallow cavities. *AIAA Journal*, 15:984–991, 1977.

Schlatter, P., Bagheri, S., and Henningson, D. S. Self-sustained global oscillations in a jet in crossflow. *Theoretical and Computational Fluid Dynamics*, 25:129–146, 2011.

Schrijer, F. Investigation of Görtler vortices in a hypersonic double compression ramp flow by means of infrared thermography. In *10th International Conference on Quantitative InfraRed Thermography*, 2010.

Serre, L. and Defoort, S. LAPCAT II : towards a Mach 8 civil aircraft concept, using advanced Rocket/Dual-mode ramjet propulsion system. AIAA 2009-7328, 2009.

Spaid, F. W. Two-dimensional jet interaction studies at large values of Reynolds and Mach numbers. *AIAA Journal*, 13(11):1430–1434, 1975.

Theofilis, V. and Colonius, T. Special issue on global flow instability and control. *Theoretical and Computational Fluid Dynamics*, 25:1–6, 2011.

Touber, E. *Unsteadiness in shock-wave/boundary-layer interaction*. PhD thesis, University of Southampton, 2010.

Touber, E. and Sandham, N. D. Comparison of three large-eddy simulations of shock-induced turbulent separation bubbles. *Shock Waves*, 19(6):469–478, 2009a.

Touber, E. and Sandham, N. D. Large-eddy simulation of low-frequency unsteadiness in a turbulent shock-induced separation bubble. *Theoretical and Computational Fluid Dynamics*, 23(2):79–107, 2009b.

Touber, E. and Sandham, N. D. Low-order stochastic modelling of low-frequency motions in reflected shock-wave/boundary-layer interactions. *Journal of Fluid Mechanics*, 671:417–465, 2011.

Vinokur, M. On one-dimensional stretching functions for finite-difference calculations. Technical report, NASA Contractor Report 3313, 1980.

Wang, H., Sun, M., Qin, N., Wu, H., and Wang, Z. Characteristics of oscillations in supersonic open cavity flows. *Flow, Turbulence and Combustion*, 90:121–142, 2013.

Wang, H., Wang, Z., Sun, M., and Qin, N. Large eddy simulation based studies of jet-cavity interactions in a supersonic flow. *ActaAstronautica*, 93:182–192, 2014.

Warburton, K. *Control jets in low density flow*. PhD thesis, University of Oxford, 1999.

Watanabe, J., Kouchi, T., Takita, K., and Masuya, G. Large-eddy simulation of jet in supersonic crossflow with different injectant species. *AIAA Journal*, 50:2765–2778, 2012.

White, F. M. *Viscous Fluid Flow*. McGraw-Hill, 1974.

Wray, A. A. Very low storage time-advancement schemes. Technical report, NASA Ames Research Centre, 1986.

Wu, M. and Martin, M. P. Direct numerical simulation of supersonic turbulent boundary layer over a compression ramp. *AIAA Journal*, 45(4):879–889, 2007.

Yao, Y., Krishnan, L., Sandham, N. D., and Roberts, G. T. The effect of Mach number on unstable disturbances in shock/boundary-layer interactions. *Physic of Fluids*, 19 (5):1–15, 2007.

Yao, Y., Petty, D., Barrington, P., Yao, J., and Mason, P. Direct numerical simulation of jets in cross-flow. *International Journal of Computational Fluid Dynamics*, 20(5): 279–285, 2006.

Yee, H. C., Sandham, N. D., and Djomehri, M. J. Low-dissipative high-order shock-capturing methods using characteristic-based filters. *Journal of Computational Physics*, 150(1):199–238, 1999.

Yee, H. C., Vinokur, M., and Djomehri, M. J. Entropy splitting and numerical dissipation. *Journal of Computational Physics*, 162:33–81, 2000.

Yilmaz, I., Ayli, E., and Aradag, S. Investigation of the effects of length to depth ratio on open supersonic cavities using CFD and proper orthogonal decomposition. *The Scientific World Journal*, pages 1–12, 2013.

Yokoi, H., Ozawa, H., Koyama, H., and Nakamura, Y. Aerodynamic heating of an open cavity in hypersonic compression ramp flow. AIAA 2012-0286, 2012.

You, Y., Luedeke, H., and Hannemann, K. Injection and mixing in a scramjet combustor: DES and RANS studies. *Proceedings of the Combustion Institute*, 34:2083–2092, 2013.

Yu, K. H. and Schadow, K. Cavity-actuated supersonic mixing and combustion control. *Combustion and Flame*, 99:295 – 301, 1994.

Yu, W., Shi-He, Y., Zhi, C., Qing-Hu, Z., and Dun-Dian, G. Experimental investigations on structures of supersonic laminar/turbulent flow over a compression ramp. *ACTA Physica Sinica*, 62:1–12, 2013.

Zak, A. Vega space launcher and its major components. http://www.russianspaceweb .com/vega_lv.html, 2012.

Zhang, K., Sandham, N., and Hu, Z. Numerical simulations of global instability in spearated flows at high Mach number. In *AIAA 2012-3123 New Orleans*, 2012.

Zhen, H., Gao, Z., and Lee, C. Numerical investigation on jet interaction with a compression ramp. *Chinese Journal of Aeronautics*, 26:898–908, 2013.

Zhuang, N. *Experimental investigation of supersonic cavity flows and their control*. PhD thesis, The Florida State University, 2007.